
1119

TRANSPORTATION RESEARCH RECORD

Geotechnology

TRANSPORTATION RESEARCH BOARD
NATIONAL RESEARCH COUNCIL
WASHINGTON, D.C. 1987

Transportation Research Record 1119

Price \$21.50

Editor: Elizabeth W. Kaplan

Typesetter: Harlow A. Bickford

Layout: Betty L. Hawkins

modes

- 1 highway transportation
- 3 rail transportation
- 4 air transportation

subject areas

- 25 structures design and performance
- 35 mineral aggregates
- 61 soil exploration and classification
- 62 soil foundations
- 63 soil and rock mechanics
- 64 soil science

Transportation Research Board publications are available by ordering directly from TRB. They may also be obtained on a regular basis through organizational or individual affiliation with TRB; affiliates or library subscribers are eligible for substantial discounts. For further information, write to the Transportation Research Board, National Research Council, 2101 Constitution Avenue, N.W., Washington, D.C. 20418.

Printed in the United States of America

Library of Congress Cataloging-in-Publication Data
National Research Council. Transportation Research Board.

Geotechnology.

(Transportation research record, ISSN 0361-1981 ; 1119)

1. Soil mechanics—Congresses. 2. Foundations—

Congresses. I. National Research Council (U.S.).

Transportation Research Board. II. Series.

TE7.H5 no. 1119 380.5 s 87-34783

[TA710.A1] [625.7'32]

ISBN 0-309-04472-3

Sponsorship of Transportation Research Record 1119

GROUP 2—DESIGN AND CONSTRUCTION OF TRANSPORTATION FACILITIES

David S. Gedney, Harland Bartholomew & Associates, chairman

General Design Section

Jarvis D. Michie, Dynatech Engineering, Inc., chairman

Committee on Photogrammetry and Aerial Surveys

Tommy F. Howell, Texas State Department of Highways & Public Transportation, chairman

Darrel L. Baker, Fred B. Bales, Thomas E. Carlsen, Roger R. Chamard, Frank F. Cooper, Lee W. Eason II, Gibson W. Fairman, Carl I. Fonnesbeck, Jack H. Hansen, Irving Isaacson, Malcolm H. Macleod, Ben R. Maxwell, Jr., Louis J. Medrano, Stanton P. Michal, Olin W. Mintzer, Harold T. Rib, Donald R. Rich, Jerry W. Robinson, Jack K. Stoll, A. Keith Turner, Robert D. Turpin, Donald E. Wilbur, Marshall S. Wright, Jr.

Committee on Mineral Aggregates

Richard C. Ingberg, Minnesota Department of Transportation, chairman
David A. Anderson, Gordon W. Beecroft, Robert J. Collins, Warren B. Diederich, James R. Dunn, Stephen W. Forster, Richard D. Gaynor, James G. Gehler, Erling K. Hansen, Robert F. Hinshaw, George J. Kassal, Dah-Yinn Lee, Charles R. Marek, Vernon J. Marks, Michael P. McCormick, John T. Paxton, Richard W. Petrarca, Kenneth R. Wardlaw, Lennard J. Wyld

Committee on Lime and Lime-Fly Ash Stabilization

Raymond K. Moore, University of Kansas, chairman
Alvin H. Meyer, University of Texas at Austin, secretary
Mehmet C. Anday, John J. Emery, James H. Gumm, Kenneth A. Gutschick, C. W. Heckathorn, Thomas W. Kennedy, Harold W. Landrum, Dallas N. Little, Eugene B. McDonald, W. C. Ormsby, Thomas M. Petry, Marshall R. Thompson, Muntaz A. Usmen, Paul J. Wright

Committee on Soils and Rock Instrumentation

William H. Hansmire, Parsons, Brinckerhoff et al., chairman
Loren R. Anderson, Harold E. Beeston, Jerry C. Chang, John B. Gilmore, Gordon E. Green, Robert D. Holtz, Kenneth A. Jackura, Richard H. Ledbetter, Anthony Minniti, Ernest T. Selig, Doug Smith, John L. Walkinshaw, Anwar E. Z. Wissa, Duncan C. Wyllie

Committee on Transportation Earthworks

Robert D. Holtz, Purdue University, chairman
Mehmet C. Anday, Thomas A. Bellatty, William A. Cutter, Joseph D'Angelo, Jerome A. Dimaggio, Raymond L. Gemme, Wilbur M. Haas, William P. Hofmann, J. M. Hoover, Robert W. Israel, Ilan Juran, James E. Kelly, Philip C. Lambe, Richard E. Landau, Robert M. Leary, Larry Lockett, Richard P. Long, C. William Lovell, Kenneth M. Miller, Lyle K. Moulton, Walter C. Waidelich, David E. Weatherby, William G. Weber, Jr., Gary C. Whited

Committee on Foundations of Bridges and Other Structures

Richard S. Cheney, Geotechnical Engineer, chairman
Arnold Aronowitz, Francois J. Baguelin, Jean-Louis Briaud, Bernard E. Butler, Murty S. Devata, Albert F. Dimillio, Bengt H. Fellenius, George G. Goble, Richard J. Goettle III, James S. Graham, Larry K. Heinig, Hal W. Hunt, Gay D. Jones, Jr., Hugh S. Lacy, Clyde N. Laughter, Robert M. Leary, John F. Ledbetter, Jr., Richard P. Long, Lyle K. Moulton, Michael Wayne O'Neill, Arthur J. Peters, Austars R. Schnore, Harvey E. Wahls

Committee on Exploration and Classification of Earth Materials

J. Allan Tice, Law Engineering Testing Company, chairman
Robert K. Barrett, P. J. Beaven, John A. Bischoff, Martin C. Everitt, H. Allen Gruen, Robert K. H. Ho, Robert B. Johnson, Jeffrey R. Keaton, C. William Lovell, B. Sen Mathur, Donald E. McCormack, Jim McKean, Olin W. Mintzer, R. L. Nanda, Zvi Ofer, Harold T. Rib, Lawrence C. Rude, Surendra K. Saxena, James Chris Schwarzhoff, Berke L. Thompson, Sam I. Thornton, A. Keith Turner, Gilbert Wilson, Duncan C. Wyllie

Committee on Engineering Geology

A. Keith Turner, Colorado School of Mines, chairman
Robert K. Barrett, William D. Bingham, Robert C. Deen, Jerome V. Degraff, Martin C. Everitt, Jeffrey R. Keaton, C. William Lovell, Stephen F. Obermeier, Peter V. Patterson, Rodney W. Prellwitz, Berke L. Thompson, J. Allan Tice, Duncan C. Wyllie

Neil F. Hawks and George W. Ring III, Transportation Research Board staff

Sponsorship is indicated by a footnote at the end of each paper. The organizational units, officers, and members are as of December 31, 1986.

NOTICE: The Transportation Research Board does not endorse products or manufacturers. Trade and manufacturers' names appear in this Record because they are considered essential to its object.

Foreword

The papers included in this Record deal with various facets of geotechnical engineering. The Record should be of use to those interested in the application of technology to highway transportation and researchers.

The subjects covered by the papers include theoretical calculation of contact stresses in granulated materials in pavement; effect of soil characteristics on hydrated-lime and portland cement treatments; use of portable data loggers, time-lapse movie cameras, acoustic emission devices, analytical photogrammetry techniques, and microcomputer technology in work related to slope stability and landslides along highways; construction and instrumentation of high approachment embankments for bridge crossings; determination of ultimate pull-out resistance of square vertical anchors in saturated clays; design, construction, and other aspects of soil nailing of retaining structures; experimental and analytical study of the behavior of 45-degree underreamed footings in a field environment; an alternate method of obtaining California bearing ratio values and moisture susceptibility of soils; effects of dilatometer penetration on soil parameters estimated from dilatometer data in sands; in situ test methods that offer significant promise in evaluation of the properties of stiff soils; and case histories on the problems and solutions related to blasting and hazardous rock stability conditions along highways.

The **Transportation Research Record** series consists of collections of papers on a given subject. Most of the papers in a **Transportation Research Record** were originally prepared for presentation at a TRB Annual Meeting. All papers (both Annual Meeting papers and those submitted solely for publication) have been reviewed and accepted for publication by TRB's peer review process according to procedures approved by a Report Review Committee consisting of members of the National Academy of Sciences, the National Academy of Engineering, and the Institute of Medicine.

The views expressed in these papers are those of the authors and do not necessarily reflect those of the sponsoring committee, the Transportation Research Board, the National Research Council, or the sponsors of TRB activities.

Transportation Research Records are issued irregularly; approximately 50 are released each year. Each is classified according to the modes and subject areas dealt with in the individual papers it contains. TRB publications are available on direct order from TRB, or they may be obtained on a regular basis through organizational or individual affiliation with TRB. Affiliates or library subscribers are eligible for substantial discounts. For further information, write to the Transportation Research Board, National Research Council, 2101 Constitution Avenue, N.W., Washington, D.C. 20418.

Contents

- v Foreword
- 1 Theory of Use of Granulated Materials in Road Construction
Valery A. Semenov
- 11 An Evaluation of Lime and Cement Stabilization
Thomas W. Kennedy, Robert Smith, Richard J. Holmgreen, Jr., and Maghsoud Tahmoressi
- 26 Automation of Monitoring of Geotechnical Instrumentation
Alan L. Hinckley, Bertrand D. Tanner, and Eric C. Campbell
- 30 Acoustic Monitoring of Landslides
David M. Jurich and Russell J. Miller
- 39 Use of Time-Lapse Movie Photography in Landslide Monitoring
Edwin P. Belknap and John B. Gilmore
- 47 Monitoring Landslide Movement with a 35-mm Camera
J. D. Ballantyne, D. R. Dean, Jr., and B. L. Thompson
- 55 Contracting for Tieback Walls in Kentucky
William Phillips
- 61 Westbound Embankment Preload on Rainier Avenue, Seattle, Washington
David M. Cotton, Alan P. Kilian, and Tony Allen
- 76 Ultimate Resistance of Vertical Square Anchors in Clay
Braja M. Das

-
- 83 Structural Behavior of 45-Degree Underreamed Footings**
Shamim A. Sheikh and Michael W. O'Neill
- 91 An Improved California Bearing Ratio Test Procedure**
Colin A. Franco and K. Wayne Lee
- 98 Lateral Response and Earth Pressure Parameters of Cohesionless Soils Related to Flat Dilatometer Data: A Laboratory Study**
E. Sabri Motan and Brian J. Jacot
- 105 Compaction Prestress**
S. O. Nwabuokei and C. W. Lovell
- 115 Tunnel "Daylighting" on the Alaska Railroad**
F. C. Weeks, T. B. Trueblood, A. Krause, and D. C. Wyllie
- 119 Resolution of Some Common Problems in Highway Blasting**
Lewis L. Oriard
- 126 Effects of Soil Properties on Microwave Dielectric Constants**
Thomas J. Jackson
- 132 Appalachian Folds, Lateral Ramps, and Basement Faults: A Modern Engineering Problem?**
Howard A. Pohn
- 134 Terrain Simulation for Transportation Planning**
Jack H. Hansen and Mitchell J. Hurst
- 139 Nailed-Soil Retaining Structures: Design and Practice**
Ilan Juran

Theory of Use of Granulated Materials in Road Construction

VALERY A. SEMENOV

The use of granulated materials (especially low-strength materials) in pavements is limited because such materials undergo significant breakage during packing and use. The breakage is mainly due to the extraordinary contact stresses in the particles of the material, which lead to its fragmentation and the formation of melkozem (fine earth) and a sharp decrease in the strength of the material. The method presented here for calculating and controlling the contact stresses in granulated material is the first attempt at the theoretical calculation of stresses in a stochastic medium. Using the model for the stochastic packing of granulated materials proposed by the author as a starting point, the packing density, the number of contacts in an arbitrary cross section through the material, the area of contact between individual particles, and the contact stresses are calculated. The theory presented in this paper makes it possible to carry out various theoretical calculations associated with engineering process control and monitoring of the strength of material over the service life of a road covering, and it can also be used for other problems.

Local low-strength materials and industrial by-products are used for highway construction in many countries. The strength of these materials averages from 30 to 40 MPa, so they undergo fragmentation in packing and a large number of fine particles (up to 22 percent) are formed. The process of particle fragmentation continues over the lifetime of the road. This lowers the usable lifetime of the pavement to from 5 to 7 years. Stronger materials (with a strength of from 80 to 140 MPa) are similarly damaged, but this process proceeds more slowly.

Particle fragmentation is due to the high contact stresses that arise in the material; reducing these stresses during the packing process and under exposure to traffic will allow low-strength materials to be used and their life span in road coverings to be increased. There are currently no methods of calculating the contact stresses in complex stochastic media (any real granulated material, such as crushed stone, gravel, sand, soil).

The purpose of this paper is to develop a theoretical model and engineering methods for calculating stresses in granulated materials. A stochastic model and theoretical nomograms have been developed for calculating contact stresses. The proposed model includes the packing of particles of various sizes and shapes. The results presented here are based on 5 years of research carried out by the author at the Vladimir Polytechnical Institute (Vladimir, USSR).

THEORETICAL MODEL FOR DETERMINING THE PACKING DENSITY OF A STOCHASTIC MEDIUM

Packing density may be determined from geometric considerations by averaging the results of a large number of iterations with respect to random packings composed of individual particles. The number of iterations is determined by the required accuracy of calculation and ranges from 100 to 300.

The particle sizes in each iteration are selected randomly (using the Monte Carlo method, the Korobov algorithm, or a table of random numbers). The continuous-sorting method may also be used. The volume packing density (ρ) is defined as

$$\rho = \frac{v_{\text{avg}}}{V_{\text{avg}}} = \frac{\int_D v(r) f(r) dr}{\int_D V(r) f(r) dr} \quad (1)$$

where

- v = the volume occupied by the particles of the material in an arbitrary tetrahedron,
- V = the volume of the tetrahedron,
- $f(r)$ = the particle size distribution function,
- D = the region in space ($r_{\min} \leq r \leq r_{\max}$, $r > 0$), and
- r_{\min} and r_{\max} = the minimum and maximum sizes of the particles of material in the packing.

This formula may be used as long as the following condition is satisfied:

$$\frac{r_1}{r_4} \leq 1 + \frac{r_1}{r_2} + \frac{r_1}{r_3} + 2 \sqrt{\frac{r_1}{r_2} + \frac{r_1}{r_3} + \frac{r_1 r_1}{r_2 r_3}} \quad (2)$$

where r_1 , r_2 , r_3 , and r_4 are the radii of the particles in the packing in a given iteration and r_4 is the minimum radius. An analysis of Equation 2 showed that the proposed model can be used for any highway construction materials or soils. The volume density (ρ_{in}) is determined by using Equation 1 to average the results of the determination of the density of a packing consisting of four random radii at each iteration. The calculation procedure presented hereafter is used to determine

Department of Civil Engineering, The University of Texas at Austin, Austin, Tex. 78712. Permanent affiliation: School of Highway and Agricultural Construction and Highway Department, The Polytechnical Institute of Vladimir Gorky, 87, Vladimir, 600 005 USSR.

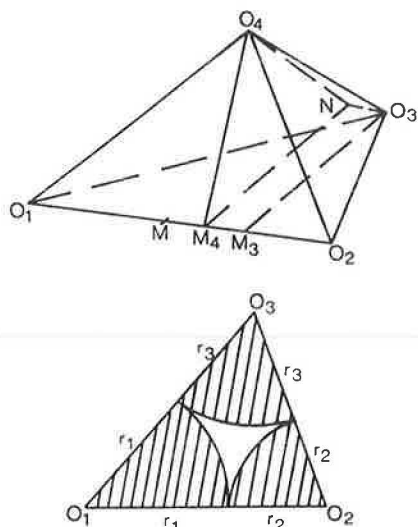


FIGURE 1 Theoretical diagram of stochastic packing.

the packing density at each iteration. Figure 1 is a diagram that shows the determination of r_{in} (where O_1 , O_2 , O_3 , and O_4 are the centers of the particles that are in contact).

The value of $O_3M_3 = h_3$ from the triangle $O_1O_2O_3$ is determined by using Heron's formula:

$$S_{O_1O_2O_3} = \sqrt{r_1 r_2 r_3 (r_1 + r_2 + r_3)}$$

At the same time,

$$S_{O_1O_2O_3} = \frac{1}{2}(r_1 + r_2)h_3$$

Equating these two expressions gives

$$h_3 = \frac{2\sqrt{r_1 r_2 r_3 (r_1 + r_2 + r_3)}}{r_1 + r_2} \quad (3)$$

To determine $|M_3M_4|$, the geometric center of the edge O_1O_2 is denoted by M ; then

$$|M_3M_4| = |X_3 - X_4| \quad (4)$$

where $X_3 = MM_3$ is the distance between the foot of altitude h_3 and Point M , and $X_4 = MM_4$ is the distance from the foot of altitude h_4 to Point M . The value of X_3 can be determined from triangle $O_1O_2O_3$ using the Pythagorean theorem:

$$(r_1 + r_3)^2 - h_3^2 = \left(\frac{r_1 + r_2}{2} + X_3\right)^2$$

and

$$(r_2 + r_3)^2 - h_3^2 = \left(\frac{r_1 + r_2}{2} + X_3\right)^2$$

from which, after a system of two equations is solved, is obtained

$$X_3 = \frac{r_1 - r_2}{r_1 + r_2} \left(\frac{r_1 + r_2}{2} + r_3 \right)$$

Similarly, the value of X_4 can be obtained from the triangle $O_1O_2O_4$, and

$$|M_3M_4| = \left| \frac{(r_1 - r_2)(r_3 - r_4)}{r_1 + r_2} \right|$$

can be determined using Equation 4. By the Pythagorean theorem, $|NO_4| = h_0$ can be obtained from the triangle O_3NO_4 :

$$h_0 = \frac{1}{r_1 + r_2} \sqrt{(r_1 + r_2)^2 (r_3 + r_4)^2 - (r_1 - r_2)^2 (r_3 - r_4)^2}$$

By the cosine theorem, from the triangle M_4O_4N is obtained

$$h_0^2 = h_3^2 + h_4^2 - 2h_3h_4 \cos \gamma_{12} \quad (5)$$

where γ_{12} is the dihedral angle with the edge O_1O_2 . Using Equation 5, it is found that

$$\cos \gamma_{12} = \frac{h_3^2 + h_4^2 - h_0^2}{2h_3h_4}$$

The volume of the tetrahedron $O_1O_2O_3O_4$ can now be determined:

$$V = \frac{1}{6} h_3 h_4 \sin \gamma_{12} (r_1 + r_2) \quad (6)$$

From Equation 6, it follows that

$$\sin \gamma_{12} = \frac{1}{2h_3h_4} \sqrt{4h_3^2h_4^2 - (h_3^2 + h_4^2 - h_0^2)^2}$$

Hence,

$$V = \frac{1}{12} (r_1 + r_2) \sqrt{4h_3^2h_4^2 - (h_3^2 + h_4^2 - h_0^2)^2} \quad (7)$$

From Expression 3,

$$h_3h_4 = \frac{4}{(r_1 + r_2)^2} \left[r_1r_2(r_1 + r_2)(r_3 + r_4) - r_3r_4(r_1^2 + r_2^2) \right] \quad (8)$$

The following notation is now introduced:

$$\begin{aligned} \sigma_1 &= r_1 + r_2 + r_3 + r_4 \\ \sigma_2 &= r_1r_2 + r_1r_3 + r_1r_4 + r_2r_3 + r_2r_4 + r_3r_4 \\ \sigma_3 &= r_1r_2r_3 + r_1r_2r_4 + r_1r_3r_4 + r_2r_3r_4 \\ \sigma_4 &= r_1r_2r_3r_4 \\ a &= r_1 + r_2 \\ A &= r_1r_2 \\ b &= r_3 + r_4 \\ B &= r_3r_4 \end{aligned} \quad (9)$$

Then,

$$h_3 h_4 = \frac{4}{a^2} \sqrt{A^2 B (a^2 + ab + B)}$$

$$h_3^2 + h_4^2 - h_0^2 = \frac{4}{a^2} (abA - a^2 B + 2AB) \quad (10)$$

Substituting Equation 10 into Equation 7,

$$V = \frac{1}{3} \sqrt{4\sigma_2 \sigma_4 - \sigma_3^2} \quad (11)$$

The volume (v) occupied by the spherical segments within the tetrahedron with centers at the Points O_i (Figure 1) can now be determined. Suppose that there is a spherical triangle ($M_1 M_2 M_3$) on a sphere of radius R (i.e., the arcs $M_1 M_2$, $M_2 M_3$, and $M_1 M_3$ are segments of great circles). The angles formed by the tangents to the arcs will be designated by γ_1 , γ_2 , and γ_3 (Figure 2).

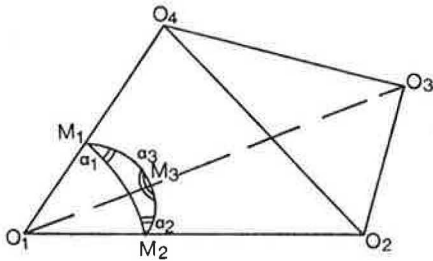


FIGURE 2 Diagram for determining the volume of solids within the tetrahedron.

By Gauss's theorem,

$$S_{M_1 M_2 M_3} = R^2 (\gamma_1 + \gamma_2 + \gamma_3 - \pi)$$

Hence,

$$v_{O_1 M_1 M_2 M_3} = \frac{R^3}{3} (\gamma_1 + \gamma_2 + \gamma_3 - \pi)$$

Note that the angle $M_1 M_2 M_3 = \gamma_2 = \gamma_{12}$, and so forth. Then

$$v = \sum_{i < j} \frac{1}{3} (r_i^3 + r_j^3) \gamma_{ij} - \frac{p}{3} \sum_{i=1}^4 r_i^3 \quad (12)$$

($i, j=1, 2, 3, 4$)

The dihedral angles γ_{ij} may be determined by transforming Equation 6 using the notation of Equation 9 and Equations 10:

$$\cos \gamma_{ij} = \frac{r_i r_j \sigma_2 - (r_i r_j)^2 - \frac{r_i + r_j}{2} \sigma_3}{\sqrt{r_i r_j (r_i + r_j) \sigma_1 \sigma_4 + \sigma_4^2}} \quad (13)$$

Equation 13 may be used to obtain all six values of the angles.

The stochastic model that has been developed for the dense packing of particles of soil and other materials can be used extensively in highway construction and maintenance. Thus it is possible to calculate the theoretical density of asphalt con-

crete, cement concrete, crushed stone, gravel, and soil. This makes it possible to substantially improve density norms and develop an optimal production technology. It is also possible to use this model to calculate the contact stresses in particles of material, for which it is necessary to determine the individual contact area between the particles in the material and the total number of contacts in a random cross section.

DETERMINATION OF THE AREA OF CONTACT BETWEEN PARTICLES IN THE MATERIAL

In determining the area of contact, it is assumed that the particle size distribution is known, and the particles will be represented by two concentric spheres with radii R_0 and R_1 given by the minimum and maximum particle radii (Figure 3). It is assumed that there is some probability $[p(x)]$ for material to be found within a sphere of radius R_1 ; this probability is equal to 1 for a sphere with radius R_0 . Probability $p(x)$ is obtained from experimental data. It is also assumed that some interpenetration of spheres is possible, and the amount of interpenetration is denoted by α (Figure 3).

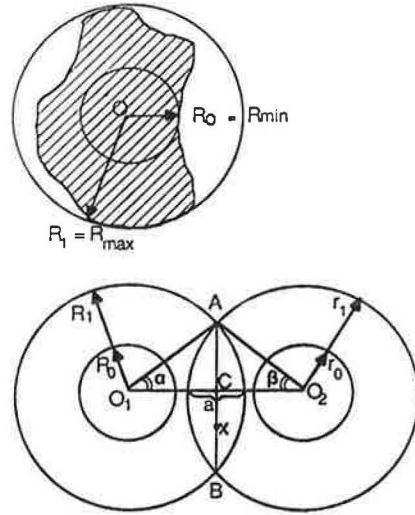


FIGURE 3 Diagram for determining the area of contact between particles.

To determine the area of contact, it will be assumed that the area is equal to the area formed by rotating line AB about Point C :

$$S_{AB} = 2\pi \int_0^{R_1 \sin \alpha} t p_1 \left(\sqrt{t^2 + R_1^2 \cos^2 \alpha} \right) dt$$

$$x = \sqrt{t^2 + R_1^2 \cos^2 \alpha} \quad (14)$$

Then,

$$S_{AB} = 2\pi \int_{R_1 \cos \alpha}^{R_1} x p_1(x) dx$$

If two particles of different sizes participate in the contact, the area of contact will be given by the arithmetic mean of the areas of contact for each particle:

$$S_a = \frac{S_{AB} + S_{BA}}{2} = \pi \left[\int_{R_1 \cos \alpha}^{R_1} x p_1(x) dx + \int_{r_1 \cos \beta}^{r_1} x p_2(x) dx \right] \quad (15)$$

The parameters A , B , and a must be expressed in probabilistic form. To do this, the contact between the particles is represented by graphs of the probabilities $p_1(x)$ and $p_2(x)$ (Figure 4).

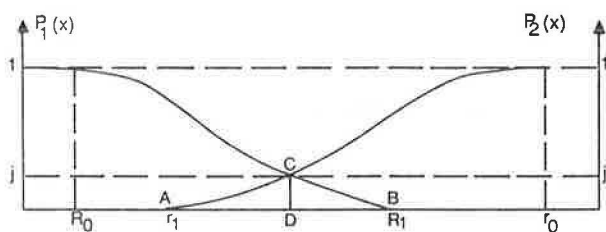


FIGURE 4 Diagram for calculating the depth of interpenetration for the spheres used to model the particles of material.

It is assumed that the parameter describing the depth to which the spheres penetrate one another is $CD = j$. From Figure 4,

$$AD = r_1 - t'_{1-j} \text{ and } BD = R_1 - t_{1-j}$$

where t_{1-j} and t'_{1-j} are the $(1-j)$ th quantiles. It is now found that $a = r_1 + R_1 - (t_{1-j} + t'_{1-j})$, so that Equation 15 takes the following form:

$$S_j = \pi \left[\int_{t_{1-j}}^{R_1} x p_1(x) dx + \int_{t'_{1-j}}^{r_1} x p_2(x) dx \right] \quad (16)$$

Rewriting Equation 16,

$$\begin{aligned} \int_{t_{1-j}}^{R_1} x p_1(x) dx &= \int_{t_{1-j}}^{R_1} x [1 - F_1(x)] dx \\ &= \frac{x^2}{2} \Big|_{t_{1-j}}^{R_1} - \int_{t_{1-j}}^{R_1} x \left[\int_{-\infty}^x f(t) dt \right] dx \\ &= \frac{1}{2} (R_1^2 - t_{1-j}^2) - \int_{(0)}^{t_{1-j}} x f(t) dt dx \\ &= \frac{1}{2} (R_1^2 - t_{1-j}^2) - \int_{-\infty}^{t_{1-j}} \left(\frac{x^2}{2} \Big|_{t_{1-j}}^{R_1} \right) f(t) dt \end{aligned}$$

$$\begin{aligned} &= - \int_{t_{1-j}}^{R_1} \left(\frac{x^2}{2} \Big|_{t_{1-j}}^{R_1} \right) f(t) dt \\ &= - \frac{\gamma t_{1-j}^2}{2} + \frac{1}{2} \int_{t_{1-j}}^{R_1} t^2 f(t) dt \end{aligned}$$

it is found that

$$S_j = \frac{\pi}{2} \left[\int_{t_{1-j}}^{R_1} t^2 f_1(t) dt + \int_{t'_{1-j}}^{r_1} t^2 f_2(t) dt - j(t_{1-j}^2 + t'_{1-j}^2) \right] \quad (17)$$

Equation 17 is a general expression for determining the contact area between particles. Several specific examples will be discussed next.

Example 1

When both particles have a uniform distribution of radii (Figure 5), it is found that

$$t_{1-j} = R_0 + (1-j)(R_1 - R_0) = R_1 - j(R_1 - R_0)$$

Then,

$$S_j = \frac{j^2 \pi}{3} (R_1 - R_0) [3R_1 - 2j(R_1 - R_0)] \quad (18)$$

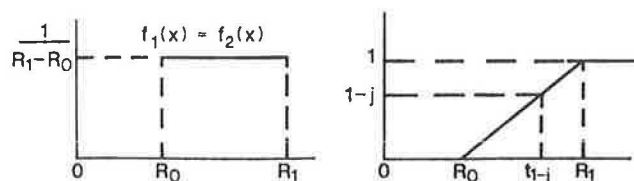


FIGURE 5 Diagram for Example 1.

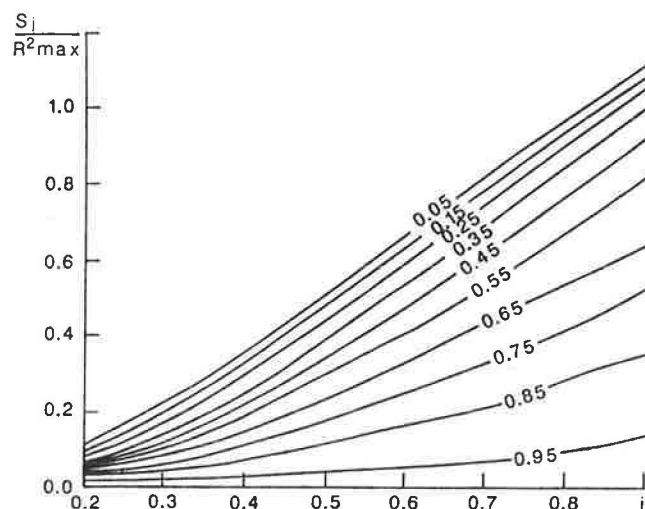


FIGURE 6 Nomogram for determining the areas of contact between particles with a normal distribution of radii.

Equation 18 was then used to construct a nomogram (Figure 6). Suppose that $R_1 = 2$ cm, $R_0 = 1$ cm, and $j = 0.5$; then,

$$S_j = \frac{3.14}{4 \cdot 3} (2.1) [3 \cdot 2 - 2 \cdot 0.5(2 - 1)] = 1.3 \text{ cm}^2$$

The surface area of the larger sphere is

$$S_1 = 4\pi R_1^2 = 50.2 \text{ cm}^2$$

Thus, the relative area of contact is

$$S_{\text{rel}} = \frac{1.3 \cdot 100}{50.2} = 2.7 \text{ percent}$$

Example 2

For the case of normally distributed particle radii, the following expressions are obtained:

$$S'_j = \pi \left((0.5 - jt_{1-j}^2) \sigma^2 + \frac{2\sigma m}{(2\pi)^{1/2}} \left\{ \left[\exp \left(-t_{1-j}^2 / 2 \right) \right] - t_{1-j} (2\pi)^{1/2} \right\} - Ft_{1-j} \right) \quad (19)$$

$$S'_j = \frac{S'_j + S''_j}{2} \quad (20)$$

where

- S'_j and S''_j = the areas of contact for the first and second particles, respectively;
- m = the mathematical expectation value of the particle radius;
- s = the root-mean-square deviation of the particle radii; and

$$Ft_{1-j} = \frac{1}{(2\pi)^{1/2}} \int_0^{t_{1-j}} t^2 \exp(-t^2/2) dt$$

The quantile t_{1-j} can now be determined by using the following equation:

$$\frac{1}{2} - j = \Phi \left(\frac{x_{1-j} - m}{\sigma} \right) \quad (21)$$

where

$$\Phi \left(\frac{x_{1-j} - m}{\sigma} \right)$$

is the Laplace function. For $j = 0.5$, the quantile $x_{(j=0.5)} = r_{\text{avg}}$, and the equation becomes much simpler:

$$S_{0.5} = \pi \sigma \left[\frac{\sigma}{2} + \left(\frac{2}{\pi} \right)^{1/2} r_{\text{avg}} \right] \quad (22)$$

A nomogram has been constructed from Equation 22 (Figure 7). Suppose that $r_{\text{avg}} = 2$ cm, and $s = 0.2$ cm. Then

$$S_{0.5} = 3.14 \cdot 0.2 \left(\frac{0.2}{2} + 0.8 \cdot 2 \right) = 1.07 \text{ cm}^2$$

which is about 2 percent of the surface area of the larger sphere.

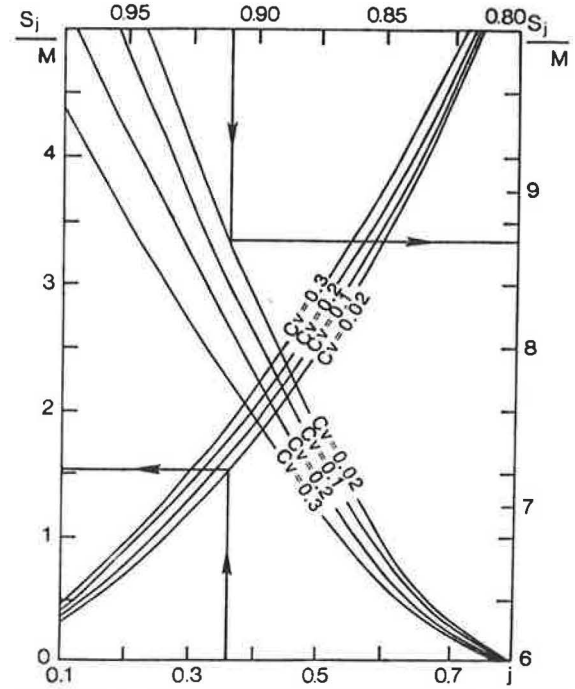


FIGURE 7 Nomogram for determining the particle contact area when the particle radii are normally distributed.

Example 3

For the Weibull distribution of particle radii Weibull's law may be written in the form

$$f(x) = \lambda k (x - r_{\min})^{k-1} \exp[-\lambda(x - r_{\min})^k] \quad (23)$$

where λ and k are the scale and form parameters, respectively. The quantile x_{1-j} may be calculated from the equations

$$j = e^{-\lambda(x_{1-j} - r_{\min})^k} \quad (24)$$

$$x_{1-j} = r + \left(\frac{1}{\lambda} \ln \frac{1}{j} \right)^{1/k}$$

By substituting Equation 23 into Equation 17 and rearranging, it is found that

$$S'_j = \pi \left(\frac{1}{\lambda} \right)^{2/k} \bar{A}_1 + 2\pi r_{\min} \left(\frac{1}{\lambda} \right)^{1/k} \bar{A}_2 \quad (25)$$

Rearranging Equation 25,

$$S'_j = (r_{\text{avg}} - r_{\min})^2 A_1 + r_{\min} (r_{\text{avg}} - r_{\min}) A_2 \quad (26)$$

where

$$A_1 = \frac{\pi}{\Gamma\left(1 + \frac{1}{k}\right)^2} \bar{A}_1$$

$$A_2 = \frac{2\pi}{\Gamma\left(1 + \frac{1}{k}\right)} \bar{A}_2$$

$$\bar{A}_1 = \Gamma\left(1 + \frac{2}{k}\right) - j\left(\ln \frac{1}{j}\right)^{2/k} - \int_0^{\ln 1/j} t^{2/k} \exp(-t) dt$$

$$\bar{A}_2 = \Gamma\left(1 + \frac{1}{k}\right) - j\left(\ln \frac{1}{j}\right)^{1/k} - \int_0^{\ln 1/j} t^{1/k} \exp(-t) dt$$

and $\Gamma(z)$ is the gamma function.

The final value of the area of contact is given by Equation 20. A nomogram (Figure 8) was constructed using these equations.

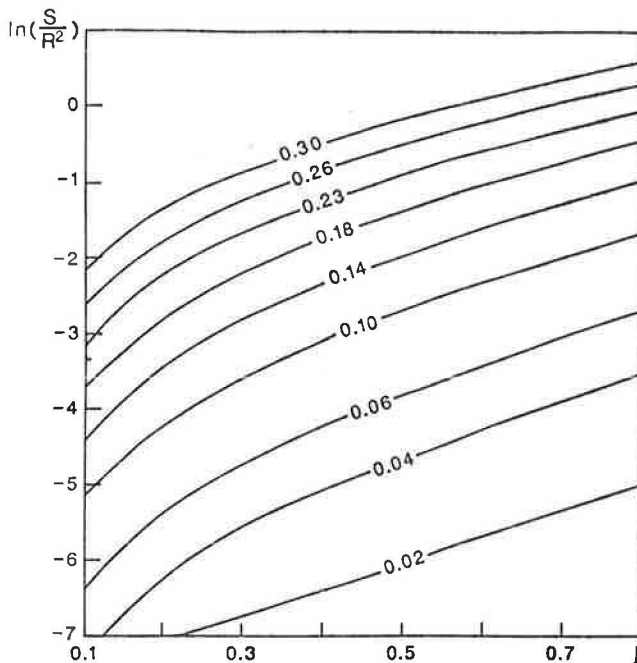


FIGURE 8 Nomogram for calculating the area of contact between particles that have a Weibull distribution with variable parameters.

Suppose that

$$\begin{aligned} R_{\text{avg}} &= 2 \text{ cm, } CV_R = 0.10: j = 0.5; \text{ therefore, } S_j = 0.26 \text{ cm}^2 \\ R_{\text{avg}} &= 2 \text{ cm, } CV_R = 0.04: j = 0.5; \quad S_j = 0.04 \text{ cm}^2 \\ R_{\text{avg}} &= 2 \text{ cm, } CV_R = 0.10: j = 0.3; \text{ therefore, } S_j = 0.10 \text{ cm}^2 \\ R_{\text{avg}} &= 1 \text{ cm, } CV_R = 0.10: j = 0.5; \quad S_j = 0.064 \text{ cm}^2 \end{aligned}$$

where CV_R is the coefficient of variation of the particle radii.

Thus, the area of contact increases with increasing j , D , and R_{avg} .

This solution has been thoroughly tested by N. M. Egorov, an engineer at the Vladimir Polytechnical Institute. The value of j for individual particles of crushed stone varied over a wide range from 0.071 to 1.000 with an average value of $j = 0.5$. The contact area between the particles ranged from 3 to 707 mm^2 . A comparison of the theoretical and experimental values of the contact area showed that the difference between them is no greater than 12 percent, so that the solution obtained may be used extensively in practical calculations.

DETERMINATION OF THE NUMBER OF CONTACTS BETWEEN PARTICLES OF MATERIAL IN A RANDOM CROSS SECTION

To determine contact stresses, an expression must be obtained for the number of contacts in an arbitrary plane passing through some volume of granulated material. Imagine that there is a connection between the particles in the form of the edge of a graph (a line connecting the centers of the particles). The probability that this edge (AB) is intersected by an arbitrary plane (Figure 9) is to be determined. The position of the edge in space may be characterized by three numbers: (a) the length of the edge (l), (b) the distance from the center of the edge to the intersecting plane (x), and (c) the angle between the edge and

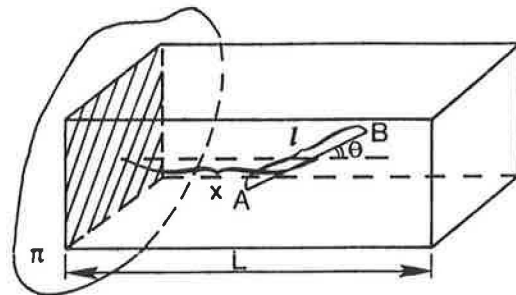


FIGURE 9 Theoretical diagram for determining the number of contacts between particles in a plane passing through the packing.

the horizontal (θ). These are all random quantities with corresponding probability density functions $p(l)$, $p(x)$, and $p(\theta)$. The limits of variation for l , θ , and x are $l_{\min} \leq l \leq l_{\max}$, $0 \leq \theta \leq \pi/2$, and $0 \leq x \leq L$. It is assumed that the quantity x is uniformly distributed, so that

$$p(x) = \begin{cases} 1/L & x \in [0, L] \\ 0 & x \notin [0, L] \end{cases} \quad (27)$$

The edge is intersected by the plane (p) if and only if $x < (l/2) \cos \theta$. The probability that the edges intersect the plane p will be designated. Then,

$$p = \int \int \int_{(V)} p(l)p(\theta)p(x) dl d\theta dx$$

$$\begin{aligned}
&= \int_0^{\pi/2} d\theta \int_{l_{\min}}^{l_{\max}} \frac{1}{2} \cos \theta p(l) p(\theta) dl \\
&= \frac{l_{\text{avg}}}{2L} \int_0^{\pi/2} \cos \theta p(\theta) d\theta
\end{aligned} \quad (28)$$

where V is the volume of the material.

The number of particles within the volume $[V(N_p)]$ may be obtained from the following equations:

$$\begin{aligned}
LS\rho &= \frac{4\pi}{3} r_{\text{avg}}^3 N_p \\
N_p &= \frac{3LS\rho}{4\pi r_{\text{avg}}^3}
\end{aligned} \quad (29)$$

where

- L and S = the dimensions of the volume being studied (see Figure 9),
 r = the volume packing density of the material, and
 r_{avg} = the mean particle radius in the packing of the material.

The number of contacts between particles in a volume $[V(N_p)]$ is

$$Q_r = \frac{1}{2} k N_p = \frac{3kL\rho}{8\pi r_{\text{avg}}^3} \quad (30)$$

where k is the coordination number.

The number of right-hand contacts intersected by plane p is

$$\bar{Q}_r = Q_r p_r \quad (31)$$

Now consider various distribution laws for the quantity θ : Suppose θ is distributed uniformly on $[0, \pi/2]$:

$$p(\theta) = \begin{cases} 2/\pi & \in \theta [0, \pi/2] \\ 0 & \notin \theta [0, \pi/2] \end{cases}$$

$$p_r = \frac{l_{\text{avg}}}{2L} \frac{2}{\pi}$$

hence,

$$\begin{aligned}
\bar{Q}_r &= \frac{l_{\text{avg}}}{L\pi} \frac{3LS\rho k}{8\pi r_{\text{avg}}^3} \\
&= \frac{3l_{\text{avg}} S \rho k}{16\pi^2 r_{\text{avg}}^3} = \frac{3S\rho k}{8\pi^2 r_{\text{avg}}^2}
\end{aligned} \quad (32)$$

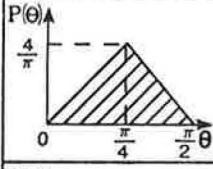
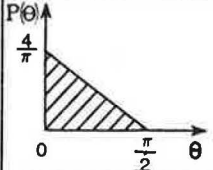
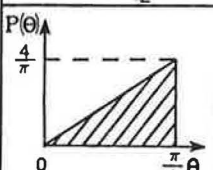
If it is assumed that, on the average, $l_{\text{avg}} = 2r_{\text{avg}}$ and that the total number of intersected contacts $Q = Q_r + Q_l = 2Q_r$,

$$Q = \frac{3\rho S k}{2\pi^2 r_{\text{avg}}^2} \quad (33)$$

Other distribution laws for θ lead to the theoretical formulas given in Table 1.

The solution obtained is in good agreement with the formula obtained by Rumpf (1)—the difference is no greater than 5 percent. A comparison of Equation 33 and the test data of Zimin and Timchenko (2) and Andriyanov and Zimon (3) showed that the difference is no greater than 12 percent, which is sufficiently accurate.

TABLE 1 THEORETICAL FORMULAS FOR DETERMINING THE NUMBER OF CONTACTS

Distribution Law for Q	Formula for Determining Number of Contacts	Transformation Coefficient to the Uniform Distribution Law
	$\bar{Q} = \frac{12kS\rho[\sqrt{2}-1]}{\pi^3 r^2}$	$n = \frac{8}{\pi}[\sqrt{2}-1] = 1.0548$
	$\bar{Q} = \frac{6 \cdot S \cdot \rho \cdot k}{\pi^3 r^2}$	$n = \frac{4}{\pi} = 1.2733$
	$\bar{Q} = \frac{6 \cdot S \cdot \rho \cdot k}{\pi^3 r^2} \left[\frac{\pi}{2} - 1 \right]$	$n = \frac{4}{\pi} \left[\frac{\pi}{2} - 1 \right] = 0.7267$

The areas of contact between particles have been determined, so it is now rather straightforward to calculate the total area of contact between the particles in a random intersecting plane and the actual contact stresses. The practical use of the theoretical solutions obtained in this paper will be discussed next.

EXAMPLES OF THE PRACTICAL USE OF THE THEORETICAL SOLUTIONS

Example 1

The contact stresses that arise on compression of a sample of asphalt concrete when the particles of the material have a uniform distribution can be calculated. The maximum and minimum radii of the spheres (which were determined by the maximum and minimum size of an individual particle) can be written in the following way with a 95 percent confidence coefficient:

$$R_1 = r_{\text{avg}}(1 + 2CV)$$

$$R_0 = r_{\text{avg}}(1 - 2CV) \quad (34)$$

The degree of interpenetration of the spheres is assumed to be $\gamma = 0.5$, and the number of contacts between particles is assumed to be 8.

The ratio of the increase in the contact stresses to the mean strength of the sample can be calculated by using

$$k_k = \frac{pS}{F_{\text{con}}p} = \frac{S}{F_{\text{con}}} \quad (35)$$

where

- p = the pressure on the sample,
- S = the area of the sample, and
- F_{con} = the area of the contacts between particles in a random cross section.

The value of F_{con} can be obtained from Equation 18 using Equation 33:

$$F_{\text{con}} = \sum_{i=1}^n \frac{2\gamma^2 \rho S k \alpha_i (R_1 - R_0)}{\pi (R_1 + R_0)^2} [3R_1 - 2\gamma(R_1 - R_0)] \quad (36)$$

where α_i is the fractional content of the i th fraction ($i = 1, 2, 3, \dots, n$). Substituting Equations 36 and 34 into Equation 35 and rearranging yields

$$k_k = \frac{\pi}{4\rho CV(3 + 2CV)} \quad (37)$$

Equation 37 was used to construct the theoretical nomogram in Figure 10. From Figure 10, it is apparent that the smaller the coefficient of variation for particle size (i.e., the closer the particles come to being spherical in shape), the higher the contact stress in the material.

Thus the strength of the sample essentially depends on the

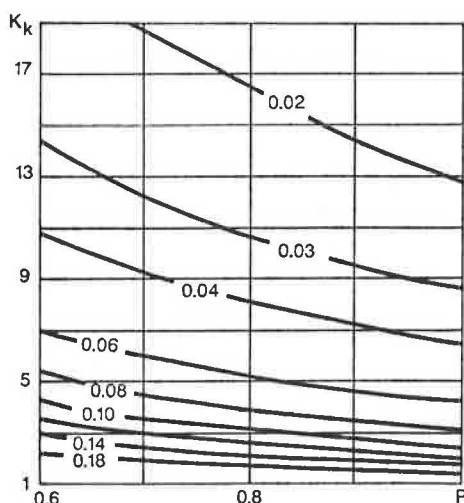


FIGURE 10 Ratio of the contact stresses and mean stresses when testing samples of material for compression, expansion, or deformation as a function of the density of the material.

shape of the particle, which is now ignored. For all practical purposes, contact stresses are inversely proportional to density.

Example 2

It is to be determined whether crushed granite will be fragmented during compaction if the particle strength is 100 MPa, the coefficient of variation of the particle sizes $CV = 0.04$, the packing load is 30 MPa, and the required density $r = 0.9$. From the nomogram in Figure 10, the permissible value of $CV = 0.07$ is obtained. Consequently, this degree of compaction can only be achieved with the material becoming fragmented.

Example 3

For the compaction of granulated material by rigid rollers (Figure 11), the exterior load is taken from the Hertz-Belyaev

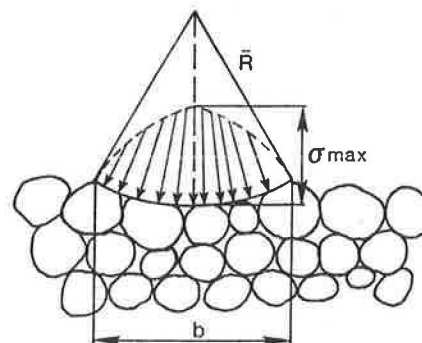


FIGURE 11 Diagram for calculating the contact stresses in the rolling of granulated (loose) materials.

solution (4) for an infinite cylinder of radius R . The maximum stress in the center of the loaded area is

$$\sigma_{\text{max}} = \frac{0.5642}{(1 - \mu^2)^{1/2}} \left(\frac{qE}{R} \right)^{1/2} \quad (38)$$

where μ and E are Poisson's coefficient and the modulus of elasticity (MPa) of the material being packed and q is the linear load per unit length of the roller (hundred weight per centimeter).

In this calculation, it is assumed that a load σ_{max} is applied to an area $d_{\text{avg}} \times d_{\text{avg}}$ (where d_{avg} is the mean size of the packed particles in centimeters). Using Equations 34–36 and 38 yields

$$k_k = \frac{12}{\pi CV(3 + 2CV)} \quad (39)$$

Equation 39 was used to construct Table 2.

Thus the shape of the crushed stone substantially affects (by a factor of as much as 12) the contact stresses directly beneath the roller. The contact stresses in the lower layers of the packed

TABLE 2 VALUE OF k_k IN THE PACKING OF MATERIAL BY RIGID ROLLERS

C_V	0.02	0.06	0.10	0.14	0.18	0.30
Value of k_k for various distributions						
U	62.82	20.40	11.94	8.32	6.32	3.54
N	78.80	25.63	15.02	10.48	7.97	4.48

Note: U = Uniform distribution and N = normal distribution.

material can be calculated using Figure 10. A comparison of the data in Table 2 and Figure 10 shows that the contact stresses in the second and subsequent layers of material are approximately a factor of 3 smaller than the stresses directly beneath the roller; this leads to fragmentation of the upper layer during rolling. To decrease the extent to which the material in the surface layer becomes fragmented, the diameter of the roller must be increased without increasing its weight, rolling should be done on a layer of elastic material (rubber, canvas, etc.), fine crushed stone or other material capable of increasing the contact area should be spread on top of the upper layer before rolling, vibrating rollers should be used, and so forth. When the sizes of the particles in the material being packed are normally distributed,

$$k_k = \frac{4}{\pi C_V \left[\frac{C_V}{2} + \left(\frac{2}{\pi} \right)^{1/2} \right]} \quad (40)$$

The theoretical results from this equation are given in Table 2. The value of k_k for the normal distribution is an average of a factor 1.255 times greater than that for the uniform distribution.

Example 4

The contact stresses for various rigid rollers will now be calculated (light rollers are less than 5 metric tons, medium rollers are 5 to 10 metric tons, and heavy rollers are 10 to 16 metric tons). A mean density $r = 0.7$ is used in the calculation. The

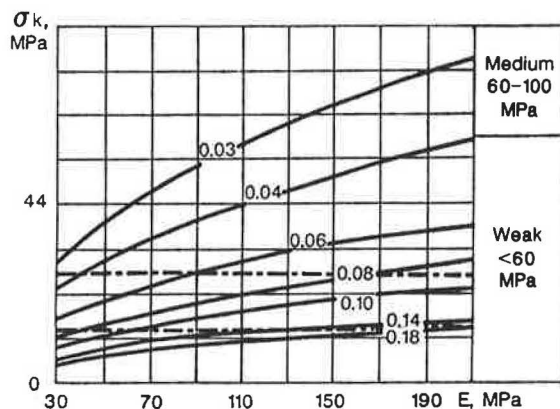


FIGURE 12 Contact stresses in crushed stone packed by a light roller.

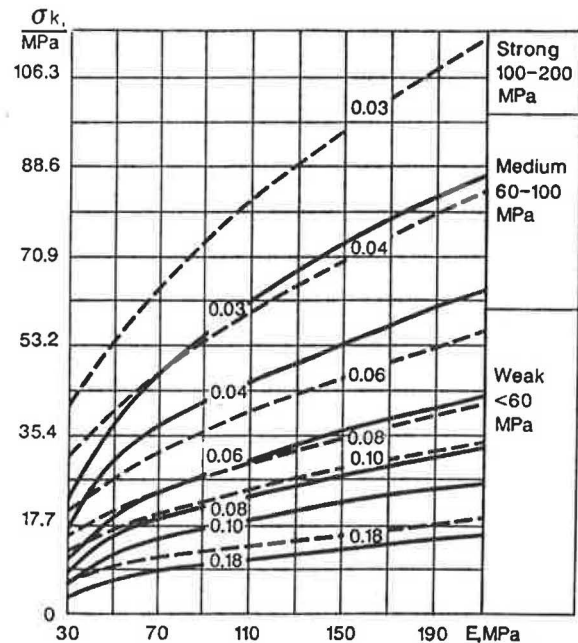


FIGURE 13 Contact stresses in crushed stone packed by a medium-weight roller.

results of the calculation are given in three nomograms (Figures 12-14), which may be used to select the roller type.

To calculate the contact stresses in the surface layer, the data in Figure 10 need to be increased by a factor of 3. The nomograms obtained (Figures 12-14) allow selection of the type of roller to be used in packing granulated materials.

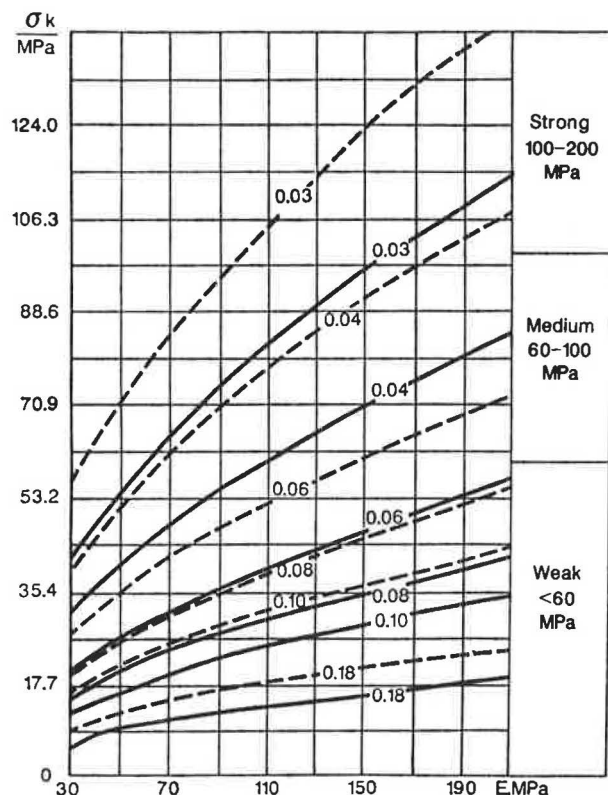


FIGURE 14 Contact stresses in crushed stone packed by a heavy roller.

Suppose that a roller must be selected to be used for packing fine limestone with a strength of 60 MPa. To avoid crushing the material, the conditions given in Table 3 must be satisfied. Thus, to preserve the particle size of the material, it must be laid on a base of less strength; the weaker the material, the weaker the base should be. The material itself should be non-uniform with respect to particle size. When the material becomes fragmented, the coefficient of variation of the particle sizes increases significantly; this leads to a sharp decrease in the contact stresses. This point is confirmed by the test data of E. A. Pospelov, obtained under the guidance of the author of this paper.

TABLE 3 SELECTION OF ROLLER TYPE

Type of Roller	Necessary Conditions for Rolling			
	For the Lower Layers of the Material Being Packed		For the Surface Layer	
	C_V	E, MPa	C_V	E, MPa
Light	≥ 0.04	≤ 210	≥ 0.08 ≥ 0.10	≤ 110 ≤ 170
Medium	≥ 0.04 ≥ 0.03	$\leq 110 - 190$ $\leq 60 - 110$	≥ 0.10 ≥ 0.08	$\leq 80 - 160$ $\leq 60 - 100$
Heavy	≥ 0.06 ≥ 0.04	$\leq 150 - 220$ $\leq 70 - 110$	≥ 0.18	≤ 170

Example 5

The packing of material by a pneumatic roller will now be discussed. When a pneumatic roller is used on packed material, the transmission of force occurs through the raised portions of the tread so that the pressure on them will be greater than the mean pressure of the wheel on the packed layer. The pressure under the raised portions of the tread for rollers in current use varies over a wide range from $q = 0.42$ to 2.4 MPa; for the most widely used rollers, $q = 0.42$ to 1.6 MPa.

Figure 10 is used for calculating the contact stresses within the layer of material being packed and Table 2 for the contact

stresses in the surface layer. Suppose that the air pressure in the roller tires is 0.6 MPa. Taking the structure of the tread into account, the pressure will be $0.6 \times 1.7 = 1.02$ MPa. The degree of packing of the material is assumed to be $r = 0.7$, and the coefficient of variation for the particle sizes $CV = 0.06$. Then the contact stresses within the layer will be $s_k = 6 \times 1.02 = 6.12$ MPa, and the stress at the surface will be $s_k = 20.4 \times 1.02 = 20.8$ MPa. If the fragmentation resistance of the material is 30 MPa, the material will not become fragmented under these packing conditions, at least not to a great extent.

CONCLUSIONS

The theoretical solution presented here allows the calculation of the engineering conditions for constructing layers with low-strength materials. Use of this method in the development of technology for packing local low-strength limestone in the Vladimir region of the USSR has made it possible to use local materials and industrial by-products widely; the usable life span of such materials in highway pavement was increased by a factor of 1.2 to 1.5, and their modulus of elasticity was increased by a factor of 1.1 to 1.3. The solution obtained can also be used to calculate the composition of the mineral mixture for asphalt concrete, cement concrete, and the like.

The theoretical solution can also be used to improve the results of laboratory tests of soils and materials.

REFERENCES

1. H. Rumpf. *Chemie-Ingenieur-Technik*, Vol. 30, No. 3, 1958, pp. 144-158.
2. M. A. Zimin and N. K. Timchenko. Standards for the Amount of Moisture in Washed Crushed Stone and Gravel to Ensure That They Do Not Freeze. In *Transactions of the All-Union Highway Scientific Research Institute* (Trudy SoyuzdorNII), No. 21, 1967, pp. 52-64.
3. A. D. Zimon and E. I. Andrianov. Autohesion of Loose Materials (Autogeziya sypuchikh materialov). *Metallurgiya*, Moscow, 1978.
4. N. M. Belyaev. Works in the Theory of Elasticity and Plasticity (Trudy po teorii uprugosti i plastichnosti), Gostekhtekhnizdat, Moscow, 1957.

Publication of this paper sponsored by Committee on Mineral Aggregates.

An Evaluation of Lime and Cement Stabilization

THOMAS W. KENNEDY, ROBERT SMITH, RICHARD J. HOLMGREEN, JR., AND
MAGHSOUD TAHMORESSI

Stabilization of clay materials is of interest to any engineer who must deal with this type of soil. Stabilization techniques can be mechanical or chemical, or both, but the addition of a stabilizing agent is generally the favored approach. Lime in one form or another has been the most widely used stabilization agent for clay. However, portland cement to stabilize clay has been promoted and used in some applications. It was the purpose of this research to define the effectiveness of hydrated lime and portland cement on three Texas clays. Variables evaluated included two levels of treatment, two levels of pulverization, two compaction efforts, two moisture conditions, and a range of curing times. On the basis of the results and conditions of this test program, lime treatment of expansive, high-plasticity soils was more favorable for compressive strength attainment than was cement treatment of these soils. In general, lime treatment produced higher dry-conditioned strengths, but the major advantage was in the wet-conditioned strengths. Lime treatment provided significantly better resistance to moisture damage when these soils were compacted by the modified compactive effort. Cement treatment of low-plasticity sandy clay produced significantly higher compressive strengths than did lime treatment of this soil.

The modification of soils to improve their engineering properties has been practiced for many years. Many investigations and research programs have addressed the development of materials evaluation and mixing techniques to determine the best combinations of soils and stabilizing agents. Economics have also played an important role in determining the best procedures and materials. Recently, material and construction economics have made more materials competitive, thus opening the way for more approaches than were previously used.

In many parts of Texas, engineers must deal with several different types of clay materials varying from extremely expansive to moderately active. Stabilization or modification of these clays is necessary for proper construction. In the past, lime has been used primarily for clay soil stabilization, and cement has been preferred for granular or sandy soils. However, cement has been promoted and used on some clay soils in Texas. To better understand this application of cement with clay soils, a research project was undertaken. Several variables were introduced to evaluate both hydrated lime and portland cement as stabilizing agents for clay materials. The experimental program and results are discussed here.

EXPERIMENTAL PROGRAM

The objectives of the study were to compare the dry and wet unconfined compressive strength characteristics of soils treated with hydrated lime and portland cement, to evaluate the importance of pulverization for the unconfined compressive strength of soils treated with portland cement, and to determine the effect of compactive effort.

The experimental program involved three soils, two stabilizing agents (hydrated lime and portland cement), two levels of treatment, two levels of pulverization, two levels of compaction, two levels of moisture conditioning, and a range of curing times.

Materials

Soils

Three Texas soils were used in the study. Two of the soils were from Dallas County and are described as Dalco sandy clay and Dalco clay. The third soil was from Harris County near Houston and is described as Beaumont clay. The characteristics of the three soils are given in Table 1.

Additives

The three soils were treated with commercially available portland cement and hydrated lime. The cement was Type I portland cement manufactured by Alamo Cement Company of San Antonio, Texas. The lime was hydrated lime manufactured by Austin White Lime Company of Austin, Texas.

The three soils were treated with 4 and 7 percent portland cement or hydrated lime, based on the dry weight of the soil. These treatment levels would be expected to fully stabilize the lime-treated soils and modify the cement-treated soils. However, these application rates are currently being used and compared.

Laboratory Procedure

The following laboratory procedures were used in an attempt to simulate field conditions.

TABLE 1 CHARACTERISTICS OF SOILS USED IN THIS STUDY

Soil	Liquid Limit	Plastic Limit	Plasticity Index	Minus No. 200 Sieve Material	Unified Soil Classification
Dalco clay	72	33	39	100	CH
Dalco sandy clay	27	16	11	49	SC
Beaumont clay	60	24	36	100	CH

Pulverization

The soils were oven-dried at 110°F for 5 days. The soils were then pulverized and separated on the 3/4-in. sieve and the No. 4 sieve. The three soil sizes were combined to produce soils that satisfied the following gradation requirements:

- Pulverized: 100 percent passing the No. 4 sieve and
- Unpulverized: 85 percent passing the No. 4 sieve and 15 percent passing the 1 1/2-in. sieve and retained on the 3/4-in. sieve.

Treatment

Portland Cement Four or seven percent cement was added to the dry soil along with sufficient water to produce the optimum moisture content for the cement and soil mixture. The soil and cement were mixed for approximately 5 min using a 1-ft³ Lancaster automatic mixer. The soils were compacted immediately after mixing without curing, which simulates the current practice of cement modification of clay soils.

Hydrated Lime Four or seven percent hydrated lime was added to the soil in the form of a lime-water slurry. The amount of water was equal to that required to produce the optimum water content for the mixture. The soil and lime were mixed for approximately 5 min using the Lancaster mixers. The lime-treated mixtures were placed in plastic bags and allowed to mellow (cure) for 3 days before compaction. This curing procedure, which may not be required if adequate pulverization can be obtained, is similar to the procedure often used in lime stabilization construction.

No Treatment The soil was mixed at the optimum water content for approximately 5 min. Compaction occurred immediately after mixing.

Compaction

The three treated and untreated soils were compacted at the optimum moisture for maximum dry density using the following compactive efforts and procedures:

- Dalco sandy clay: Modified Proctor (ASTM D 1557)
- Dalco clay: Modified Proctor (ASTM D 1557)

Beaumont clay: Modified Proctor (ASTM D 1557)
Standard Proctor (ASTM D 688)

As previously mentioned, the untreated and cement-treated soils were compacted immediately after mixing without a curing period, and the lime-treated soils were compacted after a 3-day mellowing period. Additional water was added, as needed, to bring the mixture to the optimum water content for compaction.

Curing

One set of specimens was tested immediately after compaction and served as a control. All of the other specimens were wrapped in plastic to prevent loss of moisture and were placed in a room at 72°F and 65 percent relative humidity. Specimens were under these conditions for periods of 0, 7, 28, or 119 days. After the initial curing period, the specimens to be subjected to wetting were unwrapped, removed, and placed on porous stones in a pan of water in a room at 100 percent humidity for 7 days. The specimens to be tested in the dry condition were allowed to cure for an additional 7 days. Thus the total cure times were 7, 14, 35, and 126 days, except for the specimens tested immediately after compaction (Table 2).

TABLE 2 CURING TIMES

Cure	Days				
Initial	0	0	7	28	119
Additional	0	7	7	7	7
Total	0	7	14	35	126

Testing

Immediately after the prescribed total curing period, the specimens were tested in unconfined compression according to ASTM D 1663. Specimens were loaded at a constant deformation rate of 0.115 in./min at 75°F, and the load and corresponding vertical deformations were recorded on an X-Y plotter.

Properties Analyzed

Plasticity characteristics (Atterberg limits) and unconfined compressive strengths were determined for the treated and untreated soils.

Atterberg Limits

The liquid limit, plastic limit, and plasticity index were determined immediately after treatment for portland cement and after a 3-day mellowing period for hydrated lime.

Unconfined Compressive Strength

The unconfined compressive strength was determined over the range of curing times. Tests were conducted on both dry and wet specimens as described under curing.

Experiment Design

A summary of the experimental design is given in Table 3. Two replicate specimens per cell or test condition were tested as indicated by the numbers. The specimens for the longer-term curing conditions were prepared first in order to minimize the time required for the study. All treatment levels were coded to minimize bias during testing.

PRESENTATION OF RESULTS

The primary objective of this study was to compare the strength and plasticity characteristics of three cement-treated and lime-treated Texas soils. Unconfined compression tests on compacted specimens were used to evaluate the strengths of the treated soils. The strengths of dry and wet specimens were compared to establish the moisture susceptibility, or retained strength, of the treated soils. The importance of pulverization for the strength of cement-treated soils and the effects of the degree of compactive effort on both cement-treated and lime-treated soils were evaluated.

Atterberg Limits

Both cement and lime produced no change or a slight increase in the liquid limits and a large increase in the plastic limits, thus producing a significant decrease in the plasticity indexes of the treated soils.

TABLE 3 EXPERIMENTAL DESIGN FOR UNCONFINED COMPRESSION TESTS

Soil	Compactive Effort	Moisture Condition	Total Cure Time (days)	Untreated Pulverized at 0%	Cement-Treated ^a				Lime-Treated ^a	
					Pulverized		Unpulverized		Pulverized	
					4%	7%	4%	7%	4%	7%
Dalco clay	Modified Proctor	Dry	0	2	2	2	—	—	2	2
			7	2	2	2	2	2	2	2
			14	2	2	2	2	2	2	2
			35	2	2	2	2	2	2	2
			126	2	2	2	2	2	2	2
		Wet	7	2	2	2	2	2	2	2
			14	2	2	2	2	2	2	2
			35	2	2	2	2	2	2	2
			126	2	2	2	2	2	2	2
			0	2	—	2	—	—	—	2
			7	2	—	2	—	—	—	2
			14	2	—	2	—	—	—	2
			35	2	—	2	—	—	—	2
			126	2	—	2	—	—	—	2
			0	2	—	2	—	—	—	2
Beaumont clay	Modified Proctor	Dry	7	2	—	2	—	—	—	2
			14	2	—	2	—	—	—	2
			35	2	—	2	—	—	—	2
			126	2	—	2	—	—	—	2
		Wet	7	2	—	2	—	—	—	2
			14	2	—	2	—	—	—	2
			35	2	—	2	—	—	—	2
			126	2	—	2	—	—	—	2
		Standard Proctor	0	2	2	2	2	2	2	2
			7	2	2	2	2	2	2	2
			14	2	2	2	2	2	2	2
			35	2	2	2	2	2	2	2
			126	2	2	2	2	2	2	2
		Wet	7	2	2	2	2	2	2	2
			14	2	2	2	2	2	2	2
			35	2	2	2	2	2	2	2
			126	2	2	2	2	2	2	2
			0	2	2	2	2	2	2	2
Dalco sandy clay	Modified Proctor	Dry	7	2	2	2	2	2	2	2
			14	2	2	2	2	2	2	2
			35	2	2	2	2	2	2	2
			126	2	2	2	2	2	2	2
		Wet	7	2	2	2	2	2	2	2
			14	2	2	2	2	2	2	2
			35	2	2	2	2	2	2	2
			126	2	2	2	2	2	2	2
			0	2	2	2	2	2	2	2
			7	2	2	2	2	2	2	2
			14	2	2	2	2	2	2	2
			35	2	2	2	2	2	2	2
			126	2	2	2	2	2	2	2
			0	2	2	2	2	2	2	2
			7	2	2	2	2	2	2	2

NOTE: Total specimens = 428.

^aAdditive expressed as percentage by dry weight of soil.

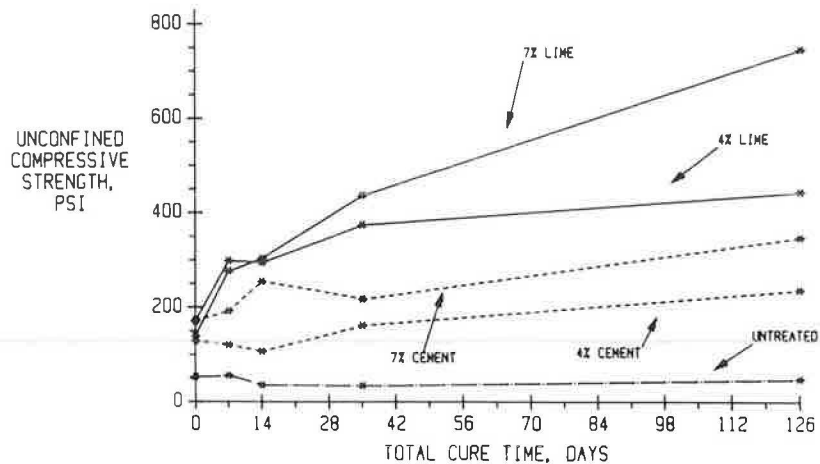


FIGURE 1 Dry unconfined compressive strength for pulverized Dalco clay treated with cement or lime (modified AASHTO).

The higher-plasticity Dalco clay exhibited approximately a 50 percent decrease in the plasticity index, whereas Beaumont and Dalco sandy clays exhibited lower reductions in plasticity indexes. The lime was slightly more effective in reducing the plasticity index; however, except for the Dalco sandy clay, the differences were of no practical significance.

Unconfined Compressive Strength

The relationships between unconfined compressive strength and total cure time are shown in the figures. In general, both cement and lime treatment increased the strengths of the three soils. In addition, the strength tended to increase with increased curing time.

Pulverized Soil

The effect of cement and lime treatment of soils that were pulverized to 100 percent passing the No. 4 sieve was dependent on soil type, or soil plasticity, and the compactive effort used to produce the specimens.

Dalco Clay Lime-treated Dalco clay specimens exhibited significantly higher strengths than did the cement-treated specimens when tested in either the dry or the wet condition.

The dry unconfined compressive strengths (Figure 1) of the 4 and 7 percent lime-treated Dalco clay were relatively high with 126-day strengths of approximately 450 and 750 psi, respec-

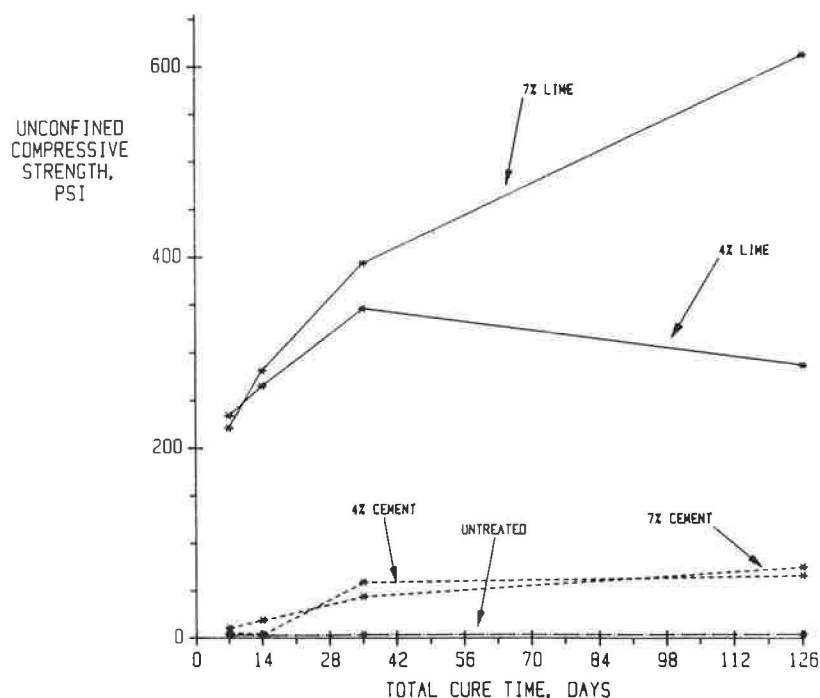


FIGURE 2 Wet unconfined compressive strength for pulverized Dalco clay treated with cement or lime (modified AASHTO).



FIGURE 3 Failure of cement-treated specimens before testing.

tively. The 4 and 7 percent cement-treated clays exhibited 126-day strengths of about 240 and 350 psi, respectively.

The wet cement-treated soil (Figure 2) had low strengths at 7 and 14 days of total curing, and in some cases the specimen could not be tested (Figure 3). The strengths increased with further curing but were still less than 80 psi after 126 days. In comparison, the 4 and 7 percent lime-treated soils had wet strengths of 286 and 612 psi, respectively, after 126 days.

Thus, for the dry condition, the strengths of the lime-treated specimens were approximately two times stronger than those of the cement-treated specimens. For the wet specimens (Figure 2), however, the differences were much greater and in some cases the lime-treated clays were 10 times stronger than the cement-treated material. Indeed, the wet-conditioned compressive

strengths of lime-treated soils were greater than the dry-conditioned strengths of the cement-treated soils at both 4 and 7 percent treatment levels (Figures 4 and 5). These trends were evident throughout the 126-day curing period.

Beaumont Clay The modified compacted Beaumont clay in the dry condition had essentially equal strengths when treated with 7 percent cement or lime (Figure 6). After 126 days of curing, however, the lime-treated soils were slightly stronger than the cement-treated soil. When tested in the wet condition, the strength of the lime-treated soils greatly exceeded the strength of the cement-treated soil, indicating a significant loss of strength for the cement-treated specimens.

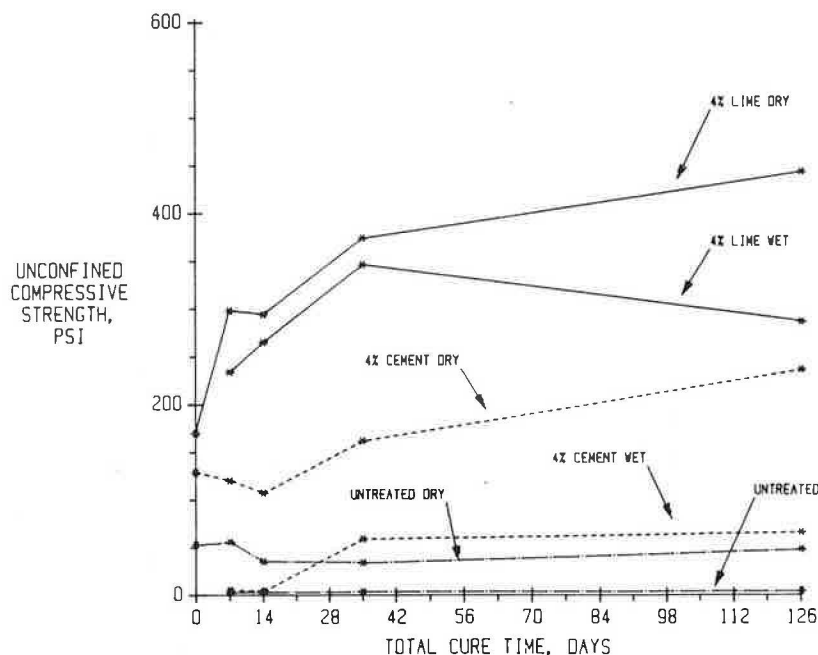


FIGURE 4 Dry and wet unconfined compressive strengths for 4 percent cement- and lime-treated pulverized Dalco clay (modified AASHTO).

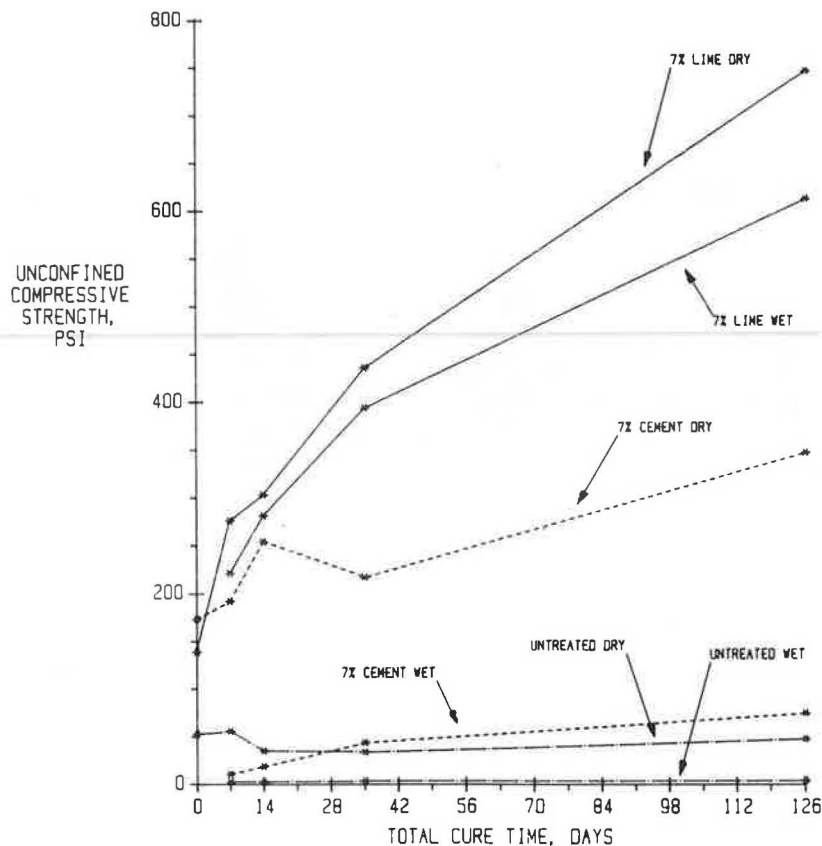


FIGURE 5 Dry and wet unconfined compressive strengths for 7 percent cement- and lime-treated pulverized Dalco clay (modified AASHTO).

In contrast, for the standard compacted Beaumont clay specimens tested in the dry condition, 4 and 7 percent cement-treated specimens exhibited greater strengths than 4 and 7 percent lime-treated specimens, respectively (Figure 7). When tested in the wet condition (Figure 8), the cement-treated specimens still had higher strengths, but the difference in strengths between the cement-treated and the lime-treated soils was slight (Figures 9 and 10). At 126 days, clay specimens treated with 7 percent lime were stronger.

Dalco Sandy Clay The relationships between strength and curing time are shown in Figures 11–14. Cement treatment of the Dalco sandy clay produced significantly greater strengths than did lime treatment in both the dry and the wet condition (Figures 11 and 12). After 126 days of curing, the dry strengths were 1,532 and 1,090 psi for the cement-treated specimens with 7 and 4 percent cement, and 478 and 372 psi for the lime-treated specimens. In the wet condition, after 126 days of curing, the strengths for the cement-treated specimens were about 720 and 400 psi, and strengths for the lime-treated specimens were about 260 and 220 psi. Thus a greater loss was exhibited for the cement-treated soils than for the lime-treated soils. Nevertheless, the cement-treated soils with both 4 and 7 percent cement were stronger than the lime-treated soils. This trend is basically opposed to the trends exhibited by the Dalco

clay and is attributed to the coarser grain size and lower plasticity of the sandy clay.

Unpulverized Soil

It has been suggested that a high degree of soil pulverization is not necessary before the addition of portland cement. This in effect would leave small clods of soil coated with cement and would not allow the cement to be intimately mixed with the soil particles. Thus, for the cement-treated portion of the study, the soil was mixed with unpulverized soil as previously described.

The relationship between unconfined compressive strength and total cure time for unpulverized cement-treated specimens, along with the comparable relationships for pulverized soil, are shown in Figures 15–20. All of these relationships show substantially lower strengths for the unpulverized specimens than for the comparable pulverized specimens. For Beaumont clay, the effects of degree of pulverization were only examined for the standard compacted specimens.

The effects of inclusion of unpulverized clods were more pronounced in the wet-conditioned specimens. This was expected because during wet curing there was more available water to cause swelling of the clods. Swelling of the clods caused disruption of the specimens and thus lowered the unconfined compressive strength.

The effects of the inclusion of unpulverized clods were more

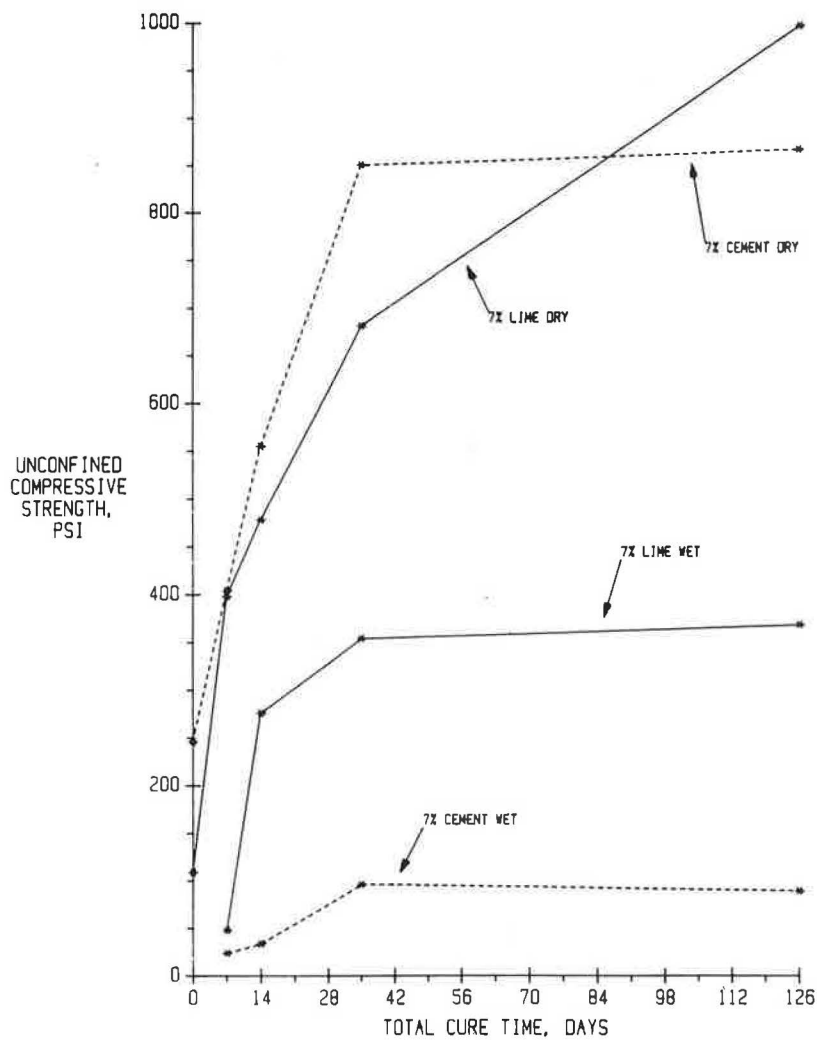


FIGURE 6 Dry and wet unconfined compressive strengths for 7 percent cement- and lime-treated pulverized Beaumont clay (modified AASHTO).

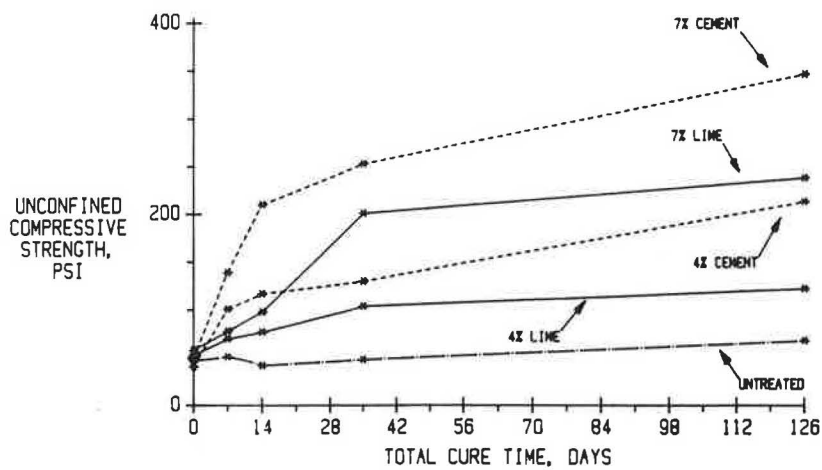


FIGURE 7 Dry unconfined compressive strengths for pulverized Beaumont clay treated with cement or lime (standard AASHTO).

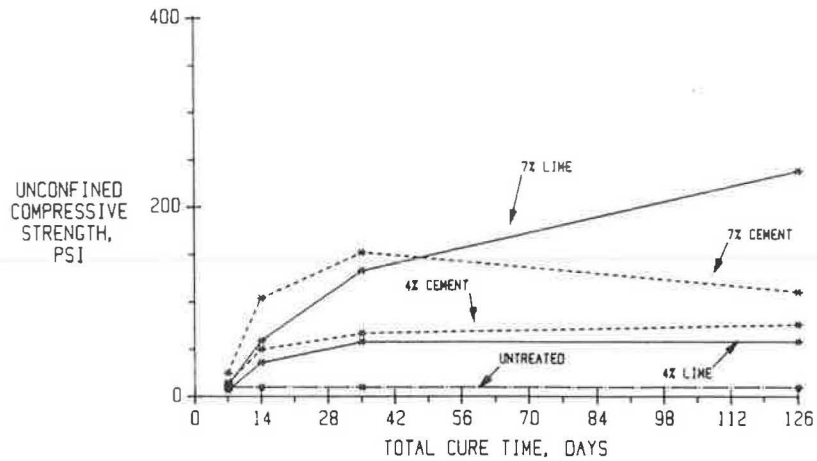


FIGURE 8 Wet unconfined compressive strengths for pulverized Beaumont clay treated with cement or lime (standard AASHTO).

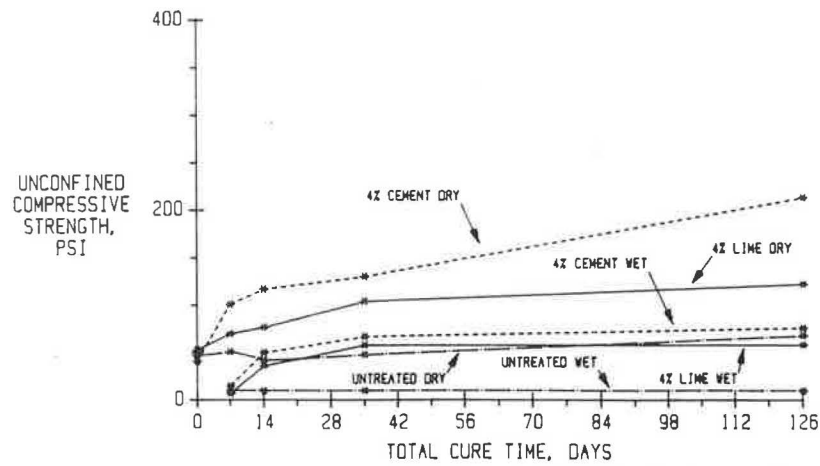


FIGURE 9 Dry and wet unconfined compressive strengths for 4 percent cement- and lime-treated pulverized Beaumont clay (standard AASHTO).

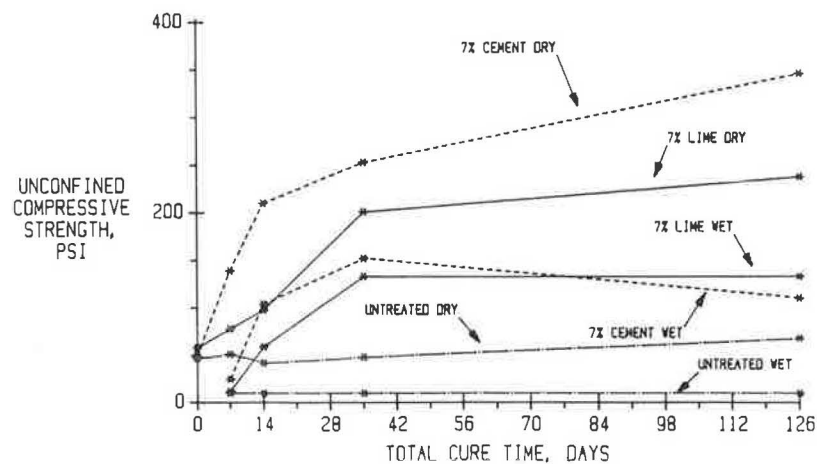


FIGURE 10 Dry and wet unconfined compressive strengths for 7 percent cement- and lime-treated pulverized Beaumont clay (standard AASHTO).

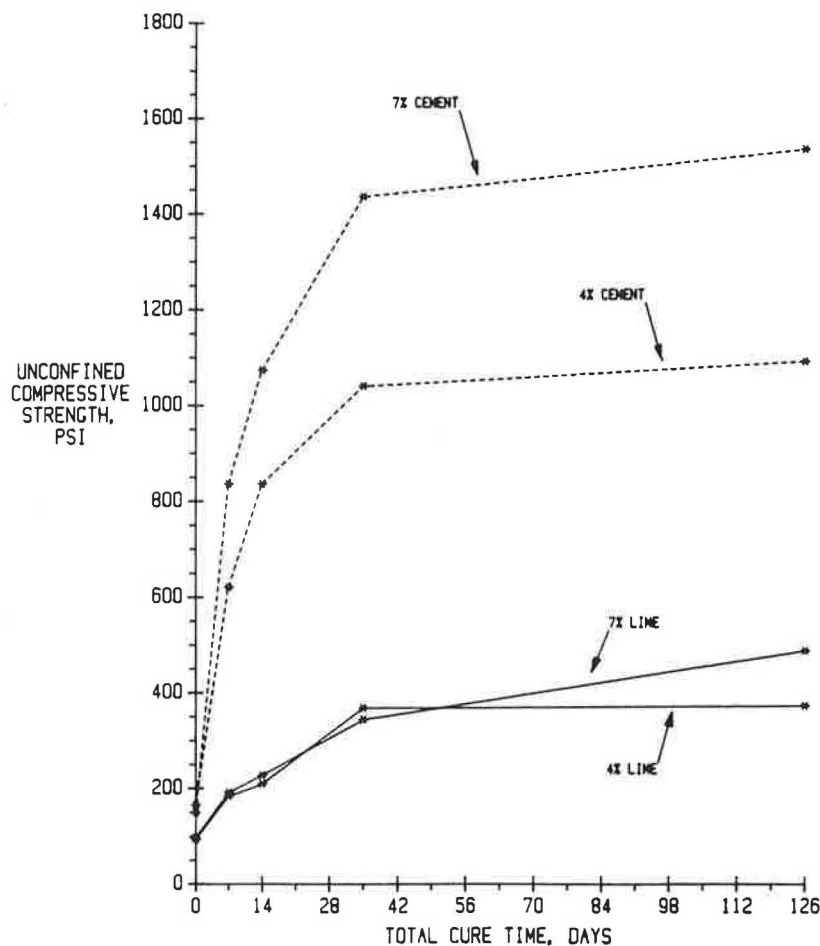


FIGURE 11 Dry unconfined compressive strength for pulverized Dalco sandy clay treated with cement or lime (modified AASHTO).

pronounced in the high-plasticity clays. The cement-treated Beaumont clay and Dalco clay had greater reductions in strength for the unpulverized specimens, especially the wet-conditioned specimens. Still, the very sandy clay, Dalco sandy clay, showed significant strength losses when unpulverized and pulverized specimens were compared.

Effects of Compactive Effort

The unconfined compressive strengths of standard and modified compacted 7 percent treated Beaumont clay specimens were compared to examine the effects of the degree of compactive effort. Unconfined compressive strength-total cure time relationships are shown in Figures 21 and 22.

In the dry condition, the increase from standard to modified compactive effort produced a two- to threefold increase in strength for the lime- and cement-treated specimens. In the wet condition, the increase in compactive effort produced a similar increase in strength for the lime-treated specimens. The modified compacted cement-treated specimens' strengths were actually about 35 percent lower than the standard compacted cement-treated specimens' strengths.

The high-plasticity Beaumont clay has a tendency to swell in the presence of water unless a stabilization treatment reduces

this tendency. An increase in compactive effort produces an increase in swell pressure along with an increase in the density of a clay. The modified compacted cement-treated specimens appeared to have the swell pressure from water content increase superimposed on the increased swell pressure from the higher compactive effort. This increased swell pressure caused disruption of the modified compacted cement-treated specimens, leading to low strengths. The lime-treated modified compacted specimens did not show a decrease in strength from the standard compacted specimens when both were tested in the wet condition. It has to be assumed that the lime treatment reduced the tendency of this soil to swell in the presence of water.

CONCLUSIONS

The following conclusions are based on the findings of this study and the conditions evaluated.

Unconfined Compressive Strength

1. Lime treatment produced higher strengths than did cement treatment for the modified compacted high-plasticity

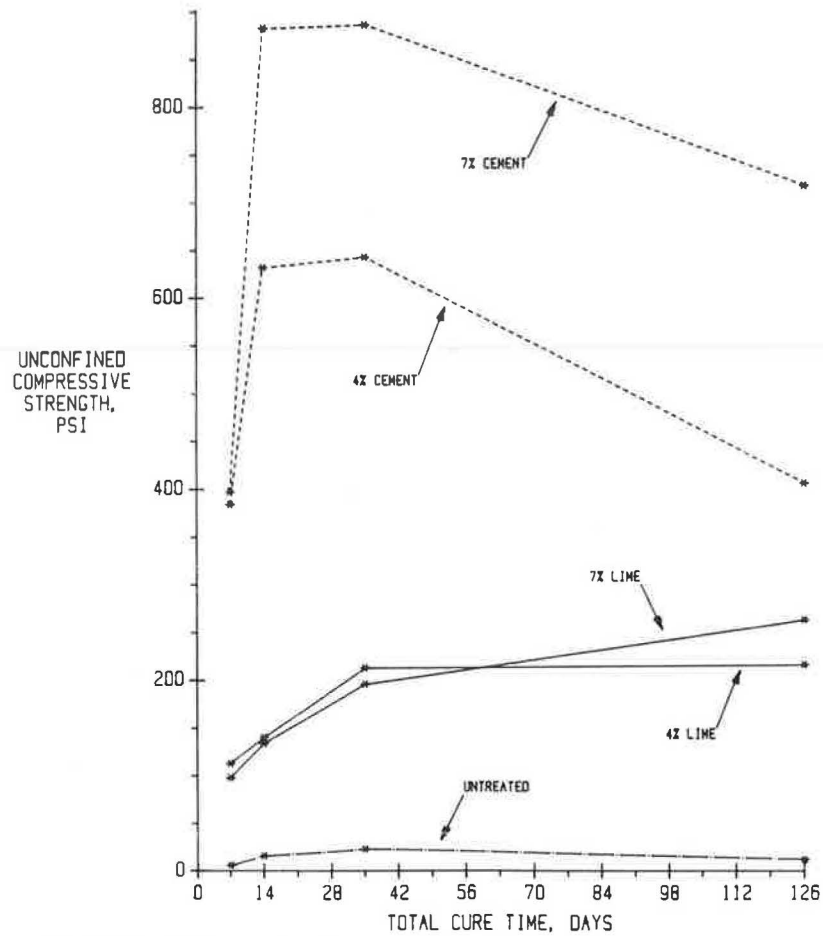


FIGURE 12 Wet unconfined compressive strength for pulverized Dalco sandy clay treated with cement or lime (modified AASHTO).

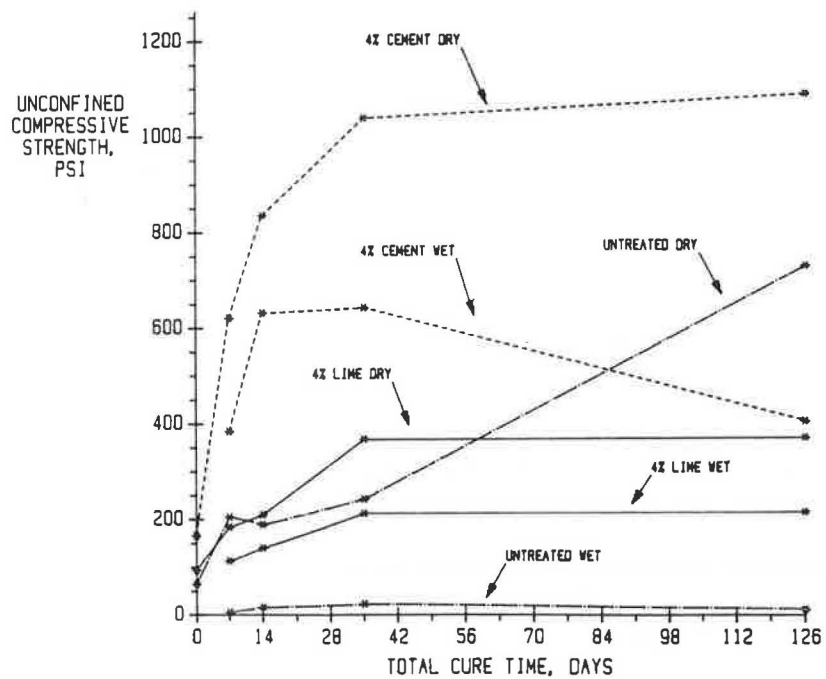


FIGURE 13 Unconfined compressive strength for pulverized Dalco sandy clay treated with 4 percent cement and lime (modified AASHTO).

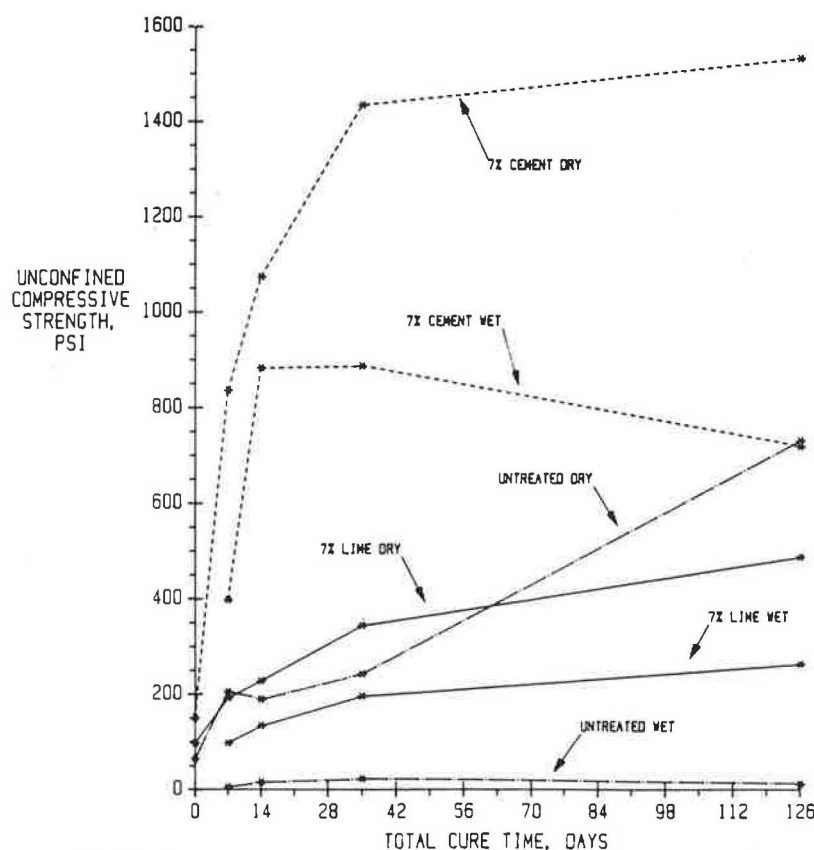


FIGURE 14 Unconfined compressive strength for pulverized Dalco sandy clay treated with 7 percent cement and lime (modified AASHTO).

Dalco and Beaumont clays. Significantly higher strengths were obtained from wet condition tests.

2. Cement treatment produced significantly higher strengths than did lime treatment for the modified compacted, low-plasticity, Dalco sandy clay. Higher strengths were obtained in both dry and wet condition tests.

3. Similar strength results were obtained from the cement- and lime-treated standard compacted Beaumont clay.

4. Wet-conditioned, modified compacted, cement-treated Dalco or Beaumont clays had low strengths. Extremely low strengths were recorded at total cure times of 7 and 14 days.

Moisture Susceptibility

1. Lime treatment of the modified compacted high-plasticity clays provided a greater retention of their dry-conditioned

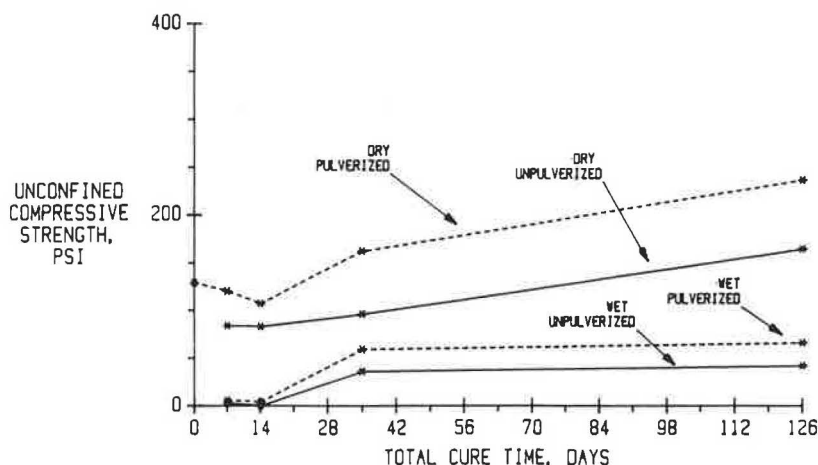


FIGURE 15 Effects of pulverization on dry and wet unconfined compressive strengths of 4 percent cement-treated Dalco clay (modified AASHTO).

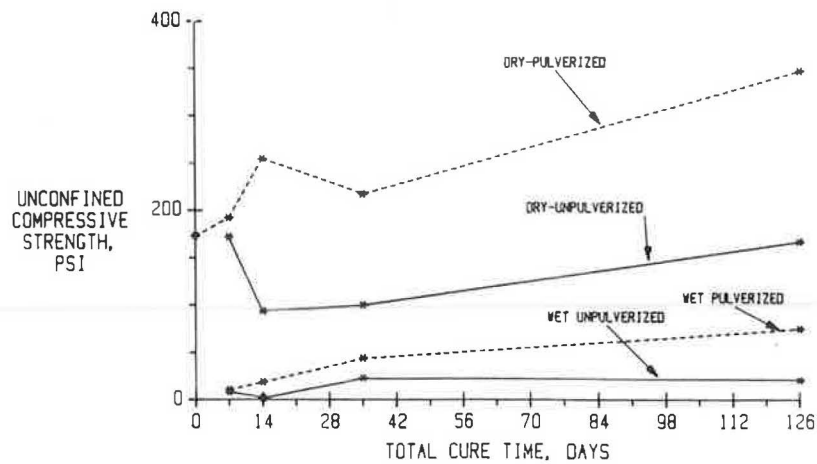


FIGURE 16 Effects of pulverization on dry and wet unconfined compressive strengths of 7 percent cement-treated Dalco clay (modified AASHTO).

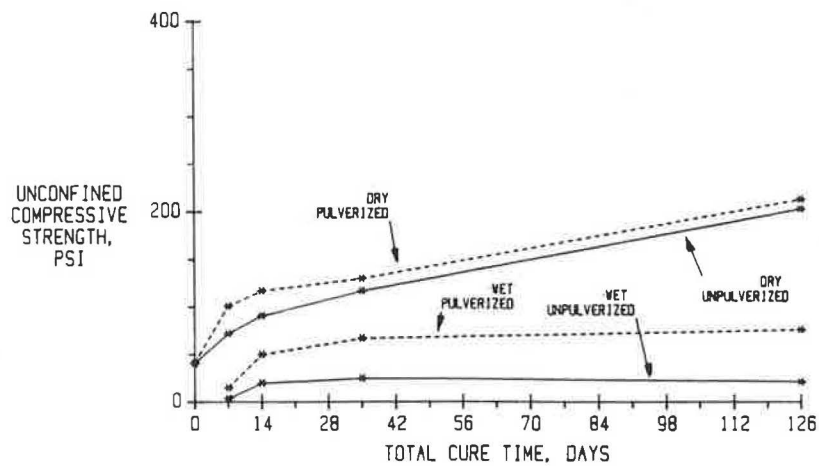


FIGURE 17 Effects of pulverization on dry and wet unconfined compressive strengths of 4 percent cement-treated Beaumont clay (standard AASHTO).

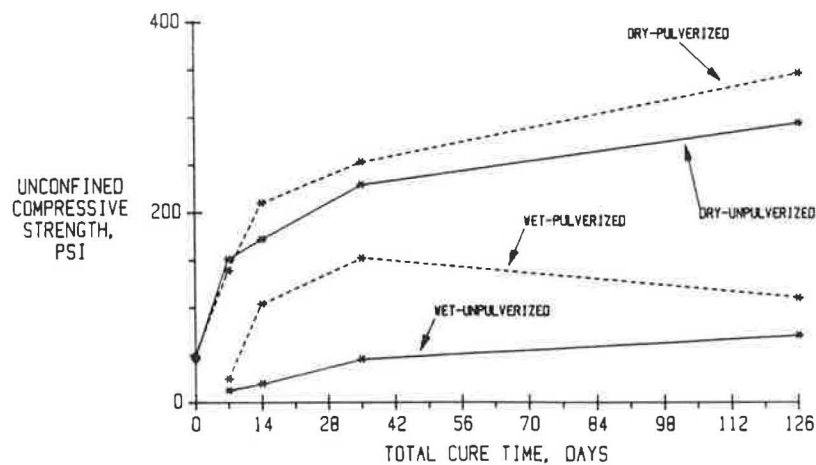


FIGURE 18 Effects of pulverization on dry and wet unconfined compressive strengths of 7 percent cement-treated Beaumont clay (standard AASHTO).

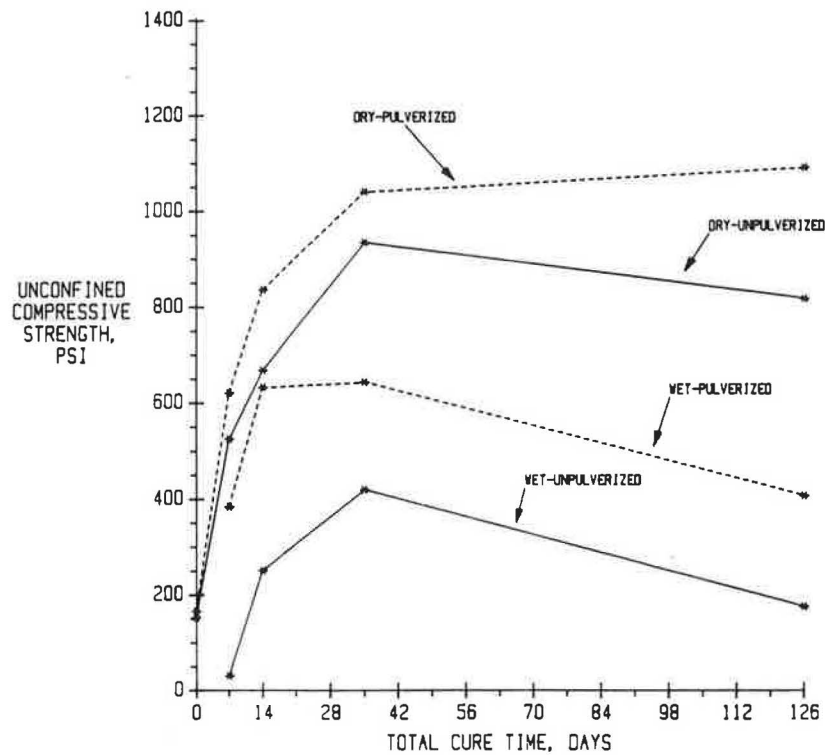


FIGURE 19 Effects of pulverization on dry and wet unconfined compressive strengths of 4 percent cement-treated Dalco sandy clay (modified AASHTO).

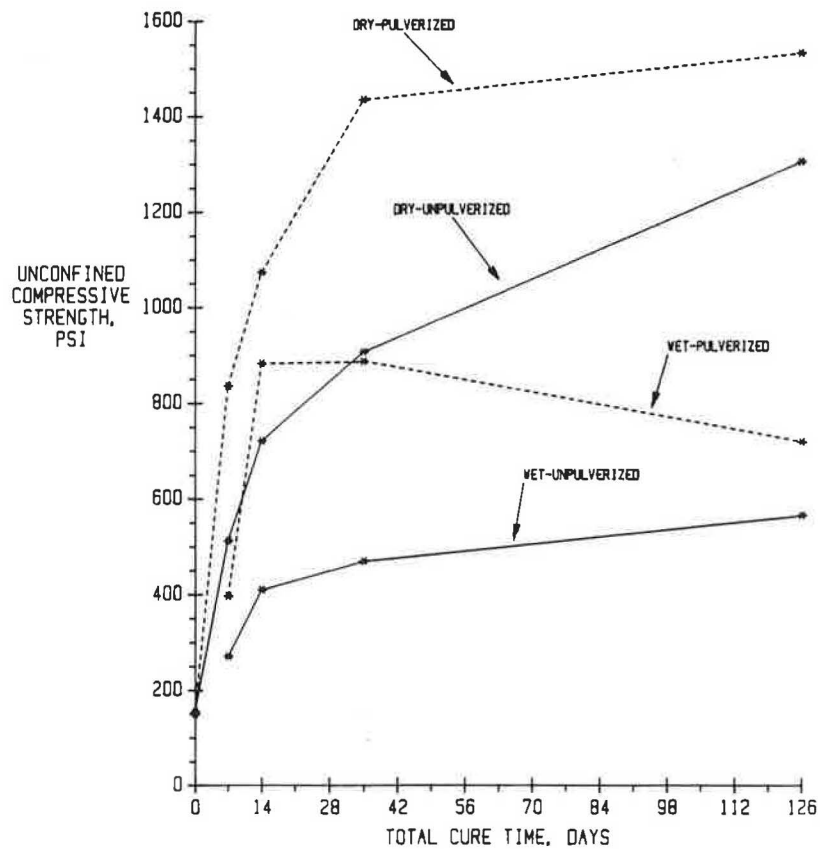


FIGURE 20 Effects of pulverization on dry and wet unconfined compressive strengths of 7 percent cement-treated Dalco sandy clay (modified AASHTO).

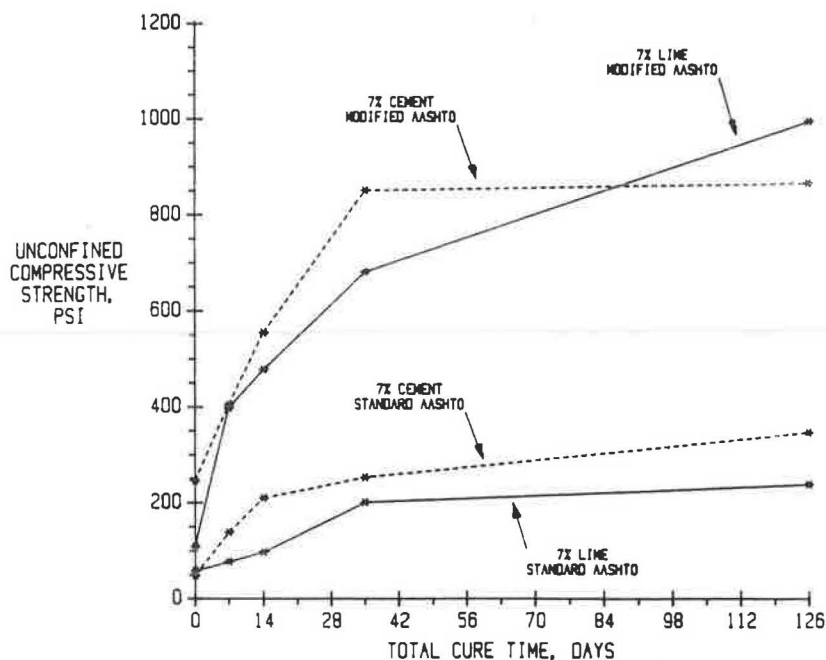


FIGURE 21 Unconfined compressive strength for dry, pulverized Beaumont clay, modified or standard AASHTO compaction with cement or lime.

strength when they were exposed to moisture. Lime treatment provided two to four times greater retention of strength than did cement treatment.

2. Lime-treated standard compacted Beaumont clay had slightly higher strength retention from the dry to the wet condition. Although cement treatment gives higher strengths for both dry and wet conditions than does lime, the amount of strength loss (difference between dry and wet strengths) is less for lime.

Effects of Degree of Pulverization

1. A small amount (15 percent) of unpulverized ($\frac{3}{4}$ in. to $1\frac{1}{2}$ in.) soil in a cement-treated soil mixture was found to cause a considerable loss in strength compared with a cement-treated completely pulverized (100 percent minus $\frac{1}{4}$ in.) soil mixture. This trend was evident for all three soils tested.

2. Lower strengths were obtained for the wet- and dry-

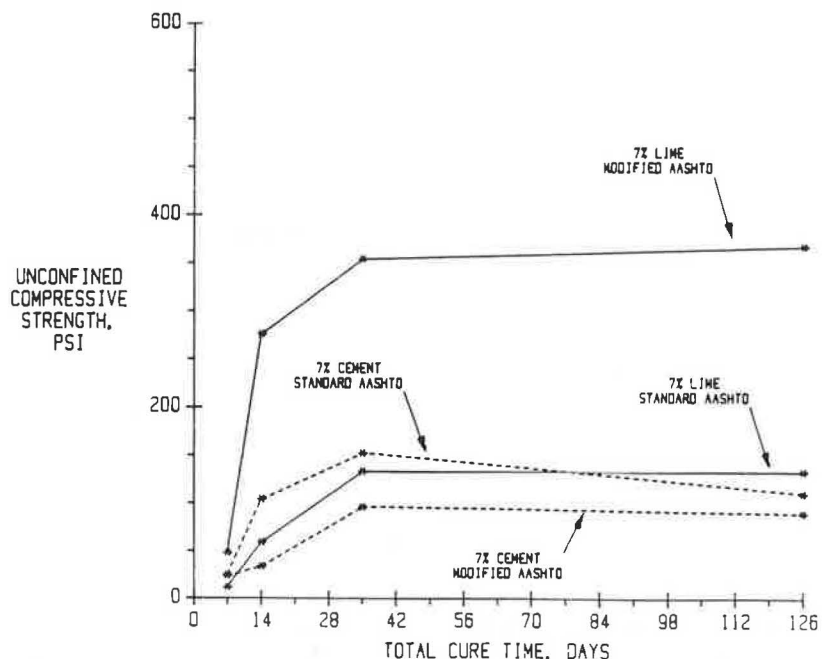


FIGURE 22 Unconfined compressive strength for wet, pulverized Beaumont clay, modified or standard AASHTO compaction with cement or lime.

conditioned unpulverized cement-treated soil specimens, but a larger decrease in strength was observed in the wet-conditioned specimens.

3. Swelling of the dry unpulverized soil clods during curing was thought to be the major cause of distress in the specimens, which led to lower strengths.

Effects of Degree of Compactive Effort

1. Dry-conditioned compressive strengths increased greatly for the lime- or cement-treated Beaumont clay when the compactive effort was increased from standard to modified compactive effort.

2. Wet-conditioned strengths decreased greatly for the cement-treated Beaumont clay when the compactive effort was increased from standard to modified compactive effort. Lime-treated Beaumont clay's wet-conditioned compressive strengths increased about the same percentage as did the dry-conditioned strengths with increased compactive effort.

3. Increased swelling pressure induced by the increased compactive effort was thought to be the cause of the loss of strength in the wet-conditioned cement-treated clay specimen.

4. Lime treatment appeared to reduce the swelling tendencies of the expansive Beaumont clay whereas the cement treatment did not.

Summary

On the basis of the results and conditions of this test program, lime treatment of the expansive high-plasticity soils was more favorable for compressive strength attainment than was cement treatment of these soils. In general, lime treatment produced higher dry-conditioned strengths, but the major advantage was in the wet-conditioned strengths. Lime treatment provided significantly better resistance to moisture damage when these soils were compacted by the modified AASHTO compactive effort.

Cement treatment of the low-plasticity sandy clay produced significantly higher compressive strengths than did lime treatment of this soil.

Publication of this paper sponsored by Committee on Lime and Lime-Fly Ash Stabilization.

Automation of Monitoring of Geotechnical Instrumentation

ALAN L. HINCKLEY, BERTRAND D. TANNER, AND ERIC C. CAMPBELL

Inexpensive, low-powered, portable dataloggers directly compatible with many sensors commonly used in slope stability and soil mechanics work provide new measurement opportunities by reducing logistic complexity and cost. Pressure, force, and position sensors employing strain gauges, vibrating-wire transducers, or potentiometers are used to obtain soil pore pressures, slope inclination, movement, and strain. Sensors for general meteorological parameters and soil moisture are also accommodated. Accurate strain gauge measurements require the datalogger to have low input noise, high resolution, and precision switched bridge excitation voltages. Vibrating-wire transducers are measured either by plucking the transducer and period averaging the decaying transient or by using a continuously excited sensor and counting the frequency. Programmable dataloggers process measurements on site, reducing data storage requirements and allowing logic decisions based on measured values such as recording of data more frequently during significant events (conditional recording) and setting alarms or controls. Real-time communication to a computer uses telephone, radio, or satellite links. On-site data storage uses solid-state memory modules or cassette tapes. The standard environmental operating range of the dataloggers is -25°C to $+50^{\circ}\text{C}$, with -50°C to $+80^{\circ}\text{C}$ available through special testing.

New, inexpensive, low-powered dataloggers designed for environmental applications greatly facilitate the measurement of parameters important to slope stability and soil mechanics work. This discussion includes a brief review of data acquisition functions followed by a list of datalogger design features important to environmental applications. The advantages of sensor compatibility and on-site processing are discussed in further detail. Several data retrieval methods are presented and a current application is discussed.

FUNCTIONAL OVERVIEW

Digital data acquisition requires the automated conversion of electronic sensor signals to a digital value [analog to digital conversion (ADC)], which is then stored or transmitted, or both. Although many hardware options exist, certain functional components are common to any data acquisition process. A broad view, from sensors to computer, is shown in the block diagram in Figure 1. In traditional data acquisition systems, each individual measurement was stored, whereas today's processing dataloggers store results from several measurements processed over time (e.g., averages, maximums, standard de-

viations). In addition, external circuitry was often required to condition sensor outputs for measurement by the datalogger. In many of today's systems, the datalogger performs all of the functions enclosed in the broken line of Figure 1.

ENVIRONMENTAL DATALOGGER DESIGN FEATURES

The design specifications for a datalogger depend on the intended application. A summary of requirements that are important for unattended operation in remote, outdoor environments follows.

1. Wide temperature and high humidity operating range: In addition to surviving, the datalogger must hold stated accuracy specifications over environmental temperatures and high humidities. Today, performance over -50°C to $+80^{\circ}\text{C}$ temperatures is attainable with standard tested components, which eliminates the need for expensive military specification components in most cases. Solar heating can raise datalogger enclosure temperatures 20°C above air temperatures. It has been found that the use of desiccant and weather-tight enclosures provides the simplest and most cost-effective means of protecting the datalogger from dust, rain, and condensing water vapor concentrations.

2. Portability and low power consumption: Field sites where slope stability is a problem generally have difficult access. A datalogger that is small and requires little power reduces installation logistics and is easier to protect from vandals. Efficient design can attain 8 months of operation from eight alkaline D-cell batteries in an application where 12 sensors are measured once per minute.

3. Input transient protection: Environmental dataloggers are vulnerable to major hardware damage caused by large, lightning-induced transients entering the system on sensor leads. Protective hardware, such as transorbs, spark gaps, and the like, and proper grounding procedures are required to minimize damage.

4. Hardware microprocessor reset: Unattended, processor-based instrumentation should contain a hardware reset to restore normal processor execution in the event that it is altered by input transients or intermittent component failure. User-entered programs should exist in write-protected memory to minimize the possibility that the processor can overwrite the program should an abnormal execution state occur.

5. Field observation of measurements: The ability to continuously observe sensor measurements on a display, in engineer-

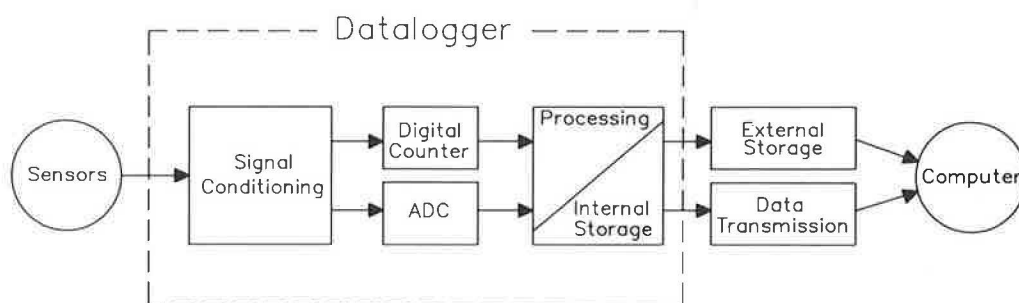


FIGURE 1 Generalized data acquisition sequence.

ing units, provides an invaluable tool for on-site system verification. Observing the processed values stored in internal memory is also necessary.

6. **Sensor compatibility:** Direct connection and measurement of sensor signals without external signal conditioning circuitry reduce cost, complexity, measurement error, and power requirements. The datalogger's ability to resolve signals to the required measurement precision dictates the choice of sensor.

7. **On-site processing:** Field processing reduces data storage requirements, scales linear and nonlinear sensor signals to engineering units, and provides logic decisions for control applications.

8. **Remote communication capability:** The need for real-time data collection is obvious in hazard warning applications such as flood forecast, but the expense of site visitation often makes telephone, radio, or satellite links cost-effective even when real-time data are not needed. Remote collection of the data allows verification of the system at any time. Experience has indicated that significant communication features should include two-way communication, with error checking and detection that result in retransmission in the event of errors. The datalogger should contain internal data storage so data can be retrieved later in the event the communication link is temporarily disabled. The ability to remotely change or restore programs or initiate control functions at the datalogger site is also desirable.

SENSOR COMPATIBILITY

A sensor possesses a property that changes in a known way with changes in the physical parameter being measured. For automated data acquisition purposes, changes in the property must result in an electrical signal. The condition of the measured physical parameter may be related to one of several electrical properties: voltage, current, resistance, frequency, AC impedance, capacitance, inductance, phase, and so forth. Table 1 gives several sensors used in soil stability work and their electrical property.

Except where noted, all of the sensors in Table 1 can be measured directly by a datalogger that makes voltage and frequency measurements. Resistance signals are converted into voltages using bridge completion resistors and precision bridge excitation voltages sourced by the datalogger. Current signals are converted to voltage signals by means of a shunt resistor. Although there are several complex sensors, which require

extensive signal conditioning, there are many useful sensors that can be measured directly without additional circuitry by dataloggers with the following features:

1. **Low input voltage noise:** Thermocouples, remote temperature detectors (RTDs), and strain gauges require input noise levels in the submicrovolt range.

2. **High-resolution analog to digital conversion:** Resolution is often more critical than accuracy when changes in time or between sensors are desired. A resolution of 1 part in 15,000 (14 bits) measures a pressure sensor with a full-scale range of 15 m (50 ft) to 1 mm (0.04 in.) of water.

3. **Programmable voltage gain:** To maintain resolution, selectable full-scale input ranges from a few millivolts (metal foil strain gauges) to several volts are required.

4. **Switched excitations:** Power consumption is reduced by applying resistance bridge excitations at the time of measure-

TABLE 1 SLOPE STABILITY SENSORS

Parameter	Sensor	Signal
Water height and pore pressure	Strain gauge	Ohms
	Vibrating wire	Frequency
Barometric pressure	Potentiometer	Ohms
	Strain gauge	Ohms
	Vibrating wire	Frequency
Linear motion	Potentiometer	Ohms
	LVDT ^a	V-ratio
	Incremental encoder	Frequency
Inclination	Electrolytic ^b	Volts
	Potentiometer	Ohms
Velocity and flow	Incremental encoder	Frequency
	Switch closure	Frequency
	Magnetic pulse	Frequency
Deformation	Strain gauge	Ohms
Temperature	Thermistor	Ohms
	Thermocouple	μ V
	RTD	Ohms
	Silicon solid-state devices	
	AD590	μ A
Precipitation	Silicon diode	μ A
	Potentiometer	Ohms
	Switch closure	Frequency
Soil moisture	AC conductivity	Ohms

^aLVDT = linear voltage displacement transducer.

^bRequires extensive signal conditioning.

ment only. Resistance measurements made as the ratio of the bridge voltage to the excitation voltage remove the inaccuracy of the voltage reference from the measurement if the excitation and voltage measurement use the same voltage reference. Switching excitation polarity eliminates thermal electromagnetic frequency errors in low-level bridge measurements. If the measurements are fast enough and the excitation at both polarities is symmetrical in time and magnitude, the same device can be used to measure AC conductivity. These types of measurements are needed for soil moisture blocks and water conductivity.

5. Frequency counting: A switch bounce elimination circuit and an amplifier for low-level AC signals are needed. Dedicated counters are required for low-frequency asynchronous events. Period averaging is required for accurate measurement of a limited-duration signal such as that from the vibrating-wire transducer.

ON-SITE PROCESSING

The advantage of processing measured values to obtain more efficient data storage has been mentioned. Data compression is particularly important in remote applications, where site visitations are costly. Processed results such as averages, standard deviations, and extremes or values recorded conditionally at designated times, events, or when changes occur all reduce data storage and handling logistics.

Linear calibration constants are entered into the datalogger to convert measurements into engineering units immediately. The datalogger displays the sensor signal in engineering units, which enables the user to verify the correctness of the signal and its conversion. Field calibration of sensors is possible. User-entered polynomial coefficients are used to linearize nonlinear measurements. Linearization and the scaling of sensor outputs into engineering units make it possible to correct sensor readings on site (e.g., correcting a piezometer reading for barometric pressure yields pore pressure). Nonlinear signals converted to engineering units can then be averaged, but in their nonlinear form they cannot. The ability to convert sensor signals into correct engineering units is most useful when verifying the performance of the sensors and the datalogger in the field.

The ability to compare values or time with programmable limits and make decisions provides useful control functions such as sampling at a faster rate, measuring a selected sensor, or initiating a radio or telephone communication for an alarm message.

REMOTE COMMUNICATION CAPABILITY AND DATA RETRIEVAL

Remote communication and data retrieval are possible over hard wire, telephone lines, radios, and satellite. Data retrieval is also possible via memory module and cassette tape.

Remote communication through most devices has been improved by the addition of large amounts of internal memory for final data storage. The storage of data at the remote site permits the retransmission of data when error detection and correction routines fail or when data are missed by the computer. The

speed of remote data transmission has also been improved by the use of a binary format that increases the effective transmission rate fivefold.

The advantages, limitations, and new developments in remote communication over hard wire, telephone lines, radios, and satellite follow.

1. Hard wire: A shielded pair of twisted leads (user installed) could be used in conjunction with a set of modems to connect one or more dataloggers to a computer. High baud rates are possible over short distances, but high cable costs are likely by the time the 5-km (3-mi) limit is reached.

2. Telephone lines: 300- and 1,200-baud DC-powered modems that meet the environmental requirements are available. The modem and telephone line combination allows remote communication over long distances as long as the line quality is "good." Long-distance telephone charges and installation costs at remote locations could limit the feasibility of this method for some sites. All things considered, telephone lines are one of the most reliable and least expensive methods of data transfer available.

3. Radio: Radio transmission is often the most practical solution to the problem of remote communication in rugged terrain. Data transmission over distances of 40 km (25 mi) is possible with good "line of sight" on voice grade radios. Any station can be used as a repeater to extend the range of a network to 200 km as long as the maximum distance of 40 km between stations is observed. As many as 255 stations are accessible on a single frequency. Data throughput rates can be as high as 30 values per second. Radio transmission may be combined with telephone line transmission [e.g., communicate 32 km (20 mi) over rugged terrain via radio, link to a telephone line, and then communicate 320 km (200 mi) via telephone to the computer].

4. Satellite: A small number of geostationary orbit earth satellite channels are available. Many of these are reserved for government agencies. Transmission rates are currently limited to 30 data values every 3 hr. A faster earth station computer and new satellites should improve channel availability and data transmission rates. Satellite transmission works well for extremely remote sites.

If immediate data transfer is not a requirement, data may be transferred back to a computer more economically by hand carrying the data in a solid-state memory module or on a cassette tape. Data storage capacity on a cassette tape is 180,000 processed values. Storage capacity of the different storage modules is 32,000, 60,000, and 360,000 processed values.

CURRENT APPLICATION

The datalogger was used to study a mudslide located in Steed Canyon above Farmington, Utah. Five semiconductor strain gauge piezometers were used to measure pore pressure. Movement and tilt were measured with a potentiometric extensometer and a potentiometric inclinometer. Air temperature was measured with a thermistor, precipitation was measured with a tipping bucket rain gauge, and barometric pressure was measured with a capacitance type of transducer. The barometric

pressure reading was subtracted from the pore pressure readings to remove atmospheric pressure fluctuations. Data were normally recorded every 6 hr. When changes in any of the pore pressure readings exceeded 1.3 cm of water in a 5-min time period, the data were recorded every 5 min. The datalogger was located in a small, unheated enclosure. The minimum outside air temperature recorded during the winter was -24°C at the site. A lead-acid battery about half the size of a car battery powered the datalogger the entire season. During the first year data were stored in memory and on cassette tape. The second year data were transmitted via satellite.

SUMMARY

Technological developments have led to the creation of new instrumentation for automating the measurement of soil stability parameters. The special design features required for unattended operation in remote outdoor environments have been discussed.

Special features in these small, low-power dataloggers have made them capable of direct measurement of resistance sensors, current sensors, and signals from voltage and frequency sensors. This measurement capability allows accurate sensing of stability and movement of a slope as well as weather factors that affect its stability. Direct measurement of these sensors reduces the complexity and cost of the system.

The processing capability of the dataloggers allows conversion of all signals to meaningful engineering units. The signals, now in engineering units, are then compared with fixed values or other signals to determine whether an alarm should be sent, additional sensors measured, or data recorded more frequently.

Remote communication and data transfer capabilities are improved in the new instrumentation. Instrumentation and software have been developed to allow data transfer via hard wire, telephone lines, radios, and satellite. Data transmission speed and reliability have also been improved.

Publication of this paper sponsored by Committee on Soils and Rock Instrumentation.

Acoustic Monitoring of Landslides

DAVID M. JURICH AND RUSSELL J. MILLER

Three active landslides located in Eagle County, Colorado, were monitored with an acoustic emission (AE) recording device for an 8-month period beginning in January 1985. AE monitoring devices are used to detect the transient elastic waves generated by the release of energy within a material undergoing failure. The slides were also instrumented with groundwater observation wells and inclinometer boreholes. Groundwater data and displacement measurements gathered from these devices and data collected from surface movement observations were correlated with the AE data. Significant increases in levels of AE activity were recorded at least 30 days before the observation of movement at each of the slides. Rises in groundwater levels recorded at many of the observation stations appear to have triggered the slides. AE signals recorded after the initial failure of the slides correlated with the rates of movement measured at surface displacement observation stations. This study has successfully demonstrated the ability of a properly installed AE monitoring system to detect premovement stresses in soil slopes. AE can be used as an early warning system to reduce hazards to life and property on high-risk soil slopes, road cuts, tailings dumps, dams, foundations, and other civil structures.

In this paper are presented the results of an analysis of three unstable soil and talus slopes using acoustic emissions (AEs) monitoring and traditional field techniques. This study was part of a Colorado Division of Highways effort to characterize landslides that are affecting major highways in Eagle County, Colorado (Figure 1).

The ability to determine the state of stress and stability of a soil mass has been a primary objective of the engineering community for many years. Instruments such as inclinometers and tiltmeters yield valuable information about the direction and amount of movement in a failing earth slope. However, they are limited to measuring movements after failure has begun. There exists a need for easily applied and inexpensive instrumentation technologies that can monitor the relative instability of a soil structure before failure.

BACKGROUND

AEs have also been called microseismics, microsonics, and subaudible rock noise (SARN). These phenomena have been defined as "the transient elastic waves generated by the rapid release of energy within a material" (1). One of the first

discoveries of acoustic emissions was made in the late 1930s by the U.S. Bureau of Mines. Researchers found that the quantity and duration of bursts of seismic energy in underground mines were a function of the state of stress of the rock (2).

AE monitoring has also been used by researchers to investigate failure in other media such as metals, concrete, and composite materials (3, 4). Recently, researchers have been investigating the possibility of adapting this technique to the evaluation of soils (5). AE monitoring has proven effective in the following fields:

- Soils
 - Dams, embankments, cuts, fills
 - Settlements
 - Lateral movement
 - Laboratory
- Rock
 - Mine safety
 - Subsidence
 - Open cuts
- Civil Structures
 - Concrete
 - Steel
- Other
 - Avalanche control
 - Composite materials

Characteristics of Acoustic Emissions

Acoustic emissions, as do all seismic signals, occur as waveforms that are characterized by transient displacements on the order of 0.00000001 in. and frequencies of 10 to 1,000,000 cycles per second (1). A record of acoustic emissions generally consists of individual bursts or events separated by periods of relative quiescence (Figure 2). Each event is composed of a series of counts. AE monitoring systems record the number of seismic events and counts per sample interval that equals or exceeds a preset signal threshold level.

AE signals are emitted over a wide range of frequencies, and monitoring systems must be tailored to the material under investigation (6). Figure 3 shows how AE frequencies compare with other types of ground vibration studies and how characteristic AE frequencies vary with types of material.

Acoustic Emissions in Soils

Friction is probably the most dominant mechanism for the release of acoustic energy in soils. As an unstable soil mass

D. M. Jurich, Stone and Webster Engineering Corporation, 800 A Street, Anchorage, Alaska 99701. R. J. Miller, Colorado School of Mines, Golden, Colo. 80401.

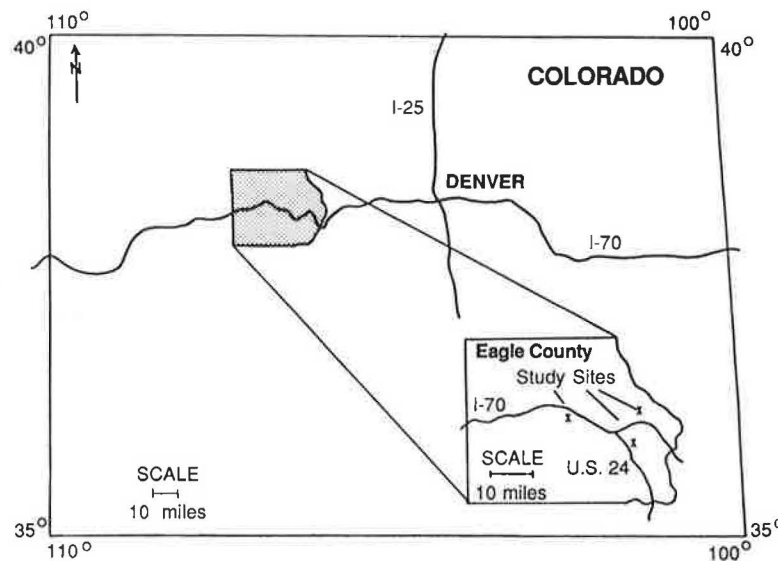


FIGURE 1 Location map, state of Colorado with Eagle County and study areas identified.

fails, individual particles of material in the failure zone or zones abrade one another (Figure 4). This abrasion releases energy in the form of heat and acoustic emissions.

Acoustic emissions are rapidly attenuated in unconsolidated materials. The signal-sensing instruments must therefore be positioned close to the source of the AE activity. Because failures in soils are often deep-seated, high modulus waveguides are used as a path to transmit the AE events to an accessible surface location. Waveguides can include metal tubing or reinforcing bars that are positioned to intercept the potential failure surface (Figure 5).

Monitoring Equipment Used in This Study

The AE monitoring system used for this project consisted of (a) an accelerometer with a 30-kHz resonance frequency, (b) a 15- to 45-kHz bandpass filter, and (c) a signal conditioning and analyzing unit. The system was equipped with variable gain and sampling rates, an adjustable threshold setting, and a digital display. Steel pipes $\frac{1}{2}$ in. in diameter were chosen as waveguides for this investigation and doubled as groundwater observation wells. The accelerometer was shielded from stray airborne acoustic signals. Figure 6 shows photographs of a typical AE monitoring station.

DESCRIPTION OF STUDY AREAS

A reconnaissance trip was made to each of the study areas to identify locations for AE and groundwater observation stations. These locations were grouped near the crown, middle, and toe areas of each slide. An additional monitoring station was located outside the boundary of each of the slides so that background AE activity recordings could be made during the course of the study for comparison with the landslide AE activity readings. Finally, a location for at least one inclinometer hole per slide was identified. Installation of these monitoring stations was accomplished in the winter of 1985.

Battle Mountain Slide

The Battle Mountain slide is located on US-24, 2 mi south of Minturn (Figure 7). This is a deep-seated rotational failure in a red, micaceous, sandy, clayey silt. In previous years this slide had been stable throughout the winter and subject to severe movement in the spring and summer. Several groundwater observation wells had been installed and it was known that the level of groundwater in the landslide fluctuated with the seasons, with highs recorded in the spring and summer and lows

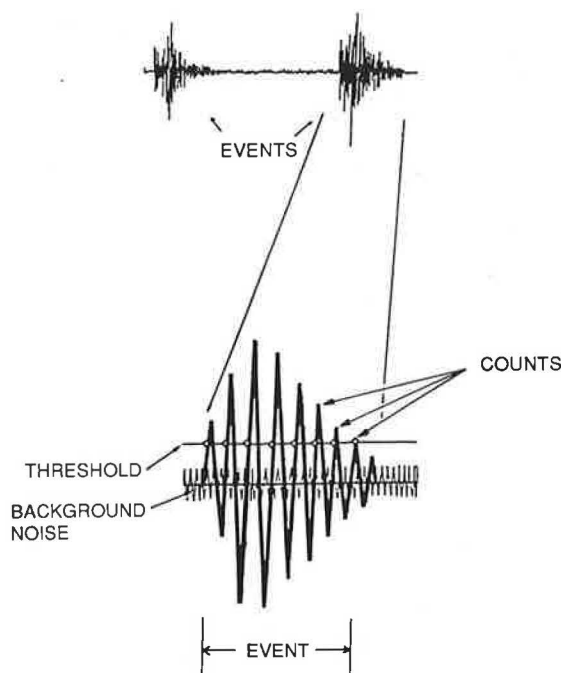


FIGURE 2 Elements of acoustic emission event.

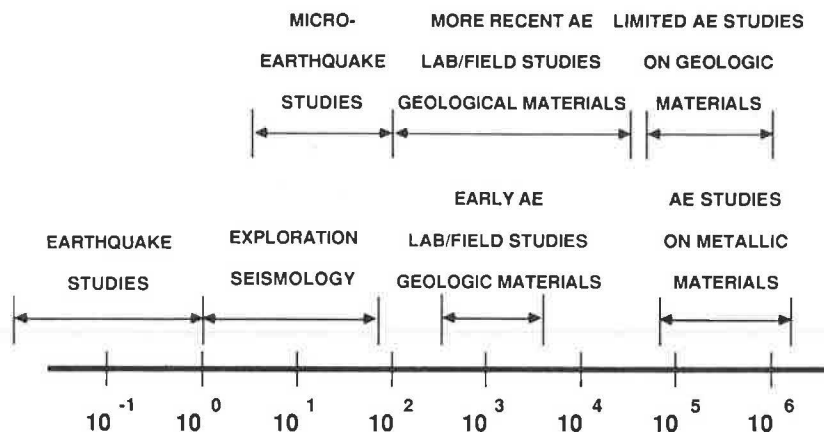


FIGURE 3 Frequency range (Hz) of monitoring facilities (6).

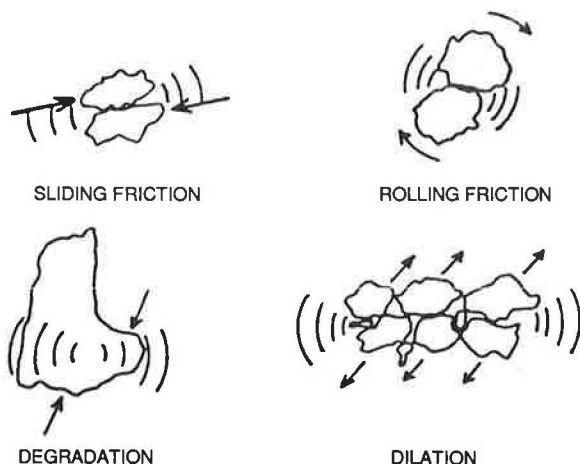


FIGURE 4 Sources of acoustic emissions in unconsolidated material.

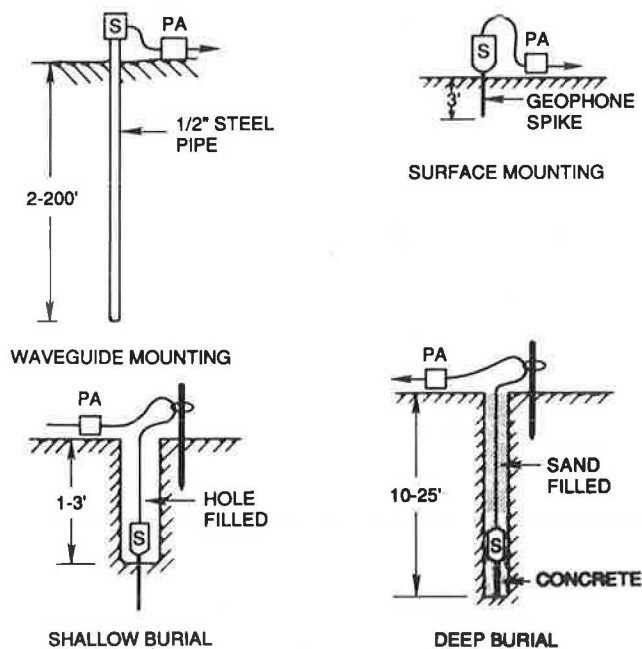


FIGURE 5 Methods used to mount AE sensors (S = sensor, PA = preamplifier).

occurring in the fall and winter. Six combination AE and groundwater observation stations were installed at the Battle Mountain study area (Figure 8).

Vail Slide

The Vail landslide is located on the north side of the westbound lanes of Interstate 70 in East Vail (Figure 9). The slide appears



FIGURE 6 Photographs of typical AE monitoring station.

to have two divergent directions of movement with the western half of the slide moving slightly to the west and the eastern half of the slide moving slightly to the east. Although the data are incomplete, features identified in both halves of the slide indicate that the western portion is failing in a fairly deep rotational fashion and the eastern half, located outside the array of AE monitoring stations, is failing as a series of wedges of soil (slumps) caused by the oversteepening of the toe of the slope during highway construction. The soil at this site is a red micaceous silt containing occasional clasts of feldspathic sandstone (Figure 10). The Vail landslide was instrumented with a total of five combination AE and groundwater observation

stations, one inclinometer hole, and six electronic distance measuring stations.

Wolcott Slide

The Wolcott slide is located along the Interstate 70 right-of-way 1.5 mi east of the Wolcott exit (Figure 11). This slide is traceable across both the east- and the westbound lanes of I-70 as well as the frontage road (US-6). This site has been subjected to recurrent movement every spring for the past several years.

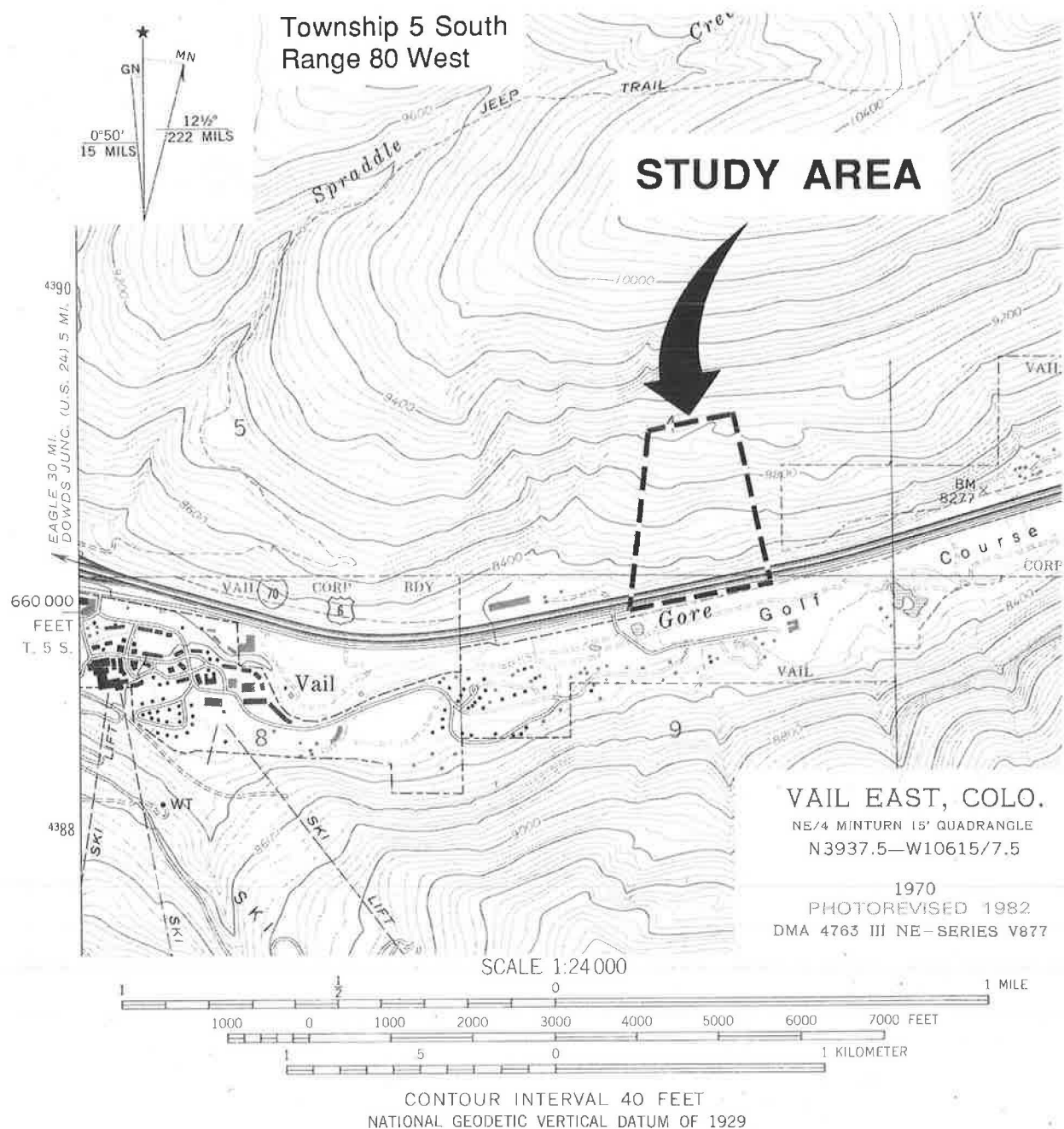


FIGURE 9 Topographical map of the Vail slide and surrounding area.

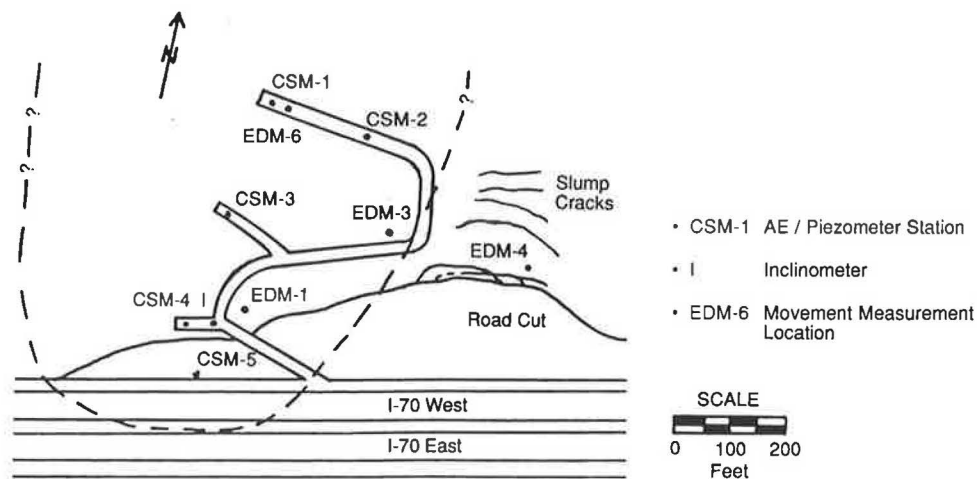


FIGURE 10 Map of the Vall slide with AE station locations.

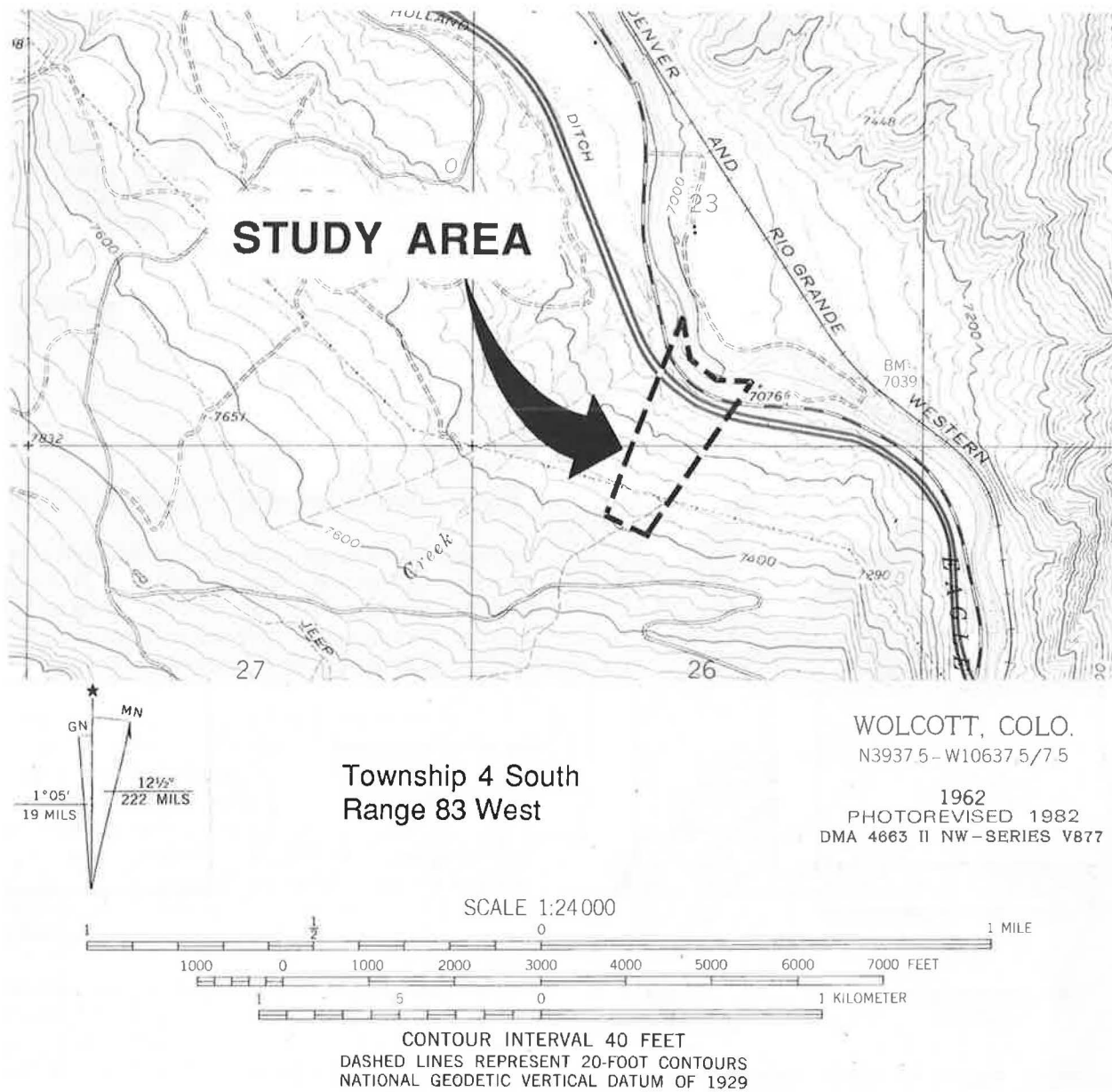


FIGURE 11 Topographical map of the Wolcott slide and surrounding area.

Six AE and groundwater observation stations and three inclinometer holes were installed at the Wolcott slide (Figure 12). All of the holes drilled at the Wolcott slide penetrated a thin mantle of soil underlain by a gray sandy silt, a massive quartzose sandstone, and thinly bedded gray silty shales.

Inclinometer readings identified a shallow dip-slope failure zone located in the thinly bedded shales. The hummocky texture of the study area and surrounding slopes indicates that the Wolcott slide is one of many failures that have occurred along slip surfaces found within the thinly bedded shales.

Movement of the slide was probably triggered by rising groundwater levels during spring runoff. Stability is further reduced by the erosive action of the Eagle River at the toe of the slide. Periods of maximum erosion occur during the high-runoff season (Figure 12) (7).

Summary Comparison of Study Sites

The Battle Mountain and Vail slides are deep-seated rotational failures of soil and colluvium. The Wolcott slide is a shallow dip-slope failure that is moving along a bedrock-controlled failure surface. Movement of all three slides appears to be triggered by rising groundwater associated with spring runoff. These slides provided an excellent opportunity to characterize AE in a variety of geologic conditions.

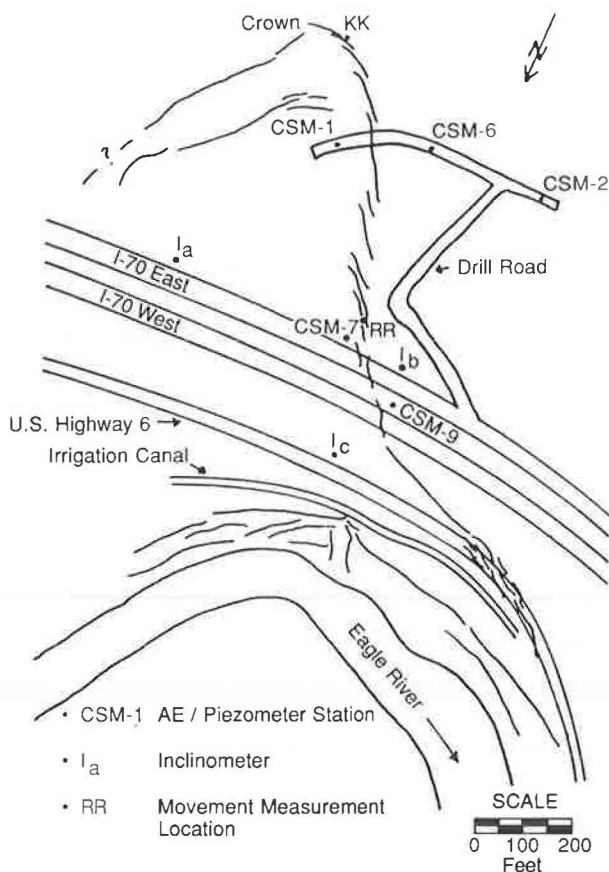


FIGURE 12 Map of the Wolcott slide with AE station locations.

DATA COLLECTION AND ANALYSIS

Installation of Monitoring Systems

One-half-inch steel pipes were slotted and placed in 4-in. drill holes to form combination groundwater observation wells and continuous waveguides from the surface to bedrock. The holes were backfilled with sand to ensure proper coupling of the waveguides with the surrounding soil.

Data Collection Procedures

The signal threshold level and gain (signal amplification factor) were set and recorded to facilitate comparisons among recording sessions. Fifteen 1-min intervals of acoustic emissions were recorded at each of the observation stations. Weather and ground conditions, groundwater levels, and highway traffic levels were recorded in order to evaluate the sensitivity of the monitoring system to environmental conditions.

Methods of Data Analysis

Individual readings of the number of counts and events recorded for each 1-min sample were averaged for each observation period to obtain representative levels of AE activity. The average AE counts and events data and the ratio of counts per event were then plotted at the proper calendar date for each observation station (Figure 13).

These data plots were correlated with data collected from the other types of instrumentation installed at each of the study sites (Figures 14 and 15).

RESULTS

Analysis of Acoustic Emissions Counts and Events Data

The number of AE counts and events recorded in the months of February and March was quite low (Figure 13). These low levels of activity, generally less than 100 counts per minute, represent baseline values considered characteristic of a stable condition as recorded at the control stations located outside the slides.

AE activity increased in March and April. These increases, representing changes in the stability of the slides in response to rising groundwater levels, were recorded at least 30 days and as much as 50 days before any movements were observed at the slides. The amount of such advance warning varied among stations within each slide, and significant increases in AE activity were not recorded at every observation station. This is because different portions of the slides experienced different loading conditions and moved at different rates as verified by field observations.

The ability to identify changes in AE activity was a function of the observation interval used in this study. The observations were made monthly in the winter, biweekly in the spring, and weekly in the summer. Because increases in AE activity recorded before failure were measured in the spring when data

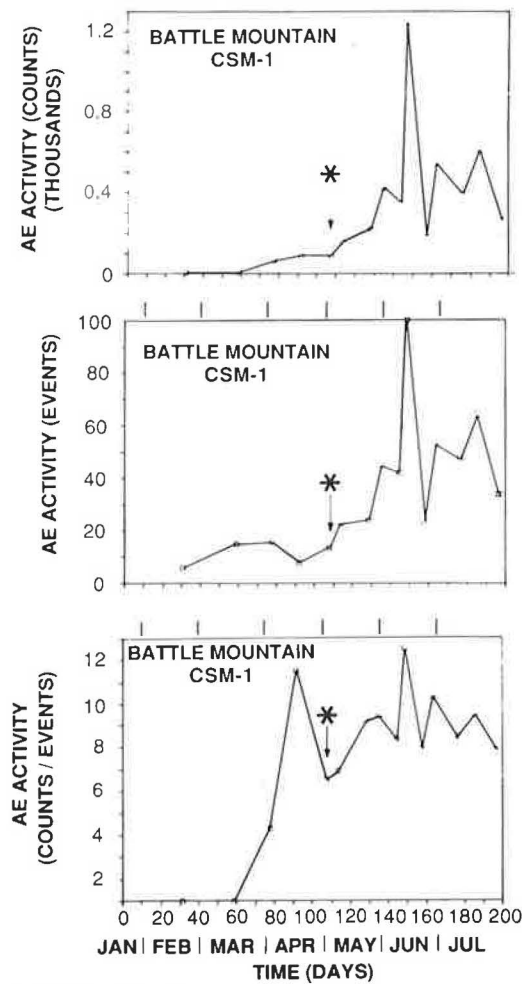


FIGURE 13 Sample AE counts, events, and counts/event ratio data plots (star indicates first observed movement of slide).

were collected on a biweekly basis, the exact time at which AE activity increased might have been as much as 13 days before the date recorded. A more detailed analysis of slide activity would suggest the use of a continuous monitoring system.

After the initiation of movement, AE activity continued to increase at many of the observation stations, but in some cases AE activity dropped off to relatively low levels. These different responses of the AE monitoring system to the initiation of movement appear to be a function of the mode of failure experienced at the slides.

Observations of displacement recorded by Shine (8) at the Battle Mountain slide revealed that movement was sporadic with periods of high rates of movement followed by periods of relative quiescence. This pattern of movement, commonly referred to as stick-slip, was identified in the records of AE activity collected at several observation stations at the slides (Figure 15). AE activity reached a maximum in mid-June that coincided with the maximum rate of movement of the slides.

Analysis of Acoustic Emissions Average Counts per Event Ratio Data

Before failure, plots of the average AE counts per event (C/E) ratio are significantly different from the plots of either the AE counts or events data. For example, at Battle Mountain slide Station CSM-1, a gradual increase in both the number of AE counts and events was recorded, whereas the C/E ratio shows a low level of activity followed by a marked increase (Figure 13). This dramatic increase occurred about 50 days before the first observed movement of the slide. Subsequent C/E ratio data closely correlated with the rates of movement of the slides.

The C/E ratio offers an additional measure of relative stability and appears to provide a more sensitive precursor to movement.

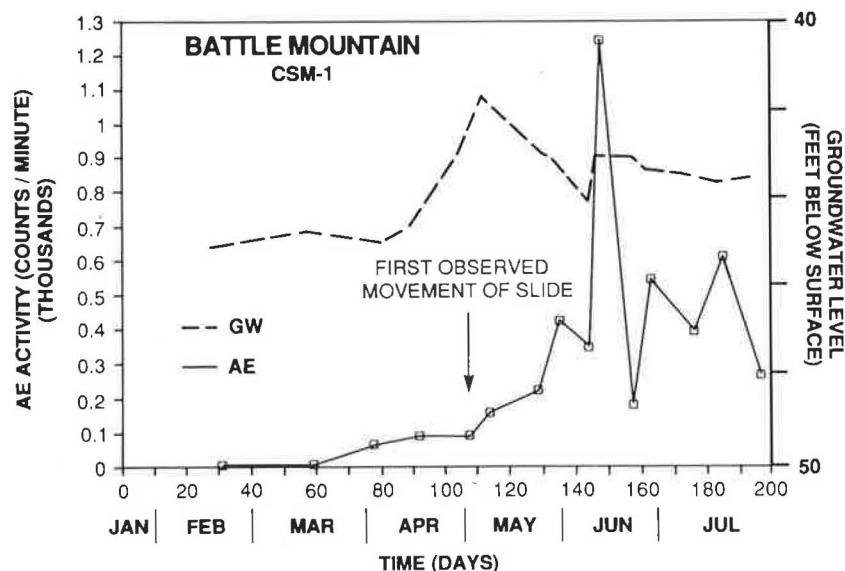


FIGURE 14 Plot of AE counts data and groundwater measurements at Battle Mountain slide Station CSM-1.

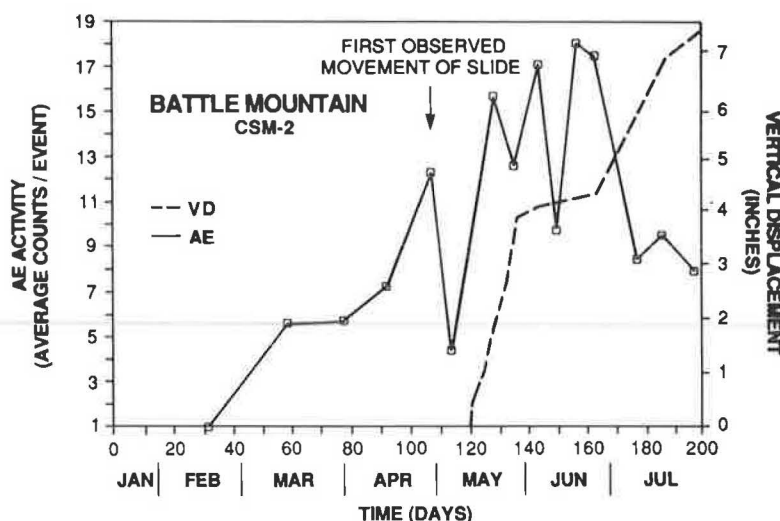


FIGURE 15 Plot of AE average counts/event ratio and surface movement data for Station CSM-2 at the Battle Mountain slide.

CONCLUSIONS AND RECOMMENDATIONS

Acoustic emissions monitoring systems installed in three distinctly different landslides accurately tracked changing conditions of stability. Increases in AE activity were recorded at least 30 days in advance of movement at each of the slides.

The location of AE observation stations at a study site is critical for recording representative data. Because acoustic emissions monitoring systems are extremely sensitive, they are also sensitive to many other acoustic signals. An AE monitoring system should include shielding and filters to eliminate noise from unrelated sources such as highway traffic and running water.

Relatively large areas can be monitored with a few carefully placed observation stations. The 1/2-in. steel pipes used as waveguides in this study were effective in transmitting low-level AE signals from deep-seated failures to sensors located at the surface.

Several methods of analysis should be used for a thorough evaluation of AE data. The number of AE counts, the number of AE events, and the ratio of average counts per event all describe different aspects of the quantity and duration of AE activity and hence slope stability.

An accurate record of changes in slope stability depends on the frequency of observation. Continuous monitoring of AE activity during critical periods would provide the most detailed record of changes in slope stability.

Monitoring of AE activity at stabilized sites would be useful for determining the long-term success of corrective actions and could be used to identify local areas within a site that might require additional attention.

Although this study was limited to landslides, AE monitoring can readily be applied to other areas. Tailings dumps, dams, and foundations are a few examples of potentially high-risk structures that can be effectively evaluated with AE monitoring systems.

ACKNOWLEDGMENTS

Sincere appreciation is extended to R. K. Barrett, District III Geologist of the Colorado Division of Highways, for sponsoring this study. Funding from the Colorado Division of Highways is acknowledged. Extra thanks are given to Brendon Shine, Javier Fernandez, and Kahlil Nassar for their assistance in the field and for making their data available.

REFERENCES

1. J. D. Leaird and J. Plenh. Acoustic Emission Monitoring of Avalanche Prone Slopes. *Proc., Third Conference on Acoustic Emission/Microseismic Activity in Geologic Structures and Materials*, Pennsylvania State University, Oct. 1981, pp. 449-466.
2. L. Obert and W. I. Duvall. *Use of Subaudible Noises for the Prediction of Rock Bursts—Part II*. Report of Investigation 3654. U.S. Bureau of Mines, 1942, pp. 15-35.
3. D. O. Harris, A. S. Tetelman, and F. A. I. Darwish. Detection of Fiber Cracking by Acoustic Emission. In *Acoustic Emission*, Special Technical Publication 505, ASTM, Philadelphia, Pa., 1972, pp. 238-249.
4. R. G. Liptai, D. O. Harris, and C. A. Tatro. An Introduction to Acoustic Emission. In *Acoustic Emission*, Special Technical Publication 505, ASTM, Philadelphia, Pa., 1972, pp. 3-10.
5. R. M. Koerner, A. E. Lord, Jr., and W. M. McCabe. The Challenge of Field Monitoring of Soil Structures Using AE Methods. *Proc., Second Conference on Acoustic Emission/Microseismic Activity in Geologic Structures and Materials*, Pennsylvania State University, Nov. 1978, pp. 276-289.
6. H. R. Hardy. Evaluating the Stability of Geologic Structures Using Acoustic Emission. In *Monitoring Structural Integrity by Acoustic Emission*, Special Technical Publication 571, ASTM, Philadelphia, Pa., 1972, pp. 80-106.
7. K. Nassar. *The Engineering Geology of the Wolcott Landslide, Eagle County, Colorado*. Master of Engineering Report. Colorado School of Mines, Golden, 1986.
8. B. F. Shine. *The Engineering Geology of the Battle Mountain Landslide, Eagle County, Colorado*. Master of Engineering Report ER-3139. Colorado School of Mines, Golden, 1985.

Publication of this paper sponsored by Committee on Soils and Rock Instrumentation.

Use of Time-Lapse Movie Photography in Landslide Monitoring

EDWIN P. BELKNAP AND JOHN B. GILMORE

In this paper is described the use of time-lapse movie photography to monitor the Muddy Creek landslide near Paonia, Colorado, during a 7-week period in the spring of 1986. Problems encountered in installation and operation of the equipment are discussed, and improvements in techniques and camera equipment are suggested.

Analysis of landslides by time-lapse photography provides the geoscientist with a unique perspective not apparent to the observer on a day-to-day basis. The method enables the study of the development and evolution of an unstable landmass as they actually take place and provides a useful supplement to traditional surface and subsurface geotechnical instrumentation. Because a camera can be installed quite quickly, the method can be used to provide information during the somewhat longer period required to install conventional observation instrumentation on rapidly moving slides. The quantity of information and the amount of detail obtained far exceed those available from any other method.

The Muddy Creek landslide along CO-133 near Paonia, Colorado, proved to be an excellent candidate for this study. The slide was large and fast moving, attaining a rate of almost 1 ft/hr in its early stages (J. Rold, Muddy Creek Slide Movement, Gunnison County. Unpublished Colorado Department of Natural Resources Memorandum to Governor Richard Lamm, May 1, 1986). The movement threatened not only burial of the highway but closure of the valley of Muddy Creek, with resultant impoundment of the stream flow and a threat to the safety of the Paonia Dam and Reservoir a short distance downstream. The film provided a record not only of the slide movement but also of the activities of the Colorado Department of Highways (CDOH) in preventing closure of the Muddy Creek Valley.

Other important information obtained from study of the film included (a) an estimated rate of landslide movement; (b) amount of total landslide movement; (c) information concerning local topographic changes and the development of dangerous situations not visible to those in the work area; (d) detailed observations of the contractor's operation, including progress in keeping the river channel open and reconstructing the highway embankment; and (e) daily weather conditions.

MUDDY CREEK SLIDE

The landslide is located in Gunnison County, Colorado, about 10 mi west of McClure Pass between the towns of Redstone and Paonia (Figure 1).

Bedrock of the Muddy Creek area consists of upper Cretaceous sandstones of the Ohio Creek formation unconformably overlain by mudstones, claystones, and shales of the lower Tertiary Wasatch formation. During the late Tertiary, the entire sedimentary sequence was intruded, uplifted, and gently tilted westward by the Ragged Mountain laccolith (1), forming a slope of from 12 to 14 degrees on the eastern side of the valley where the landslide is located.

The Muddy Creek slide is an extremely large complex of individual slides that originated in the sloping beds of the Wasatch formation at the foot of the Ragged Mountains. It is approximately 12,500 ft long by 5,200 ft wide, with an average estimated thickness of nearly 100 ft. The area of failed material is more than 1,500 acres and volumetrically encompasses approximately 140 million cubic yards (B. K. Stover, verbal communication, 1986). The slide is quite old and only minor movements associated with spring runoffs had been reported in historic times. The rapid movement in the spring of 1986 was apparently triggered by abnormally large snowpacks in the Ragged Mountains during the previous three winters. Past movement of the slide has forced the channel of Muddy Creek to the extreme western edge of the valley, where it has cut cliffs more than 100 ft high into the alternating sandstones and shales of the Ohio Creek formation. CO-133 is located along the west side of the stream between the channel and the cliffs. The distance between the slide toe and the cliffs ranges from 60 to 100 ft and the height of the toe from 35 to 40 ft along a 5,000-ft section of the road where the rapid movement of the slide threatened to close the road and dam the valley. It was this area that was photographed with the time-lapse cameras (Figure 2).

The rapid movement of the slide was discovered on April 29, 1986, by CDOH maintenance personnel, and two backhoes were immediately dispatched to the site. Movement of the slide toe had compressed the stream channel against the highway embankment to a width of less than 20 ft. This made it possible for the backhoes to reach across the stream from the road and scale material from the advancing toe into the creek, which carried it away downstream. Four more backhoes were soon added and additional construction equipment was brought in to raise the grade of the embankment, which was being eroded by the stream. Movement of the slide was also raising the grade of the stream, which threatened to flood the roadway. This work

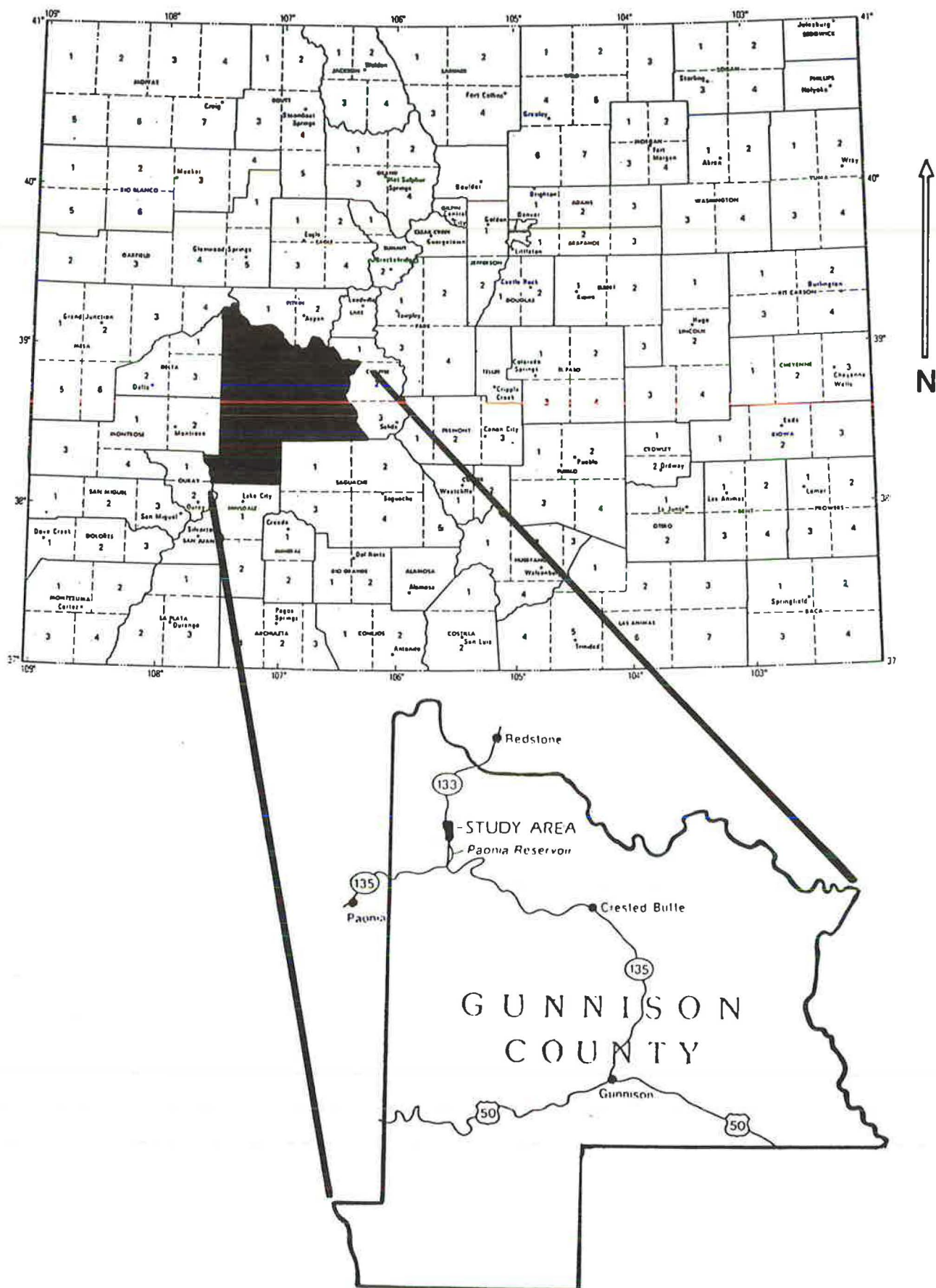


FIGURE 1 Location of study area.

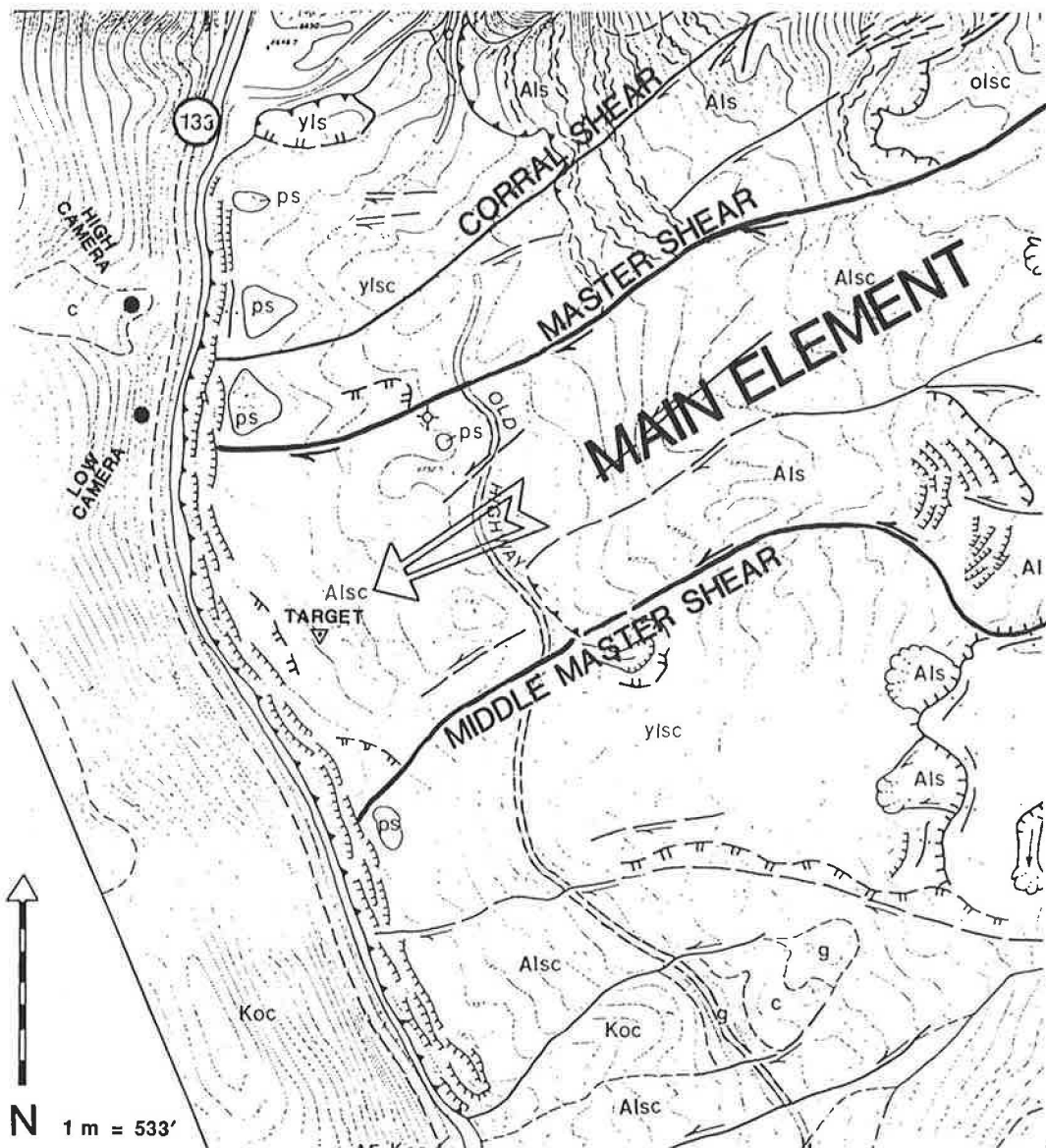


FIGURE 2 Study area showing locations of cameras and target.

continued on a 24-hr basis until June 23, at which time the grade had been raised approximately 40 ft and the slide movement had essentially stopped.

CAMERA SYSTEM

Two Kodak Analyst Super 8 time-lapse movie cameras were used in this study. The cameras, which are no longer manufactured, had been acquired at a government surplus outlet approximately 3 months before their installation on this project. Markings on the boxes indicated that the cost of the cameras in 1973 was \$175. Both came equipped with soundproof and weatherproof covers (Figure 3).

Features of this camera include a variable focal length 13 mm to 28 mm f/1.9 zoom lens, which permits latitude in selection of the field of view. Power can be supplied by 110-volt household current through an accessory transformer or, for

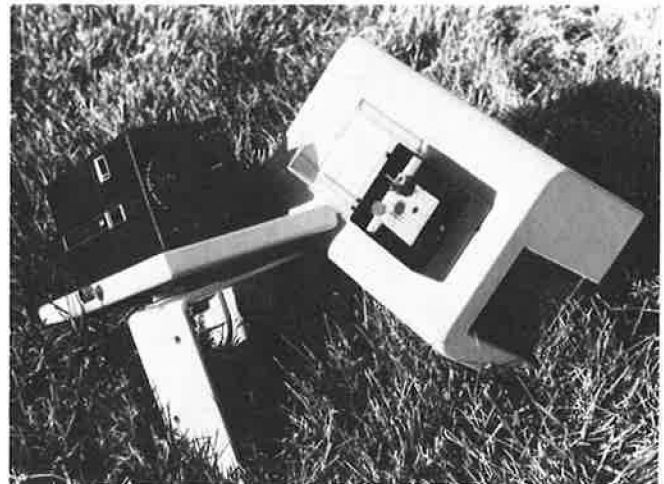


FIGURE 3 Camera, mounting platform, and protective cover.

remote operation, by four size AA 1.5-volt dry cells. Three of the cells power the film advancement motor and the fourth cell operates the automatic exposure control system. The camera is also equipped with a manual focusing adjustment, an end-of-film indicator lamp, an exposed-film indicator window, and a slide for adjusting the field of view through the reflex viewfinder. Rate of operation ranges from one frame every $1\frac{1}{4}$ sec to a maximum of one frame every 90 sec. The camera is designed to accept a standard Super 8-mm film cartridge containing 100 ft of film, but, because these are no longer available, 50-ft rolls were used. Depending on the frame rate selected, these permit continuous operation for periods ranging from $1\frac{1}{4}$ to 90 hr. The cameras used in the study are equipped with a mounting bracket that includes a gimbal, which permits the cameras to be adjusted horizontally or vertically. The upper part of the bracket contains a threaded socket hole for standard tripod installation, and the lower part has four holes to allow attachment to a mount with nails or screws.

The cameras use Kodachrome Super 8 ASA 40 or Ektachrome ASA 160 Type G Super 8 color film, both of which in the Denver area cost \$9 per roll. Processing charges are approximately \$5 per roll. Kodachrome requires shipping to a Kodak Regional Center for processing whereas Ektachrome can usually be developed locally.

CAMERA INSTALLATION

To obtain an adequate field of view, it was necessary to locate the cameras above and at some distance from the portion of the slide being photographed. Two sites were selected on the cliff west of the highway, which had previously been cut and benched north of the area where the roadway grade was being raised. One camera was positioned on one of the cut benches and the other was placed several hundred feet west and higher on the slope. Both were pointed south, which avoided problems with the rising or setting sun, and both were centered on the same scene with the high camera providing a wider field of view than the lower one (Figure 4).

At the time of installation, both cameras were thought to be



FIGURE 4 Field of view from high camera location; protective box is visible in lower right corner.

well outside the area of construction although this later proved to be incorrect in the case of the low camera.

Because the cameras were installed on quite short notice there was no time to prepare field mounts ahead of time, and it became necessary to improvise these on the job using survey lath, duct tape, and steel reinforcing bars. The resulting mounts appeared to be reasonably stable (Figure 5), but an unanticipated problem, described in the next section, was discovered during examination of the early pictures.

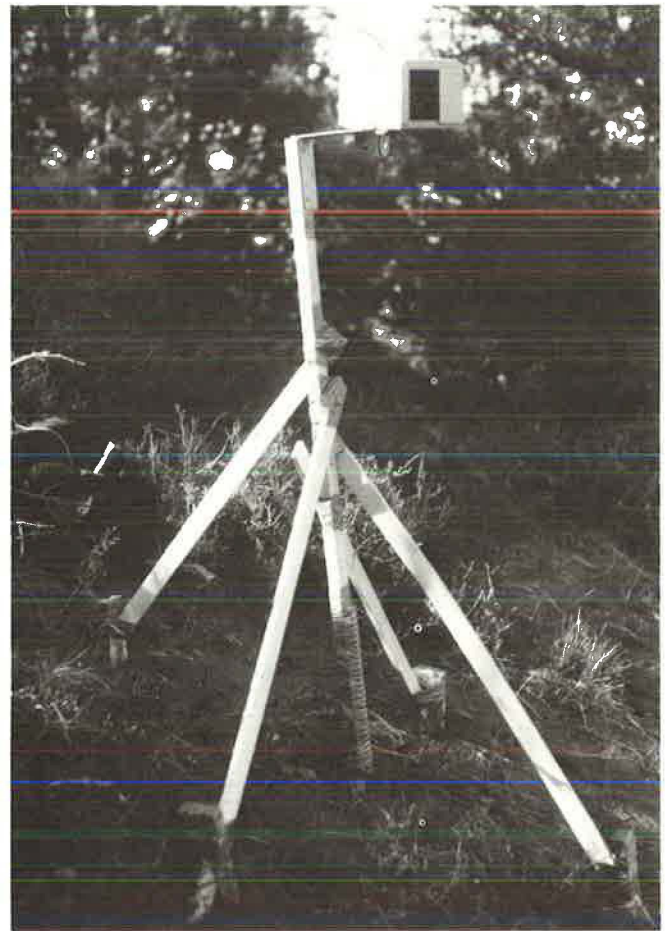


FIGURE 5 High camera installation showing wooden mount.

After the cameras had been mounted, the shutter rate was set at one frame every 90 sec. The rate was then checked for accuracy with a watch to ensure that the rate was not actually faster than indicated, which would mean that the film might run out before the camera was serviced. Both cameras were found to be operating somewhat more slowly than indicated, with between-frame intervals of 99 sec and 105 sec, respectively. Because a 50-ft roll of film provides a run time of 99 hr at the rate of one frame every 99 sec, this allowed an interval of 4 days between film changes. This time interval allowed most of the film in the cartridges to be used yet provided a moderate margin of safety. The manufacturer's instructions stated that a fresh set of batteries would last through two 100-ft rolls of film,

but it was decided that a battery change with each film change would provide inexpensive insurance against loss of coverage.

To provide an easily identifiable reference point in the pictures, a target consisting of an orange safety vest strung between two survey laths was driven into the ground at the location shown in Figure 2, near the toe of the main element of the landslide. This was unfortunately removed by construction activity early in the project, but during its brief existence it provided the marker that was later used in determining the rate of movement of the slide.

FILM RECORD

Features

Filming was started on May 4 and continued with a few minor interruptions through June 24, producing an essentially continuous record of both slide movement and construction activity throughout the 52-day period. The 13 rolls of film that were obtained from each camera were edited and spliced together in chronological order for analysis. An attempt was made to copy the low camera record on videotape, but the results were considered unsatisfactory because of poor color rendition and loss of definition. The film was later transferred to 16-mm format for more effective presentation.

Examination of the film shows that both cameras performed remarkably well in spite of changing weather, temperature, and lighting conditions. Color rendition and exposure were good and image definition was as sharp as could be expected from the type of equipment used. Mist or frost on the lens in a few of the early morning sequences degraded the image quality but dissipated rapidly as the sun rose.

Several interesting features of both the landslide and the associated construction activity were recorded on the film. The orange target vest could be observed to change position through the day during the first few weeks of filming, and trees, boulders, and large pieces of landslide material could be seen falling into the creek as the slide advanced. A few days after the beginning of construction activity, two bulldozers were set to work on the east side of Muddy Creek, scraping material from the surface of the slide toe and pushing it into the stream. As the cleared area increased in size, a pattern of small concentric cracks appeared in the bare ground near the edge of the toe and continued to expand in size and complexity for several days until obliterated by the equipment. Two small ranch ponds noted close to the edge of the toe were judged to pose hazards to the construction if they should suddenly breach into Muddy Creek, and the bulldozers were used to cut trenches to drain them into the stream. The film shows the construction of the trenches, and a rapid flow of water from one of them is briefly visible. Another, rather odd, sequence shows a small tree on the side of the pond opposite the camera actually moving past the pond. Although not apparent on the film, a longitudinal crack separating two lobes of the slide was present between the pond and the tree, and the lobe carrying the tree was moving at a faster rate. This shear is designated "Master Shear" in Figure 2.

The roadway construction activity is shown in interesting detail. Lifts of embankment material advance rapidly down the

roadway ahead of the equipment, and the increase in embankment height can be measured by comparing the daily changes in vertical distance between the grade and fixed objects on the adjacent canyon wall. At a curve in the stream, the portion of the channel visible to the camera can be seen to alternately constrict and widen as the slide advances and the backhoes remove additional material. At one point, because of topography and camera perspective, the channel appears to close completely as the backhoes fall behind schedule. The nighttime sequences show stationary construction lamps and moving vehicle headlights and include a brief interval about halfway through each night when all of the headlights stop simultaneously while the crews eat lunch. The amount of detail shown and the possibility of correlating this detail with given days and even times of day suggest that the method could also be an effective tool for construction monitoring. A record of this type could be extremely useful in resolving owner-contractor disputes and avoiding expensive litigation.

Local weather conditions at the site were recorded as part of the daily photographic record and included snow, rain, early morning mist, wind, and passing clouds. Effects of precipitation were not apparent in the day-to-day behavior of the landslide and its rate of advancement, probably because of the relatively small amount of moisture and the time required for precipitation to penetrate to the slip zone and generate a noticeable reaction. The films do show that precipitation decreased during late May and June, which probably helped slow the movement of the landslide during this period.

During examination of the daily positions of the vest on the film, it was noted that these occasionally showed retrograde, or uphill, motion. After reviewing several possibilities to account for this unlikely behavior, it was noticed that the aberration appeared to occur during and after periods of stormy weather. This suggested that the wooden survey laths of which the mount was constructed might be warping as they underwent periods of wetting and drying. Comparison of the position of a stable reference point on the cliff face relative to the edge of the picture confirmed that the camera was undergoing slow, periodic, side-to-side movements after each storm. It was soon discovered that small misalignments of the camera were also resulting from removal and replacement of the cameras when the film was changed.

Rate-of-Movement Determination

After the first rolls of film had been viewed, it was decided to use the orange target vest to attempt a determination of the rate of slide movement. This was done by projecting the film onto a cardboard screen and marking the starting position of the orange vest on the screen with a pencil. The position of the stable point on the cliff was also marked on the screen. As the film progressed and the vest moved across the screen, a new pencil mark was added at the dawn positions of both observation points for each subsequent day. To compensate for camera movement, the horizontal and vertical components of the apparent daily movement of both points were measured and the true movement of the vest determined by algebraically adding the apparent movement of the stable point components to the respective components for the vest. The scale in the field of

view near the vest was determined from the known length of nearby heavy equipment.

As can be seen in Figure 6, plots of the movement determined by this method show close agreement with similar plots of optical measurements taken by the Colorado Geological Survey. The fairly consistent discrepancy separating the rate curves is believed to result from error in scale determination of the photography or from camera perspective angle (the line of sight of the camera was not precisely perpendicular to the direction of slide movement).

An estimate of the total cumulative distance moved was not possible from the low camera film record because the camera location was changed twice to accommodate construction. Each movement changed the field of view and, along with it, the location of the reference point. The high camera was not moved, however, and a total horizontal movement of 125 ft during the 52 days was estimated from this record. This value was judged to be fairly accurate compared with a known distance scaled from recent aerial photographs of the area.

PROBLEMS AND SUGGESTED SOLUTIONS

Although time-lapse photography provides a number of obvious benefits, the system and methods used on the Muddy

Creek project were found to have some disadvantages. All appear to be easily correctable.

Camera Problems

One inconvenience is the lack of an automatic feature to turn the camera on and off at appropriate times. Because of the remote location of the Muddy Creek slide, daily visits to the camera sites were not practical, and the cameras were allowed to operate 24 hr per day. This increased film consumption by approximately 40 percent and necessitated editing the night-time sequences from the finished film.

To eliminate the need for an additional power source to operate a timer at remote locations, a simple photoelectric switch powered by the batteries in the cameras was developed by the CDOH Physical Research Section. A circuit diagram is shown in Figure 7. The switch, which consists of a cadmium sulfide photocell, a resistor, and a thyristor, was assembled from components obtained from Radio Shack at a cost of approximately \$2.50. A variety of CdS cells is available to provide sensitivity to various intensities of light.

Although not a problem on the Muddy Creek project, the maximum delay of 90 sec between frames could be a limitation

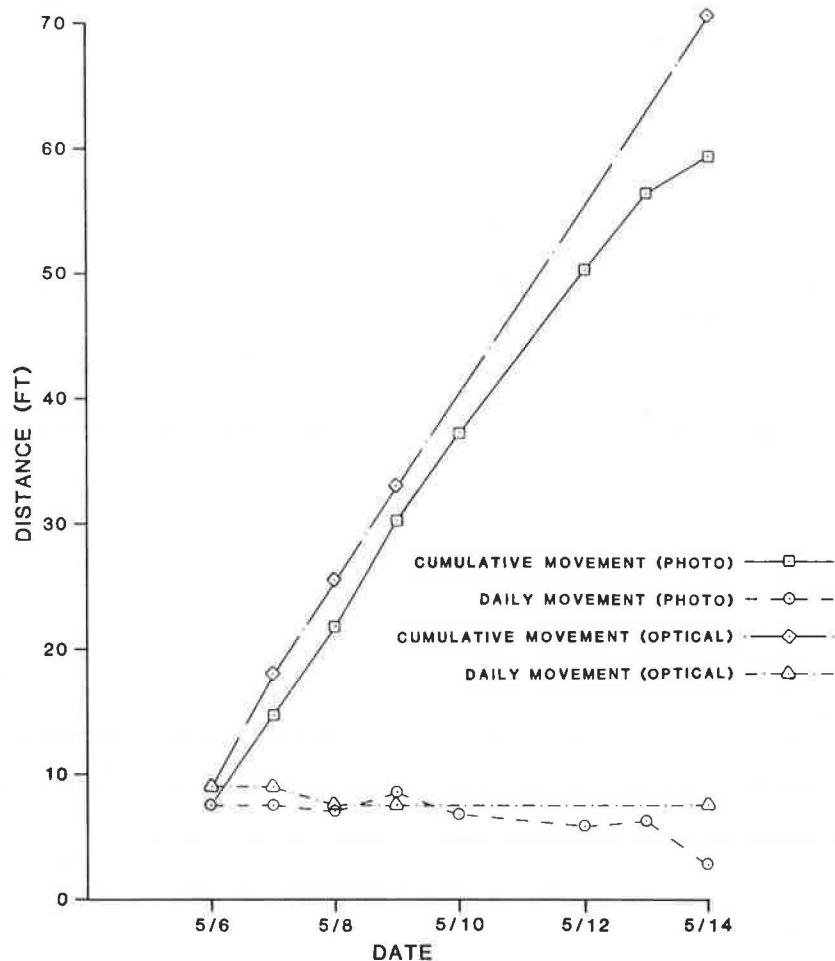


FIGURE 6 Comparison of rate-of-movement determinations from time-lapse photography and optical monitoring: Muddy Creek slide, May 1986.

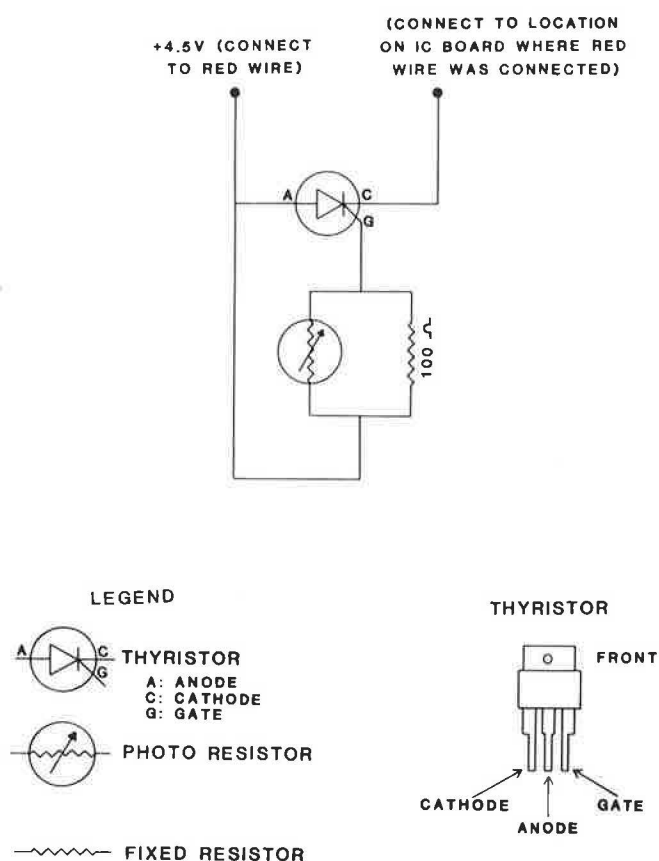


FIGURE 7 Circuit diagram of photoelectric switch.

on other slides. Delays of as much as 15 min would be beneficial in extending the coverage obtained on each roll of film and would give additional flexibility in photographing other long-term events that might be adequately recorded with fewer frames per day.

Mounting Problems

The slight changes in camera alignment, which occurred during film changes, would not constitute a problem if the only purpose of the surveillance was to provide a visual record of slide activity, although the resulting pictures would not transition smoothly between rolls. However, if rate-of-movement curves are to be plotted from the film record, misalignments will cause inaccuracies in recording daily target positions, which must be compensated by the method previously described. To maintain a more consistent alignment between film changes, CDOH is considering a simple gunsight arrangement consisting of two vertical wires attached to the front and rear of the protective case parallel to the optical axis of the camera. The sight would be aligned on a fixed point at the start of filming and realigned on the same point after every film change. A considerably more accurate system would consist of mounting an inexpensive low-power telescopic rifle sight on the case.

Changes in camera alignment resulting from warping of the frame can also be compensated in the manner described, but only if the fixed reference point remains within the field of

view. To eliminate this problem, CDOH plans to use a length of steel pipe mounted in a concrete-filled hole for future installations. This should provide a stable mount that can be readily installed. A small platform welded to a pipe connector will be fitted with suitable connections for mounting the protective box. The platform and fitting can then be easily removed for reuse at other locations while the pipe standard remains in place.

A problem encountered on this project, which would probably occur only rarely but which should nonetheless be considered, is stability of camera location. When the cameras were placed on the Muddy Creek project, project personnel provided assurances that the locations would not be disturbed by construction. However, it was shortly decided that the area in which one of the cameras was located would be a good place to obtain additional embankment material for the roadway grade change. This required moving the camera. A few days later additional material was needed, so the camera was moved a second time. Although the cameras were realigned to approximately the same orientation after each move, the change in angle of aspect caused noticeable and disconcerting changes in the continuity of the finished film. In the interest of obtaining a smoothly continuous film record and avoiding the extra labor of moving the equipment, it is important to select camera locations that are the least likely to be disturbed by later changes in plans by persons not involved in the photography.

Other Problems

A vital aspect of using photography as a measuring tool is determination of image scale. This was not considered at the outset of the Muddy Creek project although the need became apparent as soon as the idea of constructing a rate-of-movement graph was conceived. Fortunately, the construction equipment visible on the film provided objects of known dimensions whose images could be measured on the projection screen, but this would not necessarily be the case in all situations in which the method might be used. For future projects, CDOH is planning to use targets made of plywood sheets of known dimensions painted fluorescent orange. To provide backup in case of removal of a target, as happened on this project, it is planned to install a series of two or more targets spaced at measured intervals along a line crossing the field of view of the cameras. The well-defined edges of this type of target should increase the accuracy of scale determinations made from the photographs.

A potential problem, which was not encountered on this project but which appears to be a likely possibility in the future, is the effect of cold weather operation on the dry cell power supply of the cameras. No record of the temperatures encountered during the May-June duration of the filming was available, but, given the elevation at the camera locations (6,700 ft), it is likely that the temperature dropped slightly below freezing for at least a few hours during some nights in early May. The film has not been analyzed in detail for the effects of the lower-temperature episodes, but there are some indications that the filming rate may have decreased. It is thought that an external power source would be advisable if the cameras are to be operated for extended periods in temperatures below freezing.

The department is considering use of a 6-volt motorcycle battery equipped with a voltage divider to provide a higher ampere-hour source. Another advantage of the motorcycle battery would be its ability to be recharged, which would eliminate the expense of replacing the camera dry cells with every film change as was done on this project.

Another potential problem that will undoubtedly be encountered sooner or later is security. The cameras would be a tempting target for thieves or vandals and need to be either carefully concealed or located in places difficult to access. Tall poles have been used with success although ladders are required to service the cameras. Hard shelters can be considered although these would not be completely safe from determined persons even if access were difficult. No problems were experienced on the Muddy Creek project because of the cliff-top locations of the cameras and the general remoteness of the area, but these will not be the conditions in all areas where the cameras will be used.

CONCLUSIONS

Experience gained with the use of time-lapse camera equipment on the Muddy Creek slide has shown that the technique

can provide an effective, economical observational tool that can be used to measure rates of movement of relatively fast-moving landslides. In addition to providing an amount of detailed information not furnished by any other method, it also provides a permanent, minute-by-minute record of all events occurring within the field of camera view over extended periods of time. Observation of the details of the roadway construction filmed during the Muddy Creek project suggests that the method could be of value in construction monitoring as well.

REFERENCE

1. R. C. Johnson and F. May. *A Study of the Cretaceous-Tertiary Unconformity in the Piceance Creek Basin, Colorado*. Bulletin 1482-B. U.S. Geological Survey, 1980.

Publication of this paper sponsored by Committee on Soils and Rock Instrumentation.

Monitoring Landslide Movement with a 35-mm Camera

J. D. BALLANTYNE, D. R. DEAN, JR., AND B. L. THOMPSON

The methods of analytical photogrammetry and microcomputer technology are combined to generate contour maps or cross sections, or both, of landslides along roadways with minimal conventional surveying. A conventional 35-mm camera and 8-by 10-in. photographs are used for the mapping. A minimum of two overlapping photographs are needed of the area to be mapped. Also, a minimum of six well-distributed control points are needed. Control points are points for which position (X and Y coordinate pair) and elevation (Z) must be obtained by conventional surveying techniques. The photogrammetric model used is the direct linear transformation model. This model uses x and y coordinates of corresponding images on two or more photographs to determine the position and elevation of such images in a ground-based coordinate system. A microcomputer performs the calculations and an electronic digitizer connected to the microcomputer is used to obtain the image coordinates on the photograph. The output can be in the form of a coordinate list of desired points, cross sections, a contour map, or three-dimensional perspective plot. The graphics are generated by a pen plotter connected to the microcomputer. Studies indicate that the error vector at about 400 ft is 0.4 ft for this system of mapping. A slope in distress can be monitored over a period of time. To eliminate resurvey, the six control points have to be located in a stable area.

A system for economically monitoring unstable slopes along roadways would enable highway departments to predict where to concentrate remedial measures for such slopes. This concept provided the impetus for developing a monitoring system that uses photogrammetric techniques and computer technology. At the outset, the goal was to develop a mapping system that would predict the position of points to within 1 ft. How the system was developed, how it was tested, and how it is applied in the field are described.

SYSTEM DEVELOPMENT

System Components

The mapping system includes two primary components, the hardware and the software. The hardware consists of a 35-mm camera (any amateur camera), a microcomputer, a monitor, a

digitizer, a printer, and a plotter. The microcomputer used with the system software must have 256K of random access memory, two floppy disk drives, a color graphics adapter card, two serial ports, and a parallel port. The hardware is "off-the-shelf" equipment and would most likely be found in many modern design offices.

The software, which enables the system to be operational, has two aspects. One is the software that performs the photogrammetric calculations or reductions and the other is the software that performs the graphics or display operations such as outputting cross sections, contour maps, and perspective views. Both the photogrammetric and the graphics software are menu driven; that is, the user responds to prompts displayed on the monitor in order to use the system once the fieldwork has been done and photographs have been obtained. The graphics software was obtained from the U.S. Geological Survey in Denver, Colorado, as "freeware" and was modified to include the capability to output cross sections. The photogrammetric software was developed by the authors using the direct linear transformation (DLT) photogrammetric model developed by Abdel-Aziz and Karara (1) and modified by Bopp and Krauss (2). In addition, lens distortion terms, both symmetrical and asymmetrical, developed by Brown (3, 4), were included in the photogrammetric software. At this point a discussion of photogrammetric theory may be in order.

Photogrammetric Theory

Photogrammetric calculations for the position and elevation of points of interest may be thought of as involving two distinct operations. The first one is called space resection and the other is called space intersection. The resection calculations are performed one photograph at a time and the outcome of the calculations is the position and orientation of the camera. The intersection calculations are performed with two photographs and the outcome provides the position (X and Y) and elevation (Z) for the points of interest. Note that the intersection calculations must be performed with two or more photographs in order to determine the elevation and position of any point of interest. The photographs must be obtained from different locations.

Consider a camera focused on a point on a landslide. If the camera shutter is tripped, it is assumed that light will travel in a straight line from the point on the landslide through the camera lens to the film behind the lens and the point will then be imaged on the film. Now consider two coordinate systems, a two-dimensional system and a three-dimensional system. The two-dimensional coordinate system is in the plane of the film

J. D. Ballantyne and D. R. Dean, Jr., Department of Civil Engineering, West Virginia University, Morgantown, W.Va. 26506-6101. B. L. Thompson, Materials Control, Soil and Testing Division, West Virginia Department of Highways, 312 Michigan Avenue, Charleston, W.Va. 25305.

and the three-dimensional coordinate system defines the position and elevation of the point on the landslide. The former is referred to as the photo coordinate system and the latter is referred to as the object space coordinate system.

The photo coordinates of the image may be expressed as functions of the object space coordinates for the point on the landslide. These functions are as follows:

$$\begin{aligned}x &= (L1 \cdot X + L2 \cdot Y + L3 \cdot Z + L4) / (L9 \cdot X \\&\quad + L10 \cdot Y + L11 \cdot Z + 1) \\y &= (L5 \cdot X + L6 \cdot Y + L7 \cdot Z + L8) / (L9 \cdot X \\&\quad + L10 \cdot Y + L11 \cdot Z + 1)\end{aligned}\quad (1)$$

where

- x and y = photo coordinates of the image of a point,
- $X, Y,$ and Z = the object space coordinates of an imaged point, and
- $L1, L2, \dots, L11$ = the transformation parameters.

The eleven transformation parameters ($L1$ through $L11$) are functions of

- The position (X and Y) and elevation (Z) of the camera lens in the object space coordinate system;
- The three orientation angles of the camera: one about the photo coordinate x -axis (ω), one about the photo coordinate y -axis (ϕ), and one about the lens axis (κ);
- The photo coordinates ($x\omega$ and $y\omega$) of the principal point, which is the point on the film where a perpendicular line from the camera lens would intersect the film; and
- The focal length of the camera lens.

It should be noted that the 11 transformation parameters are functions of only 9 camera orientation elements, which were listed previously. This point will be considered again later. When the transformation parameters are determined, the resection step will be complete.

How are the transformation parameters determined? First, consider six points on the landslide or in object space and that the position (X and Y) and elevation (Z) of these six points have been determined by conventional surveying techniques. The six points that have a position and an elevation determined by conventional surveying techniques are called ground control points. Next, the photo coordinates of the six control points are measured. The mapping system under consideration measures the coordinates with an electronic digitizer. Using the photo coordinates and object space coordinates of the six control points, 12 DLT equations, 2 for each point of the type in Equation 1, may be written. These 12 equations include the 11 unknown transformation parameters as well as the photo coordinates and the object space coordinates of the 6 ground control points. A least squares technique is used to solve the redundant, that is overdetermined, system of equations for the 11 unknown transformation parameters.

After the transformation parameters have been obtained for a particular photograph, they apply to any point imaged on that photograph or film so the photo coordinates of images of other

points of interest can be measured and substituted into Equation 1. Even when the 11 transformation parameters are known, only two equations can be written for each image point, and these two equations are not enough to solve for the unknown $X, Y,$ and Z for a point of interest. However, if a second camera position, hence a second photograph, is used, the transformation parameters for the second photograph can be determined as they were for the first photograph. Consequently, when the transformation parameters of the first and second photographs are known, four DLT equations similar to Equation 1 can be written for each point of interest, provided that the photo coordinates of such a point are measured or digitized on each of the two photographs. Again, with four equations and three unknowns, redundancy exists so another least squares solution for the $X, Y,$ and Z of each point of interest is possible. Solving the set of four equations for $X, Y,$ and Z for each point is known as performing the space intersection mentioned previously.

In summary, the photogrammetric reductions or calculations include two basic operations, space resection and space intersection. The resection operation requires the use of at least six control points or points of known position and elevation in object space to calculate the transformation parameters that are unique to each photograph. The resection operation is performed on one photograph at a time. The analytical intersection operation requires the use of at least two photographs for which the transformation parameters have been determined. The outcome of the intersection operation is the X -, Y -, and Z -coordinates for a point of interest in object space. In the next section some numerical considerations in solving for the transformation parameters for each photograph will be addressed.

Numerical Considerations

It was pointed out in a previous paragraph that the 11 transformation parameters are functions of only 9 camera orientation elements; consequently, the 11 transformation parameters are not all independent. This was recognized by Bopp and Krauss (2) and they developed two constraint equations to account for the lack of independence of the 11 transformation parameters. The use of constraint equations when calculating the transformation parameters makes the least squares solution more rigorous. The authors used these constraint equations as well as the DLT equations to compute the transformation parameters by the method of least squares.

The DLT equations are nonlinear in terms of the transformation parameters; therefore, the Taylor series expansion including only the first-order term was used to linearize the DLT equations. A least squares algorithm was applied to the linearized equations to arrive at a solution for the transformation parameters. During the linearization stage, an approximation of the transformation parameters is needed even before they are calculated. For the DLT equations, the first approximation for the transformation parameters may be set to zero. This is a great advantage compared with another popular photogrammetric model based on linearized collinearity equations. In the case of the collinearity equations, all zero approximations cannot be used for the camera parameters. The camera parameters include the camera lens position and elevation, the photo coordinates of the principal point, the focal length, and the three

orientation angles. Realistic approximations must be substituted into the linearized collinearity equations before a solution can be obtained. A possible advantage of the collinearity equations over the DLT equations is that because there are two fewer unknowns, 9 versus 11, one fewer control point is needed.

Solving the nonlinear equations for the transformation parameters requires an iteration technique whereby a least squares algorithm is used to solve for corrections to the approximations for the transformation parameters. The iterations are continued until the corrections to the approximations are sufficiently small to terminate the iterations and assume that a solution has been obtained.

Software Coding

The photogrammetric software was written to include the theoretical considerations discussed. As mentioned before, the software is menu driven and using it typically involves typing in names of files that hold data or answering "yes" or "no" to prompts for selecting options for weighting, constraints, lens distortion correction, or output options. The photogrammetric software also includes routines for reducing transit and stadia notes in order to create data files that contain the object space coordinates for the control points. These specialized routines are addressed through the main menu that appears on the screen when the program disk is "booted." The use of the electronic digitizer to measure the photo coordinates of the images of points and to place these coordinates in a data file is also controlled by the photogrammetric software. The graphics software operates completely independently of the photogrammetric software, but it uses a data file created by the photogrammetric software. It should also be noted that the data file required by the graphics software may be created independently of the photogrammetric software.

SYSTEM TEST

The goal was to develop a mapping system that would predict the position of points to within 1 ft. Abdel-Aziz (5) developed general equations to predict the accuracy of object space coordinates derived from convergent photographs. However, the equations were for points located at special positions within the object space being measured. Points, for which coordinates are desired, are frequently distributed throughout the photograph so a practical test of accuracy for the system was needed. Also unknown was the kind of accuracy that would be possible using an electronic digitizer to measure photo coordinates on enlarged photographs obtained from amateur or nonmetric cameras. Consequently, a test field was established to test the system. The test field is an array of points on the tower and east wing of the Engineering Sciences Building at West Virginia University. Test points are located at the corners of window frame moldings and at other discrete marks present on the building. The X -, Y -, and Z -coordinates of 47 such test points were obtained by conventional surveying methods. A test of the mapping system consists of comparing the X -, Y -, and Z -coordinates for each point as determined by conventional

surveying methods and as determined by photogrammetric surveying.

Establishment of Test Points

The position of the test points on the Engineering Sciences Building was determined from two baselines that were connected by conventional surveying methods. The method of angle intersection, both vertical and horizontal, was used to determine the position of the test points. Because two baselines were used, the position of each test point could be determined by two independent sets of measurements and calculations; thus a check for the position of each point was possible. As an estimate of the test point position, the average of the two independent determinations was obtained, and this average X -, Y -, and Z -coordinate became the standard against which the photogrammetrically determined values were compared.

The mean difference between the two independent conventional determinations of the X -, Y -, and Z -coordinates for the test points on the Engineering Sciences Building and the standard deviations of the differences of the X -, Y -, and Z -coordinates are as follows:

Coordinate	Mean (ft)	Standard Deviation (ft)
X	0.006	± 0.113
Y	0.037	± 0.081
Z	0.003	± 0.021

Some of the test points were used as required control points for the photogrammetric reductions, but the points used for control were not used in subsequent tests for accuracy.

Photogrammetric Procedures

Photography

Photographs were obtained with a 35-mm camera using black-and-white film. A 50-mm lens and a zoom (70- to 200-mm) lens were used. The concept was to simply get a picture of the test points by centering the camera axis on the test field. Photographs were obtained at a number of positions, with respect to the test field, with both the 50-mm lens and the zoom lens. The various test combinations are given in Table 1. For example Test A was from a two-photograph model and the zoom lens was used. Note that there are three-photograph models and four-photograph models. Even with the multiple-photograph models, each exposure was obtained with the camera axis centered on the test field.

Film and Print Processing

After the film was exposed, it was sent to a local photo lab for developing and printing. There were no special instructions other than to make full-frame prints on 8- by 10-in. resin-coated paper. These 8- by 10-in. photographs were the prints on which the photogrammetric measurements were made.

TABLE 1 SYSTEM TEST RESULTS

Test	Difference Between Conventional Survey and Photogrammetric Survey						Error Vector	95% Confidence Interval for Mean of Error Vector	No. of Test Points	Avg Camera Distance to Center of Site	B/D Ratio	
	X-Coordinate		Y-Coordinate		Z-Coordinate							
	Mean	Stdev	Mean	Stdev	Mean	Stdev						
A	0.08	±0.17	0.19	±0.36	−0.01	±0.11	0.41	±0.20	0.34 to 0.48	38	471	0.60
B	0.08	±0.17	0.17	±0.38	0.01	±0.12	0.42	±0.22	0.35 to 0.49	38	463	0.61
C	−0.01	±0.18	0.16	±0.33	0.07	±0.14	0.39	±0.20	0.32 to 0.46	38	356	0.47
D	0.05	±0.19	−0.18	±1.78	0.11	±0.22	1.49	±0.99	1.16 to 1.82	38	435	0.23
E	0.03	±0.16	0.25	±0.32	0.04	±0.11	0.39	±0.21	0.32 to 0.46	38	401	0.56
F	0.28	±0.53	−0.43	±0.60	−0.15	±0.19	0.88	±0.38	0.64 to 1.12	12	135	0.64

Note: Confidence interval = Mean \pm Stdev * $t_{0.025, df} / [(\text{No. of points})^{1/2}]$. Error vector = $[(\text{difference in } X)^2 + (\text{difference in } Y)^2 + (\text{difference in } Z)^2]^{1/2}$. Engineering Sciences Building test field (high precision control): A = two photos, 70- to 200-mm zoom lens; B = three photos, 70- to 200-mm zoom lens; C = three photos, 50-mm lens; D = two photos, 50-mm lens; E = four photos (2 from Test A, 2 from Test C). Alternative test site (Cooper's Rock) (low precision control) stadia: F = two photos, 50-mm lens. Units are in feet unless otherwise noted. Stdev = standard deviation.

Photogrammetric Measurements and Reductions

The photo coordinates of the images of the test points on each photograph were measured with an electronic digitizer connected to a microcomputer. As the photo coordinates were measured, a file was created in which all of the photo coordinates of the test points on a particular photograph were saved or stored. These files of photo coordinates were used to run repeated photogrammetric reductions, space resections, and space intersections to obtain the X-, Y-, and Z-coordinates of the test points in the ground coordinate system that was established by conventional techniques. The photogrammetric reductions were made using the photogrammetric software described previously.

Weighting, Constraints, and Lens Distortion Corrections

Multiple photogrammetric reductions were performed on the data files of photo coordinates. These multiple runs were performed to study the effect of various weighting techniques, the effect of including constraint equations as suggested by Bopp and Krauss (2), and the effect of correcting for both symmetrical and asymmetrical lens distortion as modeled by Brown (3, 4). The photogrammetric software enables the user to select any combination of these options before performing the photogrammetric reductions.

There are two weighting options that may be used during the least squares solution for the 11 transformation parameters. One weighting option permits the user to assume that all photo coordinates have equal weights; that is, no one photo coordinate is more accurate than another. The other weighting option permits the user to assign weights to the photo coordinates on the basis of the variances for each photo coordinate. The weight is made equal to the inverse of the variance for each photo coordinate. Consequently, photo coordinates with small variances will have larger weights than coordinates with larger variances and will contribute more to the least squares solution for the transformation parameters. The least weighting option may only be selected when multiple measurements have been made for each photo coordinate or if the user assigns individual variances to each coordinate.

There are just two constraint options. Either the constraint equations for the 11 transformation parameters as developed by Bopp and Krauss (2) are enforced or they are not.

There are several possible options for corrections for symmetrical and asymmetrical lens distortions. It has been shown that three terms in an odd-powered polynomial are sufficient to model symmetrical radial lens distortion. Consequently, the user has the option of correcting for such distortion by using one, two, or three terms when making photogrammetric reductions. Two terms are always required to model asymmetrical lens distortion. The user has the option of either correcting or not correcting for asymmetrical lens distortion during photogrammetric reductions.

If the same options were selected for every photograph in a set of photographs used in a photogrammetric reduction for the X-, Y-, and Z-coordinates of test points, there would be 20 possible combinations of the options or 20 different possible photogrammetric reductions. Not all possible reductions were made, but enough were made to determine which options were important for the system under consideration.

Index of Accuracy

The accuracy of the photogrammetric reductions is indicated by observing the difference between photogrammetrically determined X-, Y-, and Z-coordinates and the conventionally determined X-, Y-, and Z-coordinates for test points on the Engineering Sciences Building. A single index of accuracy is the error vector that is computed as follows:

$$EV = [(dx)^2 + (dy)^2 + (dz)^2]^{1/2} \quad (2)$$

where

EV = error vector,
dx = difference in X coordinates,
dy = difference in Y coordinates, and
dz = difference in Z coordinates.

The error vector was computed for each test point, and the average error vector for all test points was computed for each

condition tested. If the error vector was less than 1 ft, the accuracy requirements that were established at the outset had been met.

Alternative Test Site

The system was also tested on a cut slope. At this test site the test points and control points were determined by the method of stadia. Photographs were obtained and the photogrammetric reductions were made in a manner similar to that used for the test field on the Engineering Sciences Building. The main difference was the accuracy with which the control point positions were known.

Discussion of Test Results

The test conditions are identified as A through F. The conditions are as follows:

- A = two photos, zoom lens, Engineering Sciences Building (ESB);
- B = three photos, zoom lens, ESB;
- C = three photos, 50-mm lens, ESB;
- D = two photos, 50-mm lens, ESB;
- E = four photos (two from A and two from C) ESB; and
- F = two photos, 50-mm lens, alternative site, control by stadia.

It should be noted that the control points and the test points were known with greater accuracy on the Engineering Sciences Building than on the alternative test site. Also, the error vector, as previously defined, is the index used to measure the accuracy of the system.

Effects of Options

The weighting, constraints, and lens distortion correction options were exercised in various combinations for each of the test conditions while the photogrammetric reductions were executed to determine the X-, Y-, and Z-coordinates of the test points. The same control points were always used. The average error vector for each of these reductions was studied to determine the effects of the various options used. These studies indicated that the weighting technique of assigning weights on the basis of the variance of the photo coordinate gave a slightly better error vector than did assigning weights equally to all photo coordinates. Invoking the constraint equations did not change the error vector; that is, there was no improvement in accuracy when the constraint equations were used. An unexpected result occurred when the lens distortion terms, both symmetrical and asymmetrical, were exercised. With the addition of terms to correct for lens distortion, the error vector increased in size or the accuracy decreased. It is hypothesized that the lens distortion correction terms that were used did not adequately model the lens distortion for the photographs. This is because there is not only distortion due to the camera lens but

also distortion due to the enlarger lens used to print the photograph. Some distortions may also occur because the principal point of the negative cannot be aligned with the lens axis of the enlarger. Perhaps a better model for these distortions could be derived.

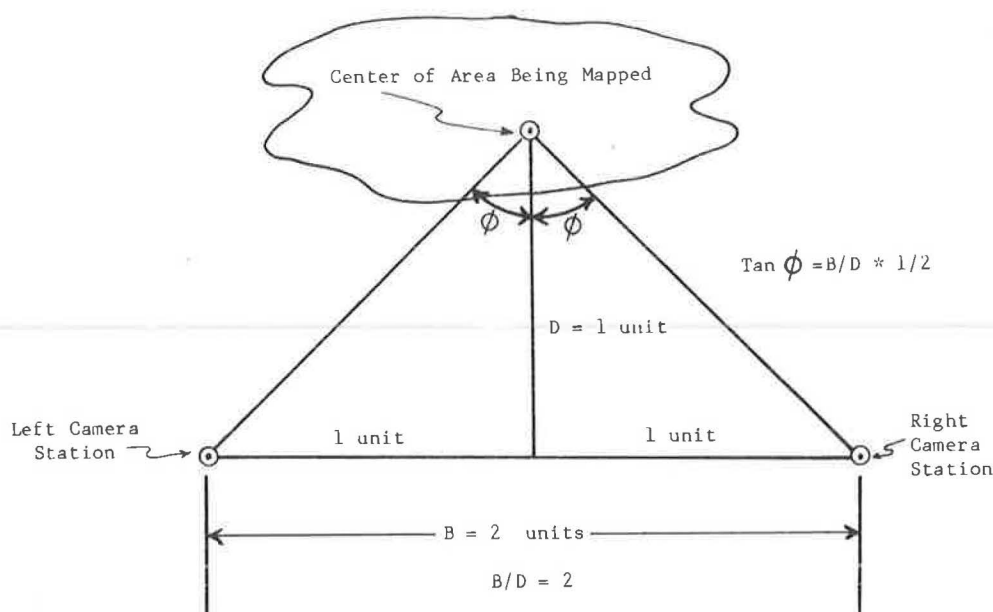
On the basis of the average error vector from the multiple reductions while various options for weighting, constraints, and lens distortion correction were exercised, it can be concluded that the only option that need be applied is weighting. The weighting option that assigns weights on the basis of photo coordinate variances should be selected. In the present study, weighting the photo coordinates in this manner decreased the error vector slightly but not significantly. Exercising the constraint equations had no beneficial effect on accuracy. The lens distortion terms, when exercised, were actually detrimental to the accuracy. Because the lens distortion terms are not required for this system, the minimum number of control points to permit redundancy in the least squares solution for the transformation parameters is six. The results of all tests discussed hereafter were obtained by executing the photogrammetric software so that only the weighting by variances option was selected. This is the recommended procedure for using the photogrammetric software.

Test for Accuracy

Photographs of the test site were obtained from a number of different positions and with different camera lenses. Camera position and lens type make up a test condition. The test conditions were identified and listed previously. The average error vector for each condition was the index for accuracy. Results of the test for each condition are given in Table 1.

The 95 percent confidence interval for the mean of the error vector was used to determine whether the mapping system met the accuracy requirement that was specified initially. If the confidence interval was within ± 1 ft, the mapping system met the accuracy requirements. An inspection of Table 1 shows that the mean error vector as determined under Test Conditions A, B, C, and E was within the required limits. Condition A was a two-photo model obtained with a zoom (70- to 200-mm) lens at about 450 ft. Condition B was similar to A except that a third photograph was included. Including the third photograph did not improve the accuracy of the system. Condition C was a three-photo model obtained with a 50-mm lens at about 350 ft. Note that the mean error vector for this condition is better than for Conditions A and B, but not significantly better. Condition E consists of the two outside photographs from Condition A and the two outside photographs from Condition C. Again, use of more than the minimum of two photographs did not increase the accuracy of the mapping system.

The mapping system did not meet the accuracy requirements under Condition D, which was a two-photo model obtained with a 50-mm lens at about 450 ft or less. The distance of about 450 ft probably was not the reason the accuracy requirement was not met. The test for Condition D probably failed because the two camera axes intersected at such a small angle that the photogrammetric intersections were weak. Note that the B/D ratio for condition D is quite small whereas the B/D ratio for the successful conditions are near 0.5 or greater. The B/D ratio



Desirable Conditions: (1) Each camera axis directed toward the center of the area being mapped and (2) camera axes intersect at 90 degrees.

FIGURE 1 Optimum camera configuration.

is the base length between camera stations divided by the perpendicular distance from the base to the point being photographed (Figure 1). The B/D ratio is not necessarily an indication of convergent camera axes. But, if the two camera axes are directed toward the center of the object being mapped, the B/D is an indication of the amount of convergence of the two camera axes. As shown in Figure 1, if the B/D ratio is 2 and the two camera axes are directed toward the center of the object, the intersection angle of the two camera axes is 90 degrees. Such an angle of intersection is optimum for computing intersections. The convergence angle of the two camera axes in Condition D is small. The distance between the camera stations was only about 100 ft ($0.23 \cdot 435 = 100$). If the distance between the camera stations had been increased and the depth to the test field maintained as before, perhaps the results would have been better.

The mapping system also failed to meet the accuracy requirement under Condition F. It should be noted that under Condition F the mean error vector was less than 1 ft and that the upper level on the confidence limit was over 1 ft by a small amount. Because the control and test point positions were established by the method of stadia, their positions were only known to within ± 1 ft to begin with.

It appears that establishing the six control points by stadia may not be adequate to meet the accuracy requirements of ± 1 ft. The method of angle intersections from each end of a measured baseline would be adequate. Other possibilities exist and additional studies are ongoing.

USE OF THE SYSTEM

Use of the proposed mapping system to monitor an unstable slope requires both field and office procedures. The procedures are not complex, but they do require some planning.

Field Procedures

Field procedures are to

1. Determine the number of photographs required,
2. Determine where control points should be located,
3. Determine position of control points,
4. Determine if artificial targets are necessary, and
5. Obtain photographs.

Number of Photographs

The number of photographs required for stereo coverage of the site is determined simply by looking through the viewfinder of the camera, visualizing the frames, and moving around the site to select the camera stations. Of course, the minimum number of photographs is two. Previous studies by Abdel-Aziz (5) and Kenefick (6) have shown that the best accuracy is obtained when the two camera axes intersect at about a 90-degree angle. This should be kept in mind when selecting camera stations, and an attempt should be made to obtain convergent photographs such that the camera axes will intersect near the center of the site being mapped at an angle close to 90 degrees (Figure 1). Because of varying site conditions this may not always be possible, but it is a rule that should be followed whenever possible. A third camera station may be selected. However, the third photograph is not necessary if 100 percent overlap is obtained with the first two photographs. In some situations the third photograph may be needed just to get stereo coverage of the entire site. The system will handle a total of four photographs. It is important to remember that every point to be mapped must appear on at least two photographs.

Location of Control Points

When the number and orientation of photographs have been determined, the next step is to determine where control points must be located. The points to keep in mind are that there must be at least six control points visible in every photograph and that they should be well distributed over the site and not clustered together. Also, to avoid having to reestablish the control before every remeasurement on the site, the control points should be located in stable areas around the border of the active landslide. Another point to remember is that if lens distortion terms are used in the photogrammetric software, an additional control point should be obtained for every lens distortion term that is added. However, it should be noted that the results of tests that were discussed in the previous section indicate that, because paper print enlargements are being used, including lens distortion terms for the system produces no significant gain in accuracy.

Determination of Control Point Position

The X-, and Y-, and Z-coordinate position of the control points may be obtained by a number of methods. The stadia method may be used if slope angles are not great. Also, the angle intersection method may be used. The angle intersection method involves measuring a horizontal and a vertical angle to the control point from each end of a measured baseline. The horizontal angle is the angle to the right from the baseline and the vertical angle may be measured from a horizontal line, zenith, or nadir. The photogrammetric software includes routines for reducing the field data from either of these methods to a file of X-, Y-, and Z-coordinates for the ground control points. Other conventional surveying methods may also be used to obtain the X-, Y-, and Z-coordinates for the ground control points. As a rule, the more accurate the control data, the more accurate the results from the photogrammetric reductions will be.

Targeting

The mapping points (that is, the high points, the low points, and the points in between where the slope changes) and the ground control points must be discernible on at least two photographs. If there are no natural features such as rocks or clumps of soil to be used to mark the mapping points, these points must be artificially targeted. Some targeting materials are sheets of paper, lime, and stakes with paper wrapped around the bottom and secured with a rubber band. It is best for the target to be larger than the crosshairs on the digitizer. If the target is slightly larger than the crosshairs, pointing precision on the digitizer is optimum.

Obtain Photographs

At this stage everything should be ready for taking photographs; that is, camera stations have been located, ground control point locations determined and measured, and targeting

completed if necessary. Care should be used to obtain photographs in sharp focus and with good depth of field. It is important that the photographs be of good quality in order to get good results from the photogrammetric reductions. A suggested practice at this point is to make a rough sketch of the site from the perspective of the camera station and note rough locations of mapping points and ground control points. The sketch will be helpful in the office in identifying and labeling mapping and ground control points.

Office Procedures

Office procedures have been simplified by the photogrammetric software. After the film has been developed and 8- by 10-in. photographs have been printed, the photographs must be studied so that conjugate mapping and ground control points can be identified with the same symbol or labeling mark. It is at this identification stage that the sketches made in the field at the camera stations may be beneficial.

After the points have been identified on the photographs, the remaining office procedures are controlled by the photogrammetric software. All that is required is that the digitizer, plotter, and printer be properly connected to the computer and that the computer equipment be in proper working order. Three floppy disks are required, one for holding the photogrammetric software, one for holding the graphics software, and one formatted blank disk to be used as a project data disk. To perform the photogrammetric operations, the photogrammetric software disk is put in Drive A, the formatted blank data disk is placed in Drive B, the microcomputer is switched on, the system is automatically booted, and a menu of instructions is displayed on the monitor. From this point on it is a matter of following instructions and responding to prompts displayed on the monitor. All office steps from inputting the ground control point data file to outputting the data file required by the graphics software are controlled by the photogrammetric software.

To produce the graphics output, the graphics software disk is placed in Drive A and the data disk is left in Drive B. The program is booted and, again, a menu prompts the user on what is needed to execute the various graphics programs to output point plots, contour plots, cross sections, or perspective plots.

CONCLUSIONS

If the proposed mapping system is used under the right conditions, an accuracy of ± 1 ft can be achieved. Desired conditions include

1. The two camera axes intersecting at about a 90-degree angle;
2. A maximum distance of about 450 ft from the camera to the site being mapped;
3. Preferably a 100 percent overlap of the site on two photographs, although three or four photographs can be used if there is sufficient ground control;
4. Six or more ground control points must be visible on each photograph;
5. The position of each ground control point should be known to within 0.1 ft; and

6. The control points and other mapping points should be distinctly visible on each photograph.

There are a number of advantages to using the proposed mapping system. One big advantage is that it allows any design office with a microcomputer, a digitizer, and a pen plotter to perform limited photogrammetric mapping without highly specialized (expensive) equipment or training. Also, the proposed system saves both field survey time and office drafting time. An estimate of the time savings would be between 25 and 50 percent. Output from the photogrammetric software can also be plotted by hand or further manipulated by other software. In addition, the photographs provide a nearly permanent record of site conditions.

An advantage from the standpoint of safety is that the mapping of inaccessible or unsafe sites such as unstable rock slopes can be accomplished with a minimum of exposure of personnel to hazardous conditions. Photographs may be obtained from a light plane or helicopter, but the requirement for the six ground control points and the B/D ratio must still be met.

The system is user friendly in a number of ways. The software is menu driven, so training to use the system is quite easy, particularly compared with systems that require the use of the floating dot. Also, the hidden error trapping or checking routine that checks the data during input reduces the possibility of the user unknowingly crashing the program.

The equipment can also be used for other tasks. This is attractive in that equipment costs can be spread among several activities. Many design departments have most of the hardware equipment necessary to perform the mapping. Cost of the equipment, exclusive of the camera, about 2 years ago was around \$7,000. Today the cost would no doubt be less. Any type of camera may be used, but an SLR 35-mm camera that can accept different lenses such as telephoto lenses is the most versatile.

The proposed mapping system also has some disadvantages. There must be at least six ground control points for each photograph. The accuracy of the photogrammetric reductions

depends to some degree on the accuracy of the ground control points. Because of the need for control points on each photograph there is some limit to the size of the area that can be mapped using the system. If the site is extremely uniform in texture, targeting of mapping points is also required.

The accuracy achieved is not as great as that obtained by more sophisticated methods. However, given that paper prints, rather than glass diapositives, are being used and that an electronic digitizer, rather than a precise photogrammetric comparator, is being used, it is the opinion of the authors that the advantages of the system outweigh the disadvantages. All indications are that, under the restrictions noted, the proposed mapping system can be used to monitor slopes with an accuracy of ± 1 ft.

REFERENCES

1. Y. I. Abdel-Aziz and H. M. Karara. Direct Linear Transformation from Comparator Coordinates into Object Space Coordinates in Close-Range Photogrammetry. *Symposium on Close-Range Photogrammetry*, University of Illinois, Urbana, Jan. 26–29, 1971, pp. 1–18.
2. H. Bopp and H. Krauss. An Orientation and Calibration Method for Non-topographic Applications. *Photogrammetric Engineering and Remote Sensing*, Vol. 44, No. 9, 1978, pp. 1191–1196.
3. D. C. Brown. *The Simultaneous Determination of the Orientation and Lens Distortion of a Photogrammetric Camera*. Technical Report 56-20. Air Force Missile Test Center, Patrick Air Force Base, Fla., 1956.
4. D. C. Brown. Decentering Distortion of Lenses. *Photogrammetric Engineering*, Vol. 32, No. 3, 1966, pp. 444–462.
5. Y. I. Abdel-Aziz. Expected Accuracy of Convergent Photos. *Photogrammetric Engineering*, Vol. 40, No. 11, 1974, pp. 1341–1346.
6. J. Kenefick. Ultra-Precise Analytics. *Photogrammetric Engineering*, Vol. 37, No. 11, 1971, pp. 1167–1187.

Publication of this paper sponsored by Committee on Soils and Rock Instrumentation.

Contracting for Tiedback Walls in Kentucky

WILLIAM PHILLIPS

The Kentucky Transportation Cabinet has used a prebid design performance specification for two permanent tiedback walls. These walls were used for control or correction of active landslides. The walls comprised steel H-sections, timber lagging, and corrosion-protected tiebacks. Only approved tiedback wall contractors were permitted to participate in these projects. These approved contractors were given a packet of information on the projects. The packets contained all technical and administrative details deemed necessary to satisfactorily complete the work. Contractor input was solicited during development of the information packets. The contractors were to develop their own tiedback wall schemes. Tieback size, tendon type, bonded and unbonded length, and tieback location were their responsibilities. They were required to submit complete design calculations, construction plans, and any notes to the cabinet for review and acceptance 30 days before bids were opened. After design acceptance, the contractors were to prepare lump sum bids for their wall systems. On one wall contract the tiedback wall contractor was the prime contractor. On the other contract the wall contractor was a subcontractor. Both walls were completed satisfactorily. The cabinet is considering developing a post-bid design performance specification for tiedback walls. This would reduce the staff time involved in design review.

In late 1982, the Kentucky Transportation Cabinet began considering tiedback walls as an engineering technique for permanent landslide correction and control. Since that time, Kentucky has successfully completed two tiedback walls to contain landslides. Kentucky elected to use a prebid performance specification for these walls. The actual wall type selected for both projects comprised steel H-piles, pressure-treated timber lagging, and corrosion-protected tiebacks. The specification required that the piles be driven to and seated in solid rock. The lagging was open faced and backed with a drain path material (Figure 1).

CARROLL COUNTY LANDSLIDE

In March 1983, the Transportation Cabinet's Division of Bridges was given the task of preparing a performance specification for control of an active landslide in the northern part of Central Kentucky. This slide is southeast of Carrollton on KY-227. This two-lane facility opened to traffic in 1974. Since

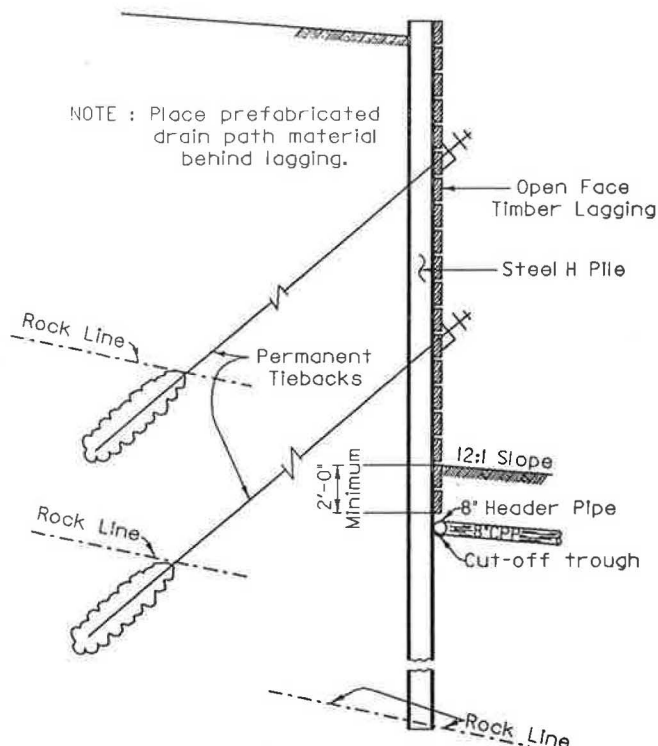


FIGURE 1 Typical section.

its opening, the facility has been plagued by slides. These slides were being monitored by the Geotechnical Section of the Division of Materials. By the summer of 1982, a major slide had affected about 400 ft of embankment and encroached on about 200 ft of roadway. The slide in question was in a cut-fill section. Slope inclinometer readings showed the zone of movement to be 23 to 25 ft below the roadway shoulder. The rate of movement was 0.2 in. per month. No structures were affected, but the railroad track approximately 100 ft from and 30 ft below the roadway was in danger. The situation was further complicated by the presence of the bank of the Kentucky River about 100 ft from and 20 ft below the railroad (Figure 2).

This slide is in the northern part of the Outer Bluegrass topographic region of Kentucky. Glacial deposits and recent alluvium exist in many areas adjacent to the Kentucky River. The overburden soil is predominately a low-plastic clay. The depth to rock at the shoulder was about 35 ft. The water table was estimated to be 2 to 4 ft below existing ground at the roadway shoulder. The bedrock is predominately interbedded

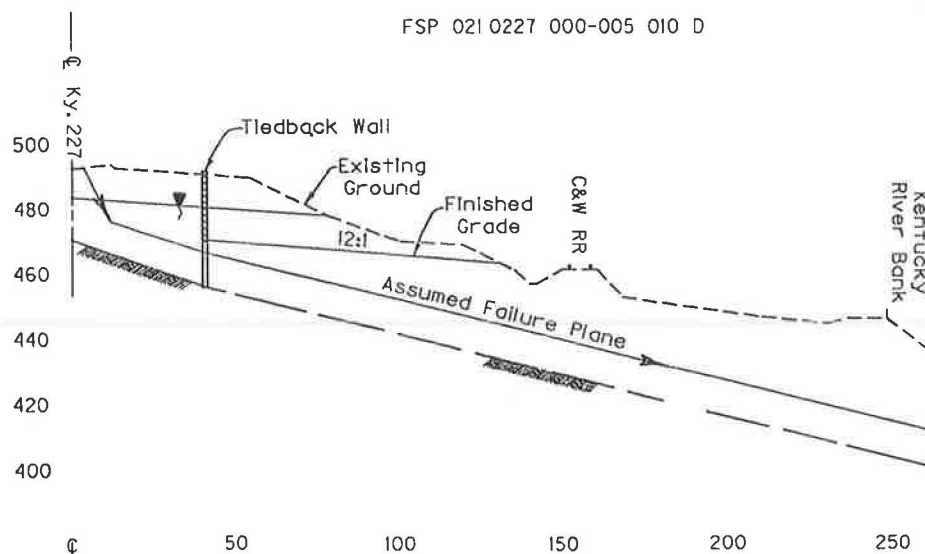


FIGURE 2 Carroll County slide correction.

Ordovician limestones and shales. The Kope formation is the main formation in the area. Highly weatherable shales make up 70 to 85 percent of this formation and are usually found in even to slightly irregular beds about 12 in. thick. Use of these shales during embankment construction for KY-227 was a major factor contributing to the problems along this roadway.

The three alternate corrective measures considered were a tiedback wall, horizontal drains, and railroad rails as driven piles. Neither moving the centerline of the road into the hill nor flattening the slope was considered a practical solution. Any alignment change would affect $\frac{1}{2}$ mi of roadway and require considerable excavation as well as significant additional right-of-way.

Stability analyses that included the effects of horizontal drains gave an insufficient factor of safety of from 1.1 to 1.2. Previous successful experience with railroad rail piles had been with lengths of from 15 to 20 ft. The soil at the site was far too deep for this to be an effective solution. The tiedback wall offered various combinations of tieback capacities and spacings to resist the calculated landslide force. The design factor of safety was to be between 1.5 and 2.0 for a tiedback wall. The wall was estimated in the planning phase to be about 400 ft long and have 15 ft of exposed face at its tallest point.

A tiedback wall was a new product or technique to Kentucky. The design, details, and construction of such walls were not covered in the standard specifications; thus a specification would have to be developed. The development of this specification, in the form of a Special Note, was somewhat complicated by the short lead time provided for the project letting.

This Special Note was patterned after the sample specification in Chapter 7 of Federal Highway Administration Report FHWA-RD-82-47, *Tiebacks* (1). The following are some of the items addressed in the note:

1. Scope of work;
2. Design criteria;
3. Tieback description, geometry, and capacity;
4. Geotechnical data;

5. Maintenance of traffic;
6. Instrumentation and monitoring;
7. Installation requirements for piles, lagging, and tiebacks;
8. Material specification and testing requirements;
9. Tieback testing including creep, performance proof, and liftoff testing;
10. Record requirements;
11. Minority business enterprise requirements;
12. Method of measurement and basis of payment;
13. Plan and elevation views, typical sections, cross sections;
14. Other references to other departments, documents, specifications, and so forth, that wall contractors would need; and
15. Staff and experience requirements of wall contractors in the design and construction of tiedback walls.

By the middle of May 1983, the first draft of the Special Note was completed. Unfortunately, time did not permit in-depth review and input by many outside agencies.

By the first part of August 1983, an information packet containing the Special Note was made available to a group of tiedback wall contractors. At this time, these specialty contractors were encouraged to review the note in detail and to provide their suggested changes or exceptions. Seven tiedback wall contractors provided critiques of the draft. Unfortunately, three of the seven contractors eliminated themselves because of the time constraints.

The Special Note required the interested contractors to submit, within 28 calendar days, a set of design and construct documents. These were to include complete design calculations and a complete set of detailed construction plans for review and approval. Their plans were to include any notes or specifications pertinent to their wall that either conflicted with or were not covered in the cabinet's current standards and specifications, guidance manuals, or special provisions. Each contractor's submission was reviewed separately. Any changes suggested by any contractor, which were approved by the cabinet,

were made available to all contractors. Proprietary items were permitted but would not be specified. The contractors were to show on their construction plans any and all details necessary to provide a satisfactory tiedback wall.

Each contractor's design calculations were to include designs for every component of their wall. Their format was to be such that engineers totally unfamiliar with tiedback wall design could follow their calculations.

The review was quite time consuming. Each contractor appeared to have a different method for attacking tiedback wall design. The shapes of the final construction pressure diagrams were not uniform. Treatment of passive pressure varied. Economics affected pile spacing, waler size, number of rows of tiebacks, and many other details. Cabinet personnel went through an educational process with each design. This was most inefficient but worthwhile when the long-term educational value is considered.

It was difficult to make comparisons of the submitted wall designs. Instead of a comparison of numbers of piles, walers, tiebacks, and the like or individual tieback loads, a comparison of resistance per foot of wall was attempted. Resistance per foot of wall varied significantly from contractor to contractor. The major reason for this variation appeared to be the cabinet's inexperience with tiedback wall design. A clear definition of the landslide problem and a specific design pressure diagram must be provided to the wall contractors.

Many telephone calls were made to the specialty contractors to clarify submissions and solicit suggestions. The cabinet had 15 calendar days to review the submissions from four contractors. According to the original note, the contractors would then have 8 calendar days to provide the cabinet with revised designs and plans.

During the review of the first submissions, a field inspection of the site revealed that the area affected by the slide had grown laterally. This was about 4 months after a tiedback wall was selected for controlling this slide. Relatively speaking, the type of work did not change. However, plans needed to be developed for a longer wall. Initially, the estimated increase in length was anticipated to be 200 to 300 ft. When the final addendum was mailed, the increase in length was 600 ft. A wall 1,000 ft long with 16 ft of exposed face at its highest point was now required.

The cabinet had to initiate and hastily complete a comprehensive drilling, sampling, and testing program for the additional wall length. This was accomplished by the cabinet's Geotechnical Section.

Numerous parts of the design criteria originally presented in the Special Note were changed. These changes affected lagging design, pile design, drainage requirements, pile and waler corrosion protection, tieback testing, and the use of a dynamic pile-driving analysis to name several. Possibly the most significant change was in the design pressure diagram or design force per linear foot of wall. This change required the specialty contractors to completely redo and submit new designs and revised plans. The date for providing the cabinet with final design and contract plans was changed. Unfortunately, the letting data was not changed. Consequently, any discrepancies or deficiencies in the final submission could disqualify a specialty contractor.

In addition to the monitoring by the cabinet's Geotechnical

Staff, the Kentucky Transportation Research Program (KTRP) received approval and funding from FHWA to monitor the wall with several types of instruments. The contractors had been forewarned that there would be some instrumentation required by the cabinet for monitoring wall movements during and after construction. This would be in addition to the normal monitoring common to tiedback walls such as tieback stressing and testing. Types of instruments to be added were extensometers, load cells, slope inclinometers, groundwater observation wells, tiltmeters, and earth pressure cells. Instrument locations would be determined in the field by KTRP, the cabinet, and the contractor. Optical surveys would be made to develop a settlement profile of the pavement behind the wall. The contractor was directed, by the Special Note, to cooperate with instrument installation by the cabinet and KTRP. None of the contractors expressed any disagreement or difficulties with incorporating this instrumentation program into their actual wall construction. Actually, tiedback wall contractors expressed considerable interest in this monitoring program. However, there is no way of determining how much, if at all, this additional instrumentation and monitoring affected their bid or their construction scheduling.

The final Special Note and contract plans were ready for bidding by September 1983. This was 6 months after the task began.

When construction began, cabinet inspectors went through an educational process. Their knowledge of permanent tieback construction methods had come from reading various industry publications.

Deficiencies in the Special Note did present some problems to the cabinet's inspectors during construction. Fortunately, there were no major or cost-affecting situations as a consequence of gaps between the Special Note and the cabinet standards and specifications. Problems such as controlling excessive pile deflection were resolved at the site, and other problems were resolved by the local district office or the Division of Bridges. All questions were settled informally in an arbitration type of effort.

The Special Note limited the allowed deflection of the wall during tieback stressing. However, the text was somewhat vague in providing guidelines for handling deflection exceeding the tolerance. The wall was constructed in the spring of 1984. That spring was wetter than normal, which contributed to excessive deflection of the soldier piles. The field decision was to place mass concrete as a reaction beam behind selected H-piles.

There also appeared to be an excessive amount of tieback failure during stress testing. The specialty contractor's previous experience in Kope shales had been high up in the formation. The consensus was that the shales at the site were lower in the formation and weaker than anticipated. Also, the drilling process could have caused slick or smeared holes that inhibited grout penetration into the formation.

Probably the most significant shortcoming that affected construction was the lack of specific instructions for stage removal of earth in front of the wall. Because the wall, not counting the required excavation, was less than 40 percent of the total contract, the specialty contractor was a subcontractor on this project. The prime or general contractor elected to do all earth moving including that required for wall construction. The cabi-

net gave no specific earth-moving directions in the tiedback wall Special Note. None of the other contract documents addressed this problem. Earth moving for a tiedback wall is significantly different from normal earthwork procedures. Staged removal is required to ensure adequate passive restraint in front of the wall until the tiebacks are stressed. This potentially difficult situation was left, by default, for the contractors to resolve. Fortunately, no serious conflicts occurred.

The wall was completed to the cabinet's satisfaction. There were some allowances in wall alignment criteria normally expected by the cabinet. However, these alignment criteria were set up for cast-in-place concrete walls and were not deemed necessary for a tiedback wall. This wall is pleasing to the eye and, in time, with vegetation on the down slope, will blend in quite well with its surroundings.

The wall was bid "lump sum" exclusive of the required earth moving. It was constructed for just over \$31.10 per square foot of face. The square foot face measurement includes the lagging buried 2 ft throughout.

The results and final report of the instrumentation program for the Carroll County tiedback wall are unavailable at this time. However, preliminary findings are encouraging. During May 1984, very little wall movement was measured. At that time, the wall was essentially complete. By November 1985, movement had virtually ceased.

CAMPBELL COUNTY LANDSLIDE

In January 1984 the Division of Bridges was notified of another potential tiedback wall use. An active landslide had closed the northbound lanes of US-27 in northern Kentucky. This was classified as an emergency project.

This slide was north of Alexandria on US-27. US-27 was initially constructed as a two-lane facility and later widened to a four-lane facility by placing additional fill. The initial two lanes at the site were constructed in a cut-fill section. The slide affected about 300 ft of embankment with cracks and scarps

reaching the roadway centerline. In places, the two northbound lanes of pavement had dropped as much as 8 ft. The failure of the added two lanes, built as a side-hill embankment, occurred during August 1983.

The geotechnical investigation of the slide was initiated at this time. The depth to rock at the shoulder was about 50 ft at the deepest point. The failure plane was estimated to be 10 ft above the rockline. The water table was deep. It was measured to be from 6 to 10 ft above the rockline. No structures were affected. The total drop from shoulder to toe was 50 ft at the critical section (Figure 3).

This slide is in the northern part of the Outer Bluegrass topographic region of Kentucky. The bedrock comprises interbedded limestones and shales. In addition to Kope formation shales, the shales are from the Fairview and Bull Fork formations. These shales are also highly weatherable and, when used in embankments, are a primary cause of slope instability. Compaction of these shales is inhibited by the presence of flaggy limestone slabs. These slabs prevent breaking down of the shales and cause voids in the fills by interfering with compaction equipment. Additional voids are created as runoff seeps through the fills and causes the shale to slake.

Three corrective measures were studied. One involved a flattened slope with a large berm at the toe. This was rejected because it required a prohibitive amount of additional right-of-way to achieve an adequate safety factor. The second alternative was a tiedback wall. This was initially rejected as being too costly. The most economical alternative was a combination shear key and berm correction.

During January 1984 the landslide problem was discussed among various divisions within the cabinet. The prudence of excavating for a shear key in an unstable area was questioned. An additional alternative, using stone columns, was suggested. However, the amount of soil to be replaced by stone columns was considered excessive. Extra right-of-way would also be required for this alternative.

The tiedback wall option was reconsidered and, in the end, selected for the correction. It was thought that actual con-

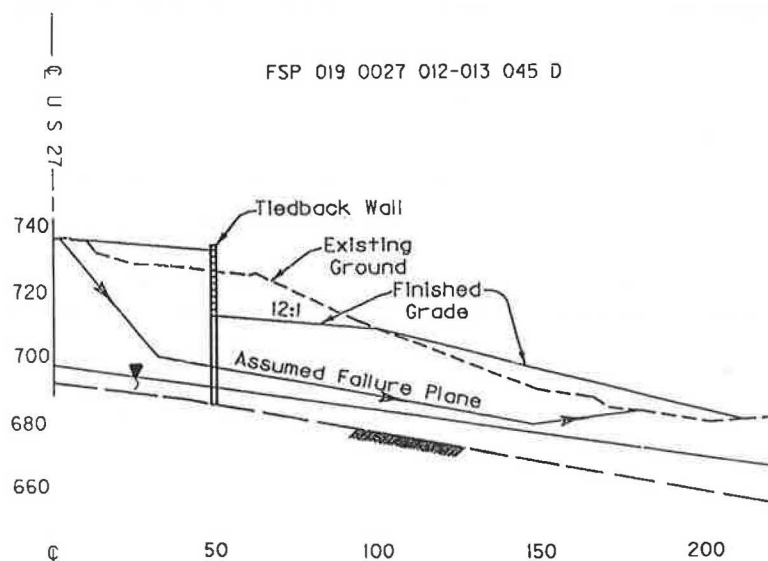


FIGURE 3 Campbell County slide correction.

struction of a tiedback wall could be initiated more quickly than the berm and shear key alternative. Construction of the berm and shear key alternative could not begin until the dry season in late spring. It was also thought that tiedback wall construction would be within the present right-of-way.

Because a Special Note for a timber-lagged, steel H-pile tiedback wall existed, the cabinet decided to use a similar wall for this landslide correction. The wall would be about 328 ft long and have 22 ft of exposed face at its tallest point.

Site-specific modifications were made to the note and it was mailed to interested wall contractors 6 calendar days after the decision was made to use a tiedback wall. These contractors were also notified of an on-site inspection of the landslide scheduled for January 18, 1984. Tentative scheduling was to have a bid opening 7 weeks from this date. This project was definitely a fast-track effort. Unfortunately, it was realized during the on-site meeting that the slide had moved significantly and new cross sections were needed. Consequently, the schedule was delayed 1 week.

The specialty contractor would be the general contractor on this project because the tiedback wall was approximately 80 percent of the project. Contractors were given 2 weeks to provide the cabinet with designs and plans for review and approval. After a week for the cabinet's review, contractors would have another 2 weeks to revise their designs and plans. Contractors who provided satisfactory final designs and plans would be notified to submit bids. Notification to the successful contractor was to be given 1 week from the cabinet's receipt of final plans.

Other than site-specific details, there were no significant changes in the note. There would not be an intensive instrumentation and monitoring program by KTRP. Slope inclinometers would be installed by cabinet personnel with the contractor's cooperation. At the ends of the lagged portion of the walls, two additional piles were to be installed. This was not done on the first project. These piles were to be identical to the piles in the last sections of the wall at each end. These end piles were in line with the wall and spaced the same as the last wall piles. This was to assist in containment of the slide and to allow for extension of the wall by cabinet personnel without the need for pile-driving equipment.

The wall contractor, as the prime contractor, was responsible for meeting the federal Minority Business Enterprise (MBE) requirements. This proved difficult because the wall itself constituted the major portion of the work to be performed on this project.

Construction of this wall had a significant difference from that of the Carroll County wall. The embankment had failed and the slide mass was still moving significantly. Many of the driven piles would have in excess of 10 ft of pile sticking out of the ground. Before tiebacks were installed, the area behind these piles would need to be partially excavated to remove loose material. Next the contractor would need to install lagging then backfill up to a certain elevation before installing any tiebacks. During the time between pile driving and tieback stressing, many piles were pushed out of alignment by slide movement. Consequently, the finished product has a lot of kinks in its alignment. This was not considered detrimental to wall performance and proved that the tieback solution could be applied to active slides.

A major oversight was the cabinet's method of paying for earthwork. The earthwork bid item for this project was "Roadway Excavation," which is paid plan quantity unless the cabinet changes the scope of work. Needless to say, the quantity bid did not agree with the quantity to be handled at the time of construction. The bid quantity was based on cross sections taken 3 months ahead of time and this was an active landslide. The problem was not so much the quantity involved as the handling of the material and the unsuitability of some of the material for backfill. In the end, material had to be hauled to waste sites and borrow material brought in for embankment construction.

The lack of sufficient geotechnical data created a problem with ordered pile lengths. Drilling was not done near the ends of the wall. A projected rockline was used on the contract plans. The rockline encountered was 10 to 20 ft below the projected rockline at the ends. Though the contractor was paid for the additional pile length required, pile splicing, which had not been anticipated, was required. Because approximately 100 ft, or one-third, of the wall was affected, this had a significant effect on construction scheduling. It was imperative to have quick and efficient wall construction to ensure that the slide did not progress to the point where the remaining two lanes of US-27 would be closed.

This wall was bid lump sum exclusive of excavation and other roadway items. In addition to the lump sum bid, the wall contractors were to submit unit price bids for wall components. This would provide a convenient method for possible wall extension during construction. It would also give the cabinet an idea of the cost of tieback installation as a function of size and capacity of the tieback.

This wall, excluding earth moving, was constructed for just over \$49.60 per square foot of face. The square foot of face measurement includes the lagging buried 2 ft throughout.

CONCLUSION

Kentucky had had essentially no experience in tiedback wall construction when the Carroll County slide correction was initiated. To prepare a detailed set of plans and specifications, the cabinet had to rely on contractor personnel for guidance. However, the cabinet wanted to maintain control of the design. The performance specification option was selected because it permitted shared responsibility for design, construction, and performance of the completed tiedback wall. By reviewing the various designs submitted by contractors, cabinet personnel would gain considerable knowledge for the future.

The intent of the technical prequalifications and design and plan development requirements was to prevent contractors inexperienced with tiedback walls from participating in the wall contract. It was thought that this would ensure adequate design, efficient construction, and a cost saving. It was particularly important that the cabinet's first attempt at tiedback wall construction be well thought out from design through construction to maintenance. Conflicts or litigation would unfairly preclude consideration of tiedback walls for future use.

Target dates are good. Otherwise, tasks may never be completed. However, completion dates that are controlled by contract letting dates can prove costly. Potential contractors are left

out of the process. Prices are inflated to cover uncertainties that time does not permit contractors and the contracting agency to address. Time did not permit predesign or prebid conferences on the Carroll County project. Still, with all these snags and difficulties, all the specialty contractors were most cooperative. They continually went above and beyond the normal effort expected to assist the cabinet in obtaining a workable Special Note.

A prebid performance specification is a good way to get started in the tiedback wall business. The contracting agency gets exposed to many different wall concepts and design philosophies. The agency establishes the scope of work and maintains control over the type, size, location, and design of the wall. The contractor is free to select an economical tieback system within the guidelines provided. Responsibility for the finished wall is shared between the agency and the contractor. An environment of cooperation is practically mandated. Cost savings through a design and construct effort are recognized. Participation and innovation by qualified contractors are certain to be obtained by the contracting agency.

It is recommended that agencies unfamiliar with tiedback wall design and construction pattern their first efforts after the sample specification in the FHWA *Tiebacks* Report (1). Modifications will certainly be necessary. In particular, the method of handling stage removal of earth in front of the wall should be covered in detail. When the wall contractor is not doing the earthwork, specific guidelines and instructions should be included in the note. In some cases, a signed agreement between the two contractors may be necessary.

Plan quantity should not be the pay item for active slides. Pay items for field measuring, soil manipulation, waste, and borrow should be considered. Flexibility in payment methods would enhance contract performance.

Contractors should be provided with identical design lateral pressure diagrams. Modifications should be permitted after tieback designers have reviewed the Special Note. However, the final design provided by all contractors should be based on the same diagram.

Kentucky is considering switching to a postbid performance specification for future tiedback walls. Now that the cabinet has gone through an in-depth educational process for two tiedback walls it is believed that there is sufficient expertise within the agency to take this step. This should increase the cost savings and would certainly decrease the cabinet's review time.

The cabinet would still set the scope of work, describe the type of wall required, and outline the design criteria. The major effort before bidding would be placed on contractor qualification requirements. In addition to company qualification requirements related to design and to professional engineers employed, emphasis would be placed on the company's people who would be doing the actual wall construction. Experience requirements would be established for the superintendent, the foremen, the drillers, and the stressing foreman. In particular, foremen, except the stressing foreman, would be required to be at the jobsite at any time construction is in process.

It is preferred that the tiedback wall contractor be the general contractor. When the wall contractor is a subcontractor, the general contractor should be required to specify the wall contractor selected. A signed agreement between the two should be a required submission of the bidding package.

A well-written postbid performance specification will permit prebid tiedback wall contractor approval with postbid design approval agreeable to all parties involved. The contracting agency obtains a design and build project and still gets a competitive bidding effort.

REFERENCE

1. D. E. Weatherby. *Tiebacks*. Report FHWA-RD-82-47. FHWA, U.S. Department of Transportation, 1982, pp. 120-128.

Publication of this paper sponsored by Committee on Transportation Earthworks.

Westbound Embankment Preload on Rainier Avenue, Seattle, Washington

DAVID M. COTTON, ALAN P. KILIAN, AND TONY ALLEN

Fifty-foot-high approach embankments recently completed for a bridge crossing of Rainier Avenue in downtown Seattle required preloading of compressible lacustrine clay sediments as much as 50 ft thick below the abutment areas. In this paper are presented results of engineering analyses and recommendations for very complex surcharge fill requirements. Vertical prefabricated drains were used in the preload to accelerate settlement and an unprecedented 55-ft-high soil-reinforced wall was used to limit the extent of the fill and thereby prevent damage to existing utilities and adjacent structures. The instrumentation program used to measure the settlement response is discussed, and the variation in magnitude and time rate of settlement measured across the site is summarized. Actual measured settlements were reasonably close to those predicted from engineering analyses done before construction. Several geotechnical-related cost-saving features, which were implemented in the final design stage and saved an estimated \$1.2 million of a total project cost of \$3.4 million, are summarized.

The project discussed in this paper is part of the reconstruction of WA-90, a major east-west freeway within downtown Seattle, Washington, which was undertaken to bring the freeway up to Interstate standards. The current four-lane freeway is being rebuilt as a three-two-three lane configuration consisting of three general purpose lanes in both the east and west direction. In addition, two central reversible lanes will be built to carry automobiles, high-occupancy vehicles (HOVs), or light rail transit.

The section of WA-90 that crosses the Rainier Valley is discussed in this paper. That section will consist of multispan bridges, retaining walls, a cut-and-cover tunnel, and major embankments. A limited-access interchange will be created to allow I-90 to cross over Rainier Avenue South.

The three-two-three lane configuration will cross Rainier Valley, as shown in Figure 1, on embankments with final grade heights of as much as 36 ft. The roadway will be carried across Rainier Avenue on three separate bridges. Westbound I-90 traffic will exit onto Rainier using either the E-RN lane or E-RS lane shown in Figure 1. The RN-E lane passes through a tunnel under I-90 rising in grade as an on-ramp to eastbound I-90.

There are compressible soils to depths greater than 60 ft near the bridge locations. Piles are required to support bridge piers. The approach fills are expected to settle approximately 2 ft. To minimize project costs, structures are kept as short as possible

and a maximum of earth fill is used. However, the compatibility of the structure-fill system became a major design issue because of the large settlement expected at the approaches.

A complicating feature is the existence of major utilities along Rainier Avenue adjacent to and below the proposed approach fills. In addition, the longer existing Lakeway Freeway bridges on the south side of the interchange must remain open during construction of the new westbound lanes shown in Figure 1. These pile-supported structures will be sensitive to downdrag loads caused by the new adjacent fills. Because of the high volume of traffic (34,000 cars per day and 5,200 cars during peak hours), construction time must be kept to an absolute minimum.

Discussed herein is a complex design that consists of vertical drains to reduce settlement time and surcharges with delay periods to accelerate consolidation, reduce settlement time, and mitigate long-term secondary consolidation.

GEOLOGIC SETTING

The site has been subjected to several major glaciations. Ice on the order of 3,000 ft thick has overridden the area. The glacial events and geologic processes that occurred during interglacial periods were responsible for shaping the topography and depositing sediments at the site. The deposits at the site are for the most part a result of the last glaciation, known as the Vashon glaciation, and interglacial deposits before and after the Vashon.

Figure 2 shows the generalized geologic units at the site. The soil deposits can be generally divided into soil that has been glacially overridden and soil that has not been overridden. The units that have been overridden are more competent, because they are less compressible, whereas those that have not been loaded tend to be more compressible.

The deposits that were previously preloaded by glacial ice are at depth at the site and consist of Older Marine hard clay and silt. Overlying the Older Marine unit is Vashon recessional outwash and then compressible recent lacustrine soft silt and clay and organic lacustrine soft peat, silt, and sand. It is in these latter two units that large consolidation settlement occurs. Overlying these deposits are recent deltaic dense gravelly sand and man-made fill including garbage.

A generalized soil profile of the site area is shown in Figure 3. The deepest deposits of compressible recent lacustrine soil are found below Rainier Avenue. At roughly middepth of this deposit, an interbedded silt and sand lens was found in some

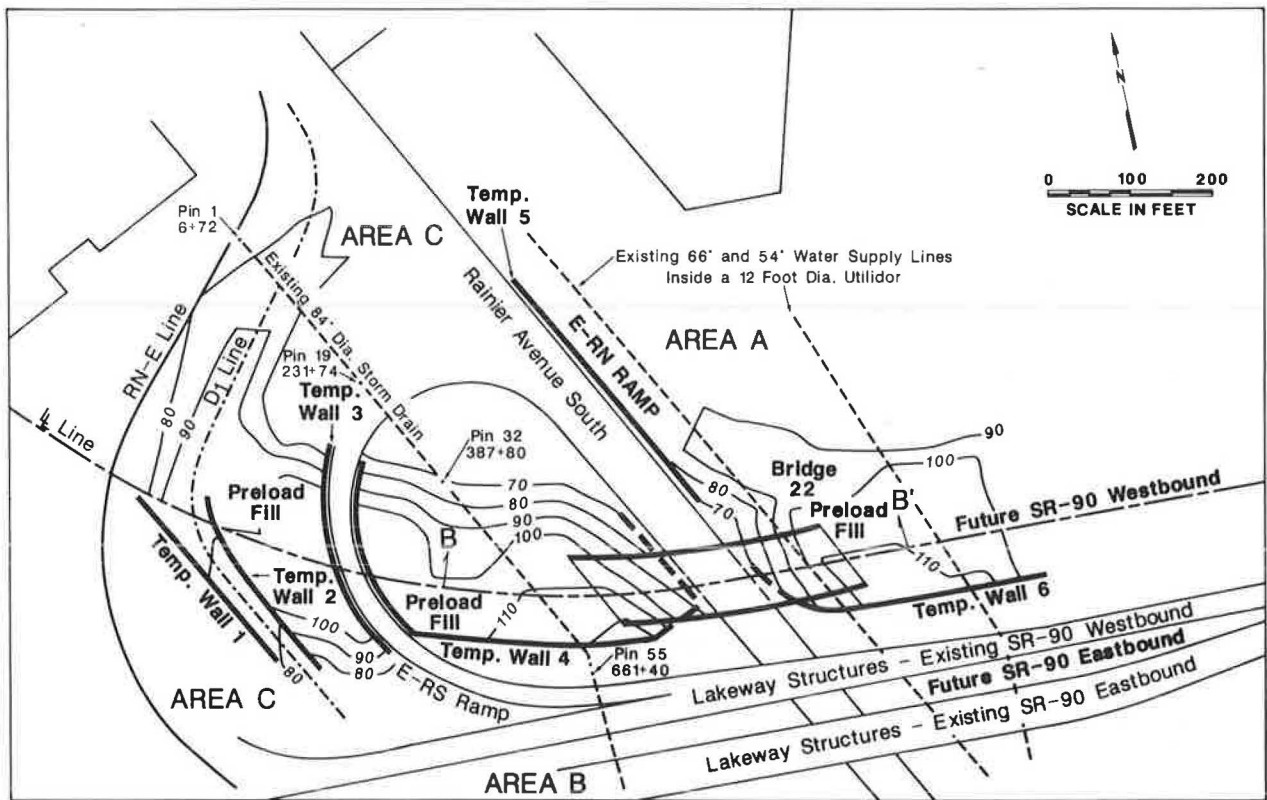


FIGURE 1 Site layout and contour grading plan.

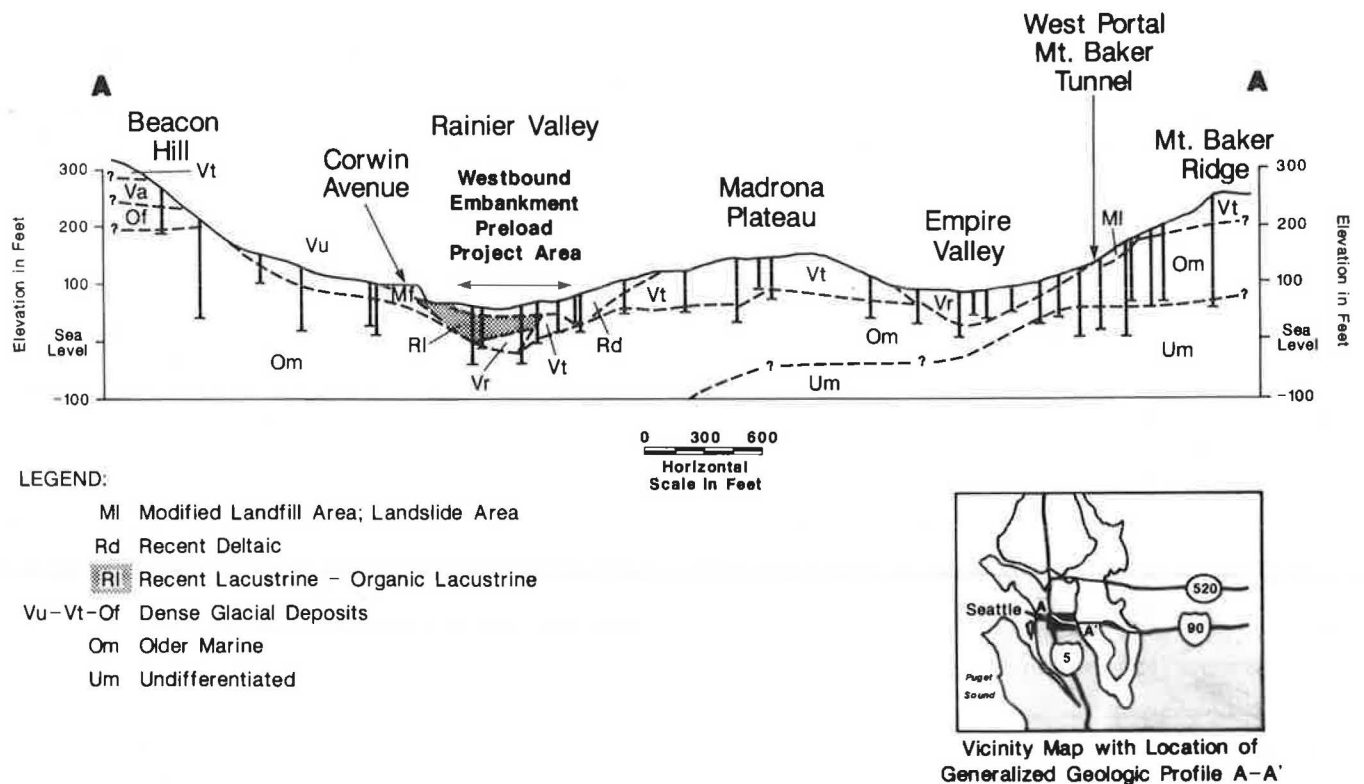


FIGURE 2 Generalized Geologic Profile A-A' along the I-90 corridor through the project area.

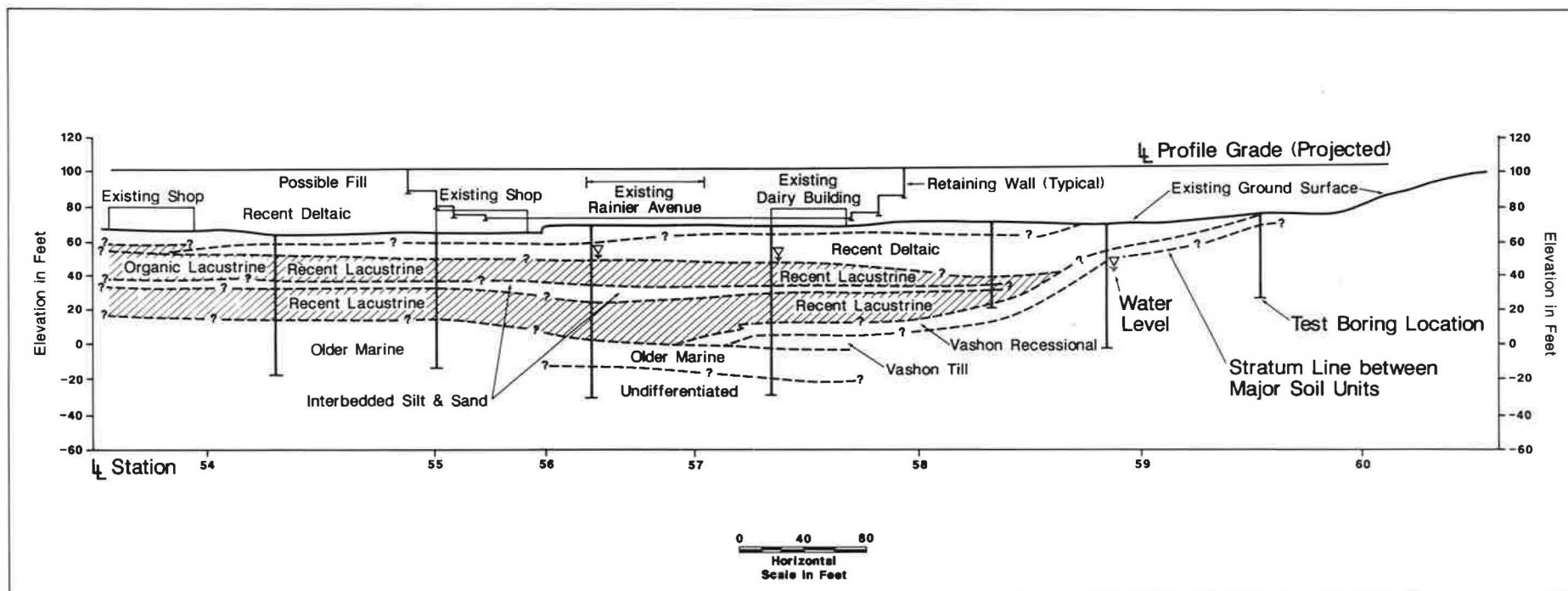


FIGURE 3 Generalized Subsurface Profile B-B'.

test holes. The approximate depth of compressible soils is 50 ft. The organic lacustrine soils were found generally in the northwest quadrant of the site, generally above elevation 50, and to a thickness of up to about 15 ft. These deposits generally exist north of the recent deltaic soils and underlie a large portion of the embankment area.

PRELOAD ANALYSIS

In this paper, "preload fill" represents the embankment required to achieve final grade, including expected settlement, placed several months before construction of bridge abutments. As indicated previously, the approach embankments are underlain by two compressible lacustrine units, the organic lacustrine and recent lacustrine soil units. Variations in the thickness of the organic lacustrine sediments within the project area are shown in Figure 4. The organic sediments typically occur in the northwest quadrant of the site. The thickness of organic material averages 6 ft and ranges from 0 to 12 ft. As indicated in Figure 5, the thickness of the compressible lacustrine clays ranges from 0 to 40 ft and then decreases to 0 ft across the area of the site. The preload analysis included evaluation of the magnitude and rate of primary consolidation as well as surcharge fill requirements for mitigating long-term postconstruction secondary settlement in these two soil units. Additional surcharge fill had to be included because of the greater long-term creep characteristics that the organic lacustrine deposits have in contrast to the lacustrine clays. Engineering analyses also included evaluation of placing surcharge fills in areas that would be subjected to future preloading, such as the ramp between Area C and Area B shown in Figure 6. The final roadway profile along the LL line, including the required sur-

charge fills to compensate for future adjacent eastbound fill placement that has its own surcharge, is shown in Figure 6.

Magnitude of Primary Consolidation

Soil properties used in the evaluation of the time rate and magnitude of settlement follow.

- Lacustrine clay
 - Maximum past pressure = 3.0 ksf
 - OCR = 1.5 to 2.0
 - $C_c = 0.20$
 - $C_r = 0.02$
 - $C_\alpha = 0.002$ to 0.004 (used 0.005 in design of surcharge)
 - $C_v = 0.5$ to $1.0 \text{ ft}^2/\text{day}$
 - PI = 20 average, 7 to 36 range
- Organic lacustrine
 - $C_c = 0.30$ compression index
 - $C_r = 0.04$ recompression index
 - $C_\alpha = 0.015$ coefficient of secondary compression

The estimated magnitude of settlement due to primary consolidation is given in Table 1 for varying fill heights over varying depths of compressible soil (1). The resultant combined settlement ranges from approximately $\frac{1}{2}$ to 2 ft, depending on the thickness of the compressible soils and the embankment height. The values given in Table 1 are for the estimated thickness of preload fill. For this project, the maximum height of the embankment required to attain final grade at the abutments was approximately 40 ft. However, additional surcharge fill was placed at the abutments, which resulted in a maximum total fill height of 57 ft.

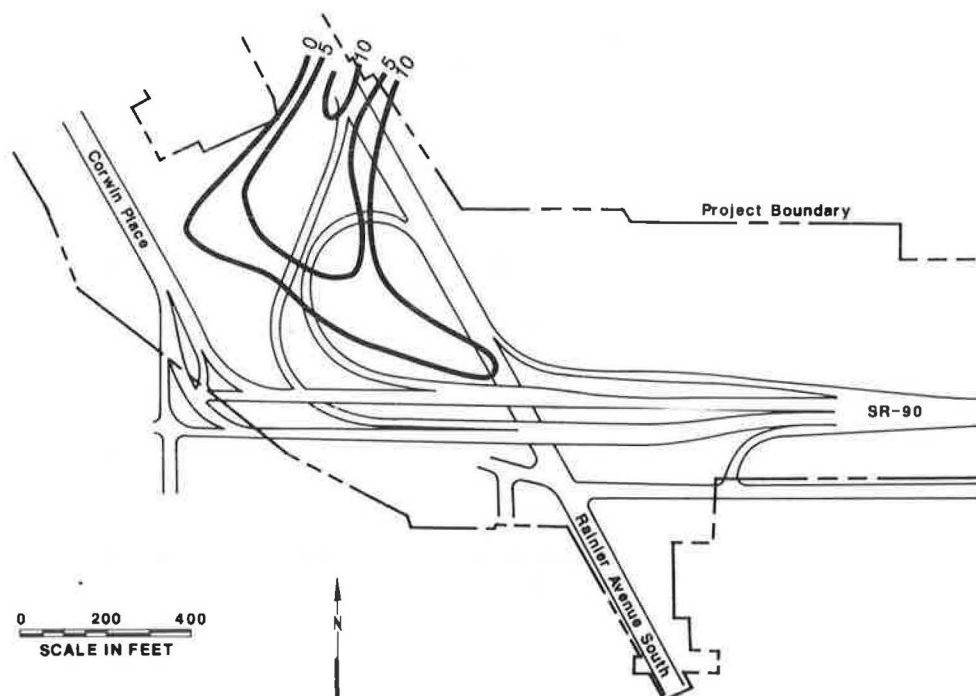


FIGURE 4 Contours of the thickness of organic lacustrine (in feet).

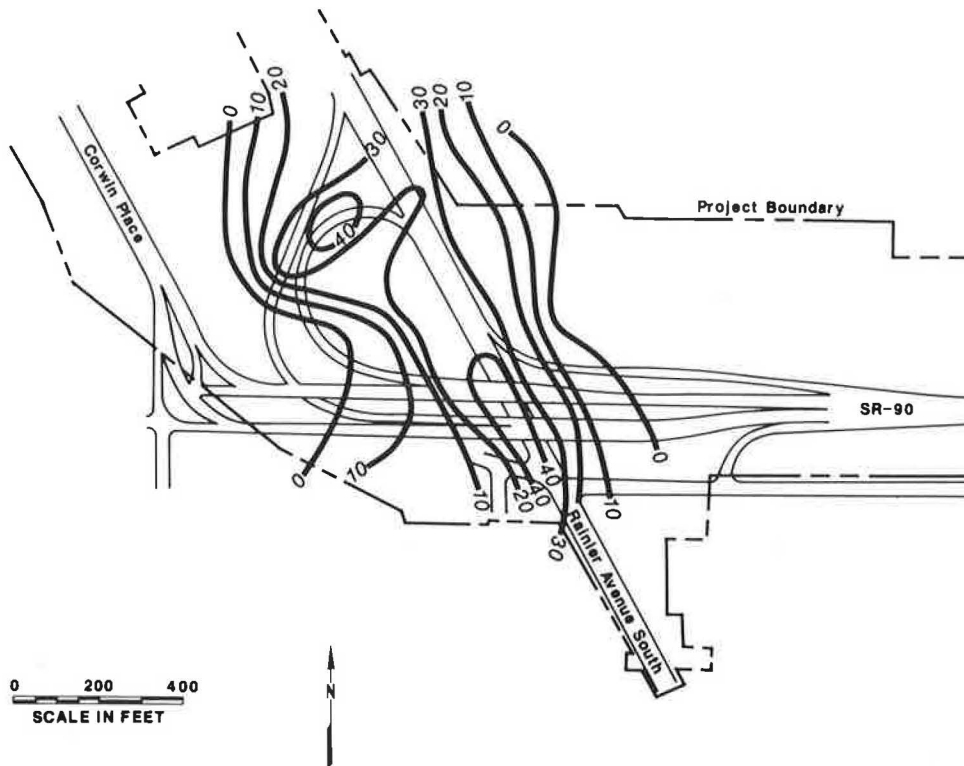


FIGURE 5 Contours of the thickness of recent lacustrine (in feet).

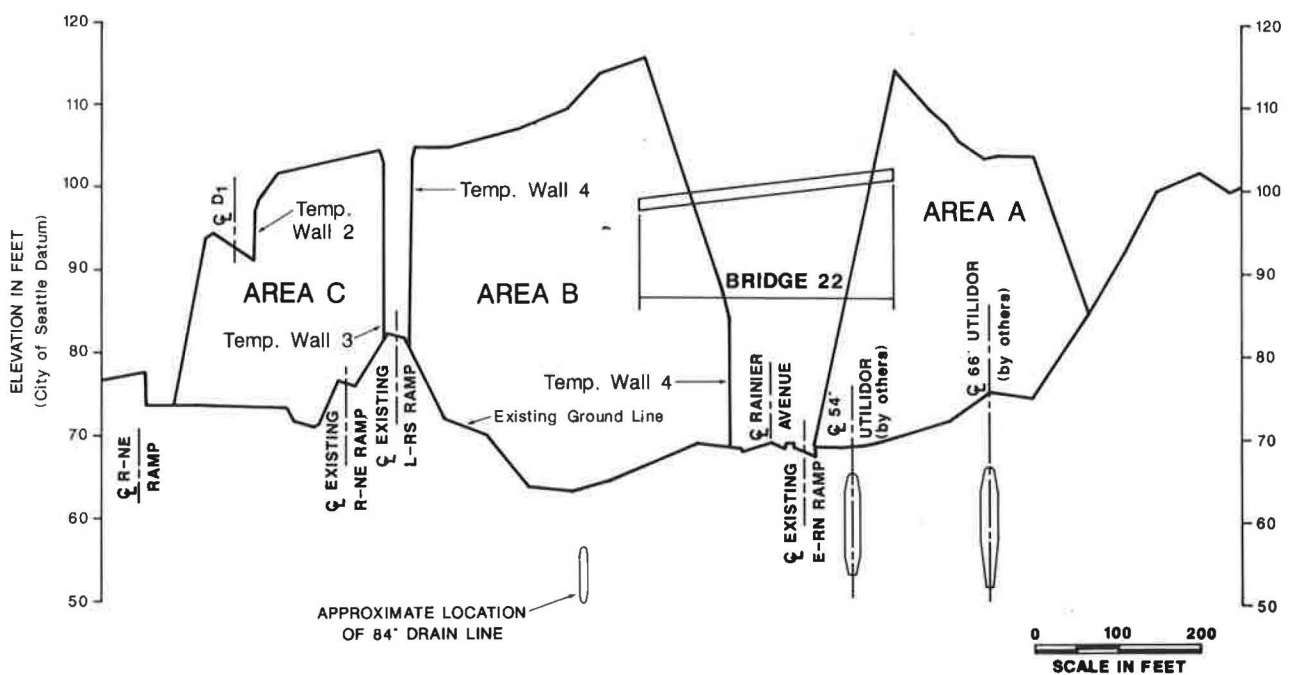


FIGURE 6 Roadway profile LL line.

TABLE 1 ESTIMATED SETTLEMENTS DUE TO PRIMARY CONSOLIDATION (in.)

Fill (ft)	Thickness of Layer (ft)				
	5	10	20	30	40
Clay					
10		0.7	1.2	1.6	2.0
20		1.1	1.9	2.6	3.3
30		2.8	5.3	7.4	9.3
40		5.1	9.6	13.6	17.3
Organics					
10	3.6	6.3			
20	7.3	13.3			
30	9.8	18.0			
40	11.7	21.7			

Surcharging To Reduce Secondary Settlement

In addition to the relatively short-term settlement due to primary consolidation, compressible cohesive soils were expected to display long-term secondary creep. Table 2 gives a summary of the amount of postconstruction secondary settlement expected for a 20-ft-high portion of embankment and various

TABLE 2 POSTCONSTRUCTION SECONDARY COMPRESSION OF LACUSTRINE DEPOSIT

Surcharge Fill (ft)	Postconstruction Secondary Settlement (in.) for Clay Thickness		
	40 ft	30 ft	20 ft
0.0	4.6	3.4	2.3
2.5	2.1	1.5	0.9
5.0	0.5	0.3	0.2

NOTE: 40-year design life, 6-month surcharge period, and 20-ft embankment height.

heights of surcharge fill. Surcharge fill in this case is the extra temporary fill that must be placed above the final grades to reduce long-term secondary creep to acceptable design values (1). The design criteria used in the evaluation of the surcharge fill height included

1. For abutments, limit long-term secondary settlement to less than $\frac{1}{2}$ in. for a 40-year design life to utilize spread footings;
2. For embankments outside abutment areas, limit the long-term settlements to less than 2 in. for a 40-year design life; and
3. Include the additional surcharge for embankments underlain by organic lacustrine deposits.

The magnitude of secondary compression was determined by the slope of the final portion of the time-compression curve on a semilog plot (2). The estimated postconstruction secondary settlements indicated in Table 2 without the application of a surcharge fill are clearly greater than the allowable design limits. Therefore surcharge fills were recommended to limit postconstruction secondary creep to acceptable levels. Also summarized in Table 2 are the estimated reductions in the secondary settlement resulting from surcharging a 20-ft-high

TABLE 3 SURCHARGE FILL CRITERIA

Planned Embankment Height (ft)	Surcharge Height (ft) for Clay Depth (ft)			
	10	20	30	40
No Organics, No Nearby Structures, and 1 to 2 in. Postconstruction Secondary Settlement				
10	1	1	1	1
20	1	1	2	2
30	1	2	3	4
40	2	3	4	5
5-ft Organics, No structures, 1 to 2 in. Postconstruction Secondary Settlement				
10	2	2	2	2
20	2	2	3	3
30	3	3.5	4	5
40	4	5	5	6
No Organics Adjacent to New Structures and 0.25 to 0.5 in. Postconstruction Secondary Settlement				
10	2	2	3	4
20	2	3	5	6
30	3	4	7	8
40	4	6	9	10

embankment with 2.5 and 5.0 ft of additional fill above the final grade. Table 3 gives a summary of the recommended surcharge fill requirements for the total project including abutments, the roadway embankment, and areas underlain by organic lacustrine sediments. The application of these surcharges reduced the long-term fill settlement to within the design values based on measurements in the field. It was recommended that all surcharge fill extend horizontally 5 ft beyond the limits of the final embankment for embankments up to 20 ft in height and 10 ft beyond design limits for embankment heights between 20 and 40 ft.

Surcharging for Future Fill Placement

Surcharging was also used to reduce primary consolidation under areas that are immediately adjacent to and through the current embankment construction fill areas but could not be filled during this contract period and will be filled at a later date. One example of this case was the E-RS ramp shown in Figure 1, which had to remain open during preloading. A typical section showing the surcharge fill above the final grade along the centerline of the ramp is shown in Figure 7. During design, consideration was given to both a 36- and a 24-ft-wide

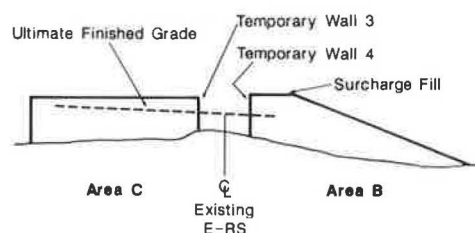


FIGURE 7 Typical cross section of the E-RS ramp with surcharge fill.

TABLE 4 SURCHARGE FILL REQUIREMENTS FOR THE E-RS RAMP AREA

Thickness of Clay Layer (ft)	Surcharge Height (ft)	
	36-ft-Wide Roadway	24-ft-Wide Roadway
0-10	4.0	2.5
10-20	6.5	5.0
Greater than 20	12.5	10.0

roadway. A summary of the surcharge fill recommended for achieving adequate precompression beneath the centerline of the ramp is given in Table 4. These loads were consistent with measured settlement response at the site.

Consideration also had to be given to potential settlements of the completed westbound structure during future placement of the eastbound preload fill. The eastbound lanes are scheduled to be constructed 4 to 6 years after the westbound lanes in the area of the existing Lakeway structures, shown in Figure 1. The structural fill for the westbound embankments was selected such that the maximum stress change that might be induced in the compressible layer by any future loading could be accomplished during the current construction period. As shown in Figure 8, the total surcharge must be that which would be necessary to mitigate secondary settlement below the westbound fills if no other fill were to be placed plus additional surcharge to mitigate settlement caused by the future eastbound fill with its surcharge.

DESIGN AND CONSTRUCTION OF PREFABRICATED VERTICAL DRAIN

The 3-ft-thick intermediate sand layer encountered at about Elevation 30 to 40 within the compressible clay unit, as indicated in Figure 3, was typically in the area north of the WA-90 main line and slightly west of Rainier Avenue. For the settle-

ment analyses, the sand layer was considered discontinuous and limited, which eliminated consideration of double drainage. In addition, the natural materials underlying the compressible clay unit, which include older hard lacustrine clays and dense glacial till, have a very low permeability, which results in a single-boundary drainage condition.

Evaluation of the consolidation process indicated that primary consolidation would not be complete for a period ranging from 3 months to 4 years after fill placement. However, construction of a new bridge within the settlement areas was proposed to begin within 12 months. To accelerate consolidation, wick drains were recommended within those areas that have a clay thickness greater than 15 ft. Those areas with less than 15 ft of clay were expected to have primary consolidation complete within 6 to 8 months. A summary of the estimated time to complete 90 percent of primary consolidation for different wick drain spacings is given in Table 5 (3, p. 718; 4, p. 302).

Approximately 165,000 lineal feet of wick drains were installed before fill was placed. The length of vertical drains varied between 30 and 60 ft, and they terminated at the ground surface in a 30-in.-thick sand drainage blanket at the base of the

TABLE 5 COMPUTED CONSOLIDATION TIME WITH WICK DRAINS

Wick Spacing (ft)	Time for 90 Percent Primary Consolidation (days) ^a
5	20
6	30
7.5	51
10	100
12.5	168

^aThe time for completion of primary consolidation when preloading with vertical drains is controlled by the spacing of drains and not the thickness of clay.

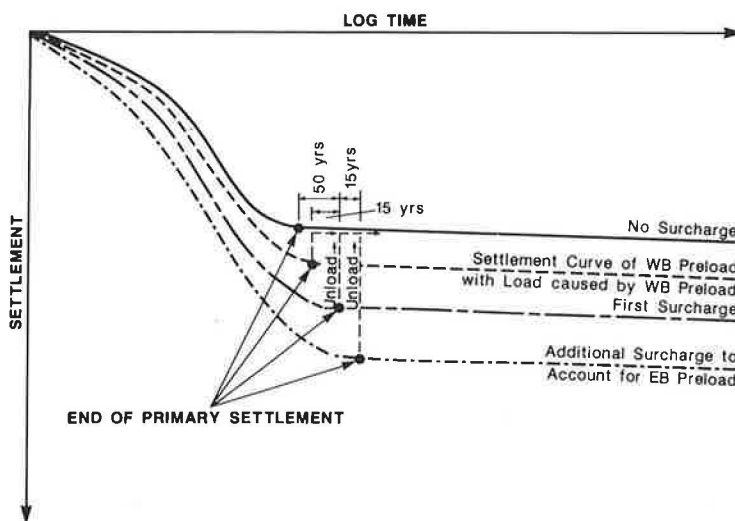


FIGURE 8 Simplified theoretical concept to reduce long-term settlement of the westbound Rainier Avenue overcrossing embankments.

embankment. In addition, approximately 37,500 ft of predrilling was required to get through 15 to 25 ft of medium-dense, natural deltaic deposits and fill material before the 15 to 40 ft of compressible clay was penetrated. The drains consisted of a thin, 4-in.-wide plastic core within a geotextile envelope (sleeve) and were spaced at 8 ft on centers in a triangular pattern. The 8-ft spacing was chosen because the bridge construction contract required completion of primary consolidation within 60 to 90 days after placement of the fill.

Installation techniques were restricted to vibratory, constant load, or constant rate methods. Jetting methods or jacking of the mandrel with consecutive in and out movements was not allowed because of an increased tendency to smear the interface area. During construction, a vibratory hammer attached to a steel mandrel and guided by pile-driving leads was used to install the drains. The area of the mandrel was limited to 12 to 14 in.² (again for the purposes of reducing the effects of smearing), and the mandrel was periodically checked during construction for damage. The contractor was prequalified on the basis of experience and equipment, and details of the sequence of installation, method of installation, and tools and equipment were submitted and approved before construction was begun.

Each drain was driven to refusal at approximately the depth predicted during design. The final location of each drain was maintained within 6 in. of the designated location and within 5 degrees of vertical. The wick drains were installed with relatively few problems. Occasionally, the aluminum shoe attached to the wick at the bottom of the mandrel would collapse inside the mandrel. The shoe is a thin aluminum plate slightly larger than the mandrel with a hook on the back side where the drain is attached. This only occurred when the predrilled hole did not penetrate the relatively dense fill material and deltaic deposits that overlie the soft lacustrine silts and clays, resulting in hard driving conditions. The predrilling operation was also relatively problem free, although it was sometimes difficult to determine when the auger had completely penetrated the upper dense-soil strata.

The predrilling operation was by nature a slower operation than was actual wick drain installation. Depending on the timing and sequencing, wick drain installation was sometimes hindered by the slowness of predrilling. The average rate of predrilling was approximately 1,900 ft/day, with a maximum rate of 3,000 ft/day under optimum working conditions and with few breakdowns. The rate of wick drain installation averaged approximately 5,000 ft/day, with a maximum rate of 11,000 ft/day under optimum working conditions and with few breakdowns.

REINFORCED-SOIL WALL DESIGN AND CONSTRUCTION

As shown on Figure 1, the existing WA-90 eastbound and westbound roadways currently consist of the Lakeway structures, which are pile-supported, elevated, concrete roadway decks. The exact depth and capacity of the existing piles is not known. To prevent pile downdrag loads and the potential for structural distress, caused by differential settlement, to the existing roadway, the lateral extent of the westbound embank-

ment had to be limited to a minimum horizontal distance from the Lakeway structures equal to one-half the depth from the ground surface to the bottom of the compressible layer.

More restrictive geometric constraints existed along Rainier Avenue where the adjacent embankment height including the surcharge fill would be a maximum of 52 ft. In this area and the area adjacent to the Lakeway structures, potential differential settlements and damage to the existing roadways and major utilities, combined with the problem of encroachment of the fill, could not be prevented without a retaining system. Because total and differential settlements would be on the order of 2 and 1½ ft, respectively, the wall systems required flexibility, and the retaining walls were temporary, a reinforced-soil system was recommended for design of the preload and surcharge retaining walls to limit the extent of fill placement and reduce the impact on existing structures and utilities. The following reinforced-soil retaining walls were recommended for use and included in the final design documents:

- Temporary Reinforced Earth wall,
- Fabric wall,
- Geogrid wall, and
- Hilfiker welded wire mesh wall.

Wall Design Recommendations and Procedures

All four wall systems were included in the design documents for the purpose of improving the potential for cost savings through competitive bidding. It should be noted, however, that the fabric and geogrid wall systems were limited to areas in which the wall height did not exceed 30 ft. This limiting criterion was established because of a lack of construction experience with and proven performance of walls of this type in excess of 50 ft in height. In addition, detailed specifications were shown on the drawings for the forming system required at the face of the wall for these two wall systems. Fabric and geogrids require forms to hold the shape of the wall face during construction. A typical wall section is shown in Figure 9 and the plan view of the wall locations is indicated in Figure 1. Table 6 is the temporary soil-retaining wall schedule used in

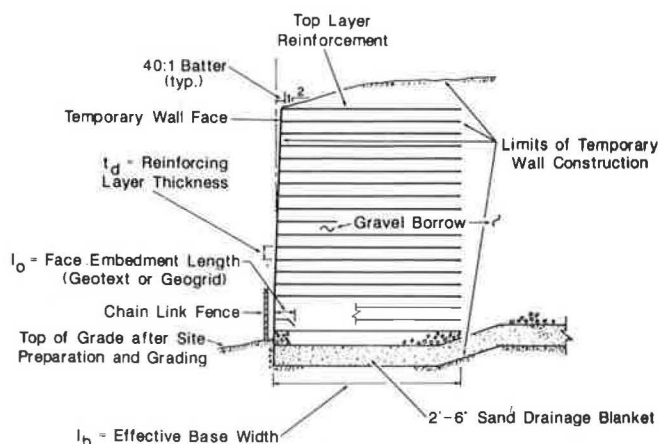


FIGURE 9 Typical wall section.

TABLE 6 TEMPORARY SOIL-RETAINING WALL SCHEDULE

Wall Type	Distance from Top of Wall (ft)	Wall Layer Thickness (in.)	Base Width (ft)	Face Embedment (ft)	Reinforcing Material	Remarks
A	0-20	12	15	5	Tensar SR-2	Geogrid
A	9-20	18	15	5	See special provisions	Geotextile
A	0-20	18	15	N/A	WWF 6x9 W4.5xW3.5	Hilfiker
A	0-20	18	15	N/A	Bar 2 X8GA @ 24 in. C-C	Reinforced Earth
B	0-20	12	23	5	Tensar SR-2	Geogrid
B	20-30	8	23	5	Tensar SR-2	Geogrid
B	0-20	18	23	5	See special provisions	Geotextile
B	20-30	12	23	5	See special provisions	Geotextile
B	0-20	18	23	N/A	WWF 6x9 W4.5xW3.5	Hilfiker
B	20-30	18	23	N/A	WWF 6x9 W7xW3.5	Hilfiker
B	0-20	18	23	N/A	Bar 2 X8GA @ 24 in. C-C	Reinforced Earth
B	20-30	18	23	N/A	Bar 2 X8GA @ 18 in. C-C	Reinforced Earth
C	0-20	18	35	N/A	WWF 6x9 W4.5xW3.5	Hilfiker
C	20-30	18	35	N/A	WWF 6x9 W7xW3.5	Hilfiker
C	30-47	18	35	N/A	WWF 6x9 W9.5xW4.0	Hilfiker
C	0-20	18	35	N/A	Bar 2 X8GA @ 24 in. C-C	Reinforced Earth
C	20-30	18	35	N/A	Bar 2 X8GA @ 18 in. C-C	Reinforced Earth
C	30-47*	18	35	N/A	Bar 2 X8GA @ 12 in. C-C	Reinforced Earth
D	0-20	18	44	N/A	WWF 6x9 W4.5xW3.5	Hilfiker
D	20-30	18	44	N/A	WWF 6x9 W7xW3.5	Hilfiker
D	30-47	18	44	N/A	WWF 6x9 W9.5xW3.5	Hilfiker
D	47-57	18	44	N/A	WWF 6x9 W12xW5.0	Hilfiker
D	0-20	18	44	N/A	Bar 2 X8GA @ 24 in. C-C	Reinforced Earth
D	20-30	18	44	N/A	Bar 2 X8GA @ 18 in. C-C	Reinforced Earth
D	30-47	18	44	N/A	Bar 2 X8GA @ 12 in. C-C	Reinforced Earth
D	47-57*	18	44	N/A	Bar 2 X8GA @ 9 in. C-C	Reinforced Earth

NOTE: An asterisk (*) denotes maximum total height of wall. N/A denotes not applicable. All WWF shall have large-diameter wire placed perpendicular to wall face geogrid and geotextiles shall be placed with main tensile strength placed perpendicular to wall face.

the design documents. The Hilfiker welded wire mesh wall system was chosen by the contractor for the project because it was determined to be the lowest cost system during the bid process. The cost included manufacturer's material cost plus costs associated with ease of construction and schedule impact. Final construction costs are summarized in Table 7. Figure 10 is a photograph of the welded wire mesh wall under construction.

Analysis of the external stability of the wall system included an evaluation of the potential for sliding and overturning with corresponding minimum factors of safety of 1.5 and 2.0. For internal stability, active lateral earth pressure coefficients and a factor of safety of 2.0 were used to design the geogrid soil-reinforced system and temporary Reinforced Earth system, consistent with the standard of practice at the time [personal communication from J. R. Bell of Oregon State University,

TABLE 7 COST BENEFITS FROM DESIGN RECOMMENDATIONS

	Cost (\$)	Savings (\$)
Use of zoned embankment fill permitted use of native soils in the Seattle lid area		535,000
Sand drains (original): 164,622 ft @ \$4/ft	(658,500)	
Wick drains: 164,622 ft @ \$1.07/ft	176,150	
Predrilling: 47,425 ft @ \$2.80/ft	132,800	349,550
Reinforced Earth wall (original) 43,723 ft ² @ \$25/ft ²	(1,094,000)	
Hilfiker welded wire mesh reinforced-soil retaining wall		
5,107 ft ² @ \$7.80/ft ²	467,200	626,800
15,421 ft ² @ \$8.80/ft ²		
13,958 ft ² @ \$11.50/ft ²		
9,237 ft ² @ \$14.20/ft ²		
Pile support at abutments (original)	(350,000)	
Surcharge fill at abutments	50,000	300,000
Total savings		1,276,350
Project cost		3,400,000



FIGURE 10 Welded wire mesh wall under construction.

1985 and Haliburton et al. (5)]. The geotextile fabric-reinforced system and the Hilfiker welded wire mesh system were designed using an at-rest lateral earth pressure coefficient with a factor of safety of 1.5. The allowable working tensile stress was limited to 55 percent of the yield strength of the steel for the Reinforced Earth and welded wire mesh system. The allowable tensile stress for the geotextile fabric-reinforced system was limited to 40 percent of the ultimate for nonwoven fabrics as determined by the ultimate grab tensile strength (ASTM D 1682-75) and 33 percent of the ultimate tensile strength for woven fabrics, which was based on the state of practice at the time (J. R. Bell). State of practice currently is to use 40 percent of the ultimate grab tensile strength for all fabrics excluding polyesters for which 60 percent is typically used. Geogrid working stress was also limited to 40 percent of the ultimate tensile strength. The state of the practice on limiting the working stress levels to the values in geotextiles and geogrids has been rapidly changing during the past few years because of recently available creep data and steadily improving standardization. Long-term creep stability of geotextiles and geogrids in soil is still, in general, unknown, which results in conservative allowable tensile stresses. Since completion of design, these standard practices have changed as noted previously. This is a reflection of how rapidly design methods using fabrics are currently changing.

To evaluate corrosion protection, both the pH and the apparent electrical resistivity of the fill material were included in the analysis for the alternative system utilizing steel.

The recommended embankment material was Washington State Department of Transportation's standard specification for gravel borrow, which consists of 1¹/₄-in. minus, well-graded, clean sand and gravel. It was recommended that the walls could be built vertically but that some minor batter should be considered because of the lateral strain that might occur during loading of the wall. In addition, it was recommended that the lower 10 ft of wall be protected from vandalism by gunite or a fence.

Comments on Construction

The westbound embankment preload shown in Figure 1 covers

a 3-acre site. The embankment includes 256,000 yd³ of sand and gravel borrow that consists of a clean, fine to medium sand with trace coarse sand and fine gravel. Temporary earth walls completed totaled 43,725 ft² and extended to a maximum height of 52 ft above Rainier Avenue. Use of the temporary walls allowed fill to be placed immediately adjacent to Rainier Avenue and prevented encroachment of the fill into the area of the Lakeway structures, thus preventing damage to those pile-supported structures. An additional application for the soil wall system along the E-RS ramp was noted previously and is shown in Figure 7. This ramp had to remain in service during preloading, and it was recommended that surcharge fill be placed above the final grade to achieve the primary consolidation necessary beneath the centerline of the ramp.

Face batter tolerance during wall erection was limited by specification to ≤ 1 in./10 ft of wall height. Actual vertical tolerances in the field were within the specified tolerances. Wall construction went smoothly, though slowly at first. The first month of wall construction was a time of learning for the contractor. Because welded wire retaining walls are relatively new to the Pacific Northwest, most contractors have had little or no experience building welded wire walls. The contractor's greatest difficulty during this early period was in developing an acceptable method for aligning the welded wire mats properly. After the contractor had made it through this initial period, wall construction rates varied from 250 to 650 ft² per day. All of the temporary walls, when completed, were within the tolerances for wall face batter and alignment specified in the contract. Though the walls were subjected to what was in some cases substantial differential settlement (more than 18 in. over 150 ft of wall) no distress was visible in the wall face.

INSTRUMENTATION PROGRAM

The actual settlement response due to the preload and surcharge loads was measured to determine the time of completion of primary consolidation and to compare the actual settlement characteristics of the soil with those used in design. This is particularly important for creep characteristics and secondary settlement because design parameters obtained in laboratory tests are not always reliable and accurate. Another potential source of differences between the predicted and measured settlements is induced changes in the consolidation characteristics of the soil resulting from the wick drain installation.

The following instrumentation program was recommended for use at this site:

1. Twelve pneumatic settlement-sensing devices at the base of the fill with four remote readout stations,
2. Four downhole settlement-measuring devices,
3. Three pneumatic piezometers for pore pressure measurements,
4. Ten surface monuments for settlement monitoring along existing streets and at the base of soil-reinforced walls,
5. Survey control of the wall face to measure outward deflection, and
6. Instrumentation of welded wire mats for stress-deformation response.

The recommended instrumentation location plan is shown on Figure 11. Minor modifications to the locations of the readout stations were made at the time of construction because of site grading considerations.

For improved accuracy, pneumatic settlement-sensing devices consisting of three-tube liquid systems instead of the standard two-tube devices commonly available were used. It was specified that settlement sensitivity be accurate to 0.3 in. and that all devices be proof-tested before approval. Each readout station and reservoir was protected by a vandalproof, waterproof protective cover. Readings were taken at weekly intervals during filling and the first month following completion of embankment construction; thereafter, readings were required at least twice a month.

As indicated previously, as much as 15 to 25 ft of surficial fill and deltaic deposits were observed across the site. The contribution to total settlement from these surficial materials was expected to range between approximately $\frac{1}{4}$ and $\frac{1}{3}$ of total settlement. Because these materials were granular in contrast to the more compressible cohesive lacustrine sediments at depth, the settlement response in this zone was also expected to be predominantly elastic and occur immediately during fill placement. Therefore the actual response of the more compressible clay unit measured from the surface settlement devices was expected to be masked to some extent by the settlement response of the upper fill and deltaic deposits. More important,

the overall shape of the time-deformation curve obtained from field measurements could be distorted; and corresponding critical indications of completion of primary consolidation and actual creep characteristics could be misinterpreted. To reduce the potential inaccuracies due to this site condition, four down-hole settlement devices were installed so that a vertical settlement profile of the clay, deltaic deposits, and fill material could be measured and field settlement characteristics could be compared with those assumed on the basis of laboratory tests during design.

The residual long-term settlement response was critical to the overall design, particularly in the area of the abutments where long-term settlement had to be limited to $\frac{1}{4}$ to $\frac{1}{2}$ in. Therefore it was required that the four downhole devices be placed at the two bridge abutments. Six to eight settlement rings were placed in the fill and natural soils below the ground surface to profile the vertical settlement.

Pneumatic pore pressure devices were specified for use in evaluating the pore pressure response during filling and preloading. Because of the relatively high, nearly vertical walls along the perimeter of the fill, shear stresses comparatively higher than those that might be expected below standard fill slopes were expected in the natural soils below the perimeter. Therefore one function of these devices was to aid in evaluating the stability of the foundation support. In addition, the pore pressure devices provided a means of monitoring the degree of

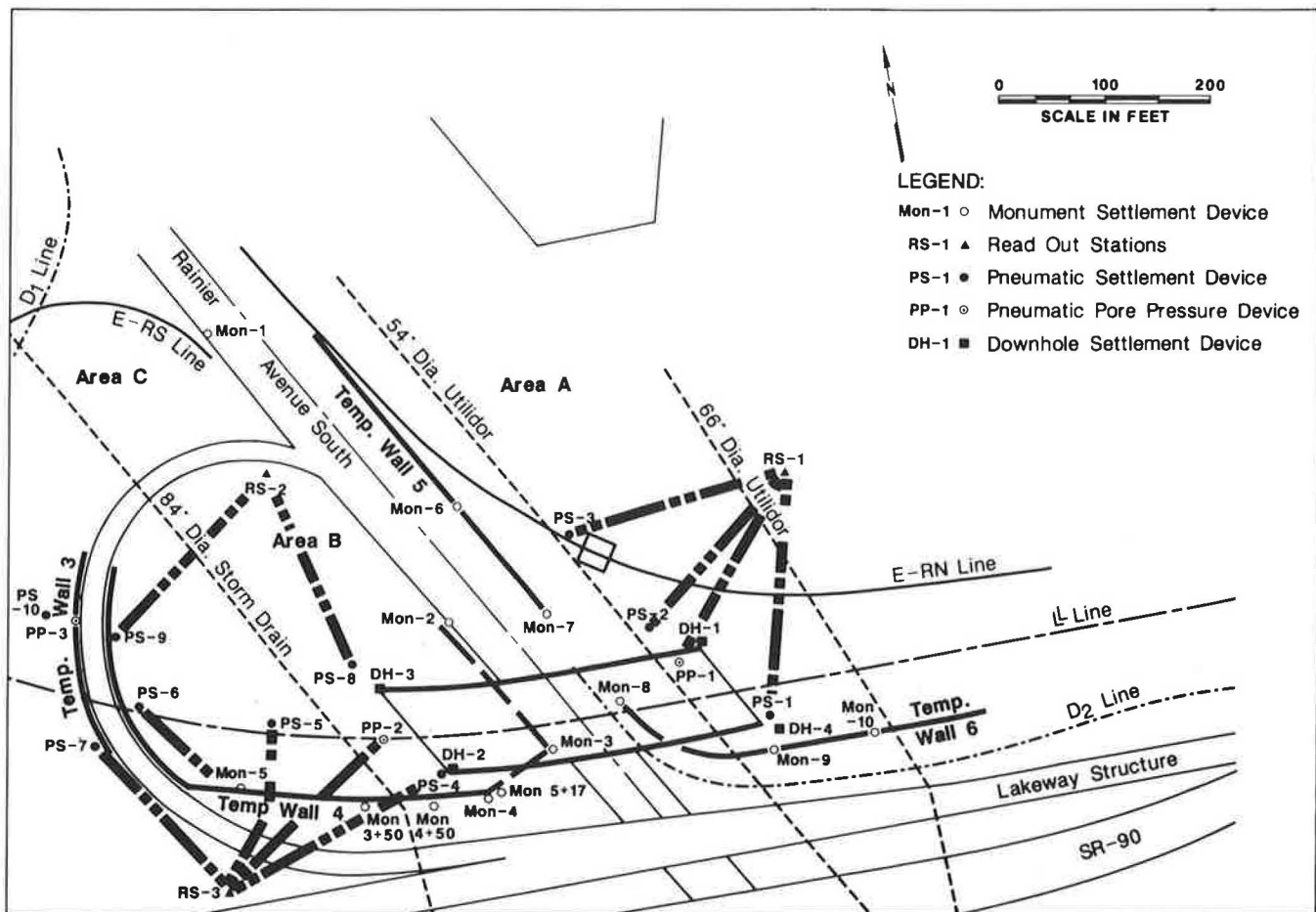


FIGURE 11 Recommended instrumentation location plan.

consolidation for comparison with the time-deformation curves obtained from the other field measurements.

To provide some redundancy in the field settlement data, it was recommended that surface monuments be placed around the perimeter of the fill area and measured during and after filling operations. This would allow comparison with the measurements obtained from the pneumatic devices, and, in the case of a system failure, the field measurements from surface monuments would provide backup data.

Outward tilting of the wall and resultant loss of batter were also of concern. Survey control was maintained during construction to monitor wall face movement, and only minor deflection occurred. Finally, it should be noted that detailed stress conditions in the welded wire mesh behind the wall face and corresponding earth pressures were evaluated (L. R. Anderson et al., unpublished data).

SETTLEMENT RESPONSE

Magnitude of Primary Consolidation

Summarized on Figure 12 are the predicted and measured settlements of the embankment and surcharges. In general, it was thought that the total magnitude of primary consolidation was reasonably close to the predicted values. In the area of the

east abutment, the settlements were generally equal to or less than the predicted values. The 12-ft-diameter utilidor (Figure 1) through this area may act to reinforce the soil mass in the upper 15 to 20 ft of material. This could lead to a stress reduction in the lower, more compressible clay layer and result in correspondingly lower settlements.

West of Rainier Avenue, a number of causes could have led to the variation between the predicted and measured values. It is believed that the variability in the extent and thickness of the organic lacustrine sediments accounts for those areas having measured settlements both higher and lower than predicted. In addition, the 84-in.-diameter storm drain just west of the west abutment would act to reinforce the soil mass and possibly to limit the amount of settlement. The variability in the thickness of the clay layer (Figure 5), combined with the variability in the relative density and thickness of the fill and deltaic deposits, would also contribute to the relatively minor differences between the predicted and the measured values.

Time Required To Complete Primary Consolidation

The time-related response indicating the time to completion of primary consolidation and the creep characteristics of the clay unit are shown in Figure 13. This figure also includes the response curve for Downhole Device 2 beneath the west abut-

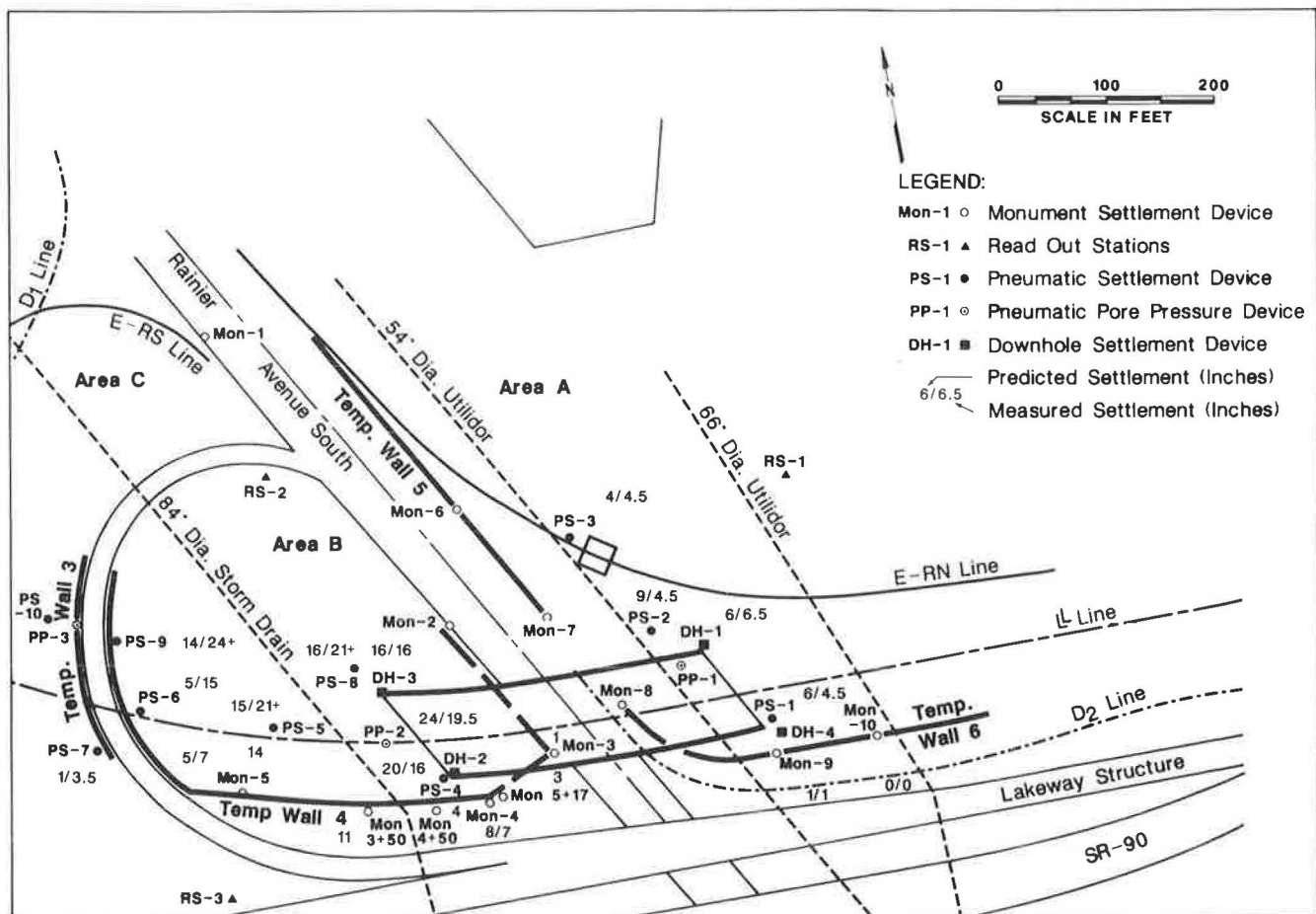


FIGURE 12 Summary of predicted and measured settlement.

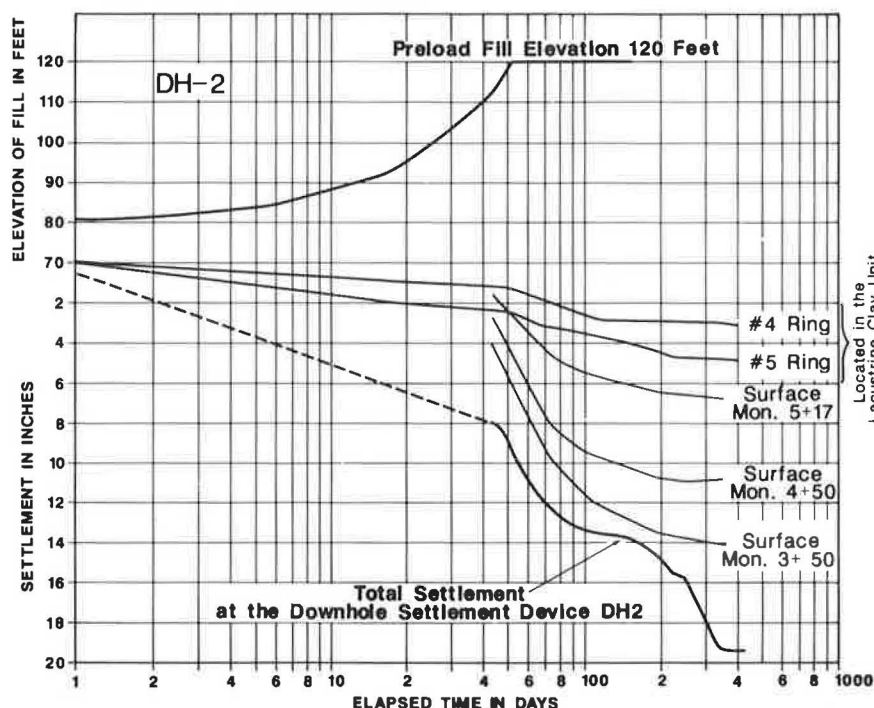


FIGURE 13 Settlement response at Downhole Device 2 on the west abutment of Bridge 21.

ment. This curve is typical of the settlement curves at other locations and is considered representative of this area. The curves include the total settlement curve, the settlement for Rings 4 and 5 located within the clay unit, and monuments 3+50, 4+50, and 5+17 located at the ground surface near the base of Temporary Wall 4 (Figure 12).

In general, the time required to complete primary consolidation varied between 65 and 170 days for all three areas of preloading (Areas A, B, and C in Figure 1). In particular, Area B, represented in Figure 13, varied between approximately 65 and 150 days. The estimated time was approximately 75 days, or one-half the maximum time recorded. However, the actual time available to complete primary consolidation was approximately 210 days; therefore there were no delays imposed on future construction.

A primary factor associated with the longer measured time required to complete primary consolidation is thought to be smear effect. Smearing of the clay interface with the wick drain during installation can lead to reduced lateral drainage. Another possible factor may be the shape of the plastic core of the wick drain. The plastic core of the wick drain consisted of alternating linear channels. If the wicks were bent during consolidation, a substantial reduction in flow could result, which would increase the time required to complete primary consolidation. Also, it is thought that the potential for reduced drainage rates during consolidation may be attributed to compression and possibly localized shear of the clay unit. In the latter case, shear planes might result in reorientation of the soil particles and reduce the horizontal permeability of the soil. There was no observed evidence of any of these factors, but, even though the causes are speculative, others also believe them to be likely (6).

Secondary Settlement

Laboratory results indicated that the coefficient of secondary compression varied between 0.002 and 0.004 [$C_\alpha = (\Delta H/H)/\Delta \log_{10} t$, (2)]. Because the laboratory-measured value of secondary compression is typically lower than that measured in the field, a value of 0.005 was assumed in this analysis. The backcalculated value of the coefficient of secondary compression was generally less than or equal to the assumed value of 0.005. Therefore additional surcharge fill was not required after construction of the embankment.

SETTLEMENT OF THE UTILIDOR AND STORM DRAIN

Three large utility lines pass beneath the preload fills (Figure 6): an 84-in.-diameter precast reinforced concrete storm drain, which was to have been replaced, located beneath the west embankment and two 12-ft-diameter precast reinforced concrete utilidors located beneath the east embankment. Each utilidor consists of a 54- or 66-in. water line with two 10-in.-diameter cased electrical lines. The tops of these utility lines are approximately 5 to 7 ft below the base of the preload fills. The plan locations of the utilidors and storm drain are shown in Figure 1.

The 84-in.-diameter storm drain was monitored for settlement and was also visually inspected for damage 6 months after the preload fill was constructed. The total settlement measured along the length of the storm drain is shown in Figure 14. The maximum settlement of 15 in. occurred in the vicinity

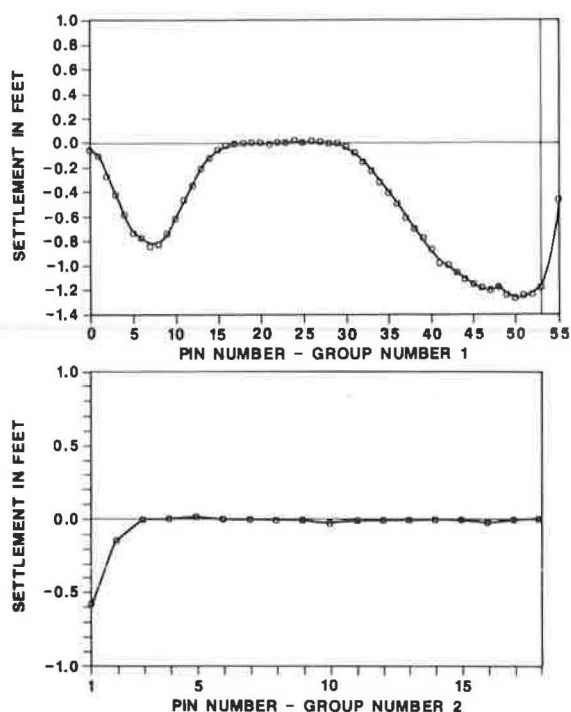


FIGURE 14 Settlement profile of 84-in. storm drain.

of the face of the temporary wall. Settlement of the preload fill above the storm drain was approximately 16 to 19 in. Differential settlement was as much as 0.5 in./ft. The storm drain had no settlement at a distance of 50 ft in front of the temporary wall. Visual inspection of the drain revealed that the pipe joints in the vicinity of the temporary wall face had suffered severe distortion. One of the joints suffered a 4-in. vertical offset. The other joints suffered some obvious displacement and cracking that were less severe than those observed at the first joint. The settlement also caused a manhole located in the vicinity of the temporary wall face to be driven down into the pipe. This caused some cracking in the joint between the pipe and the manhole. Despite this damage, the storm drain was still functional, though with reduced flow capacity, at least on a temporary basis. It is anticipated that the drain will remain usable until the planned replacement of the storm drain with a new line near Rainier Avenue.

Settlement of both utilidors was also monitored and was found to be minimal. Though the preload fill above the utilidor settled as much as 6 in., the utilidor nearest Rainier Avenue only settled 0.5 in., and the other utilidor only settled 1.5 in. Both utilidors were designed to handle up to 2 in. of settlement. The utilidors functioned normally after settlement was complete.

STAGED EXCAVATION

Immediately adjacent to the westbound embankment preload project is the Seattle lid section (or cut-and-cover tunnel) of the I-90 project, approximately 2,000 ft east. This section of the roadway was going to require a massive excavation of native glacial outwash and moisture sensitive glacial till materials

consisting of layers of silt, sand, gravel, and silty sand and gravel. Because of wet weather conditions in the region, most of this material was to be wasted. As part of this study, it was recommended that the lidded section be evaluated as a potential borrow source for that portion of the fill beyond the reinforced embankment areas. A subsequent investigation indicated that the materials and site conditions were suitable for a borrow source. The embankment was subsequently designed as a zoned embankment and the native materials were used beyond the wall areas, which made optimum use of on-site soils.

COST BENEFITS TO THE PROJECT

Several recommendations made during the final design study for this project resulted in a significant cost savings over the concepts developed during the preliminary studies for this project. A summary of the cost benefits is given in Table 7. The cost savings realized from the use of a zoned embankment was estimated to be approximately \$535,000. During the preliminary studies, it was thought that predrilling and wick drains were not amenable to the site conditions. Therefore augercast sand drains were proposed for use at that time. Evaluation completed during design indicated that wick drains and predrilling were appropriate for the site conditions. This resulted in a savings of about \$350,000.

At the completion of the preliminary studies in 1981, the types of reinforced-soil wall systems in common use were basically limited to temporary Reinforced Earth walls. During these final design studies, the design team sought to incorporate all of the currently available reinforcing materials now in use for constructing temporary, flexible, soil-reinforced wall systems. By including all four types currently in use in a competitive bidding process, a savings of approximately \$627,000 was realized.

It was also recommended in 1981 that the bridge abutments for Bridge 22 be pile supported. However, during this study the use of surcharge fills to eliminate long-term settlements at the abutments was evaluated and determined feasible. This resulted in a cost savings of approximately \$300,000. It is worthy of note that this foundation cost does not include the potential added cost and problems of predrilling piles through 40 ft of compacted fill and welded wire mesh soil reinforcement. Total combined cost benefits amounted to nearly one-third of the total cost of the project.

SUMMARY

In summary, it is believed that the measured settlements compared well with the calculated settlements. However, the time required to complete primary consolidation in some areas was twice the time predicted from conventional consolidation theory for application of prefabricated vertical drains. Although there was no observable evidence of the cause, such effects as smear, changing soil consolidation properties due to compression, shearing of the soil, or bending of the prefabricated drain could increase the time required to complete consolidation (6). In general, it was thought that the soil-reinforced walls, design

heights of which ranged from 10 to 55 ft above the existing ground surface, performed well. Finally, it was the intent in this paper to show how numerous geotechnical-related features of this design were implemented at a substantial cost savings to the project compared with the more conventional methods previously used in similar projects.

ACKNOWLEDGMENTS

The authors would like to acknowledge the contributions of R. L. Plum of Golder Associates who was the initial project manager and provided much of the direction for the project and R. G. Chassie, FHWA Region 10 Geotechnical Engineer, for his invaluable support and assistance during the design of this project.

REFERENCES

1. S. J. Johnson. Precompression for Improving Foundation Soils. Proceedings Paper 7020. *Journal of the Soil Mechanics and Foundations Division*, ASCE, Vol. 96, No. SM1, Jan. 1970, pp. 11-144.
2. T. W. Lambe and R. V. Whitman. *Soil Mechanics*. John Wiley & Sons, New York, 1969, Figure 27.17.
3. R. A. Barron. Consolidation of Fine-Grained Soils by Drain Wells. *Transactions*, ASCE, New York, No. 113, 1948.
4. W. Kjellman. Accelerating Consolidation of Fine Grained Soils by Means of Cardboard Wick. *Proc., Second International Conference on Soil Mechanics*, Rotterdam, The Netherlands, Vol. 1, 1948.
5. T. A. Haliburton, J. D. Lawmaster, and V. C. McGuffey. *Use of Engineering Fabrics in Transportation-Related Applications*. Office of Development, FHWA, U.S. Department of Transportation, 1981.
6. *Vertical Drains*. Thomas Telford, Ltd., London, England, 1982.

Publication of this paper sponsored by Committee on Transportation Earthworks.

Ultimate Resistance of Vertical Square Anchors in Clay

BRAJA M. DAS

Laboratory model test results for the ultimate pullout resistance of square vertical anchors in saturated clay are presented. Pullout resistance can be expressed in the form of a nondimensional breakout factor. The breakout factor increases with the embedment ratio of the anchor up to a maximum value and remains constant thereafter. A tentative empirical procedure, based on the laboratory test results, for estimating anchor pullout resistance is outlined.

Vertical anchor slabs (Figure 1a) are used in many instances in the construction of earth-retaining structures. They are also used in the design of pipeline bends. Recently, the results of a number of experimental and theoretical studies related to the ultimate resistance of vertical anchors in sand have been published (1-5). Most of the important findings of those studies have been summarized elsewhere by Das (6). In contrast, few attempts have so far been made to estimate the ultimate resistance of vertical anchors of limited height and width embedded in clay soils. The purpose of this paper is to present the results of some laboratory experimental studies of the ultimate pullout resistance of square anchor plates embedded in saturated or nearly saturated clayey soils.

ULTIMATE RESISTANCE OF VERTICAL ANCHORS IN CLAY

Mackenzie (7) conducted a number of laboratory model tests on strip anchors in two different saturated clay soils. According to this study, the ultimate resistance of vertical anchors can be conveniently expressed in a nondimensional form as

$$F_c = \frac{Q_u}{(BL)c_u} \quad (1)$$

where

- F_c = breakout factor,
- Q_u = ultimate anchor pullout resistance,
- B = height of anchor plate,
- L = length of anchor plate, and
- c_u = undrained cohesion of clay.

It needs to be pointed out that the term "breakout factor" was not used by Mackenzie (7). For convenience only, it has been introduced here.

The average variation of the breakout factor with embedment ratio H/B (where H = depth of embedment of the anchor plate as shown in Figure 1) as obtained by Mackenzie (7) is shown in Figure 2. This has also been shown by Tschebotarioff (8). On the basis of Figure 2, the following general conclusions can be drawn:

1. The magnitude of F_c for a given anchor plate in a given soil increases with H/B .
2. There appears to be a critical value of embedment ratio, $H/B = (H/B)_{cr}$, at which the magnitude of the breakout factor approximately attains a maximum value, $F_c = \bar{F}_c$.
3. For $H/B \geq (H/B)_{cr}$, the value of F_c remains constant (i.e., equal to \bar{F}_c).

In Figure 2, the value of $(H/B)_{cr}$ is approximately equal to 12 or 13, and $\bar{F}_c \approx 9$. Hence, anchors with $H/B \leq (H/B)_{cr}$ may be referred to as shallow anchors for which general shear failure in soil takes place and the failure surface extends to the ground surface as shown in Figure 1b. For anchors with embedment ratios of $H/B > (H/B)_{cr}$, local shear failure in soil takes place, and these anchors may be referred to as deep anchors, as shown in Figure 1c. Tschebotarioff (8) has commented that in the field the unit weight of the soil (γ) should have some influence on the ultimate resistance of an anchor. The effect of unit weight on the ultimate resistance (Q_u) obtained from the laboratory tests is somewhat negligible. However, for actual design work the use of laboratory test results will provide conservative estimates.

Meyerhof (9) has suggested that a conservative estimate of the breakout factor (F_c) with embedment ratio may be given as follows:

For strip anchors,

$$F_c = 1.0(H/B) \quad (\text{with a maximum of } 8) \quad (2)$$

For square anchors,

$$F_c = 1.2(H/B) \quad (\text{with a maximum of } 9) \quad (3)$$

Equations 2 and 3 imply that the critical embedment ratio of strip anchors is about 8 and that for square (or circular) anchors it is about 7.5. For comparison purposes, these equations have also been plotted in Figure 2.

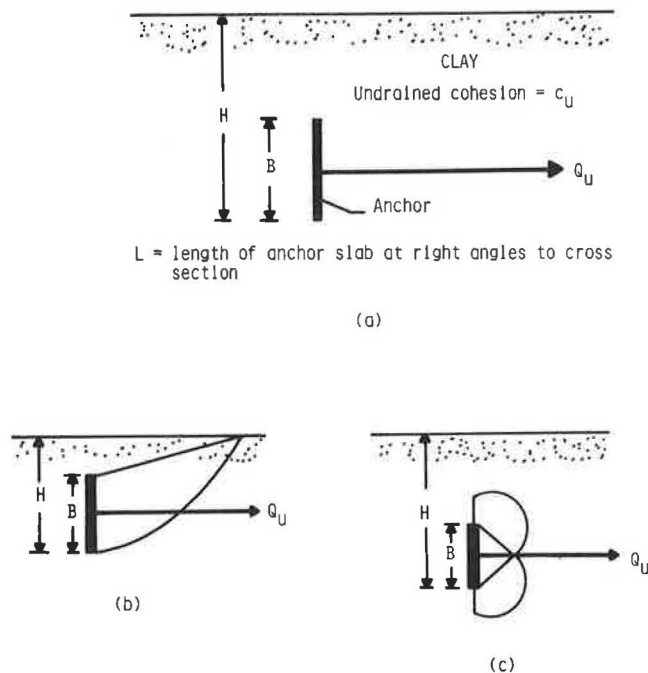


FIGURE 1 Parameters of a vertical anchor slab (a); definition of a shallow anchor (b); and definition of a deep anchor (c).

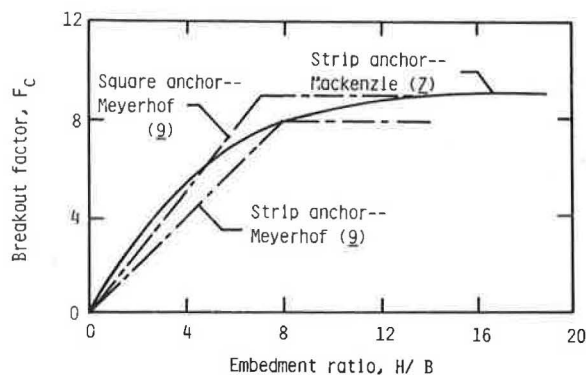


FIGURE 2 Variation of breakout factor with embedment ratio as given in the studies of Mackenzie (7) and Meyerhof (9).

The present study relates to the ultimate resistance of square anchors only, because there are practically no experimental results available in the literature. Also, it needs to be realized that the magnitude of $(H/B)_{cr}$ may change with the consistency of clay [i.e., the undrained shear strength (c_u)]. This is true in a closely related problem—the uplift capacity of horizontal anchors in clay (10).

LABORATORY INVESTIGATION

To estimate the ultimate resistance of horizontal anchors in saturated or nearly saturated clay, a number of model tests were conducted in the laboratory with two model anchors measuring 38.1×38.1 mm and 50.8×50.8 mm ($B \times L$). The anchors were made from a steel plate 9.5 mm thick.

Two different clay soils were used for the testing program. The grain-size distributions of the two soils were determined by sieve and hydrometer analyses in the laboratory, along with their Atterberg limits. A summary of the preliminary tests is given in Table 1.

TABLE 1 PROPERTIES OF SOILS USED FOR LABORATORY TESTS

Item	Quantity	
	Soil A	Soil B
Percent passing No. 200 U.S. sieve	78	68
Percent finer than 0.002 mm	29	26
Liquid limit	32	39
Plastic limit	19	14
Plasticity index	13	25
Unified soil classification	CL	CL

The soils were initially pulverized in the laboratory, and desired amounts of water were added to them. After thorough mixing the moist soils were transferred to several plastic bags. The bags were then sealed and kept in a moist curing room for about a week before use.

All model tests were conducted in a box with inside dimensions of $0.915 \times 0.508 \times 0.915$ m (height). A schematic diagram of the laboratory test arrangement is shown in Figure 3. To conduct a test, the anchor was rigidly attached to a steel rod 7.94 mm in diameter. The rod, in turn, was attached to a steel cable with a diameter of 4.76 mm. The cable passed over a pulley, and the other side of the cable was attached to a load hanger.

TABLE 2 LABORATORY TEST PARAMETERS

Test Series	Soil Used	Width of Plate (B) Used (mm)	Average Moist Unit Weight of Compacted Soil (kN/m^3)	Average Moisture Content of Compacted Soil (%)	Average Degree of Saturation of Compacted Soil (%)	Average Undrained Shear Strength (c_u) (kN/m^2)	Range of Embedment Ratio (H/B) Tested
1	A	50.8	19.65	24.5	97	20.3 ^a	1–8
2	A	38.1	20.76	17.6	94	42.4 ^b	1–9
3	B	50.8	19.03	28.5	98	12.5 ^a	1–7
4	B	38.1	20.29	18.5	92	28.1 ^b	1–8
5	B	38.1	20.65	16.2	93	52.0 ^b	1–9

^aDetermined from laboratory vane shear tests.^bDetermined from unconsolidated, undrained triaxial tests.

The moist soil from the plastic bags was poured into the box and compacted in 50.8-mm-thick layers to the desired height. The compaction was done in sections using a flat-bottomed rammer. Proper compaction around the anchor plate was a difficult task. A small flat-bottomed rammer with sides measuring 101.6×101.6 mm was used to compact the clay around the anchor.

After compaction, step loads were placed on the load hanger, and the corresponding horizontal movements of the anchor were observed by a dial gauge. A time lapse of from 5 to 8 min was allowed between the placement of each step load, and the loading continued until failure occurred. The time lapse was allowed because a steady movement of the anchor was noted immediately after load application (primary creep). After the time lapse of from 5 to 8 min, the horizontal movement of the anchor plate was practically zero.

A total of five series of tests were conducted in the laboratory. Details of the tests are given in Tables 2 and 3. It needs to be pointed out that the values of the unit weight and moisture content given in Table 2 are the arithmetic average values. For each test, five or six samples were taken from various depths at random for determination of the unit weight of compaction and moisture content. This was done at the end of the pullout tests using a 76.2-mm-diameter, thin-wall tube 152.4 mm long. The difference between the minimum and the maximum values of the unit weight for any given series was no more than about 6 percent, which was to be expected when working with moist clay soil. Some of the thin-wall tube samples for Test Series 2, 4, and 5 were trimmed to prepare triaxial test specimens (35.56 mm in diameter and 76.2 mm in height). The triaxial test specimens were tested with a chamber confining pressure of 70 kN/m^2 . In Test Series 1 and 3, which involved softer clays, the trimmed specimens were not particularly good for triaxial tests.

TABLE 3 DETAILS OF LABORATORY TESTS

Test Series	Soil Used	Embedment Ratios of Tests
1	A	1, 2, 3, 4, 5, 6, 7, 8
2	A	1, 2, 3, 4, 5, 6, 7, 8, 9
3	B	1, 2, 3, 4, 5, 6, 7
4	B	1, 2, 3, 4, 5, 6, 7, 8
5	B	1, 2, 3, 4, 5, 6, 7, 8, 9

For that reason, laboratory vane shear tests were used to determine c_u , although it is well known that laboratory vane shear tests are not extremely reliable (11). The stress-strain curves of triaxial tests were somewhat similar in shape to the load-displacement plots obtained in the anchor pullout tests. However, it is difficult to compare the peak axial strain levels of triaxial tests with the horizontal displacement levels of the anchors at ultimate load.

MODEL TEST RESULTS

Typical net load versus displacement plots obtained from the laboratory model tests are shown in Figure 4. For all tests, the ultimate loads were defined as the points at which sudden pullout occurred or the load-displacement plots took an almost linear shape.

The ultimate loads for all tests determined in this manner are shown in Figures 5 and 6. Figure 5 shows the values of Q_u for tests conducted with Soil A (i.e., Test Series 1 and 2); and, similarly, results of the tests conducted using Soil B (i.e., Test Series 3, 4, and 5) are shown in Figure 6. It needs to be pointed

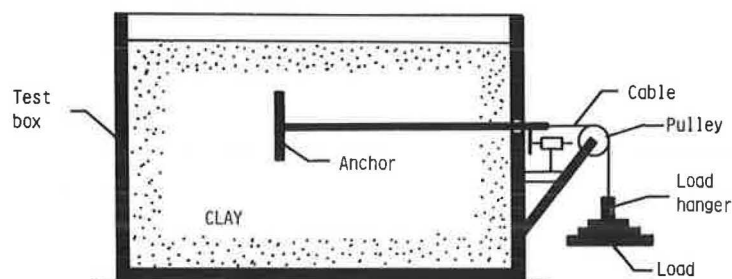


FIGURE 3 Schematic diagram of the model test arrangement in the laboratory.

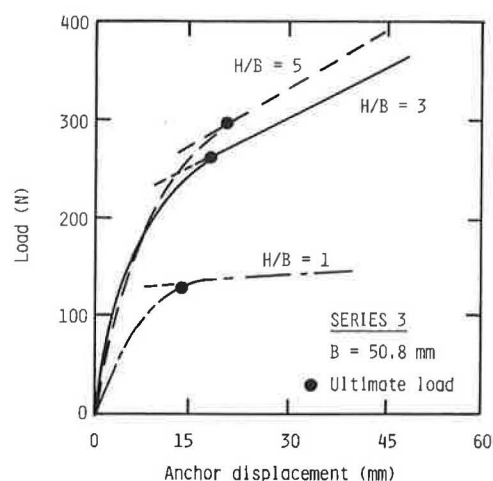


FIGURE 4 Typical load versus displacement plots obtained from the laboratory tests.

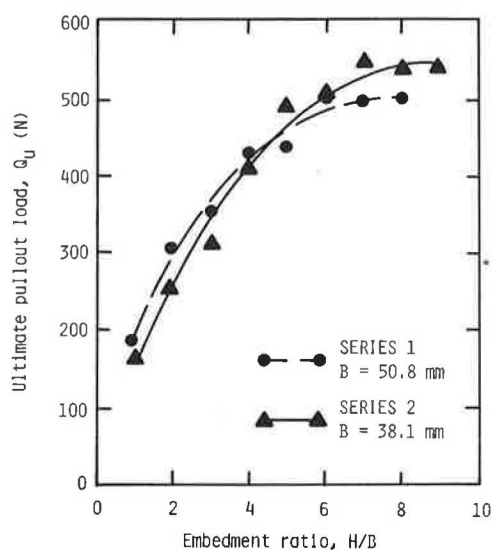


FIGURE 5 Plot of ultimate pullout load versus embedment ratio—Series 1 and 2.

out that the horizontal rod attached to the center of the anchor plate had a large diameter compared with the anchor plate dimensions. For that reason, before the start of the actual model test, the adhesion between the rod and the clay was separately determined. In plotting the variation of the load Q and the anchor displacement, the adhesive force between the soil and the rod at corresponding displacement levels was subtracted from the observed load. The maximum adhesive forces between the rod and the clay determined from the laboratory were 36, 59, 29, 55, and 66 N for Test Series 1, 2, 3, 4, and 5, respectively.

Using these net ultimate load values and Equation 1, the breakout factors at various embedment ratios have been calculated and are shown in Figures 7 and 8. It needs to be pointed out that, for square anchors, $B = L$; hence, Equation 1 takes the form

$$F_c = \frac{Q_u}{B^2 c_u} \quad (4)$$

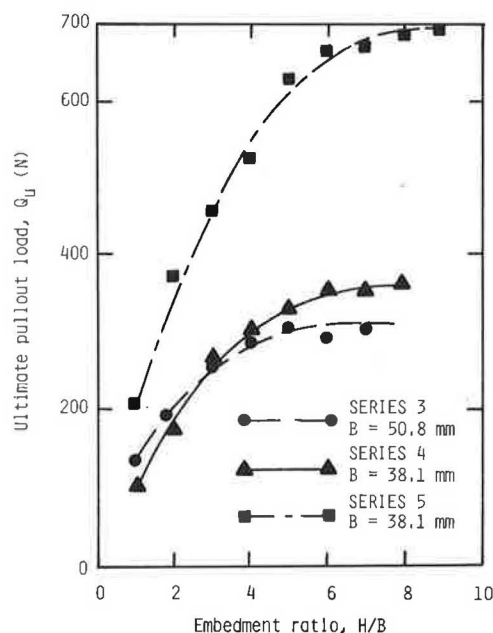


FIGURE 6 Plot of ultimate pullout load versus embedment ratio—Series 3, 4, and 5.

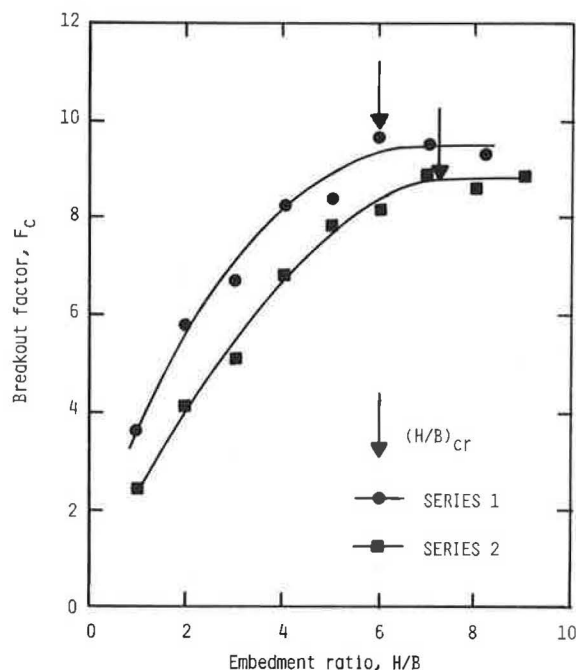


FIGURE 7 Plot of breakout factor (F_c) against embedment ratio—Series 1 and 2.

In evaluating the values of F_c shown in Figures 7 and 8, the average undrained shear strength values (c_u) given in Table 2 have been used. It can be clearly seen from Figures 7 and 8 that the general trend of the variation of F_c with H/B is similar to that obtained by Mackenzie (7) as shown in Figure 2. Some scattering of experimental results can well be expected in tests of this type.

It is also of interest to note that the plots of F_c versus H/B for 50.8-mm plates (Test Series 1 and 3) as shown in Figures 7 and 8 are higher than those for 38.1-mm plates. This is because

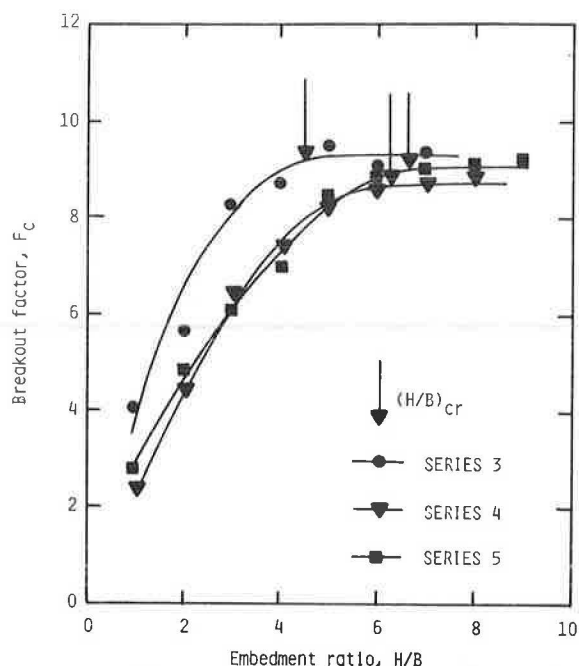


FIGURE 8 Plot of breakout factor (F_c) against embedment ratio—Series 3, 4, and 5.

tests in softer clays were conducted with 50.8-mm plates. The nondimensional breakout factor for softer clays increases more rapidly with H/B up to a maximum value than do those for stronger clays. In other words, for shallow anchors at similar embedment ratios, $\Delta F_c / \Delta (H/B)$ increases with the decrease of c_u .

The critical embedment ratio $[(H/B)_{cr}]$ as estimated from the average plots of all test series is also shown in Figures 7 and 8. These values of $(H/B)_{cr}$ have been plotted against the undrained shear strength of clay in Figure 9. The average plot can be approximated as

$$(H/B)_{cr} = 4.33 + 0.067c_u \leq 7 \quad (5)$$

where c_u is in kN/m^2 .

The maximum value of $(H/B)_{cr} = 7$ is consistent with Meyerhof's (9) recommendation of 7.5. These values need to be confirmed by large-scale field tests during which extreme

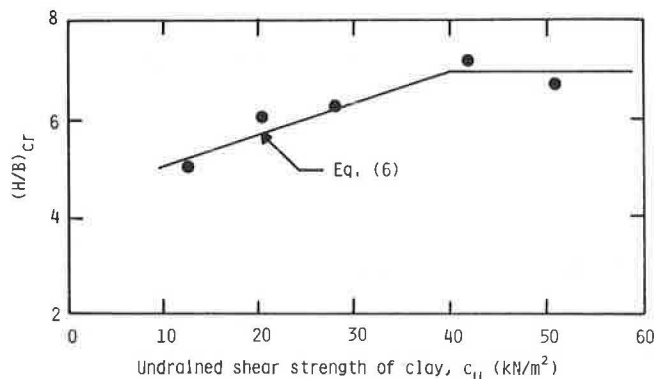


FIGURE 9 Plot of $(H/B)_{cr}$ versus undrained shear strength of clay.

care is taken to assure consistency of soil parameters, which are not available in open literature at the present time.

Figure 10 shows the plot of the maximum value of the breakout factor $F_c = \bar{F}_c$ as obtained from the average plots given in Figures 7 and 8. The magnitude of \bar{F}_c varies between 8.8 and 9.5 with an average value of 9.1. This is similar to the magnitude of the bearing capacity factor $N_c = 9$ as obtained for deep square and circular foundations on saturated clay under compressive loading conditions. Considering the errors involved in laboratory tests of the present type, the value of \bar{F}_c may be conservatively assumed to be about 9.

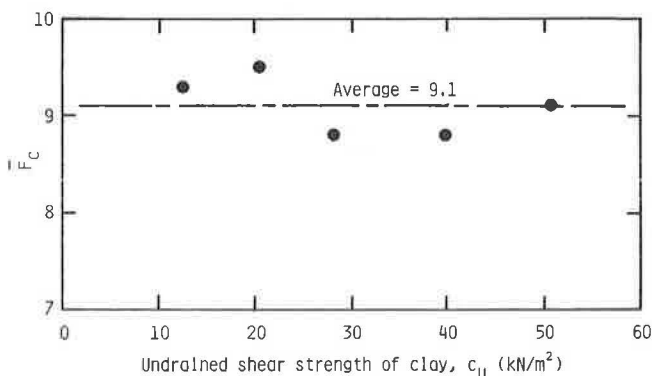


FIGURE 10 Variation of \bar{F}_c with undrained shear strength of clay.

EMPIRICAL PARAMETRIC EVALUATION OF ULTIMATE PULLOUT RESISTANCE

Das (12) has used two nondimensional parameters to propose a design procedure for the ultimate pullout resistance of horizontal anchors in saturated clays subjected to vertical pullout forces. A similar procedure can also be adopted for the problem under consideration by defining the two nondimensional parameters as follows:

$$\alpha = F_c / \bar{F}_c \quad (6)$$

and

$$\beta = \frac{H/B}{(H/B)_{cr}} \quad (7)$$

Using the average plots of F_c versus H/B shown in Figures 7 and 8, the magnitudes of several β/α versus β have been calculated, and these have been plotted in Figure 11. Although there is some scattering, the points fall within a narrow range. The average plot can be represented as

$$\frac{\beta}{\alpha} = 0.4 + 0.6\beta$$

or

$$\alpha = \frac{\beta}{0.4 + 0.6\beta} \quad (8)$$

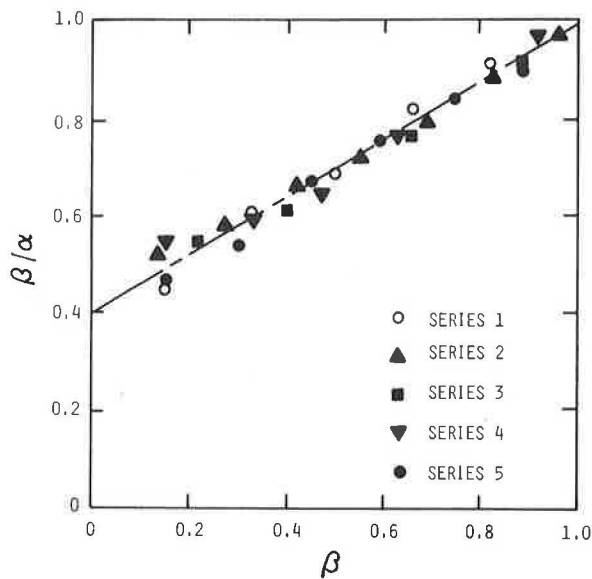


FIGURE 11 Plot of β/α versus β obtained from the average plots shown in Figures 7 and 8.

The preceding equations can now be used to propose a tentative design procedure for estimation of the ultimate pullout resistance of square vertical anchors in clay. The procedure can be modified in the future when the results of more laboratory and field tests are available. A step-by-step approach to the proposed procedure follows:

1. Obtain B , H , and c_u
2. Calculate H/B
3. Using Equation 5, estimate $(H/B)_{cr}$
4. If the actual H/B (Step 2) is greater than $(H/B)_{cr}$ (Step 3), it is a deep anchor so

$$Q_u = \bar{F}_c B^2 c_u \cong 9 B^2 c_u \quad (9)$$

5. If $H/B < (H/B)_{cr}$, obtain β by using Equation 7. With an estimated value of β , use Equation 8 to obtain α . Now

$$Q_u = (\alpha \bar{F}_c) (B^2 c_u) \cong 9 \alpha B^2 c_u \quad (10)$$

The ultimate loads obtained by using this method may appear large compared with the present conventional approach for field design. However, many of the conventional procedures have been developed using a simplistic approach without full-scale field tests. Similarly, analogy can be made to the ultimate load determination of vertical anchors embedded in sand. In many design problems, the determination of ultimate load of shallow anchors in sand is made by using the simplistic procedure outlined by Teng (13). However, recent centrifugal tests in the laboratory by Dickin and Leung (14) have shown that good agreement exists between their tests and the semiempirical procedure developed by Ovesen and Stromann (5) based on laboratory model tests. The ultimate load calculated by using Ovesen and Stromann's procedure gives higher values of Q_u than those obtained by using Teng's conventional procedure. However, with a factor of safety of about 2 the difference

between the conventional approach and the present findings should not be too great.

CONCLUSIONS

A number of small-scale laboratory model test results on square vertical anchors in clay have been presented. The following conclusions, based on the present results, can be drawn:

1. The ultimate pullout resistance of an anchor can be expressed in the form of a nondimensional breakout factor (F_c).
2. The magnitude of the maximum breakout factor (\bar{F}_c) is approximately equal to 9 for square anchors.
3. The critical embedment ratio increases with the undrained shear strength of clay (Equation 5). However, for stiff clays the magnitude of $(H/B)_{cr}$ is about 7.
4. The variation of the breakout factor with embedment ratio in clays of various consistencies can be expressed by a single nondimensional parametric equation (Equation 8).
5. A tentative empirical procedure for estimation of the ultimate pullout resistance of square vertical anchors has been suggested.

The major contribution of this study is the development of Equations 5 and 8, which show the effect of the undrained shear strength of clay on the critical embedment ratio $[(H/B)_{cr}]$ and the hyperbolic relationship for the normalized parameters of $\alpha = F_c/\bar{F}_c$ versus $\beta = (H/B)/(H/B)_{cr}$. However, the study has some limitations:

- Only two soils have been tested under remolded conditions.
- The effect of gravity has not been modeled. Large-scale field tests are expensive. However, this needs to be done to verify the proposed relationships.
- For each test, the profile of c_u has been assumed constant with depth. In the field this may not be the case; hence, care needs to be taken in using the proposed laboratory-obtained relationships in the field.
- During the present model tests, a delay time of from 5 to 8 min was used after each step load application. This was done to take into account primary creep. However, the test results do not account for possible secondary creep at allowable load levels. In the field a factor of safety of 2 or more will probably be used. At that loading, secondary creep will be substantially minimized.

REFERENCES

1. B. M. Das. Pullout Resistance of Vertical Anchors. *Journal of the Geotechnical Engineering Division*, ASCE, Vol. 101, No. GT1, 1975, pp. 87-91.
2. B. M. Das and G. R. Seeley. Load-Displacement Relationship for Vertical Anchor Plates. *Journal of the Geotechnical Engineering Division*, ASCE, Vol. 101, No. GT7, 1975, pp. 711-715.
3. B. M. Das, B. R. Seeley, and S. K. Das. Ultimate Resistance of Deep Vertical Anchors in Sand. *Soils and Foundations*, Vol. 17, No. 2, 1977, pp. 52-56.

4. W. J. Neeley, J. G. Stuart, and J. Graham. Failure Loads of Vertical Anchor Plates in Sand. *Journal of the Soil Mechanics and Foundations Division*, ASCE, Vol. 99, No. SM9, 1973, pp. 669-685.
5. N. K. Ovesen and H. Stromann. Design Method for Vertical Anchor Slabs in Sand. *Proc., Specialty Conference on Performance of Earth and Earth-Supported Structures*, ASCE, Vol. 1, Part 2, 1972, pp. 1481-1500.
6. B. M. Das. Holding Capacity of Vertical Anchor Slabs in Granular Soil. *Proc., Coastal Structures '83*, ASCE, 1983, pp. 379-392.
7. T. R. Mackenzie. Strength of Deadman Anchors in Clay. M.S. thesis. Princeton University, N.J., 1955.
8. G. P. Tschebotarioff. *Foundations, Retaining and Earth Structures*. McGraw-Hill Book Co., New York, 1973.
9. G. G. Meyerhof. Uplift Resistance of Inclined Anchors and Piles. *Proc., VIII International Conference on Soil Mechanics and Foundation Engineering*, Vol. 2, 1973, pp. 167-172.
10. B. M. Das. Model Tests for Uplift Capacity of Foundations in Clay. *Soil and Foundations*, Vol. 18, No. 2, 1978, pp. 17-24.
11. A. Arman, J. K. Poplin, and N. Ahmad. Study of Vane Shear. *Proc., Conference on In-Situ Measurement of Soil Properties*, ASCE, Vol. 1, 1975, pp. 93-120.
12. B. M. Das. A Procedure for Estimation of Ultimate Uplift Capacity of Foundations in Clay. *Soils and Foundations*, Vol. 20, No. 1, 1980, pp. 77-82.
13. W. C. Teng. *Foundation Design*. Prentice-Hall, Englewood Cliffs, N.J., 1962.
14. E. Dickin and C. F. Leung. Evaluation of Design Methods for Vertical Anchor Plates. *Journal of Geotechnical Engineering*, ASCE, Vol. 111, No. 4, 1985, pp. 500-520.

Publication of this paper sponsored by Committee on Foundations of Bridges and Other Structures.

Structural Behavior of 45-Degree Underreamed Footings

SHAMIM A. SHEIKH AND MICHAEL W. O'NEILL

In this paper is described an experimental and analytical study aimed at developing a better understanding of the structural behavior of 45-degree underreamed footings. Two instrumented 45-degree footings 7.5 ft (2.29 m) in diameter with shafts 2.5 ft (0.76 m) in diameter were load tested under differing geotechnical conditions. One footing was situated in a very stiff clay, and the other was placed on a stratum of clay shale. In both tests failure occurred because of either bearing capacity failure of the footing itself or pullout failure of an anchor shaft. The footings sustained mean net bearing pressures of 100 psi (clay) and 157 psi (clay shale) without developing observable structural distress. Finite element analyses predicted well the measured base pressure distribution and the load-settlement characteristics of the footings; however, the maximum predicted tensile stresses in the underream under the imposed loads exceeded the tensile strength of concrete beam specimens tested to failure in flexure. Because no tensile cracking was actually observed in the test footings, a more realistic tensile strength criterion that relates to the status of stress in the footing needs to be established.

Ongoing research suggests that shallow foundations are as reliable as deep foundations for the support of bridge structures in many situations. One efficient way of constructing a shallow footing in cohesive soil is to machine-excavate an underream at a shallow depth and to concrete the excavation without reinforcing the bell. This raises the issue of footing capacity being controlled by structural strength rather than soil bearing capacity. Historically, to avoid premature structural failure, bridge engineers have either specified conical underreams with angles of 60 degrees (with the horizontal) or have disallowed unreinforced underreamed footings altogether. Unfortunately, the use of 60-degree underreams often requires more concrete than a spread footing constructed in the usual manner, and the diameter of the footing that can be excavated with mobile truck-mounted drilling equipment is quite limited. On the other hand, it is possible to construct 45-degree conical underreams to a diameter of 10 ft (3.05 m) or more with truck-mounted equipment and to reduce by one-third the volume of concrete required in the underream, which makes 45-degree underreamed footings economically viable alternatives to spread footings. To realize the benefits of using 45-degree underreams, factors that affect their structural capacity must be understood.

A recent study (1) has suggested that 45-degree underreamed footings may be considerably weaker structurally than 60-degree underreams. On the basis of a series of tests conducted

in a laboratory environment on small-scale footings and associated analytical work, it was concluded that 45-degree underreams can fail at a uniform bearing pressure in the range of 8 to 12 ksf (0.34 to 0.43 MPa), whereas the bearing stress at failure in 60-degree underreams varied between 16 and 20 ksf (0.77 and 0.96 MPa). Failure initiated in most footings at the base because of tensile cracks in the concrete. Tand and O'Neill (2) conducted elastic finite element analyses of a 45-degree underreamed footing along with the surrounding soil, with similar results. The findings of these two studies have resulted in most designers specifying 60-degree bells for resisting high bearing stresses.

The purpose of this research was to experimentally and analytically study the behavior of 45-degree underreams in a field environment. The experimental part of the study involved the testing of two full-scale instrumented underreamed footings. Each footing had a 2.5-ft (0.76-m) nominal shaft diameter and a 7.5-ft (2.29-m) nominal bell diameter. One footing, tested in Houston, Texas, at the University of Houston-University Park Foundation Test Facility, was 7.75 ft (2.36 m) deep and founded on overconsolidated Beaumont clay, a Pleistocene soil deposited in a deltaic environment. The bearing stratum for the second footing, which was 12.5 ft (3.81 m) deep, was Eagle Ford shale, a Cretaceous clay-shale of marine origin. The site of this test was the grounds of Southwestern Laboratories, Inc., in Dallas, Texas.

In the analytical part of the study a finite element model of the 45-degree footing and the surrounding soil was developed. Stress-strain properties of Beaumont clay were used in the analysis to evaluate the behavior of the soil surrounding the footing. After a reasonable approximation of the behavior of the footing-soil system was established from the analytical work, the same discretization was used to analyze the two footings without the surrounding soil. A comparison of the experimental and the analytical results is presented in this paper for the tests conducted during this study as well as for tests reported earlier (1).

GEOTECHNICAL CONDITIONS

The soil at the test site for Footing 1 (Houston) is in the Beaumont clay formation, which was heavily preconsolidated by desiccation. Extensive soil tests have been conducted at this site (3). The undrained shear strength profiles for the depth of primary interest, as obtained from the UU triaxial compression tests and static cone penetration test (CPT) soundings (4), are shown in Figure 1. The undrained shear strength profile for the

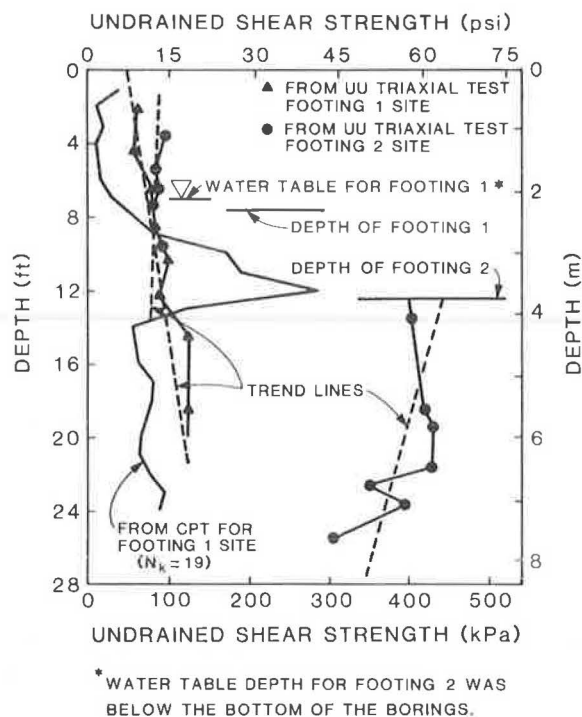


FIGURE 1 Undrained shear strength profiles.

CPT was obtained by dividing total cone tip pressures minus hydrostatic pore water pressures by a factor $N_k = 19$. The CPT profile suggests the presence of a soil layer of high undrained shear strength just below Footing 1. However, the high indicated shear strength values are manifestations of the presence of sand partings and calcareous nodules, which probably have little influence on the actual bearing capacity of the footing (5).

On the same figure the variation with depth of the undrained shear strength of the soil at the Dallas site, as obtained from UU triaxial tests, is also shown. There is a sudden break in the strength profile at a depth of about 12.5 ft (3.81 m), below which hard blue clay shale exists. The soil above this depth was dark brown to gray clay fill. Both types of soil at this site, clay and shale, possess quite high degrees of preconsolidation. The unconfined compressive strength of the shale, the bearing stratum for Footing 2, is estimated at more than 100 psi (0.73 MPa) from the tests conducted on samples from the borings.

DETAILS OF TESTING

Details of the two test footings are shown in Figure 2. The depths of the footings were selected at the depth of the shallowest strong bearing stratum. The dimensions of the underreams, shown in Figure 2, were measured from within the excavations just before concreting. To break the bond between the concrete and the surrounding soil along the straight shaft portion of the footing, cardboard tubes with inside diameters of 2.5 ft (0.76 m) were used in both footings. In the case of Footing 1, there was no gap between the cardboard tube and the surrounding soil, which caused some side shear development at low values of applied load along the shaft. In the case of Footing 2, the borehole was 34 in. (0.86 m) in diameter, which

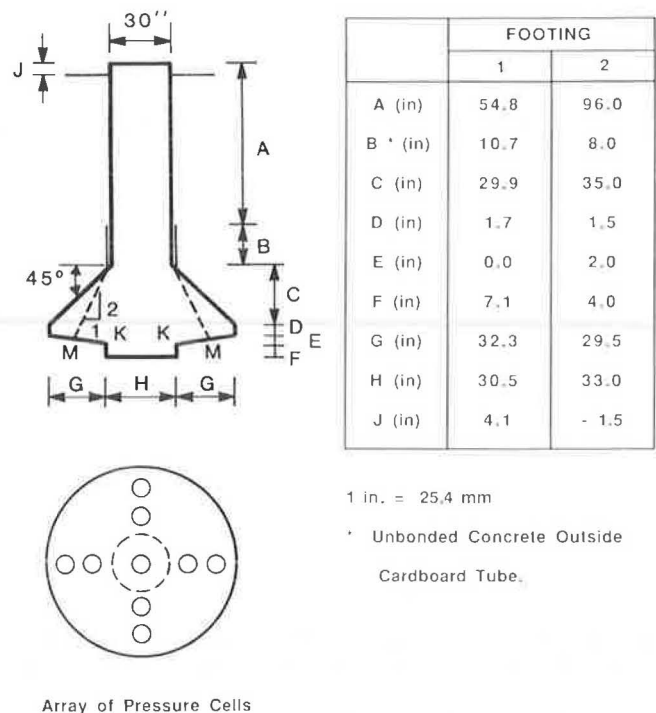


FIGURE 2 Details of test footings.

resulted in an air gap of just under 2 in. (51 mm) between the outside of the tube and the surrounding soil.

Ready-mix concrete with a nominal compressive strength of 3,000 psi (20.7 MPa) at 28 days was used in both footings. Slight vibration was provided to assure concrete free of honeycombing. Footings 1 and 2 were tested 69 and 63 days after casting, respectively. The compressive strength of concrete samples was measured using standard 6- × 12-in. (152- × 305-mm) cylinders, and modulus of rupture was determined from 6- × 6- × 20-in. (152- × 152- × 508-mm) beams. At the time of testing, the actual compressive and tensile strengths of concrete used in Footing 1 were 3,970 and 538 psi (27.4 and 3.71 MPa), respectively. Using an 18 percent coefficient of variation between the laboratory and in situ concrete strengths (6), the most probable lower limits of in situ compressive strength and modulus of rupture can be estimated at 3,255 and 441 psi (22.4 and 3.0 MPa), respectively. For Footing 2, the corresponding laboratory and lower limit of in situ compressive and tensile strength values for the concrete were 4,680 and 696 psi (32.3 and 4.8 MPa) and 3,840 and 570 psi (26.5 and 3.9 MPa), respectively.

The reinforcement cage in both of the footings consisted of eight No. 7 deformed steel bars, equally spaced around the circumference, and No. 3 ties at 6-in. (152-mm) spacing. Because it was observed during the testing of Footing 1 that some load transfer to the soil took place along the straight portion of the shaft, two opposite bars in Footing 2 were instrumented with eight strain gauges to evaluate the variation of load along the depth. The strain gauge data confirmed that no load transfer along the straight portion of Footing 2 took place.

In both footings, an array of nine total pressure cells 9 in. (229 mm) in diameter was used at the contact between the base of the footing and the soil, as shown in Figure 2. All nine cells

in Footing 1 and four cells in Footing 2 were of the pneumatic type. The other five cells in Footing 2 were of the vibrating-wire type. All pneumatic cells were calibrated up to a pressure of 140 psi (0.96 MPa), and the vibrating-wire cells were calibrated up to a pressure of 150 psi (1.0 MPa). All of the cells used exhibited linear behavior, which allowed extrapolation of the data with some confidence during the footing test for one of the vibrating-wire cells that recorded a pressure of about 180 psi (1.24 MPa).

To measure the movement of the base, two telltales were used in each footing. Movements of the base and the top of each footing were measured using four dial indicators with least counts of 0.001 in. (0.025 mm). The reference frames used for these measurements were anchored to the ground at a distance of about 10 ft (3.05 m) on each side of the center of the footings.

Two underreamed drilled shaft anchors with shafts 2.5 ft (0.76 m) in diameter, bells 7.5 ft (2.29 m) in diameter, and depths of 18 ft (5.49 m) were used for the application of load on Footing 1. These anchor shafts were installed at a distance of 9.5 ft (2.9 m) from the center of the test footing. The anchor shafts for Footing 2, situated 9 ft (2.75 m) from the center of the test footing, were cylindrical shafts 4 ft (1.22 m) in diameter and 30 ft (9.14 m) deep. The movements of the anchor shafts were monitored continuously during both tests. The test setup for Footing 1, showing the reaction beams, is shown in Figure 3.



FIGURE 3 Overall test setup for Footing 1.

Footing 1 was loaded to 500 kips (2224 kN) in 100-kip (445-kN) increments, beyond which the loading increment was reduced to 50 kips (222 kN). After each 100-kip (445-kN) increment, load was maintained for 60 min; after each 50-kip (222-kN) increment, the load was maintained for 30 min. The loading steps for Footing 2 were 100, 300, 500, 650, 750, 850, 950, and 1,040 kips (445, 1335, 2224, 2892, 3336, 3780, 4226, and 4626 kN). Each load level except the last was maintained for 60 min. Most of the readings were taken at 2, 29, and 59 (if any) min after the application of a load increment.

RESULTS

It was stated earlier that the use of the cardboard tube in the

shaft portion of Footing 1 may not have completely broken the bond between the concrete and the soil. It is also plausible that load was transferred from the roof of the underream to the overlying soil through suction. Figure 4 compares two curves, top load versus base settlement and base load versus base settlement, for Footing 1 that indicate that initially very little of the applied load reached the bearing surface. The difference between the top load and the base load (load transferred above the base) is also shown in the same figure. The maximum non-base-bearing load transfer occurred at a settlement of about 0.5 percent of the base diameter, beyond which the shaft bond or roof suction, or both, broke, and essentially all of the load was thereafter transferred to the bearing surface.

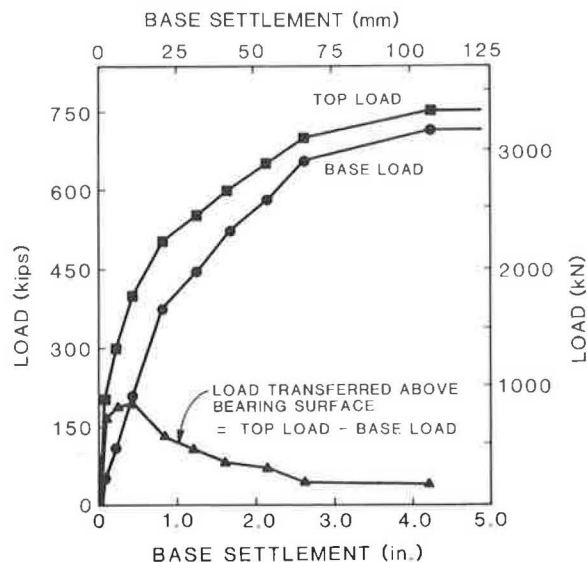
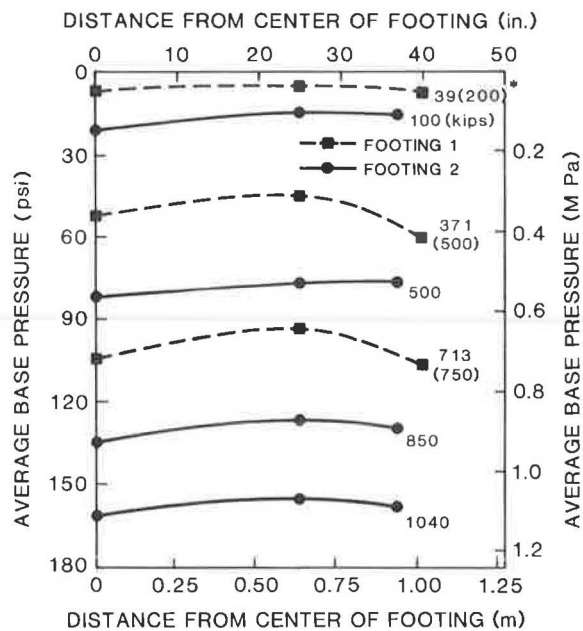


FIGURE 4 Transfer of load in Footing 1.

The base load in Figure 4 was calculated as the summation of the product of average base pressures and the areas over which each average pressure acts. Details are available elsewhere (4, 7). The variations of the contact pressure along the radius of the base, based on the average of the readings taken during the time a particular load was maintained, are shown in Figure 5 for various top-load levels for both footings. The base pressures are reasonably uniform for both footings, although the soil characteristics at the two bases were significantly different. A tendency of higher stresses close to the circumferences of the bases is consistent with the elastic continuum solution. Three-dimensional plots of the distribution of net base pressures for the two footings at their maximum loads are shown in Figure 6. The distribution appears reasonably uniform except for the east-west direction in Footing 2. This was probably because on the east side there was about 6 to 12 in. (152 to 305 mm) of fill material between the base of the footing and the shale. This soft material resulted in lower stiffness on the east side and hence lower bearing stresses. The average stress in the east-west direction is, however, almost equal to that in the north-south direction.

In both footings, no sudden variations were observed in the base pressure readings during testing, which indicated that no

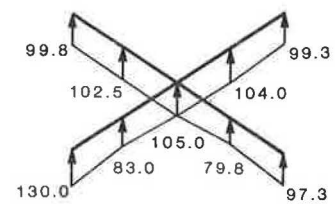


* THE TOP LOAD IS GIVEN IN PARENTHESES FOR EVERY BASE LOAD IF BOTH LOADS ARE NOT EQUAL.

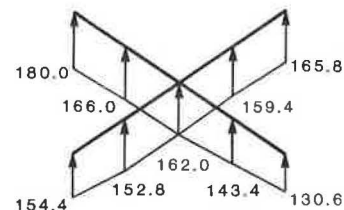
FIGURE 5 Average net base pressure for various loads.

sudden changes of stiffness of the footings took place during the course of loading, and hence no tensile cracking of concrete occurred in the bell.

The base load versus base settlement curves for the two footings are shown in Figure 7, in which significantly higher initial stiffness of the bearing surface for Footing 2 with respect to Footing 1 and a lack of any appreciable stiffness reduction up to the maximum pressure experienced are quite obvious.



FOOTING 1



FOOTING 2

FIGURE 6 Variation of base stress (psi) at maximum loads.

Although one of the main purposes of this work was to evaluate the structural capacity of 45-degree underreams and to study the failure mechanism in the bell, both tests had to be terminated because of failure in the soil. The structural capacity of Footing 1 exceeded the estimated value based on the available information on 45-degree underreams (1, 2). The most convenient location for the test was the University of Houston Foundation Test Facility, where the net ultimate bearing capacity of the near-surface soil is about 15 ksf (0.72 MPa). This soil capacity was twice the average stress at which Farr reported that most model footings failed structurally (1). In addition, at

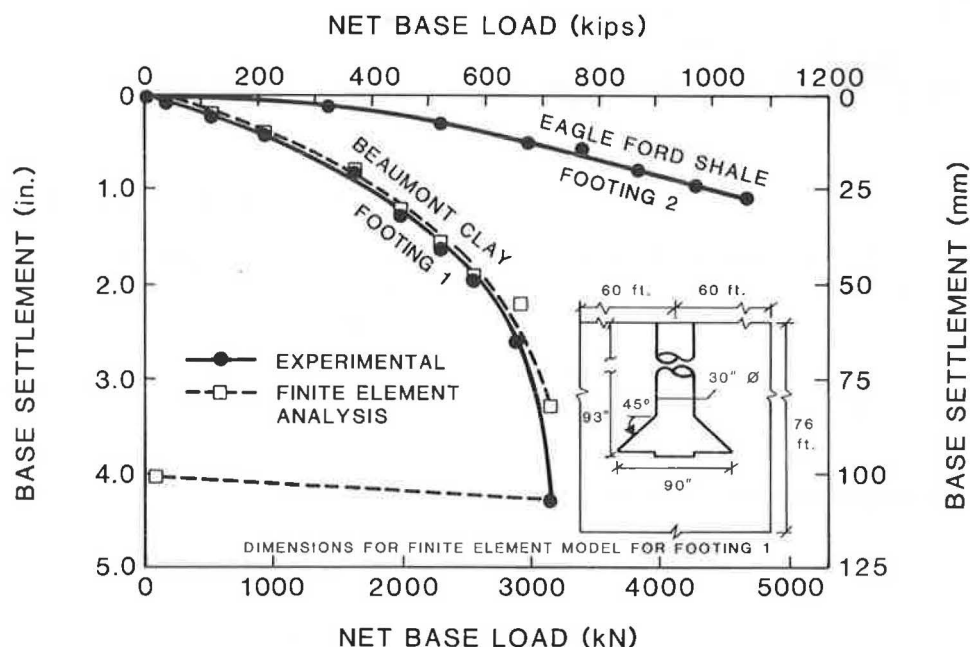


FIGURE 7 Comparison of experimental and analytical net base load versus base settlement.

this bearing stress the maximum analytically determined tensile stress in bell concrete exceeds the largest of the tensile strengths measured from available laboratory tests.

The second test was planned for a maximum load of 2,000 kips (8900 kN) to produce a bearing stress of about 300 psi (2.1 MPa). The anchor shafts were designed on the basis of the commonly used undrained adhesion of 28 psi (193 kPa) for the blue shale in the Dallas area. The shearing resistance offered by the top 10 ft (3.1 m) of clay fill as well as the suction developed at the base of the reaction shafts were neglected to provide an apparently conservative design. One of the anchor shafts, however, failed at a total load of about one-half the maximum design load. At a footing load of 950 kips (4226 kN), the anchor shaft started failing, and between 950 and 1,040 kips (4226 and 4626 kN) the uplift movement increased from 0.126 in. (3.2 mm) to 0.524 in. (13.3 mm). The test was terminated because the load could not be maintained beyond this point. At failure, the average side shear in the lower 20 ft (6.1 m) of the shaft was only about 14 psi (97 kPa). The load-uplift behavior of the two anchor shafts for Footing 2 is shown in Figure 8.

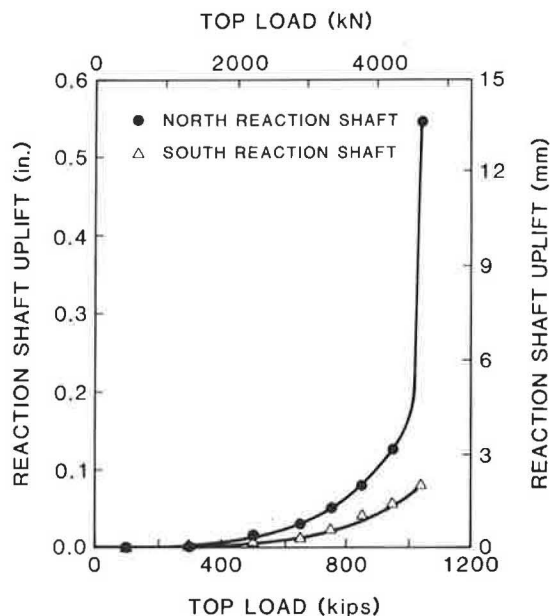


FIGURE 8 Uplift of reaction shafts versus top load on Footing 2.

COMMENTARY ON TEST RESULTS

Structural failure of an underreamed footing is most likely to initiate at the base. Simple analyses for flexural or diagonal tension failure, following the logic applied to the analysis of single column footings, ideally can be carried out to estimate the onset of failure. Flexural failure may cause the initiation of cracking at the point of maximum moment (Point K in Figure 2). Based on the maximum measured base pressure, the upper limits on the flexural stresses in Footings 1 and 2 are 399 and 460 psi (2.75 and 3.17 MPa), respectively. The lower limit on the modulus of rupture of concrete is estimated at 441 and 570 psi (3.04 and 3.93 MPa) for Footings 1 and 2, respectively. Flexural failure was therefore not imminent.

Diagonal tensile stresses are assumed to initiate cracks at the base at Point M (Figure 2). The maximum values of these stresses for Footings 1 and 2 were calculated to be 135 and 169 psi (0.93 and 1.17 MPa), respectively. These stresses are considerably less than the shear strength of concrete in these footings, which is estimated at least to be equal to $4\sqrt{f'_c}$ (f'_c in psi) or at least 228 psi (1.58 MPa) in Footing 1.

Standard simplified analysis therefore would not appear to predict structural failure in the two footings tested at the values of the loads applied.

FINITE ELEMENT ANALYSIS

A finite element study of the footing-soil system was carried out to supplement the experimental results. A commercially available ANSYS software package was used for analysis. By taking advantage of the axial symmetry of the structure and the loading, only one radial wedge of the structure and soil was discretized, and two-dimensional axisymmetric elements were used for both soil and concrete over the entire region of interest. Because the main purpose of the study was to investigate the underream, the soil-structure interaction along the straight side of the shaft was not included in the analysis. Gap elements were introduced along the interface between soil and concrete and also placed horizontally in the soil region close to the level of the shaft base. This was done to release the erroneously high tensile stresses in the soil and to simulate approximately the development of soil cracks in the tension zones. The gap elements were released in shear initially along the shaft and at the roof of the underream. Gap elements at the base of the underream were released when the interface shear stress exceeded the undrained shear strength of the soil.

The complete finite element mesh is shown in Figure 9. Figure 10 shows the detailed discretization of the bell region. The size of the elements used is reduced in the area of high stress concentration. To reflect the actual observed field measurements, the notch (Point K in Figure 2) was chamfered as shown in Figure 10. The centerline of the shaft was constrained against horizontal movement, and the bottom and side boundaries were completely fixed.

Mechanical properties of both soil and concrete were estimated from the results of the laboratory sample tests. Nonlinear material characteristics were modeled as bilinear stress-strain curves. Properties were assumed to be identical in both tension and compression. For concrete, the initial stiffness of 390,000 ksf (18 670 MPa) was used up to a von Mises yield stress of 400 ksf (19.2 MPa), beyond which the stiffness was reduced to 78,000 ksf (3735 MPa). For the soil for Footing 1, the stiffness values used were 840 ksf (40 MPa) up to a von Mises yield stress of 4 ksf (0.19 MPa) and 42 ksf (2 MPa) beyond that. These properties were based on the standard concrete cylinder tests in compression and UU triaxial tests on soil specimens recovered from beneath the elevation of the bearing surface.

A comparison of the analytical and experimental base load-base settlement curves is shown in Figure 7 for Footing 1. An iterative procedure for analysis was employed to account for the inelastic material properties. In the initial stages of loading, the solution converged rapidly. At higher loads, however, the convergence required several iterations, particularly to satisfy

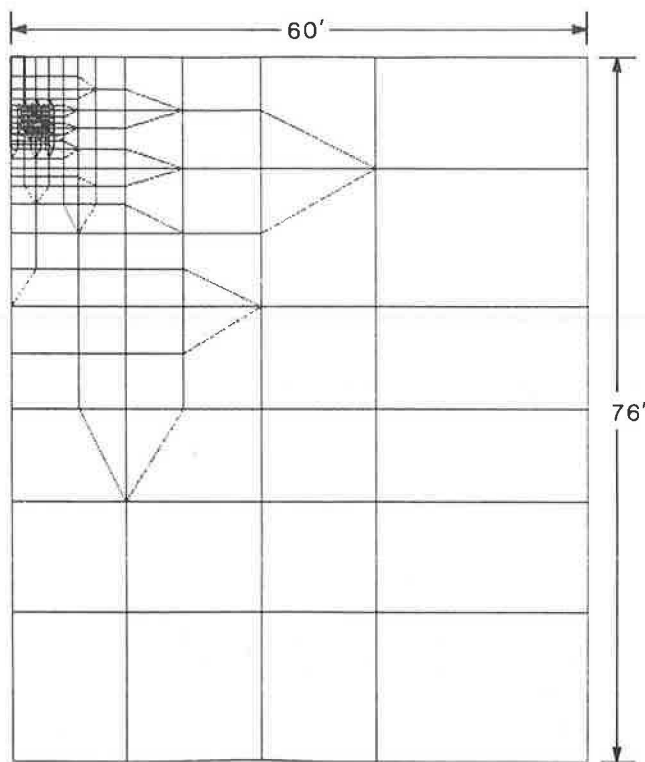


FIGURE 9 Full mesh for the shaft-soil system for Footing 1.

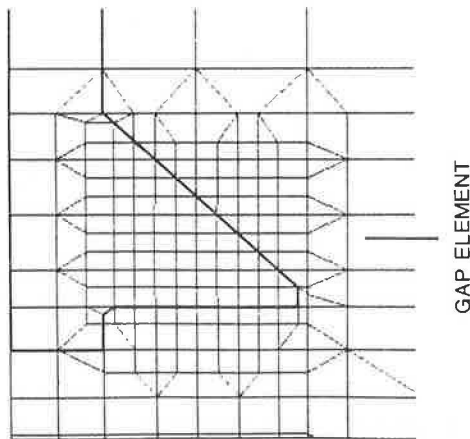


FIGURE 10 Enlarged portion of the mesh for the shaft-soil system for Footing 1.

limits on soil properties. Because of computer system limitations, it was therefore decided to relax the convergence criterion for the last two points on the analytical curve in Figure 7.

Analytical base reaction pressure distribution near the maximum load is compared with both the equivalent uniform pressure distribution and the measured values for Footing 1 in Figure 11. Analytical results compare well with measured values. However, at the notch, which is an area of stress concentration, the analytical solution indicates pressure almost twice the value of the uniformly distributed pressure. It should be noted that the base reaction was not measured directly at the

DISTANCE FROM CENTER OF FOOTING (in.)

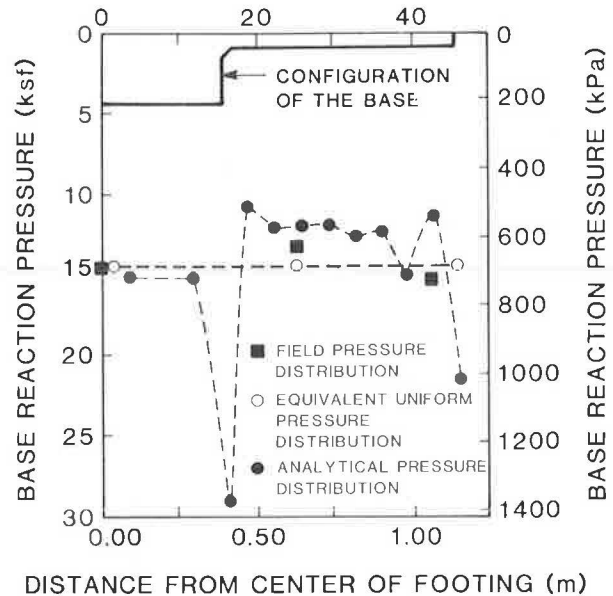


FIGURE 11 Base pressure distribution at base load of 713 kips in Footing 1.

notch. The analytical value may be more representative of the actual pressure in the notch area compared with either the average pressure or the pressure interpolated from the measured values.

Footings 1 and 2 were then analyzed without the surrounding soil, subjected to top load, and constrained by a uniform base pressure and no other surface tractions. The mesh of the concrete structure was not changed from the previous analysis because that mesh provided base pressure distribution and load-settlement behavior for Footing 1 that were reasonably close to the experimental results. Table 1 gives a comparison of the analytical and the experimental maximum stress values in concrete for footings tested during this study and the earlier laboratory study (1).

When the soil was included in the mesh, the maximum calculated concrete tensile stresses in Footing 1 (just above the notch) were about 13 percent higher than those calculated without the soil. This difference can be explained by the higher Poisson's ratio of the nearly incompressible soil (0.45) compared with that of concrete (0.20). Maintenance of compatibility between soil and concrete at the base results in additional tensile stresses in the concrete. The maximum tensile stress under the maximum load in Footing 2, when analyzed with the surrounding soil mass, would therefore have been about 970 psi (6.69 MPa).

It is apparent that, for both of the footings tested during this investigation, the analysis predicted the occurrence of tensile stresses in the bell at the maximum base load that significantly exceeded the maximum tensile strength (modulus of rupture) of the concrete. Even then there was no cracking or other signs of distress in these footings, as was confirmed by careful observation of the footings after they were extracted and cleaned at the completion of the tests (Figure 12). For the reduced-scale tests reported earlier (1), the calculated tensile stresses caused by

TABLE 1 MAXIMUM CALCULATED CONCRETE STRESSES

Full-Scale Tests	Base Load (kips)	Tensile ^a		Compressive		Toe Height (in.)
		Stress (psi)	Strength (psi)	Stress (psi)	Strength (psi)	
Present investigation						
Footings 1 ^b	713	668	565	1,323	3,960	7
	713	584	565	1,337	3,960	7
Footings 2	1,043	848	696	1,950	4,680	7
Model tests from Farr (1)						
Average of 7 tests	50.6 ^c	371	315		4,234	0
Average of 5 tests	59.5 ^c	534	395		4,974	3

^aTensile strength for Footings 1 and 2 refers to modulus of rupture. For other tests split tensile strength of concrete was reported, which is about 20 percent lower than modulus of rupture.

^bFinite element analysis of the footing was performed with the surrounding soil in place. In all other cases soil was not included.

^cAt failure.

failure loads were found to be higher than the split cylinder strength of concrete and approximately equal to the modulus of rupture. The maximum compressive stresses in both of the footings in this study were found to be well below the concrete compressive strength.

The apparent difference between the results of the present investigation and those of the model tests of the earlier study (1) can be explained as follows.

The model footings were tested in a laboratory on a non-yielding bearing surface. This may have caused a concentration of bearing stresses that produced tensile stresses in excess of those calculated from the finite element analysis. The model footings were cast upside down, which may have resulted in weak concrete at the base due to bleeding and segregation. The unique features of the curing of the concrete in a saturated-soil environment and the confinement of concrete by the surrounding soil may have caused an improvement in the in situ properties of the concrete in Footings 1 and 2.

Tensile strength of concrete is commonly measured by application of direct tension, splitting a concrete cylinder by applying load along its length, or by the modulus of rupture test. Split cylinder strength and modulus of rupture strength are about 25 and 50 percent, respectively, higher than direct tensile strength. Recently Chen and Yuan (8) suggested a new indirect method for determining the tensile strength of concrete. In this method, known as the double punch method, a compressive load is applied to a concrete cylinder along its axis through two steel punches placed on the top and bottom surfaces of the cylinder. This results in an almost uniform tensile stress across all diametrical planes. The tensile strength of concrete was observed to be between $4\sqrt{f'_c}$ and $7\sqrt{f'_c}$ (f'_c in psi), which is comparable with the usual split cylinder strength of concrete.

Given such a large variation in the indicated tensile strength of concrete, which depends on several factors including the type of test (which determines the state of stress), size and shape of specimen, and shrinkage, it is difficult to estimate the in situ tensile strength of concrete in the footings.

In the analysis, although bilinear stress-strain curves were used for the material properties, stresses in concrete were still within the elastic range at maximum loads. Because of softening of concrete in both tension and compression, the stresses

may be overestimated, although an attempt was made to reduce this overestimation by using a lower-limit value of initial stiffness of the concrete. [A ratio between the stresses calculated from an elastic analysis and actual stresses of 1.2 has been suggested for dams (9, p. 26).] It has also been suggested that the tensile stresses thus calculated should be compared with the split cylinder strength or the apparent stresses should be checked against the modulus of rupture (10).

It appears that the tensile stresses in the footing concrete would be slightly lower than those calculated from finite element analyses. Even then, the stresses appear to have exceeded the modulus of rupture values for samples taken of the concrete in the footing. Because full-sized footings did not develop tensile failure, it appears that the in situ tensile strength is greater than that indicated by moduli of rupture of the samples. This conclusion suggests that a more realistic tensile strength criterion, which can account for the state of stresses in underreamed footings, needs to be established.

CONCLUSIONS

A well-formed 45-degree underreamed footing was capable of resisting base bearing pressure in excess of 157 psi (1.08 MPa) without structural failure or any other sign of structural distress.

In Beaumont clay the service limit load for the footings would be dictated by soil constraints and not by underream structural constraints. The finite element method, which accounts for the nonlinear behavior of soil, predicts the load-settlement behavior and the distribution of base bearing stresses in a reasonable manner.

The structural failure of the bell is more likely to be caused by the combined effects of flexure and shear than by flexure or punching shear alone.

The tensile stresses calculated under the maximum applied loads exceeded the maximum tensile strength of concrete as measured from flexure tests on samples from both of the footings. This indicates that the in situ tensile strength of the concrete in the underream is significantly higher than the sample modulus of rupture. A more realistic tensile strength criterion, which can account for the complex state of stress in the footings, is needed.

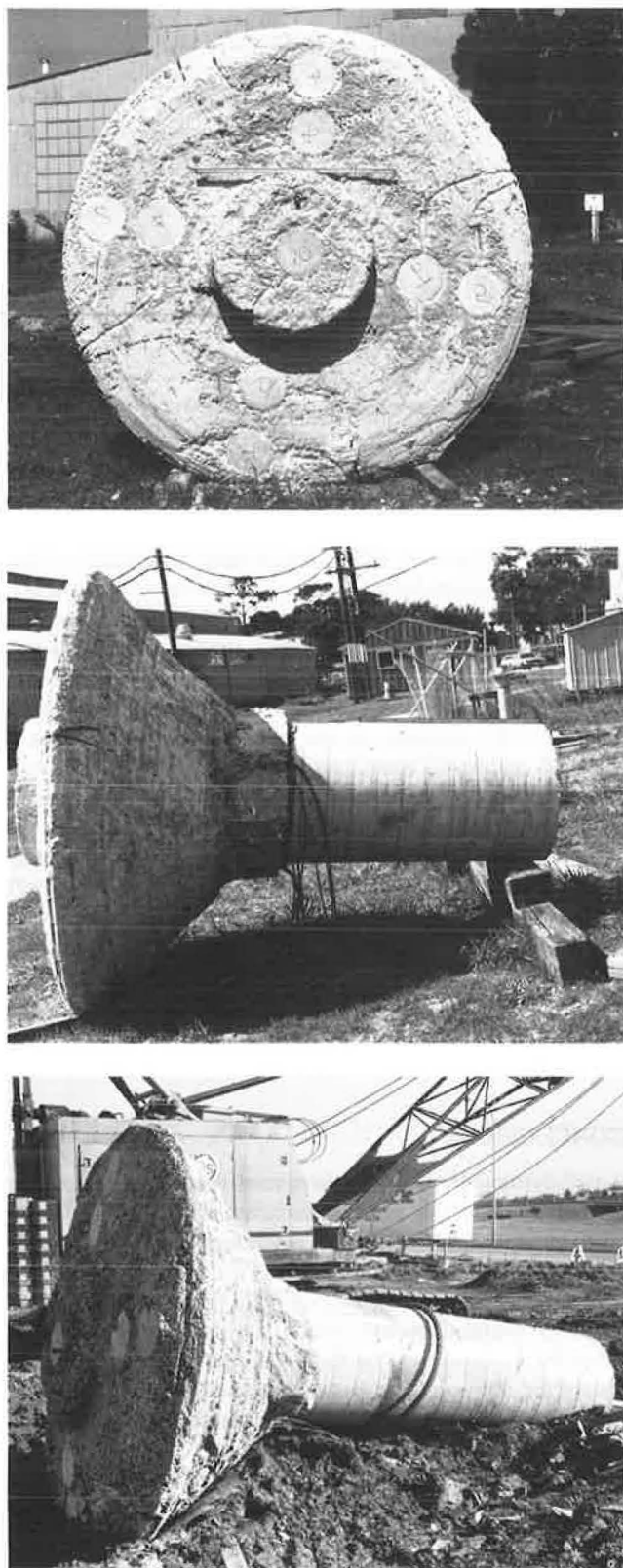


FIGURE 12 Extracted footings.

Further full-scale field tests, particularly tests conducted to structural failure, are needed to increase the confidence level in this type of foundation. However, it would appear, pending the development of new methods of evaluation of concrete tensile strength in underreams, that shallow 45-degree underreamed footings with concrete of the quality described here can be safely employed as bridge foundations at ultimate limit-state bearing pressures of the order imposed in the tests reported.

ACKNOWLEDGMENTS

The research reported here was supported in part by a grant from the International Association of Drilled Shaft contractors. The authors are grateful to Farmer Foundation Company of Houston and N. L. Schutte, Inc., of Dallas for providing drilling and concreting services and to Southwestern Laboratories, Inc., of Dallas for their technical support. The assistance of former graduate students Ketan Kapasi, David Menzies, N. Venkatesan, and Albert Wu in conducting the tests and analyses is also appreciated.

REFERENCES

1. J. S. Farr. Study of the Load Capacity of Plain Concrete Underreams. M.S. thesis. The University of Texas at Austin, 1974, 106 pp.
2. K. E. Tand and M. W. O'Neill. Prediction of Load-Settlement Response for Deep Footing. Preprint, ASCE, Tri-Sectional Meeting, Albuquerque, N.M., Oct. 1977, 22 pp.
3. L. J. Mahar and M. W. O'Neill. Geotechnical Characterization of Desiccated Clay. *Journal of Geotechnical Engineering*, ASCE, Vol. 109, Jan. 1983, pp. 56-71.
4. S. A. Sheikh, M. W. O'Neill, and N. Venkatesan. *Behavior of 45° Underreamed Footings*. Research Report UHCE 83-18. Department of Civil Engineering, University of Houston-University Park, Tex., Nov. 1983, 126 pp.
5. M. W. O'Neill and S. A. Sheikh. Geotechnical Behavior of Underreams in Pleistocene Clay. In *Drilled Piers and Caissons II* (C. B. Baker, Jr., ed.), ASCE, May 1985, pp. 57-75.
6. J. G. MacGregor, S. A. Mirza, and B. Ellingwood. Statistical Analysis of Resistance of Reinforced and Prestressed Concrete Members. *ACI Journal*, Vol. 80, No. 3, June 1983, pp. 167-176.
7. S. A. Sheikh, M. W. O'Neill, and K. J. Kapasi. *Behavior of 45° Underreamed Footing in Eagle Ford Shale*. Research Report UHCE 85-12. Department of Civil Engineering, University of Houston-University Park, Tex., Dec. 1985, 129 pp.
8. W. F. Chen and R. L. Yuan. Tensile Strength of Concrete: Double-Punch Test. *Journal of the Structural Division*, ASCE, Vol. 106, No. ST8, Aug. 1980, pp. 1673-1693.
9. *Feasibility Design Summary, Auburn Dam, Concrete Curved-Gravity Dam Alternative (CG-3)*. Water and Power Resources Service, U.S. Bureau of Reclamations, Denver, Colo., Aug. 1980.
10. J. M. Raphael. Tensile Strength of Concrete. *ACI Journal*, Vol. 81, No. 2, March-April 1984, pp. 158-165.

Publication of this paper sponsored by Committee on Foundations of Bridges and Other Structures.

An Improved California Bearing Ratio Test Procedure

COLIN A. FRANCO AND K. WAYNE LEE

The California bearing ratio (CBR) test is one of the most common strength tests conducted to evaluate subgrade quality of soils and the suitability of soils for subbase and base courses in pavements. Yet there are variations in the procedures used by various transportation agencies; this results in confusion among highway engineers. To improve the existing CBR procedures, an alternative method has been employed successfully to obtain CBR-values of soil and to evaluate the moisture susceptibility of soils. This method is not only easier to perform but also requires less effort because only four samples need be compacted and tested. There are also fewer sources of error in that obtaining the "correct" optimum moisture content for compaction is not required because the test is considered an extension of the compaction tests (i.e., AASHTO T99 and T180). This method has been used successfully on various soil types as well as on soil-cement mixtures. The possibilities of, and the potential for obtaining additional data by, this improved procedure should make it an attractive alternative option and possibly the standard method for determining CBR. Finally, it could be used as a tool in evaluating the frost susceptibility of subgrade soils and subbase and base course materials, studies of which are presently being pursued by the authors.

The California bearing ratio (CBR) test was originally developed by the California Division of Highways (1). This test has been further developed by others and is the most commonly used strength test for evaluating the subgrade quality of soils (ASTM D 1883 and AASHTO T193-81). Yet there are variations in the procedure used by various transportation agencies, which result in confusion among highway engineers. One significant observation is that the CBR test procedures prescribed by the American Society for Testing and Materials (ASTM) and the American Association of State Highway and Transportation Officials (AASHTO) are different. ASTM D 1883 allows for the preparation of specimens using a 5.5-lb rammer with a 12-in. drop and a 10-lb rammer with an 18-in. drop; only the former compactive effort is used in AASHTO T193.

Recently the Rhode Island Department of Transportation (RI DOT) and the University of Rhode Island (URI) have engaged in a cooperative effort to improve the existing CBR procedure. The objectives of the study were threefold: (a) to examine the conditions that led to the development of the CBR procedure, (b) to improve existing procedures, and (c) to study the effect of test variables.

BACKGROUND

A statewide investigation at the California Division of Highways was conducted to determine local drainage conditions and other factors that affect the stability of pavement during 1928 and 1929. The study indicated that pavement failures could be traced directly to poor compaction during construction or was brought about by insufficient thickness of pavement and by the existence of a base course over soils inherently weak in shear strength. Therefore a static field load test was first tried for establishing the density that should be used in the construction of subgrades and the shear strength that was required. However, it was practically impossible to moisten the soil properly in the field to the depth affected by the load test, and, as a consequence, the results of such tests could represent a test condition that was unrelated to the ultimate condition and did not simulate the subgrade reaction during the service life of the pavement.

The CBR test was devised in 1929 in an attempt to eliminate some of the deficiencies of field loading tests and to provide a quick method for comparing local base and subbase materials available for reinforcing the subgrade (1). In this study, samples of the material were first thoroughly consolidated to the density obtainable with good construction methods or to approximately the density of good subgrade materials ultimately produced by traffic. This procedure eliminated, to a large degree, most of the inelastic and consolidation deformation that often influences static load tests made in the field. The compacted specimen was next soaked for 4 days under a surcharge representing the weight of the pavement, which permitted the specimen to swell and absorb moisture, with consequent loss of strength. The CBR test was made on the specimen to determine the resistance to lateral displacement, thus measuring the combined influence of cohesion and internal friction. Figure 1 shows the penetration and the expansion (soaking) parts of the CBR test. The resistance to penetration in the test is expressed as a percentage of the resistance of a standard crushed stone of a CBR-value of 100 percent.

The specimen was compacted under a static pressure of 2,000 psi using a standard laboratory compression machine. The static pressure of 2,000 psi was adopted after it was found that this pressure was necessary to produce a density equivalent to that present under old highways that had been subjected to traffic for a period of years. For field control, where a compression machine was not available, an impact method of compaction using 20 blows of a 10-lb tamper with an 18-in. drop on each 1-in. layer was adopted.

Investigations in California between 1928 and 1942, on both

C. A. Franco, Construction Section, Public Works Division, Rhode Island Department of Transportation, 229 State Office Building, Providence, R.I. 02903. K. W. Lee, Department of Civil Engineering, University of Rhode Island, Kingston, R.I. 02881.

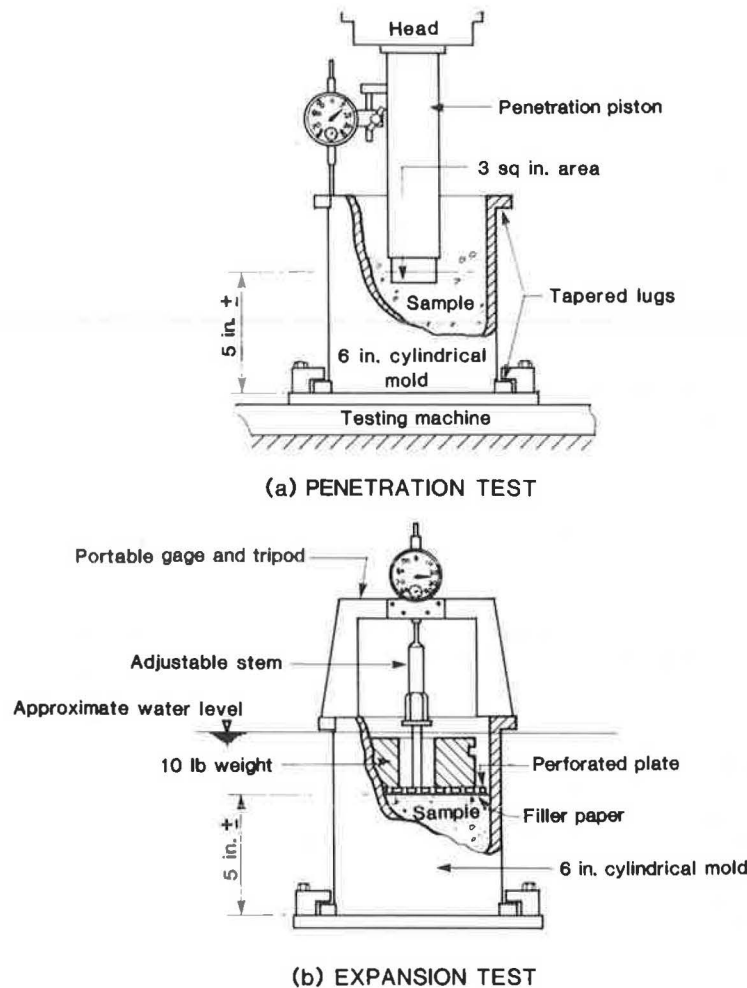


FIGURE 1 California bearing ratio test apparatus.

adequate pavements and flexible pavements that failed, furnished considerable empirical data for correlation of the CBR requirements with service behavior. From these data, curves were formulated for determining the thickness of pavement and base course required to carry traffic adequately over compacted subbase and subgrade materials (2, p. 6).

Gradually it was realized that neither the California static nor the California dynamic compaction test is desirable in the field (3). The U.S. Army Corps of Engineers (USACE) modified the AASHTO designation T99-38 for compaction control testing (4). This modification consisted of increasing the weight of the hammer from 5.5 lb to 10 lb, the height of drop from 12 in. to 18 in., and the number of layers in which the soil was placed in the mold from three to five. A comparison of compactive efforts from limited data available indicated that the density results obtained by this modification of the AASHTO compaction test closely approximated those obtained by the California dynamic compaction tests (3). The modified compaction test first appeared as a construction control in June 1942 (5) and has since become known as the modified AASHTO compaction test. However, the densities of samples prepared for the CBR test were at considerable variance with those obtained by field equipment, especially for sandy materials of low plasticity. This led to further modification so that, when penetrated, the

specimens would more nearly reflect the relative stability of the soil as compacted during construction and as later affected by moisture changes. The use of the impact method for the preparation of remolded specimens for design tests was adopted as a second modification by the USACE in September 1942.

A program for the further modification and refinement of the CBR procedure was formulated in November 1942 and conducted by the USACE (6). The laboratory investigation showed that variations in CBR test results are largely explained by the method of preparing the test specimens: mainly molding water content, density, and method of compaction. The USACE stipulated that the compaction test should be performed in a 6-in.-diameter CBR mold using 55 blows per layer, whenever the modified AASHTO method of control compaction is specified. Two methods of specimen preparation were also recommended: Method 1 for plastic soils that exhibit little or no swell when no unusual construction or weather conditions exist and Method 2 for plastic soils that exhibit little or no swell when unusual construction and weather conditions occur and for soils that are very susceptible to changes in moisture. These compaction and penetration test procedures were standardized as ASTM D 1557-58T and D 1883-61, respectively. It should be noted that specimens are prepared using only a 5.5-lb hammer dropped from a height of 12 in. in AASHTO T193.

IMPROVED CBR PROCEDURE

The new procedure was conceived by the authors who had worked in Africa and the Middle East where an expedient method that used less physical effort was required. As in the traditional method specified in ASTM D 1883 and AASHTO T193, the objective of this improved procedure is to determine the CBR value of a soil. In addition to the CBR the following information is also obtained:

- Variation of CBR with moisture content and
- Comparison of dry CBR- versus soaked CBR-values, which gives a measure of CBR moisture susceptibility.

Sample Preparation

In this method, a 30-kg sample is dried and pretreated for compaction per AASHTO T99 or T180 depending on the use that the soil is to be put to. The soil is split into four portions of approximately 6 kg each. To each portion, a definite quantity of water is added such that each of the portions of soil has a gradually increasing moisture content that ranges around the optimum moisture content. The individual portions are then compacted (the moisture content samples are taken at the beginning and end of the individual compactings; 100 g for fine-grained soils and 500 g for coarse-grained soils). The compacted soil in the mold is trimmed even with the top surface, and the specimen and mold are weighed to determine wet density and finally dry density.

Penetration Test

The CBR of a material is obtained for the dry and the soaked condition. For the dry condition, the penetration test is performed directly on one side of the specimen in the mold (i.e., either top or bottom). For the soaked condition, the soaking procedure of AASHTO T193 or ASTM D 1883 is followed. After the percent swell has been determined, the penetration test is run on the other side.

Calculations

Data obtained from the four specimens are plotted with the moisture content as the common axis or abscissa and the density as the left-side ordinate. The moisture content corresponding to the peak of the curve shall be termed the optimum moisture content (OMC). Two more curves are plotted on the same graph with the moisture content as abscissa and the dry and soaked CBR-values as right-side ordinate. The point where these curves intercept the OMC line will be the CBR-values of the soil (Figure 2).

Variables and Discussion

The original CBR procedure, which ordinarily requires at least seven specimens, provides three relationships: dry density

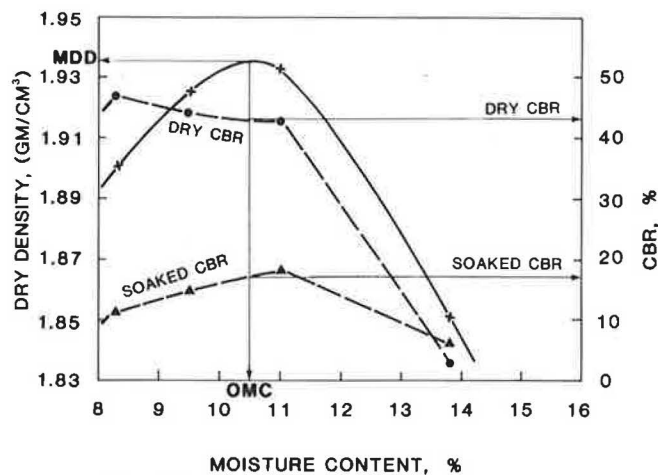


FIGURE 2 Calculation of dry and soaked CBR-values with the improved procedure (Sample 5).

versus moisture content, dry CBR versus dry density, and soaked CBR versus dry density. The suggested procedure requires only four specimens and gives three more relationships: dry CBR versus moisture content, soaked CBR versus moisture content, and dry CBR versus soaked CBR.

In the improved procedure, the moisture content of the sample is not predetermined nor is it a prerequisite that a definite value be attained. The original method requires the attainment of the OMC as a prerequisite for each of the three specimens, and this is not easy to achieve. According to Rhode Island's experience, it was found that the target OMC was off by $\pm 1/2$ to 1 percent. This may not appear to be much of a variation, but going back to the CBR curves obtained in the improved procedure it was observed that the CBR generally falls sharply with increased moisture content when the moisture content is greater than optimum (7, pp. 163–171). This could introduce an error in the CBR-values obtained. In addition, it is known that in most cases the moisture content of a soil has a considerably greater effect on the CBR-value than the maximum dry density (MDD). This suggested procedure ably demonstrated the same.

The relationship between dry CBR and soaked CBR is quite useful because it can give a quantifiable measure of CBR moisture susceptibility. The moisture susceptibility here is defined as

$$\text{CBRMS} = \frac{\text{Soaked CBR}}{\text{Dry CBR}} * 100$$

where CBRMS is California bearing ratio moisture susceptibility.

It is worth noting that the greater the percentage CBRMS, the less critical is the moisture susceptibility. This value could be used in determining the suitability of a soil as subgrade, subbase, or base in areas where excessive moisture would pose a problem. For example, it can generally be said that a sandy gravel soil would not be as susceptible as a fine-grained silty clay soil. The point here is that sandy gravels are better suited as subgrades than are silts and clays.

Table 1 gives a comparison of the "new improved method"

TABLE 1 COMPARISON OF CURRENT AASHTO T193 AND NEW METHOD

AASHTO Method (T-193)	New Improved CBR Method
1. Sample size approximately 35 kg	1. Sample size approximately 30 kg
2. Pretreat sample as for ASTM/AASHTO procedure for compaction test	2. Pretreat sample as for ASTM/AASHTO procedure for compaction test
3. Divide the pretreated soil from 2 into one portion weighing 12 kg for obtaining the compaction curve (T 99/T 180) and three portions weighing 6 kg each for CBR testing	3. Divide the pretreated soil from 2 into four portions weighing 6 kg each
4a. Perform compaction test according to standard procedure (T 99/T 180) using either four or five points	4a. Perform compaction test per T 99/T180 on the four portions to make four molded specimens (similar to 3 of AASHTO method except that the soil used in the previous compaction is not reused)
4b. Moisture determination made for each point by sampling material from the mixing bowl before and after completing compaction of the mold	4b. Moisture determination made for each point by sampling material from the mixing bowl before and after completing compaction of the mold
5. Plotting of compaction curve: compaction curve plotted from where MDD and OMC are then determined	5. Plotting of compaction curve: compaction curve plotted with dry density as ordinate and MC as abscissa from where MDD and OMC are found
6a. The three portions of soils are molded using exact amounts of mixing water (to obtain OMC-value); the three samples are compacted with different compactive efforts to obtain three different dry densities	6a. Not necessary
6b. The dry density is calculated for the three samples	6b. Not necessary
7. CBR test performed on the three specimens from 6 for dry CBR-value, soaked CBR-value, and swell test	7. CBR test performed on four specimens for dry CBR-value, soaked CBR-value, and swell test
8. Plot CBR curves for each of the three specimens for both the dry and the soaked cases and find the 0.1- and 0.2-in. CBR-values for dry and soaked specimens using curve corrections where necessary	8. Plot CBR curves for each of the four specimens for both the dry and the soaked cases and find the 0.1- and 0.2-in. CBR-values using curve correction where necessary
9. Plotting of results: plot CBR-values versus the dry density for each of the three molds for the dry and the soaked case; the CBR-values for the soil are then the CBR-values at the MDD obtained from the compaction test	9. Plotting of results: on the plot of the compaction curve (already plotted in 5) plot CBR versus an MC for each of the four molds for the dry and the soaked case; the CBR-values for the soil are then obtained by finding the intercept of the OMC ordinate with the CBR curves

with the AASHTO T193 method. It is assumed that testing is generally carried out by a team of two persons, a materials technician and an assistant. The data in Table 2 further highlight significant differences and improvements, and Table 3 is a summary of the time (or cost) saving and benefits to be had if the new procedure is used.

In addition, two observations have been made that call for further investigation:

- The CBR-values obtained by the original method are not as consistent as those obtained with the improved method and

- CBR-values at 55 blows are not always greater than those at 45 blows or less than those at 65 blows in all cases as is expected.

IMPLEMENTATION OF IMPROVED PROCEDURE

Gravel base course material from Post Road (US-1), Westerly, Rhode Island, consisting of cohesionless material (sandy gravel with silt) was tested and the results are summarized in Table 4 and Figures 2 and 3.

TABLE 2 SUMMARY OF SIGNIFICANT DIFFERENCES OR IMPROVEMENTS

AASHTO Method (T-193)	New Improved Method
1. From Steps 4 and 6 (Table 1) a total of seven compacted specimens are made in this method	1. A total of four compacted specimens are made in this method
2. Lag time is needed to calculate OMC before preparing and compacting the three specimens for CBR testing	2. Not required
3. CBR penetration test performed on three specimens for the dry and the soaked cases, respectively	3. CBR penetration test performed on four specimens for the dry and the soaked cases, respectively
4. Two plots are required for each of the cases (dry and soaked) for the three specimens	4. Two plots are required for each of the cases (dry and soaked) for the four specimens

TABLE 3 TIME STUDY COMPARISONS FOR EACH OF THE METHODS

AASHTO Method (T-193)	New Improved Method
1. Preparation of sample and compaction test (four specimens): 2 hr 30 min	1. Preparation of sample for compaction of four molds: 2 hr
2. Calculate and plot compaction curve: 30 min	2. Calculate and plot compaction curve: 30 min
3. Prepare and compact three specimens for compaction test: 2 hr	
4a. Testing CBR dry specimens at 20 min each: 1 hr	4a. Testing CBR dry specimens at 20 min each: 1 hr 20 min
4b. Testing CBR soaked specimens at 20 min each: 1 hr	4b. Testing CBR soaked specimens at 20 min each: 1 hr 20 min
5. Plotting CBR results and determining CBR for each specimen: 30 min	5. Plotting CBR results and determining CBR for each specimen: 40 min
6. Plotting CBR versus dry density curve: calculate dry density of each of three molded specimens: 20 min; plot CBR versus dry density: 10 min (total = 30 min)	6. Plotting CBR-values on compaction curve (already plotted in 2): 10 min
Total time = 8 hr	Total time = 6 hr

Testing Procedures and Assumptions

The material was sampled from the sides and median of the existing road. The majority of the samples tested belonged to the A-1-b soil group, with the remainder in the A-1-a, A-2-4, and A-3 groups. Because 15 percent of material was retained on the 3/4-in. sieve, compaction was carried out per AASHTO T180. The CBR penetration test was performed per

AASHTO T180. The CBR penetration test was also performed per AASHTO T193 to determine the dry and soaked (96 hr) CBR of the soils.

Results and Observations

Most soils from the A-1-b group indicated a relatively high MDD and lower OMC for those samples that had little fines

TABLE 4 CBR TEST RESULTS ON MATERIAL FROM POST ROAD (US-1)

Sample No.	AASHTO Soil Class	MDD (g/cm ³)	OMC (%)	MC (%)	Dry Density (g/cm ³)	Dry CBR at 0.1 in.	Dry CBR at 0.2 in.	Soaked CBR at 0.1 in.	Soaked CBR at 0.2 in.
1	A-1-b	2.059	7.8	5.0	2.038	33	44	22	30
				8.4	2.058	18	26	16	22
				9.5	2.030	12	16	18	23
				5.6	2.041	60	79	15	13
2	A-1-b	1.982	8.3	8.1	1.983	53	71	35	37
				11.5	1.906	6	8	5	7
				6.9	1.933	45	60	12	16
3	A-1-b	1.933	10.5	8.3	1.901	37	47	8	11
				11.0	1.933	32	43	13	18
				13.8	1.851	3	4	3	6
				9.5	1.926	34	44	11	15
4	A-1-b	2.050	8.5	7.1	2.015	33	41	18	26
				8.6	2.050	36	48	52	61
				10.4	1.987	17	22	43	53
5	A-1-b	2.120	6.7	4.2	2.031	33	44	17	17
				7.9	2.064	31	40	42	54
				7.2	2.115	22	29	32	44
5A	A-1-b	2.035	8.3	7.2	2.015	32	40	27	36
				8.5	2.032	37	50	28	36
				10.5	1.977	15	20	32	39
9	A-1-b	2.060	7.8	4.4	1.997	53	66	15	66
				7.8	2.056	100	111	28	38
				10.4	1.972	20	26	11	15
3A	A-2-4	1.880	11.0	7.7	1.849	47	51	12	10
				11.2	1.878	33	42	18	24
				12.9	1.867	11	14	6	8
				16.1	1.741	1	2	1	2
6	A-1-a	2.050	7.2	5.8	2.040	39	52	18	21
				12.8	1.966	38	52	46	82
				7.9	2.044	18	25	40	46
8	A-3	1.862	10.0	7.5	1.814	33	42	8	8
				9.9	1.862	33	44	14	19
				13.4	1.788	5	7	6	7

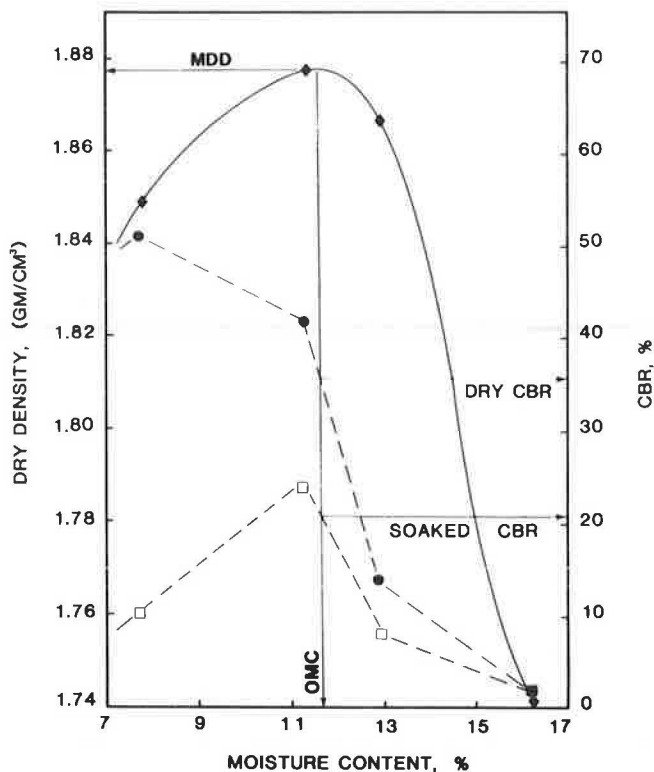


FIGURE 3 Calculation of dry and soaked CBR-values with the improved procedure (Sample 3A).

(i.e., the amount passing the No. 200 sieve is less than 10 percent and that passing the No. 40 sieve is less than 35 percent). It appears that there should be further research efforts to study the effect of the amount passing the No. 200 sieve versus CBR.

Another unusual observation was that, in all cases, the 0.1-in. CBR-value was less than the 0.2-in. value. It was observed that the higher the MDD of the soils the lower was the OMC. This lower OMC contributed to the higher CBR-values of the soil. It is also apparent that the greater the amount of fines the higher the OMC and subsequently the lower the CBR.

The new improved method had been initially implemented by the author with lateritic soils (A-2-6 or A-2-7) in the tropical areas of Africa. The method was routinely used to evaluate (a) the CBR of subgrade soils in earth cuts for pavement design and the suitability of materials for subgrades and (b) the CBR of materials from prospective borrow pits for use as subbase and base course material. From the hundreds of CBR test results obtained, it has been observed that the CBR curves for the lateritic soils have shapes that are similar to those of the curves for the soils in Rhode Island; notably,

- The dry CBR curve has higher values and peaks to the left of the OMC point and
- The soaked CBR curve follows a similar pattern as shown in the Figures 2-4.

As a broad generalization, it may be said that the CBR-values of soils are relatively higher when the MC is less than optimum. For the case in which the compaction of a subbase or base course is specified to be 95 percent minimum, it will be observed from Figure 4 that the strength of the layer varies

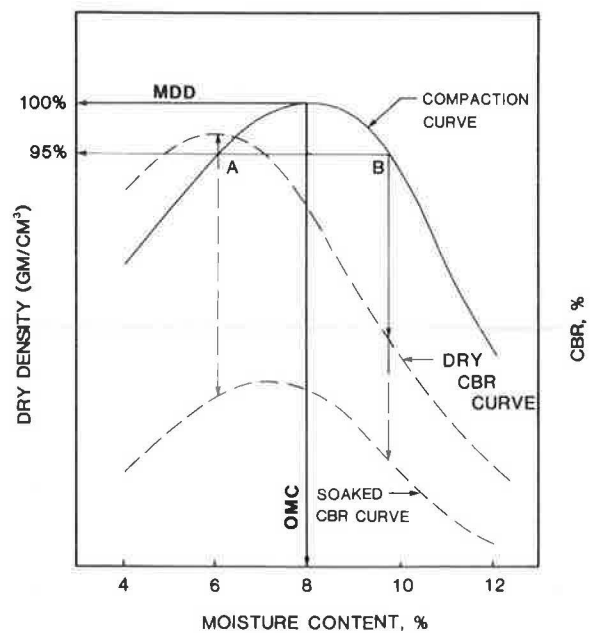


FIGURE 4 Typical curve shape for the new improved CBR procedure.

substantially from Point A to Point B. If a moisture specification is included (generally OMC \pm 2 percent), it will again be seen that the CBR-value on the dry side (less than optimum moisture) will be greater than that on the wet side (greater than optimum). This could have a significant impact on the performance of a soil as a subbase or base course.

Finally, it should be noted that if the specimen is prepared in either too dry condition (low moisture content) or two specimens are not prepared with moisture contents greater than the OMC, then the shape of the curve may not be as shown in Figure 4. Because most materials engineers and technicians have a relatively good feel for "guestimating" the OMC, the foregoing should not be a major obstacle in implementing the new procedure.

CONCLUSIONS

This alternative method has been employed successfully to obtain CBR-values of soil and to evaluate the moisture susceptibility of soils. This method is not only easier to perform but also requires less effort because only four samples need be compacted and tested. There are also fewer sources of error because obtaining the "correct" optimum moisture content for compaction is not required (the test is considered an "extension" of the AASHTO T99 and T180 compaction tests). This method also has been used successfully on soil-cement mixtures.

The possibilities of, and potential for obtaining additional data by, this alternative method should make it an attractive option and possibly the standard method for determining CBR. Currently, RI DOT and URI are conducting experiments in a CBR versus freeze-thaw study, which it is hoped will shed some light on the influence of temperature on frost susceptibility of various pavement subgrade, subbase, and base materials.

ACKNOWLEDGMENTS

The authors wish to thank William Carcieri, Chief Engineer, RI DOT, for his encouragement and the materials section at RI DOT for their help in performing required tests. Special appreciation is extended to William D. Kovacs for his suggestions in preparing this manuscript. Finally, the authors would like to express their thanks to the Department of Civil Engineering, University of Rhode Island, which provided the typing and drafting support required for this paper.

REFERENCES

1. O. J. Porter. Development of the Original Method for Highway Design. *Transactions, ASCE*, Vol. 115, 1950, pp. 461-467.
2. F. J. Grumm. *Designing Foundation Courses for Highway Pavements and Surfaces*. California Highways and Public Works, Sacramento, March 1942.
3. W. H. Jervis and J. B. Eustis. Accepted Procedure for the CBR Test. *Transactions, ASCE*, Vol. 115, 1950, pp. 472-484.
4. *Standard Specifications for Highway Materials*. AASHTO, Washington, D.C., 1947, Test T99-38.
5. Airfield Pavement Design. In *Engineering Manual for War Department Construction*. Office of Chief of Engineers, U.S. Army, Washington, D.C., June 1942, Part II, Chapter XX.
6. *The California Bearing Ratio Test as Applied to the Design of Flexible Pavements for Airports*. Technical Memorandum 213-1. U.S. Waterways Experiment Station, Vicksburg, Miss., July 1945.
7. *Soil Mechanics for Road Engineers*. Road Research Laboratory, London, United Kingdom, 1954.

Publication of this paper sponsored by Committee on Exploration and Classification of Earth Materials.

Lateral Response and Earth Pressure Parameters of Cohesionless Soils Related to Flat Dilatometer Data: A Laboratory Study

E. SABRI MOTAN AND BRIAN J. JACOT

In situ evaluation of soil parameters in the lateral direction such as the at-rest lateral earth pressure coefficient, lateral subgrade coefficient, and lateral soil modulus is required for a variety of soil-structure interaction analyses. A practical device to estimate these parameters is the flat dilatometer. The flat dilatometer requires, however, as do most other in situ penetrometer-type devices, calibration under simulated in situ conditions for possible extrapolation of the results to undisturbed soil conditions. A series of laboratory experiments was conducted to investigate the effects of dilatometer penetration on the soil parameters estimated from the dilatometer data in sands. With regard to the at-rest lateral earth pressure coefficient, the results indicated that the relation between the in situ earth pressure and the lateral earth pressure measured after dilatometer penetration is a function of particle shape characteristics as well as relative density and vertical overburden pressure. The lateral subgrade coefficient and the lateral soil modulus were found to be reasonably linear functions of the corresponding soil parameters determined from the dilatometer data, namely the dilatometer subgrade reaction coefficient and the dilatometer modulus. The range of uncertainty, however, was found to increase with the angularity of the particles in soil. Both particle shape and relative density become controlling factors for the slope and the linearity of these relationships in soils composed of angular particles.

As a result of the rapidly increasing data base during recent years for a variety of in situ test devices involving a wide range of soil types and conditions, and improvements in the design of these devices, there is a growing confidence among geotechnical engineers in predicting soil properties by in situ test methods.

The flat dilatometer is capable of yielding data that can be related to various geotechnical parameters by means of a series of empirical correlations. Field data are obtained by penetrating a rectangular flat blade tapered at the tip into the soil and expanding a vertically mounted steel diaphragm on the blade against the soil. The diaphragm is expanded by introducing gas under pressure into the chamber behind it. Two readings are taken: (a) the pressure to start the outward movement of the

diaphragm (p_0), as determined by the silencing of a continuous beeper tone on the control unit, and (b) the pressure necessary to displace the diaphragm center toward the soil by one millimeter (p_1) as determined by reactivation of the beeper tone. Previous applications of the flat dilatometer include the profiling of subsurface soils in a nearly continuous manner and the estimation of a number of soil parameters such as the at-rest lateral earth pressure coefficient, the overconsolidation ratio, the coefficient of volume compressibility, and the liquefaction susceptibility of saturated fine sands. The flat dilatometer also promises to be a useful tool for assessing soil response against lateral loading for soil-structure interaction analyses.

The study described herein was conducted to relate the at-rest lateral earth pressure coefficient, the lateral subgrade coefficient, and the lateral soil modulus for sands of different grain shape characteristics to the dilatometer data obtained during a penetration test. The scope of work of this study is wider than that of a similar study reported elsewhere (1) in terms of materials used and improvements made to the laboratory and to the test methodology.

LABORATORY STUDY

The experimental work was conducted in a steel bin under controlled relative density and simulated overburden pressure using three sands of different particle shape characteristics and somewhat different grain size distributions. The grain size distribution in all three sands can, however, be characterized as uniform. Figure 1 shows an overall view of the laboratory setup. The improvements made to the original equipment described elsewhere (1) include the enlargement of the pressure plate to distribute the load over the entire surface area of the specimen and the insertion of a "face" plate to improve the initial lateral stress conditions. The at-rest pressure and the at-rest condition dilatometer modulus were obtained by using a dilatometer diaphragm mounted on a rectangular aluminum block as shown in Figure 1.

To obtain the pressure-diaphragm deflection curve in a continuous form, a leaf-type cantilever beam deflection sensor, instrumented with a half-bridge strain gauge arrangement, was used behind the diaphragm. A steel pipe section was attached to the back of the aluminum block and was extended out through a hole on the short side of the bin and the face plate. To

E. S. Motan, Department of Civil Engineering and Construction, Bradley University, Peoria, Ill. 61606. B. J. Jacot, Fred C. Hart Associates, 294 Washington Avenue Extension, Albany, N.Y. 12203.

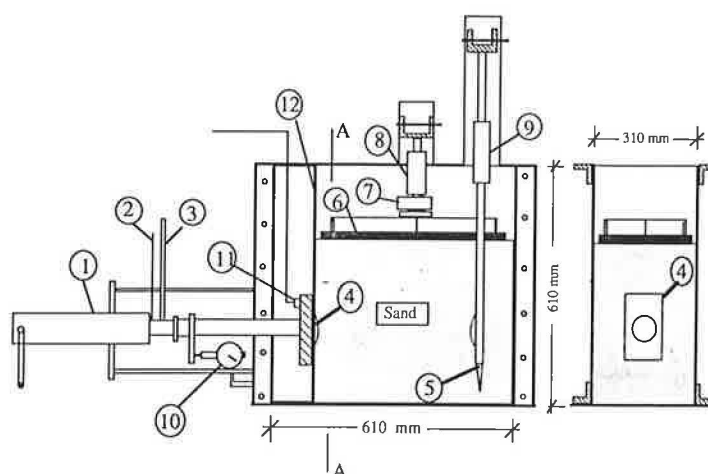


FIGURE 1 Experimental setup for penetration testing: 1. trailer jack, 2. deflection sensor leads, 3. pressurized nitrogen line, 4. aluminum block, 5. flat dilatometer, 6. pressure plate, 7. load cell, 8. and 9. hydraulic jacks, 10. dial gauge, 11. pressure transducer, 12. aluminum rectangular block.

simulate the lateral separation of the soil during dilatometer penetration, the aluminum block was laterally forced into the soil using a trailer jack mounted rigidly on a steel frame that, in turn, was welded to the short side of the bin. Overburden pressure was simulated by applying a vertical force through a hydraulic jack on a rigid steel plate placed on the surface of the soil specimen. The vertical force was measured by a load cell mounted between the steel plate and the hydraulic jack. During the tests, a standard dilatometer blade was also penetrated into the sand to the same depth as the aluminum block.

As indicated earlier, the scope of this study covered three sands with different particle shape characteristics from extremely angular (mine tailings) to subrounded (Ottawa sand), with a local dune sand included to represent the intermediate particle shape properties. The degree of angularity of Ottawa, dune, and mine tailings sand particles was determined as 100 to 199, 400 to 499, and 1000 to 1099, respectively, according to the Krumbein charts (2) on visual examination of the particles under a microscope. Before penetration testing, the sand specimens were deposited by pluviation through a funnel and were subsequently compacted by lateral tamping to nominal relative densities of 15, 30, and 45 percent. Actual relative density was determined in each test by measuring the height of the sand after the application of the overburden pressure. At each nominal density, tests were performed under simulated overburden pressures of 12.5, 25, 50, and 100 kPa. With the block, complete pressure-deflection curves between 0- and 1-mm deflection of the diaphragm center were taken twice; the first time while the block was flush with the face plate, the second time after the block was advanced laterally 7 mm into the soil. This information was supplemented with intermediate p_0 readings taken while the block was advanced 2 and 4 mm into the soil. With the regular flat dilatometer, p_0 and p_1 readings were taken after penetration.

A total of 36 tests were performed, four at each nominal test relative density for each sand. In addition, direct shear tests were conducted to determine the range of internal friction angle for the sands used.

PRESENTATION AND DISCUSSION OF RESULTS

The discussion in this section pertains to relating the dilatometer test data to various parameters of significance from the engineering design point of view such as

- At-rest lateral earth pressure coefficient (K_0),
- Horizontal subgrade reaction coefficient (k_h), and
- Soil modulus (E_s) for lateral loading.

Lateral Earth Pressure Coefficient (K_0)

The lateral earth pressure coefficient was calculated from the test data as the ratio of p_0 obtained with the block for the at-rest condition (block flush with the face plate) to the overburden pressure applied. Average values of K_0 for Ottawa, dune, and mine tailings sands were determined as 0.58, 0.51, and 0.35, respectively. The set of K_0 -values (0.45, 0.44, and 0.36) was obtained for the same sands using the angle of friction determined from direct shear tests and the approximate formula $K_0 = 1 - \sin \phi$ (3).

The literature contains two correlations between dilatometer test data and K_0 ; the first was developed by Marchetti (4), and the second by Schmertmann (5) based on chamber test data. The Marchetti correlation was developed as a result of a series of in situ tests on uncemented clays. The Schmertmann correlation applies specifically to normally and overly consolidated sands. In both cases, the test data were related to K_0 through a calculated parameter (K_D), the "horizontal stress index." K_D is defined as the ratio of ($p_0 - u_0$) to the vertical effective stress. In dry sand, u_0 will naturally be zero. The major difference between these correlations is that Marchetti's empirical formula, $K_0 = (K_D/1.5)^{4.7} - 0.6$, shows that K_0 will increase as K_D increases whereas Schmertmann's correlation indicates that K_0 actually decreases as K_D increases substantially with friction angle.

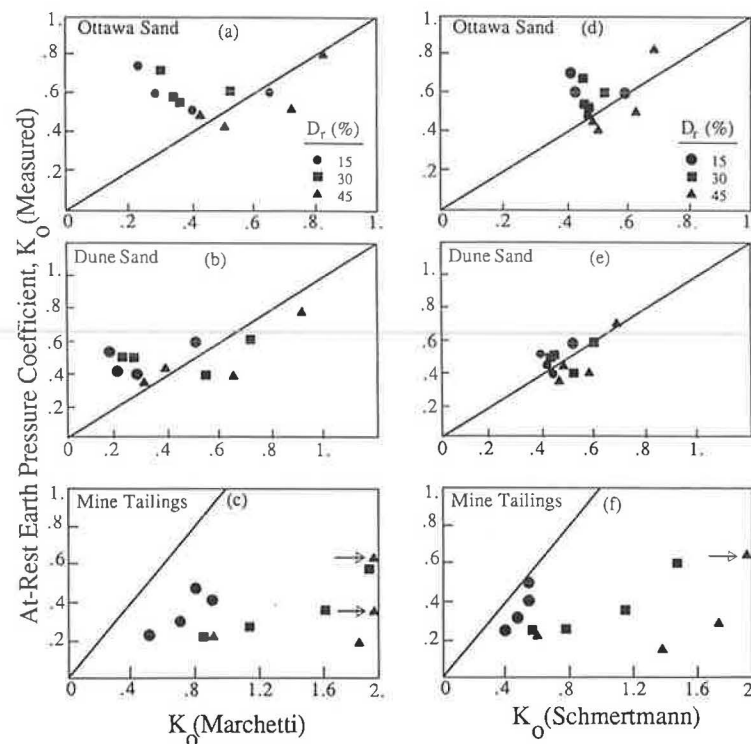


FIGURE 2 Comparison of measured at-rest lateral earth pressure coefficient values with those obtained from Marchetti's formula and Schmertmann's procedure.

Schmertmann recommends the use of his procedure for predicting K_0 in soils with a material index (I_D) greater than 1.2, where $I_D = (p_1 - p_0)/p_0$ for dry sand. The range of material index values in this study varied between 1.43 and 3.94 for Ottawa sand, 2.31 and 4.60 for dune sand, and 1.72 and 3.35 for the mine tailings sand.

As can be seen in Figures 2a–2f, when Schmertmann's correlation is applied the scatter around the equal K_0 lines, clearly visible for the Marchetti correlation, is significantly reduced. The vertical axis in the figures represents the K_0 -values determined from the lateral pressure measurements using the aluminum block. For mine tailings, however, both techniques predict substantially higher K_0 -values than those experimentally determined, although Schmertmann's method definitely proves to be an improvement in this case also.

Figures 3a–3c present the plots of K_0 versus K_D for all three sands tested. The curves for Ottawa and dune sands clearly indicate an initially decreasing K_0 versus K_D followed by a reversal in the trend. This is seen to be the case for all three test relative densities. Behavior of this type is believed to be the result of the volume change tendency of the soil being modified in response to the increasing overburden pressure.

The initial part of the curves (decreasing K_0 with K_D) is the result of a tendency toward volumetric decrease, under high overburden pressures, when shear is effected by the penetrating dilatometer blade. Under these conditions, even though a substantial portion of the vertical pressure is transferred in the horizontal direction (large K_0), penetrating the dilatometer blade will cause shear, accompanied by volume decrease in the immediate vicinity of the blade, that results in relatively small p_0 and K_D . On the other side of the minimum point the volume

change tendency reverts from contractive to dilative under small pressures. In this region K_0 and K_D vary in the same direction.

A somewhat different relationship (Figure 3c) represents the mine tailings sand test data. For the same overburden pressure, at-rest p_0 -readings from the block were significantly lower than

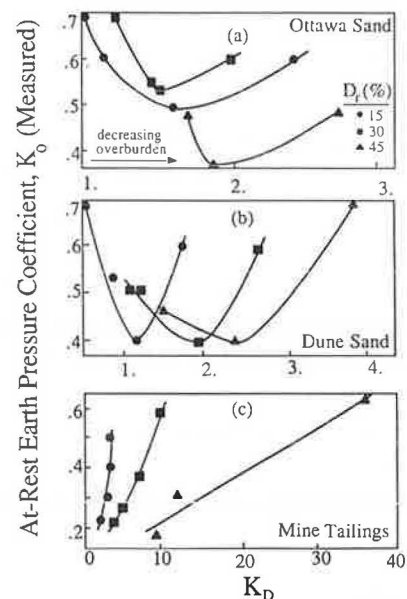


FIGURE 3 Measured at-rest lateral earth pressure coefficient as a function of the horizontal stress index (K_D).

p_0 -values measured with the other sands, whereas the p_0 -readings from the regular dilatometer blade were significantly higher. Here the volume change tendency is apparently dilative regardless of overburden pressure. The effect of relative density, however, is much more pronounced in mine tailings sand than in the other two sands tested.

The preceding discussion indicates that a generalized relationship between K_0 and k_D should involve terms to account for the effects of relative density, particle shape characteristics, and overburden pressure. The authors recognize that an effort to derive such a relationship requires a substantially larger sized study than the one presented herein. At first sight, it appears to be somewhat out of the ordinary to include overburden pressure, which is not a physical parameter of soil, in such a relationship. The modifying effects, however, of overburden pressure on the volume change behavior of soil in response to blade penetration, and ultimately on the estimated value of K_0 , cannot be overlooked.

Coefficient of Horizontal Subgrade Reaction (k_h)

Analysis of soil response in problems involving loading of soil in the lateral direction, such as laterally loaded vertical piles, is usually performed using the coefficient of horizontal subgrade reaction (k_h). This is a parameter based on an artificial concept of modeling soil behavior by a bed of equally spaced and compressible springs, each one independent of the others (6). However, given the usual complexity of the soil-structure interaction problems, its use may often be necessary.

Although the present design of the flat dilatometer does not allow for obtaining k_h directly, the dilatometer data can provide

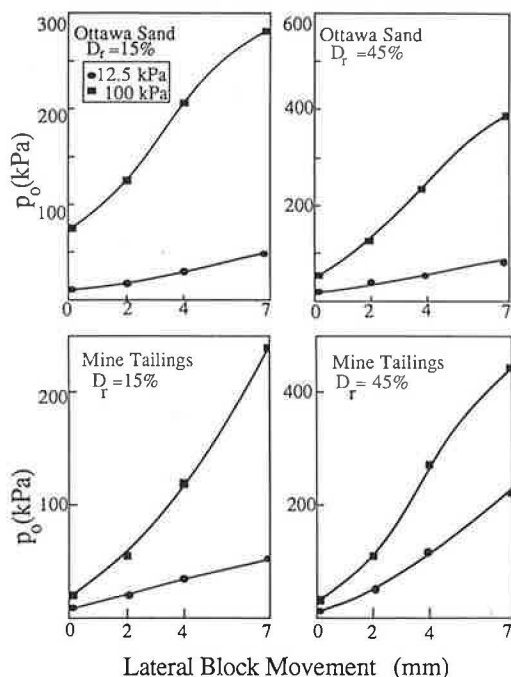


FIGURE 4 Typical p_0 versus lateral block movement curves for Ottawa and mine tailings sands.

for the estimation of k_h . The response of the undisturbed soil to lateral separation can be qualitatively observed in Figure 4. These responses were obtained by laterally advancing the block into the soils tested inside the test bin. For Ottawa sand, linear approximation of lateral pressure buildup with increasing separation is reasonable over the range of test relative densities and vertical pressures. The same is true of mine tailings at low relative density and vertical pressure. However, for mine tailings, as the vertical pressure is increased at small relative densities, the p_0 versus lateral block movement relationship tends to show nonlinearity, which is due to densification of sand as a result of the lateral movement of the block. At higher relative densities, this effect is substantially reduced. Instead, continued lateral separation appears to initiate yielding in the soil. The same trend is also noticeable in Ottawa sand to a certain extent at all test relative densities and vertical pressures.

Figures 5a–5c show the block subgrade reaction coefficient (k_{hb}) versus the dilatometer subgrade reaction coefficient (k_{hd}) for the three sands. The k_{hb} -values used to plot the figures were obtained by taking the difference between p_0 for at-rest and 7-mm lateral block movement conditions and dividing it by

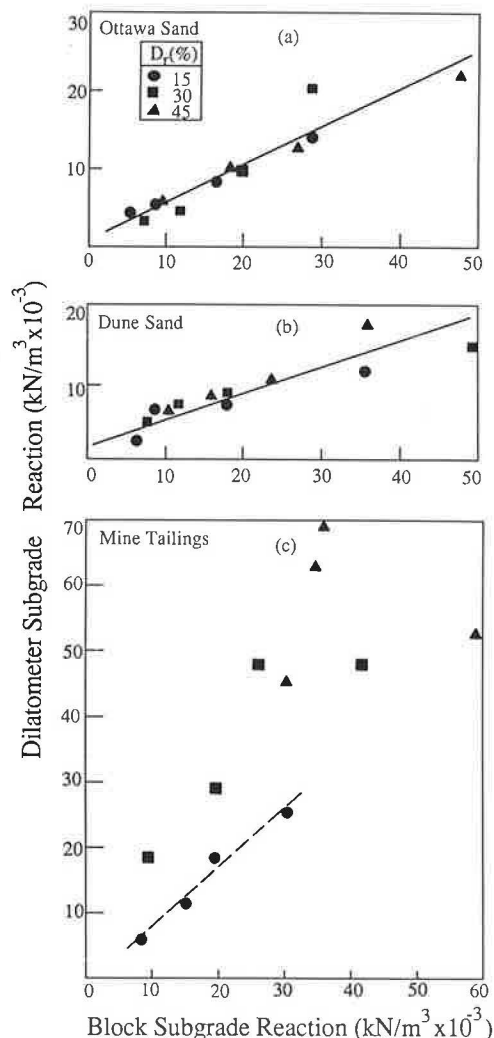


FIGURE 5 Dilatometer versus block subgrade reaction relations for the sands tested.

7 mm, which is half the dilatometer blade thickness. Because no data on the at-rest pressure are readily available in the field, as a first approximation, the k_{hd} -values were obtained by simply dividing p_0 by the separation distance (7 mm) to reflect this condition. Schmertmann (7) suggests an approximation to relate the subgrade reaction coefficient obtained with a standard dilatometer to the subgrade reaction coefficient adjusted to the pile width for lateral response analyses of piles.

Because of the soil disturbance resulting from the penetration of the blade, the k_{hd} -values obtained from the standard dilatometer data were significantly different from those obtained with the block. As can be seen in Figure 5, the plot of subgrade reaction values obtained with the dilatometer and the block indicates approximately a straight line relationship for Ottawa and dune sands with little dependence on relative density. In the case of mine tailings, the data plot approximately as a straight line at low relative densities. However, with increasing relative density, the straight line approximation is no longer valid.

The slope of the lines in Figure 5 has been termed the "disturbance index" (1) and represents the correction factor by which the standard dilatometer k_{hd} -value should be divided to obtain the disturbance-free k_h (obtained by the aluminum block). This value was found to be approximately 0.48 for Ottawa sand, 0.28 for dune sand, and 1.0 for mine tailings at low relative densities. The coefficient of correlation obtained from linear curve-fitting was 0.95 and 0.91 for Ottawa and dune sands, respectively. In mine tailings, at higher relative densities, the k_{hd} -value obtained from the dilatometer may actually need to be reduced to represent the disturbance-free k_h .

In addition to linear regression, despite a limited amount of data, a two-parameter statistical formulation in the form of

$$k_h = a \cdot \sigma_v^b \cdot D_r^c \quad (1)$$

or

$$\log k_h = \log a + b \cdot \log \sigma_v + c \cdot \log D_r \quad (2)$$

where

- k_h = horizontal subgrade reaction coefficient (obtained with the block),
- a, b, c = coefficients,
- σ_v = effective overburden pressure, and
- D_r = relative density

was attempted to relate k_h for undisturbed in situ conditions to the test variables. It was assumed in the selection of the relationship that the effects of the variables involved were multiplicative rather than additive. The following table gives the coefficients a , b , and c and the correlation coefficient for the three logs. The correlation coefficient was calculated using the logarithmic form in Equation 2.

Soil Type	a	b	c	Correlation Coefficient
Ottawa sand	4609	0.620	0.780	0.994
Dune sand	2467	0.705	0.478	0.974
Mine tailings	13754	0.423	0.637	0.918

The formulation requires that the vertical pressure and the relative density be known, so that k_h can be estimated. Because it may not always be possible to estimate these parameters reliably in the field, the significance of the statistical relation assumed and the coefficients determined does not go much further than simply indicating the relative importance of each parameter included.

The overconsolidation ratio is estimated to be another contributing factor in the type of formulation described. Because of the nature of the specimen preparation used in this study, however, it was not possible to assess the overconsolidation ratio accurately enough for inclusion in the analysis.

The empirical formula introduced (Equation 2) was used once again in the same form but this time to extract the in situ lateral stress from the standard dilatometer measurements of p_0 . The dependent variable chosen on the left side was $p_0/(p_0 - \sigma_h)$, where σ_h is the lateral in situ effective stress. The a , b , and c coefficients determined (following table) yield reasonably good estimates for Ottawa and dune sands within the bounds of the experimental data obtained. In mine tailings sand, however, despite a relatively high correlation coefficient, for certain combinations of overburden pressure and relative density the formula predicts negative lateral stress due to the small magnitude of σ_h in comparison with p_0 (coupled with statistical uncertainty in the data).

Soil Type	a	b	c	Correlation Coefficient
Ottawa sand	0.361	0.254	-0.490	0.670
Dune sand	0.386	0.254	-0.397	0.867
Mine tailings	0.889	0.019	-0.080	0.864

Dilatometer Modulus and Lateral Soil Modulus

A second approach to predicting soil response under lateral loading in soil-structure interaction problems is to use analytical models to represent the structure and the surrounding soil and solve the interaction equations (8). This method requires knowledge of the soil modulus as well as of the structural rigidity. The following discussion centers on relating the lateral soil modulus to the dilatometer modulus measured in the field. Marchetti (4), assuming linear elasticity, defined a "dilatometer modulus" (E_D) that can be calculated with the data obtained during the expansion of the diaphragm against the soil as

$$E = \frac{E_s}{1 - \mu^2} = \frac{2D \cdot \Delta p}{\pi \cdot s} \quad (3)$$

where

- E_s = soil "elastic" modulus,
- μ = Poisson's ratio of soil,
- D = diaphragm diameter,
- s = deflection of diaphragm center, and
- Δp = difference between p_1 and p_0 .

During the testing program the dilatometer modulus was obtained three times for each test:

1. With the block for at-rest condition,
2. With the block after 7-mm lateral movement, and
3. With a standard dilatometer.

The values obtained in 1 and 3 yielded the relationships that relate the in situ undisturbed lateral soil modulus to the dilatometer modulus, whereas comparison of the data obtained in 2 and 3 indicated the extent of soil disturbance after penetration of the blade and the resulting vertical shear deformations in soil in the immediate vicinity of the blade in addition to a total of 14-mm lateral separation of the soil.

Given the generally nonlinear stress-strain response of soils, the modulus values obtained in 1, 2, and 3 are actually secant moduli within 0- to 1-mm deflection range of the diaphragm center. At all three relative densities in all three sands, however, no significant nonlinearity was observed on the pressure-deflection curves taken before the lateral movement of the block. This indicates that if the diaphragm inflation were to be started at at-rest conditions, the deflection range of the diaphragm would be too small to detect the nonlinearity in the pressure-deflection curve that would surely occur at larger deflections. In light of the fairly linear p_0 versus the lateral block movement curves presented in the preceding section, it is evident that an essentially linear soil response against lateral separation continues to be the case at substantially larger strains than the diaphragm can impose on the soil when expanded.

Apparently increased stiffness of the soil for small deflections of the diaphragm was obtained after advancing the block 7 mm laterally (Figure 6). This is thought to be the result of the significant soil strains being largely confined to the volume immediately adjacent to the blade stiffened by densification on lateral movement of the block. At larger diaphragm displacements, with increasing volumes of soil affected by the strains due to diaphragm expansion, the response assumes essentially a linear form with substantially reduced slope. Reducing the chamber pressure results in a much steeper return curve, with most of the diaphragm center deflection being nonrecoverable, that indicates that a second loading cycle will result in a substantially increased soil modulus. Continuous recording of

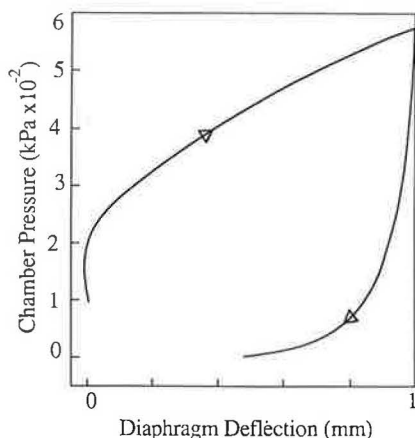


FIGURE 6 Typical chamber pressure versus diaphragm deflection curve taken with the block after 7 mm of lateral movement of the block.

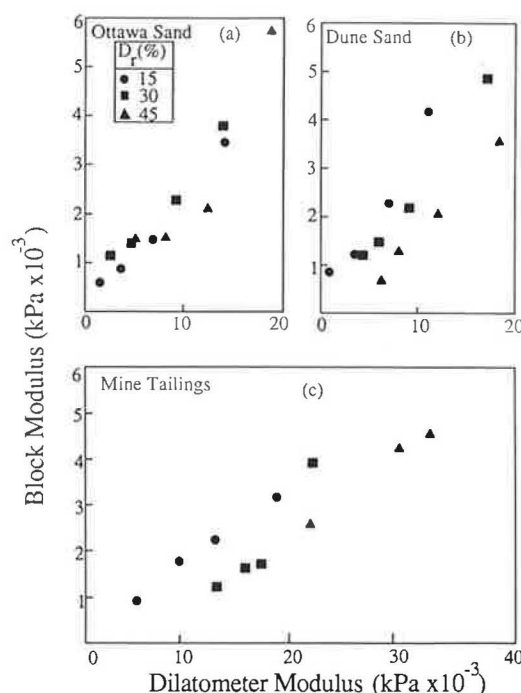


FIGURE 7 Block versus flat dilatometer modulus relations for the sands tested.

the pressure-diaphragm deflection curve during a dilatometer test therefore appears to be of advantage when the soil response under repeated pressurizing of the diaphragm is of interest.

The soil stiffness for small-strain lateral response analyses can be obtained from a relationship between the dilatometer modulus and the at-rest condition lateral soil modulus. A reasonable estimate of the Poisson's ratio, however, is required if the actual value of the soil modulus is sought. The relationships between the moduli obtained in this study are shown in Figure 7. The scatter in data for Ottawa and dune sands leaves uncertainty about the type of the relationship, although particularly in Ottawa sand some nonlinearity is evident. The slope of the curves appears to be dependent on the sand type; higher values for the dilatometer modulus result for mine tailings for the same at-rest lateral soil modulus whereas the results from Ottawa and dune sands are comparable. Correlation coefficients determined with the straight-line assumption were 0.93, 0.81, and 0.93 for Ottawa, dune, and mine tailings sands, respectively. Such relationships can be used effectively in estimating the soil modulus for interaction analyses that require the relative stiffness of the surrounding soil compared with that of the structure.

The statistical regression formula in Equation 2 was also used here to determine the coefficients a , b , and c . The formula relates the at-rest condition lateral soil modulus to the overburden pressure and the relative density. The results are given in the following table.

Soil Type	a	b	c	Correlation Coefficient
Ottawa sand	2740	0.612	1.01	0.989
Dune sand	96	0.766	-0.146	0.962
Mine tailings	1675	0.356	0.609	0.809

CONCLUSIONS

The following conclusions, based on the test results reported in this study, can be drawn:

- In estimating K_0 , Schmertmann's technique, which accounts for the friction angle of the sand, gives superior results compared with the original empirical correlation proposed by Marchetti. Both techniques appear to work better with normally consolidated sands.
- For subrounded to subangular sands, the relationship between the at-rest lateral earth pressure coefficient (K_0) and the horizontal stress index (K_D) appears to be a function of overburden pressure as well as test relative density. This means that the depth of penetration testing should also be considered a factor in evaluating dilatometer data for the in situ lateral earth pressure coefficient. Establishing the exact nature of the relationship for such soils, however, requires extensive experimental and analytical effort.
- For sands largely composed of subrounded to subangular particles, the disturbance index appears to be independent of in situ relative density and overburden pressure. The implication is that the in situ dilatometer test results for such sands can be used to obtain the disturbance-free lateral subgrade reaction coefficient with relatively high accuracy. In sands with angular particles, however, the relation between the dilatometer subgrade reaction coefficient and the disturbance-free lateral subgrade reaction coefficient is influenced by relative density and overburden pressure. Further research is needed to define the disturbance index more accurately over a broad range of soil, density, and in situ stress conditions.
- The relationship between the dilatometer modulus and the at-rest condition soil modulus (block modulus) appears to be approximately linear for sands composed of very angular particles. For sands with subrounded to subangular particles, some nonlinearity is evident. A relationship of this type should be useful in estimating the soil modulus directly from the dilatometer data for soil-structure response analyses.

REFERENCES

1. E. S. Motan and M. A. Gabr. A Flat-Dilatometer Study of Lateral Soil Response. *Analysis and Design of Pile Foundations: Proceedings of a Symposium on Deep Foundations*, ASCE National Convention, San Francisco, 1984, pp. 232–248.
2. W. C. Krumbein. Measurement and Geological Significance of Shape and Roundness of Sedimentary Particles. *Sedimentary Petrography*, Vol. 11, No. 2, 1941, pp. 64–72.
3. J. Jaky. Earth Pressure in Silos. *Proc., Second International Conference on Soil Mechanics and Foundation Engineering*, Rotterdam, The Netherlands, Vol. 1, 1948, pp. 103–107.
4. S. Marchetti. In-Situ Tests by Flat Dilatometer. *Journal of the Geotechnical Division*, ASCE Vol. 106, No. GT3, 1980, pp. 299–321.
5. J. H. Schmertmann, ed. *DMT Digest No. 1*. GPE, Inc., Gainesville, Fla., 1983.
6. K. Terzaghi. Evaluation of Coefficient of Subgrade Reaction. *Geotechnique*, Vol. 5, No. 4, 1955, pp. 297–326.
7. J. H. Schmertmann, ed. *DMT Digest No. 4*. GPE, Inc., Gainesville, Fla., 1984.
8. H. G. Poulos and E. H. Davis. *Pile Foundation Analysis and Design*. John Wiley and Sons, New York, 1980.

Publication of this paper sponsored by Committee on Exploration and Classification of Earth Materials.

Compaction Prestress

S. O. NWABUOKEI AND C. W. LOVELL

The compressibility and shear strength characteristics of compacted soils, for both short- and long-term periods, are dependent on, among other factors, the as-compacted prestress and saturated prestress induced in the soil. Their presence is manifested in the consolidation and undrained shear test results available in the literature. Consequently, for an accurate interpretation of these test results, a knowledge of the induced compaction prestresses is essential. A procedure for the prediction of as-compacted prestress based on the precompaction soil conditions and the relevant compaction independent variables is presented. The procedure is based on general soil behavior using results from simple laboratory tests. The calculated values of the as-compacted prestress were compared with experimentally determined as-compacted prestresses, and a good correspondence was obtained. Using statistical regression techniques, prediction equations were derived for the experimentally determined as-compacted prestress, volumetric strain due to saturation, and saturated prestress. The volumetric strain and saturated prestress show a strong dependence on the values of as-compacted prestress. Thus, with a better understanding of the compaction prestresses, which can be controlled through compaction specifications, fills and embankments can be constructed with more predictable compressibility and shear strength behavior.

Excavation, transportation, dumping, and spreading in the field (or degradation in the laboratory) before compaction substantially obscure the geologic preconsolidation stress. Compaction causes densification by reduction of air voids caused by a change in the relative positions of the soil aggregates or grains, or both. This induces a compactive prestress in the soil, which, though analogous to preconsolidation stress, represents the fraction of the compaction energy/pressure that is effectively transmitted to the soil matrix by plastic deformation. The ensuing amount of plastic deformation depends on the duration of application of the compaction energy/pressure and the constraint posed by the induced pore fluid (water and air) pressures.

For an engineer to quantitatively predict and control the compressibility and shear strength characteristics of a compacted fill for both short- and long-term periods, an explicit knowledge of the magnitude of the as-compacted and saturated prestresses is essential.

The as-compacted prestress in a fill is influenced by compaction water content, compaction energy/pressure, and mode of compaction. Its value decreases with water content for a given compaction energy/pressure. Also, for a given water content, particularly on the dry side of optimum moisture content, the as-compacted prestress increases with compaction energy/pressure. Load levels greater than the as-compacted prestress are

accompanied by relatively large deformations (just as is the case for preconsolidation stress in saturated soils) due to the ensuing soil aggregate and particle reorientation.

Unavoidable changes in environmental conditions during the long-term period will result in a probable saturation of a compacted fill under existing fill pressures. A reduction in the value of the as-compacted prestress accompanies the saturation, and the magnitude of the resultant saturated prestress is dependent on the magnitude of fill confining pressure.

The presence of saturated prestress is also manifested in many test results including

1. Compressibility tests by DiBernardo and Lovell (1) and Lin and Lovell (2) that demonstrated distinct changes in slope for e versus $\log P$ curves for samples saturated under various confining pressure levels.
2. Consolidated undrained shear tests by Johnson and Lovell (3) and Liang and Lovell (4), for which the induced pore pressures during shear decreased with strain and the effective stress paths curved up and to the right.

In addition, the prediction models for volume changes associated with the saturation of compacted soil samples, subjected to various confining pressures, and the resultant saturated prestress show strong dependency on the as-compacted prestress.

Consequently, in this paper a theoretical procedure is proposed for the determination of as-compacted prestress from simple laboratory compaction tests. The values obtained from the equations are compared with experimentally determined as-compacted prestress. The effects of the various compaction variables (compaction water content, compaction energy/pressure), equivalent fill pressure, and subsequent saturation on the as-compacted prestress are examined.

Prediction equations are developed for the as-compacted prestress, volume changes due to saturation, and saturated prestress generated in a clay soil, compacted to various energy and water content levels and saturated under various levels of confining pressure.

EXPERIMENTAL APPARATUS AND PROCEDURE

The soil used for this study was a plastic fine-grained lacustrine clay deposit from New Haven in northeastern Indiana. The classification test results are given in Table 1.

The soil was sieved through a No. 4 sieve, mixed with a desired amount of water, and then cured for 5 days. Three compaction energy levels (15-blow low energy, standard AASHTO, and modified AASHTO) were subsequently applied at the various water content levels of interest. The relationships

TABLE 1 PROPERTIES AND CLASSIFICATION OF NEW HAVEN CLAY

Category	Property and Classification
Liquid limit (%)	47
Plastic limit (%)	20
Plastic index (%)	27
Specific gravity	2.75
Clay fraction <2 μm (%)	33.0
Skempton's activity	0.82
Unified soil classification	CL
AASHTO soil classification	A-7-6

among dry density (γ_d), water content (w), and degree of saturation (S_r) are shown in Figure 1.

After compaction at a desired moisture content, the soil sample was transferred to an adjustable Proctor mold in which test sampling, using an oedometer ring, was accomplished.

Testing of the soil was conducted in Karol-Warner fixed ring oedometers. The oedometer ring was 63.5 mm (2.5 in.) in inside diameter, 101.6 mm (4.0 in.) in outside diameter, and 25.4 mm (1.0 in.) high. Loading was accomplished by a lever arm weight system. A seating pressure of 10 kPa was used after which the total applied pressure was increased, using a load

increment ratio (LIR) of 0.5, to 14.86, 22.3, 33.44, 50.16, 25.24, 112.86 kPa and so forth until the as-compacted prestress was well defined. The duration of each load increment was 16 min. This time was adequate to define all presecondary effects.

During the service life of a fill, environmental changes can lead to a near saturation condition, with attendant changes in volume and in the as-compacted prestress in the soil mass. This was approximated by compressing the soil, using an LIR of 0.5 and load duration of 16 min, until vertical consolidation pressures of 10.0, 69.4, 137.5, and 276.2 kPa were achieved. These consolidation pressures, at standard AASHTO optimum dry density, correspond to fill heights of 0.61, 4.2, 8.4, and 16.9 m (2.0, 13.9, 27.5, and 55.3 ft), respectively. The soil samples were subsequently saturated by a back pressure process, then unloaded and reloaded at an LIR of 0.5 until the saturated prestress and compression indices were well defined. The end of 100 percent primary consolidation was determined by plotting dial reading versus the logarithm of time.

ANALYTICAL PROCEDURE FOR THE DETERMINATION OF AS-COMPACTED PRESTRESS

Using the results of impact compaction tests, a procedure is proposed for the computation of as-compacted prestress. The

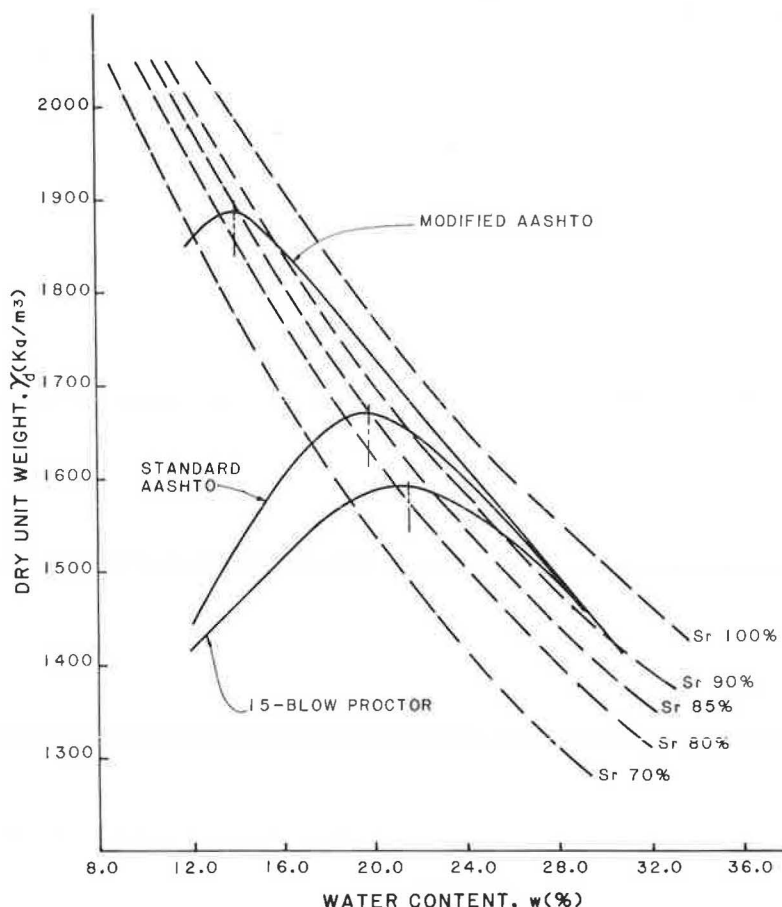


FIGURE 1 Dry unit weight versus moisture content curves for New Haven clay.

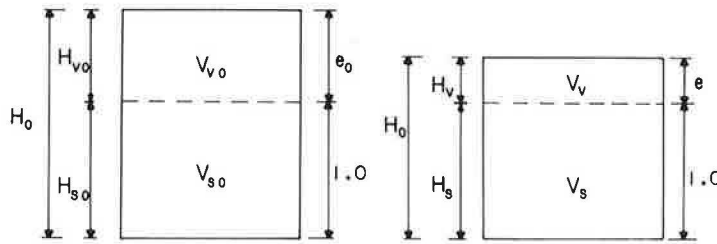


FIGURE 2 Phase diagram for a compacted soil.

following assumptions were made in the derivation of the relationship:

1. The void ratio of the compacted soil in the mold is uniform;
2. There is no energy loss in the drop of the hammer; and
3. The as-compacted prestress, which is the fraction of the compaction energy/pressure effectively transmitted to the soil matrix due to plastic deformation, is uniform throughout the sample.

The plastic deformation (δ_p) that occurs at any energy level for a soil at an initial void ratio (e_o) and water content (w) is derived as follows (Figure 2):

$$\frac{H_{so}}{H_o} = \frac{1}{1 + e_o} \quad (1)$$

$$\frac{H_s}{H} = \frac{1}{1 + e} \quad (2)$$

but

$$H_{so} = H_s$$

Hence

$$\frac{H_o}{H} = \frac{1 + e_o}{1 + e} \quad (3)$$

$$H_o - H = \delta_p = \frac{H(e_o - e)}{1 + e} \quad (4)$$

where

e_o = initial void ratio corresponding to a loosely filled mold,

H_o = height of soil corresponding to a void ratio (e_o) required to produce a compacted height (H),

e = void ratio at the end of compaction, and

H = height of mold.

The nominal compaction energy for the Proctor-type compaction test is given by

$$E = W \times h \times N_B \times N_L \quad (5)$$

where

E = nominal compaction energy,

W = weight of hammer,

h = height of drop of hammer,

N_B = number of blows per layer, and

N_L = number of layers.

For the Proctor-type test, which produces one-dimensional deformation, the strain energy per unit volume (U) stored within the soil is

$$U = \frac{1}{2} \sigma_s \epsilon_{zp} \quad (6)$$

Equating the strain energy per unit volume (U) stored in the soil to the external work done per unit volume,

$$\frac{1}{2} \sigma_s \epsilon_{zp} = \frac{E}{V_o} \quad (7)$$

$$\frac{1}{2} \sigma_s \frac{\delta_p}{H_o} = \frac{E}{AH_o} \quad (8)$$

$$\frac{1}{2} \sigma_s \delta_p A = E \quad (9)$$

where

σ_s = stress generated in the soil as a result of plastic deformation,

ϵ_{zp} = plastic strain in the soil at a given water content,

δ_p = plastic deformation of the soil at a given water content,

H_o = sample height corresponding to an initial (loose) void ratio (e_o), and

A = cross-sectional area of mold.

From the results of the laboratory compaction tests (Figure 3) the relationship between E and δ_p is seen to be nonlinear. Thus, multiplying both sides of Equation 9 by δ_p yields

$$\frac{1}{2} \sigma_s \delta_p^2 A = E \delta_p \quad (10)$$

$E \delta_p$ in this expression represents the area under the E versus δ_p curve. Observe (Figure 3, Curves 3 and 4) that for water contents wet of optimum there are specific energies required for the mobilization of the maximum plastic deformation.

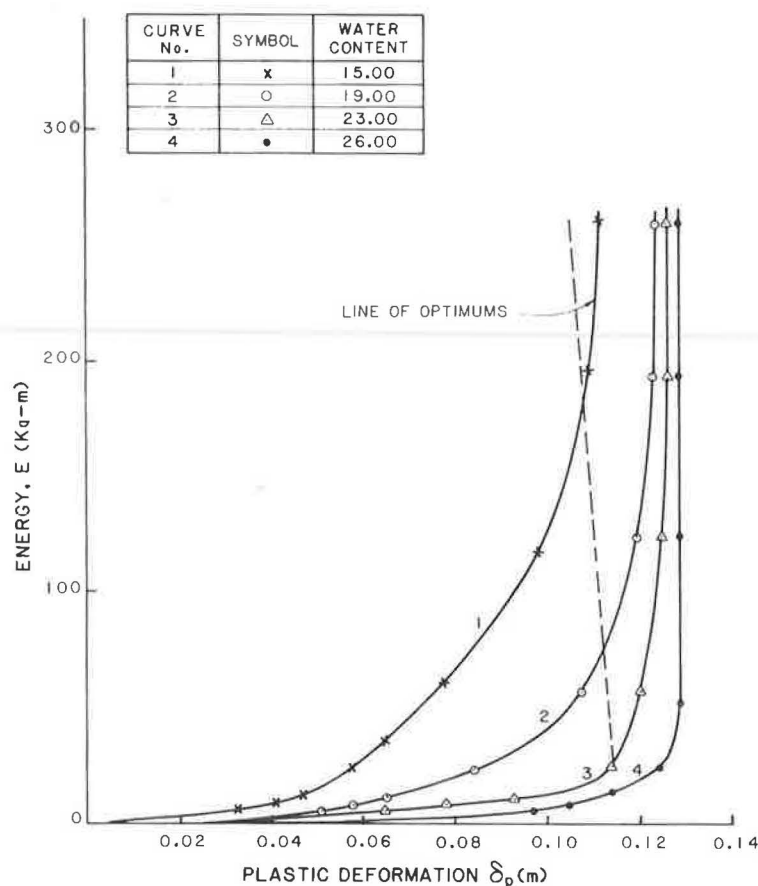


FIGURE 3 Compaction energy versus plastic deformation for New Haven clay.

Determination of the area under an E versus δ_p curve can be effected by two procedures:

1. Application of a numerical technique for the evaluation of the area (A_{EP}). Then

$$\frac{1}{2} \sigma_s A \delta_p^2 = A_{EP} \quad (11)$$

$$\sigma_s = \frac{2A_{EP}}{A \delta_p^2} = \frac{2A_{EP}(1+e)^2}{AH^2(e_o - e)^2} \quad (12)$$

2. The plot of energy versus plastic deformation for the New Haven clay, as typified by the curves in Figure 3, can be represented by a hyperbolic function of the form

$$\delta_p = \frac{E}{a + bE} \quad (13)$$

If the E versus δ_p data are plotted on transformed axes as shown in Figure 4, Equation 13 can be rewritten as

$$\frac{E}{\delta_p} = a + bE \quad (14)$$

where a and b are the intercept and slope of the resulting

straight line, respectively. The area under the curve (Figure 5) is then given by

$$\begin{aligned} & \int_0^{RCE} E d(\delta_p) \\ &= \int_0^{RCE} E d\left(\frac{E}{a + bE}\right) \\ &= \int_0^{RCE} \frac{E a dE}{(a + bE)^2} \\ &= \left\{ \left[\ln(a + bRCE) + \frac{a}{a + bRCE} \right] \right. \\ & \quad \left. - [\ln(a) + 1] \right\} \frac{a}{b^2} \end{aligned} \quad (15)$$

Hence

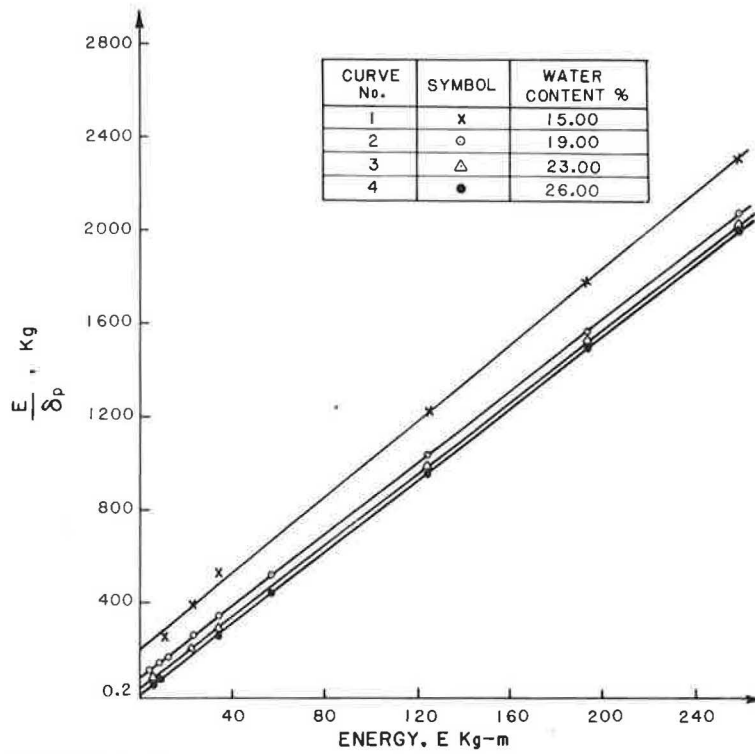


FIGURE 4 Transformed hyperbolic compaction energy-plastic deformation curve.

$$\sigma_s = \frac{2a(1+e)^2}{Ab^2H^2(e_o - e)^2} \left\{ \left[\ln(a + bRCE) + \frac{a}{a + bRCE} \right] - [\ln(a) + 1] \right\} \quad (16)$$

where

a = intercept of the transformed E versus δ_p curve for a desired moisture content representing the initial force (kg) that can be sustained by the soil,

b = slope of the transformed E versus δ_p curve at a desired moisture content representing the reciprocal of the plastic deformation that will occur when a great deal of energy is applied, and

RCE = applied compaction energy for which the as-compacted prestress is desired.

where

a = intercept of the transformed E versus δ_p curve for a desired moisture content representing the initial force (kg) that can be sustained by the soil,

b = slope of the transformed E versus δ_p curve at a desired moisture content representing the reciprocal of the plastic deformation that will

occur when a great deal of energy is applied, and

RCE = applied compaction energy for which the as-compacted prestress is desired.

Observe from Figure 6 the variations of a and b parameters

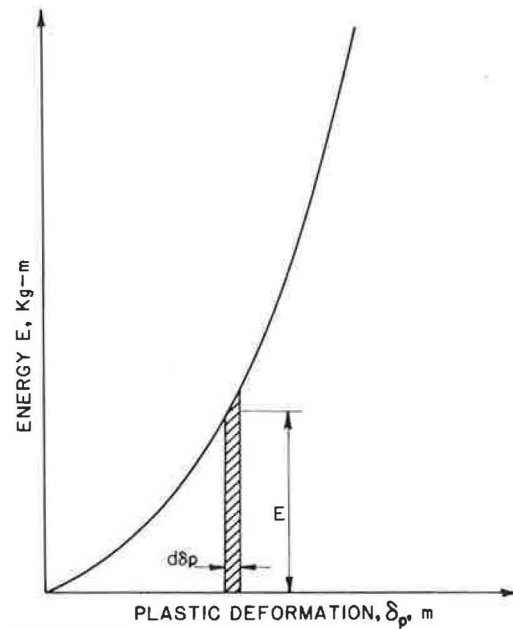


FIGURE 5 Integration scheme for the area under E versus δ_p curve.

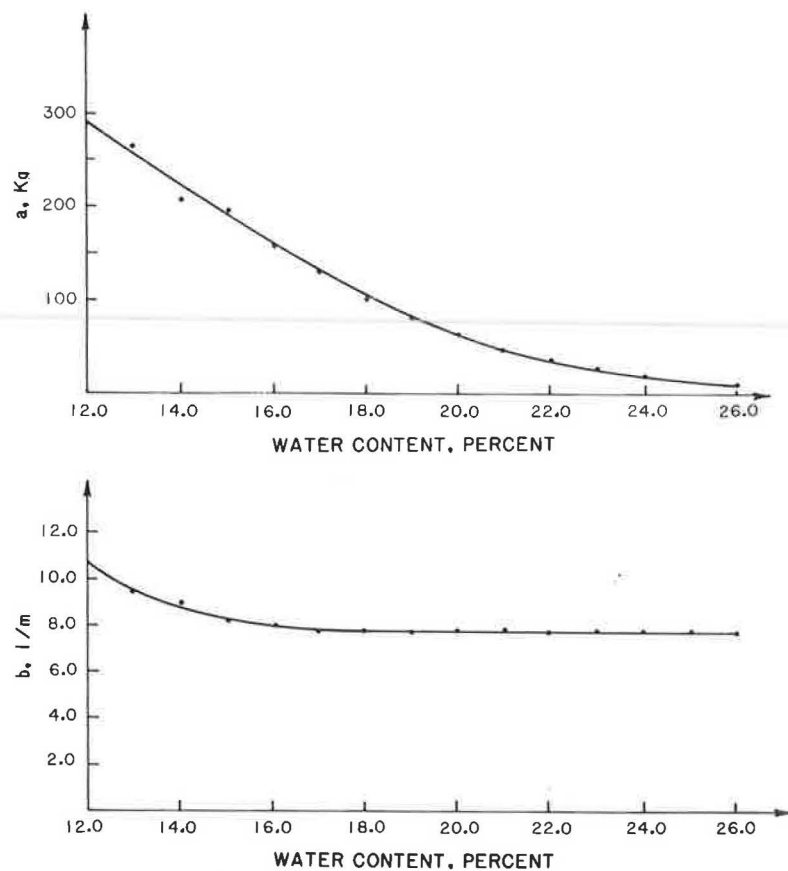


FIGURE 6 Variations of a and b with water content.

with water content. The a parameter shows a continuous decrease with water content whereas the b parameter decreases to a constant value at a water content of about 18 percent.

The calculated total stress generated in the soil as a result of the plastic deformation is the predicted prestress (σ_p). It was computed for various water contents and energy levels and shown in Figure 7.

RESULTS AND ANALYSIS

As-Compacted Prestress

Typical as-compacted compressibility curves are shown in Figure 8. The following codes were adopted for sample identification: L, S, and M refer to 15-blow (low-energy) Proctor-type compaction, standard AASHTO, and modified AASHTO efforts, respectively. The letters D, O, and W refer to moisture content conditions of dry of optimum, optimum, and wet of optimum. The numbers 1, 2, and 3 are used to differentiate among samples of identical moisture content dry of optimum, optimum, and wet of optimum.

The relative compressions (compression at any given time divided by compression at 16 min) for dry-of-optimum samples (e.g., LD1) were greater than those of wet-of-optimum (e.g., LW1). The higher relative compression is attributable to the more readily achievable outflow of air through interconnected voids due to the higher air permeability. Observe in Figure 8

the effect of increasing water content and degree of saturation on the compressibility of the low-energy samples. At low consolidation pressure levels, less than the as-compacted prestress, the wet-of-optimum samples (e.g., LW1) are more compressible than the dry-side samples (LD1) whereas at high pressure ranges (pressures greater than their respective as-compacted prestress) the dry-side samples exhibit a more compressible behavior. Also note in Figure 8 that, for a given energy level, the as-compacted prestress decreases with increasing compaction water content. Consequently, for fill design, especially for the short-term period, the as-compacted prestress should be determined.

Laboratory as-compacted prestresses, which are the fractions of the compaction energy effectively transmitted to the soil skeleton due to plastic deformation and represent the stress level beyond which significant particle orientation occurs, were determined and plotted as points on the predicted curves (Figure 7).

By using a statistical regression procedure, a prediction equation for as-compacted prestress was also developed for the impact computed for New Haven clay:

$$\begin{aligned} \sigma_p = & -45.9398 + 131337.66 \frac{\sqrt{E}}{w^2} - 18982.205 \frac{\sqrt{E}}{w} \\ & + 1023.6757 \sqrt{E} - 17.80117w \sqrt{E} \\ & - 0.12497 \cdot 10^{-4} w^2 E^2 \end{aligned} \quad (17)$$

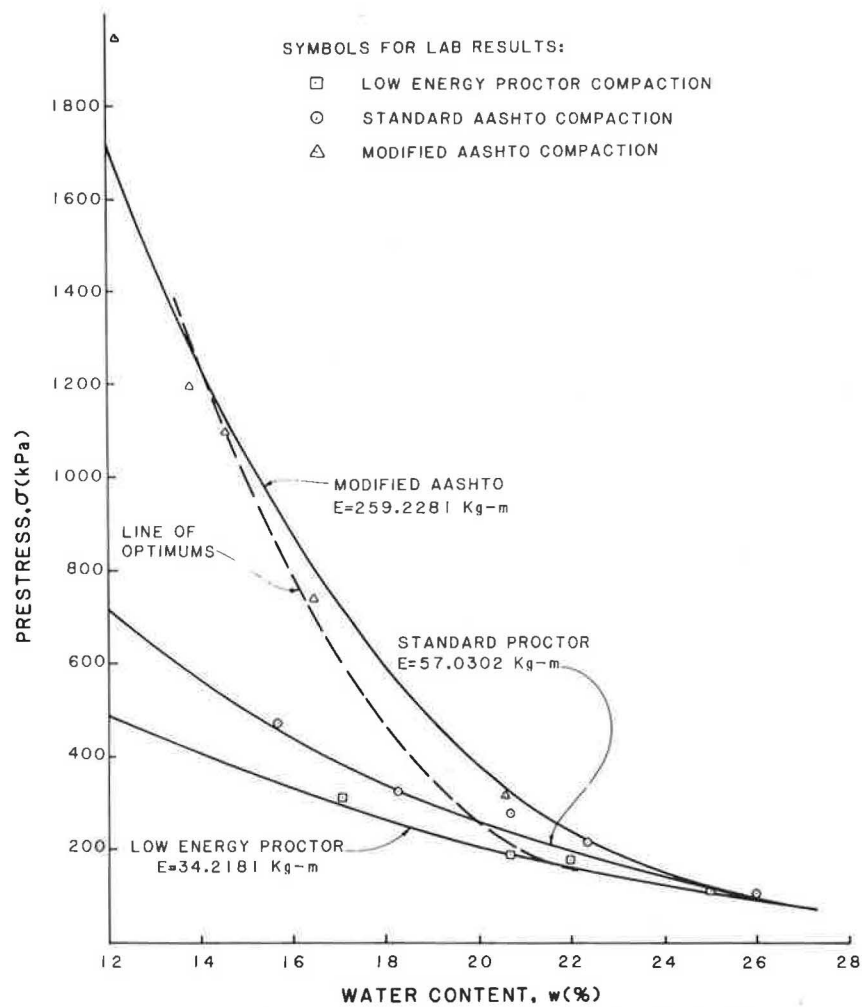


FIGURE 7 As-compacted prestress-water content relationship for New Haven clay.

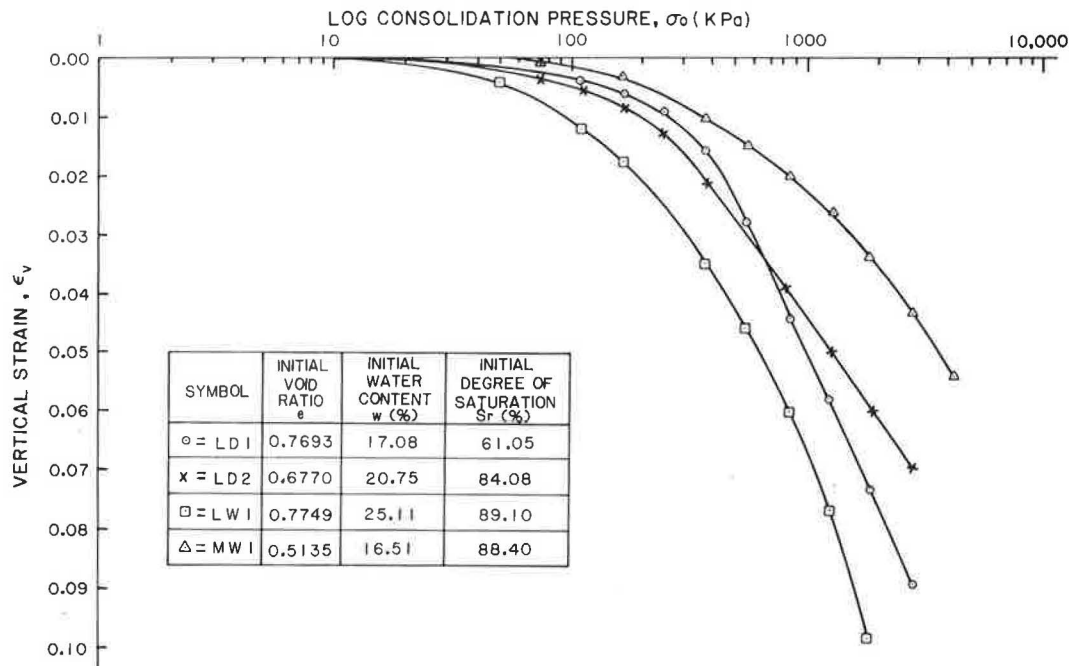


FIGURE 8 Effect of water content on compressibility behavior of as-compacted New Haven clay.

where

- σ_s = as-compacted prestress in kPa,
 E = nominal compaction energy in kg-m, and
 w = compaction water content.

The coefficient of determination (R^2), which represents the amount of variation explained by Equation 17 is 0.9974. The as-compacted prestress is a function of compaction energy and water content with the prestress value decreasing with water content at a given energy level. Also, the as-compacted prestress at a given water content increases with compaction energy. At very wet of optimum, beyond 26 percent for the New Haven clay, identical values of the as-compacted prestress were obtained for the compaction energies used.

Volume Change and Saturated Prestress

The effects of saturation due to changes in environmental conditions were approximated by loading compacted samples to different levels of confining pressures and then saturating them in an oedometer by a back-pressure process. The one-dimensional volume changes ($\frac{\Delta V}{V_o}$) were measured.

The samples were subsequently unloaded and reloaded at LIR = 0.5 until the saturated prestress and compressibility indices were well defined. Load increments were applied at the end of 100 percent primary consolidation, which was determined by the Casagrande dial reading-log time procedure. The saturated prestress values were determined by the Casagrande

construction procedure. Typical results are shown in Figure 9.

By using statistical regression techniques, a prediction equation was developed for one-dimensional percent volume change, ($\frac{\Delta V}{V_o}$) percent. The percent volume change is described in terms of as-compacted void ratio (e), compaction water content (w), confining pressure (σ_o) and as-compacted prestress (σ_s).

$$\begin{aligned} \frac{\Delta V}{V_o}(\%) = & -0.7595 + 0.3094 * 10^{-3} w^2 \sqrt{\sigma_o} \\ & - 0.2242 * 10^{-2} e \sigma_s - 0.7839 * 10^{-6} w \sigma_o^2 \\ & - 0.1221 * 10^{-2} \frac{\sigma_o^2}{w^2} + 1.8653 \frac{\sigma_o}{w^2} \end{aligned} \quad (18)$$

The coefficient of determination (R^2) of this prediction model is 0.8437. For this model, a positive value of percent volumetric strain ($\frac{\Delta V}{V_o}$) percent indicates compression, and a negative value represents swelling.

The percent volumetric strain at zero confining pressure is a function of the interaction term ($e \sigma_s$) only. Observe that, for constant values of water content and confining pressure, the compacted samples exhibit increased swelling tendencies with the interaction term ($e \sigma_s$). Thus, soil compacted at dry of optimum with a very high void ratio and as-compacted prestress will swell the most. Samples compacted on the dry side of optimum moisture content possess high negative pore pressures. Introduction of water to the compacted clay samples

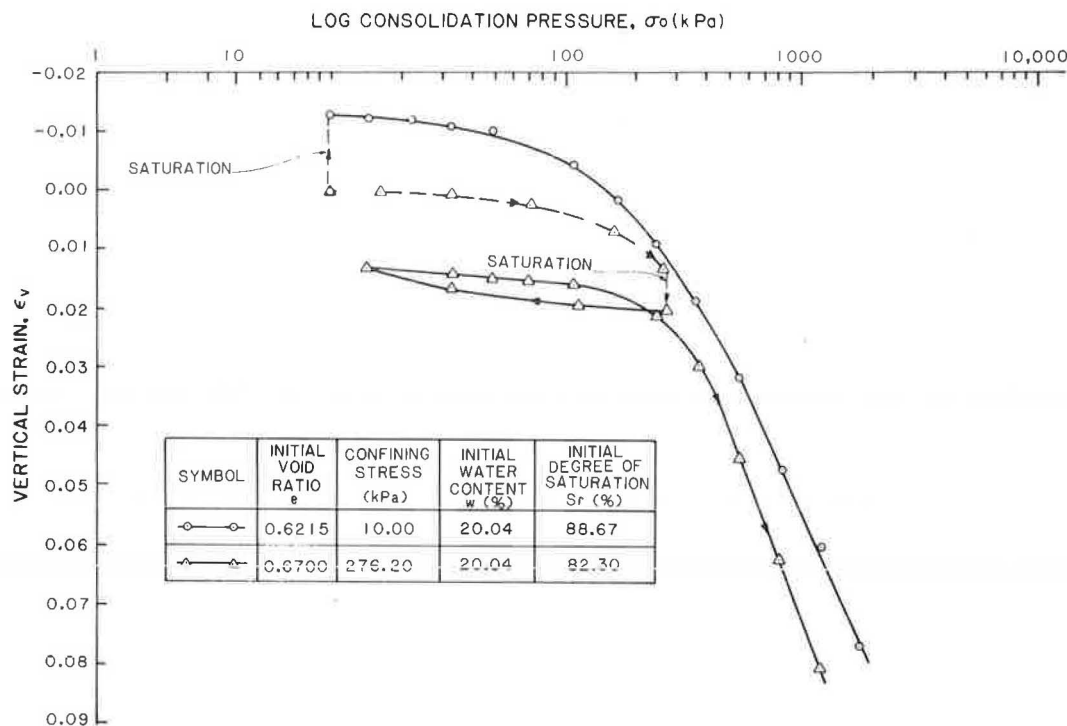


FIGURE 9 Effect of confining pressure on compressibility behavior of standard AASHTO-compacted New Haven clay.

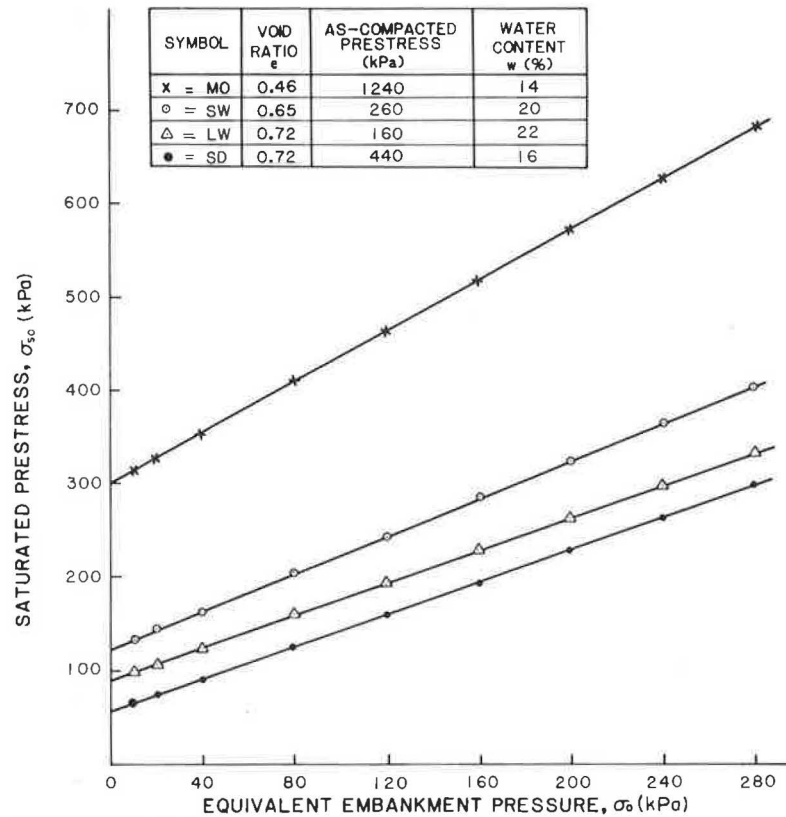


FIGURE 10 Relationship between saturated prestress and equivalent embankment pressure for various void ratios, water contents, and prestresses.

results in a decrease in their negative pore pressures and consequently a decrease in their effective stresses, giving rise to the swelling tendencies and the observed reduction in the as-compacted prestress.

The amount of swell also depends on the type of clay minerals present in the soil, initial compaction moisture content, and confining pressure. The amount of water adsorbed by dry-of-optimum samples is required to satisfy the clay micelles. The resultant expanded clay lattice, together with the adsorbed water, softens the clay aggregates, which under the influence of the confining pressure are compressed. Wet-of-optimum samples consist of more plastic and swollen aggregates. When compacted at various energy levels, the clay particles within the aggregates have a more parallel orientation, and the collection of particles and aggregates has a minimum volume of large voids, a maximum volume of small voids (5), a decreased negative pore pressure, and a decreased as-compacted prestress. A reduced amount of water is required to satisfy the micelles and hence the soils show reduced swelling tendencies.

The independent variables used for the predictions of saturated prestress (σ'_{so}) are confining pressure (σ_o), compacted void ratio (e), compaction water content (w), and as-compacted prestress (σ_s). The prediction equation is

$$\sigma'_{so} = 1559.6762 + 2.24866\sigma_o(1 - 0.85007e) - 4707.3684e(1 - 0.63896e)$$

$$- 5.9509\sigma_s(1 - 0.12317w + 0.003621w^2) + 0.83127w^2 \quad (19)$$

The coefficient of determination (R^2) of this prediction equation is 0.937. It should be noted that the prediction equations given are valid for the ranges of the independent variables for which they were derived.

Figure 10 shows the relationship between saturated prestress and confining pressure for various as-compacted void ratios, compaction prestresses, and water contents. Observe that, depending on the nature of the volumetric strain and the magnitude of the confining pressure, the saturated prestress equals or exceeds the as-compacted prestress and confining pressure during saturation. For the soil samples in which compression occurred, during saturation and under relatively large confining pressure, the obtained saturated prestresses are a result of plastic deformations (primary and secondary compressions) that have oriented and arranged the clay particles into a more stable configuration. Consequently, for a compacted fill, the soil at various depths will be at different overconsolidation ratios ($OCR = \sigma'_{so}/\sigma'_o \geq 1$) after saturation.

CONCLUSIONS

A procedure for the determination of as-compacted prestress based on precompaction soil conditions, relevant independent

compaction variables, and test results from simple laboratory compaction tests has been presented. The curve representing the relationship between energy and plastic deformation has been approximated by a hyperbolic function. Transformation of axes has helped in the determination of parameters essential to the prediction of as-compacted prestress. These parameters are essentially functions of compaction water content only. A good agreement was obtained for predicted and experimentally determined as-compacted prestress. The analytical procedure could be extended, with appropriate modifications, for the prediction of field as-compacted prestress using data from test pads.

As-compacted prestress has been shown to be dependent on compaction water content and compaction energy/pressure. The as-compacted prestress decreases with water content for a given compaction energy level. Also, at a constant water content, particularly for dry-of-optimum soils, the as-compacted prestress increases with compaction energy.

From the prediction models developed, using linear regression procedures, the volume changes associated with saturation and the resultant saturated prestress showed strong relationships with as-compacted prestress. The soil samples exhibit an increased swelling tendency with increase in as-compacted prestress. The volumetric strain due to saturation is also a

function of the compaction water content, confining pressure, and compacted void ratio. The saturated prestress was also shown to increase with confining pressure. Its magnitude is also dependent on compacted void ratio (e), compaction water content (w), and as-compacted prestress (σ_p).

REFERENCES

1. A. DiBernardo and C. W. Lovell. Compactive Prestress Effects in Clays. In *Transportation Research Record 945*, TRB, National Research Council, Washington, D.C., 1983, pp. 51–58.
2. P. S. Lin and C. W. Lovell. Compressibility of Field-Compacted Clay. In *Transportation Research Record 897*, TRB, National Research Council, Washington, D.C., 1982, pp. 51–60.
3. J. M. Johnson and C. W. Lovell. Shearing Behavior of Compacted Clay After Saturation. In *Laboratory Shear Strength of Soils*. Special Technical Publication 740. ASTM, Sept. 1981, pp. 277–293.
4. Y. C. Liang and C. W. Lovell. Strength of Field Compacted Clays. *Canadian Geotechnical Journal*, Vol. 20, No. 1, Feb. 1983, pp. 36–46.
5. R. J. Hodek and C. W. Lovell. A New Look at Compaction Process in Fills. *Bulletin of the Association of Engineering Geologists*, Vol. CVI, No. 4, 1979, pp. 487–499.

Publication of this paper sponsored by Committee on Quality Assurance and Acceptance Procedures.

Tunnel "Daylighting" on the Alaska Railroad

F. C. WEEKS, T. B. TRUEBLOOD, A. KRAUSE, AND D.C. WYLLIE

In June 1984 routine scaling of loose rock from above the north portal of the 175-ft-long Tunnel 5 on the Alaska Railroad's Seward-Anchorage line revealed some large cracks and very unstable rock. Before stabilization work could be started, a 10-ft length of the tunnel collapsed, burying the track. Traffic was stopped for 48 hr while the track was cleared and an assessment was made of stability conditions. In this paper are described the emergency procedures that were undertaken during the next month to correct the hazardous rock stability conditions in this area. The stabilization procedure consisted of blasting to daylight the 150-ft-long tunnel, thus forming a steep rock cut as much as 120 ft high. Because of the very unstable condition of the rock, it was necessary to remove the tunnel in a single blast consisting of about 600 holes. Most of the holes, with lengths of up to 80 ft, were drilled on the slope above the tunnel on a 6-ft-square pattern. Exceptions were the shear line holes, which were drilled on 2-ft centers, and two rows of holes drilled from the tunnel into the outside rib pillar. The holes were laid out in rows at 45 degrees to the track centerline and were detonated at 25-msec intervals using an electronic sequencer. The rib holes were detonated last in the sequence. The blast produced a stable face that required no stabilization and the total track closure time for loading and mucking was 50 hr.

Tunnel 5 is one of six tunnels on a half-mile length of track, running on the west side of Placer Canyon about 50 mi north of Seward (Figure 1). The canyon is about 250 ft deep and the side slopes are as steep as 70 degrees. Construction of the railroad through this terrain required the excavation of almost continuous rock cuts and six tunnels with lengths of between 150 and 600 ft. The original construction was carried out in about 1910, and only minor remedial work has been required on the slopes and tunnels since that time.

On Thursday, June 21, 1984, a collapse occurred involving a 10-ft length of the north portal, with a volume of about 1,000 yd³, that buried the track to a depth of 12 ft. A front-end loader was immediately mobilized to remove the fallen rock, and by Saturday morning the track was cleared. However, observation of the new portal face revealed areas of very loose, hazardous rock, and there was concern that vibration produced by the passage of a train could cause a further collapse. This loose rock occurred both in the rib on the outer side of the tunnel and on the slope surface above the portal where there were a number of open tension cracks as much as 10 in. wide

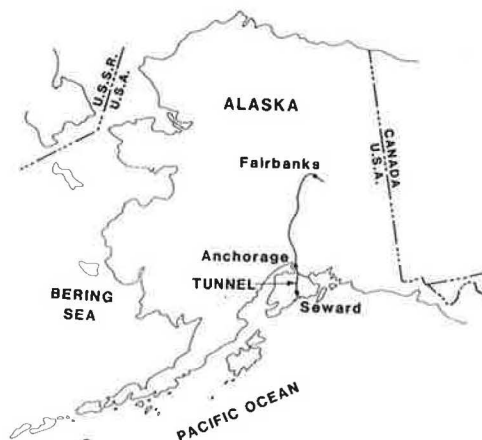


FIGURE 1 Site location plan.

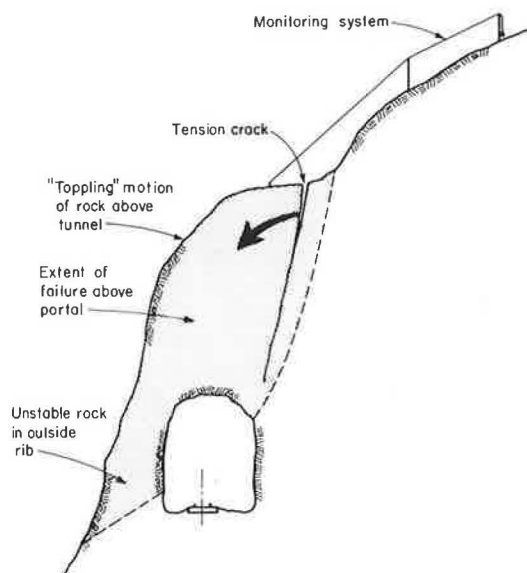


FIGURE 2 Extent of instability above portal.

(Figure 2). Fortunately, the area of instability was confined to the north portal; the rest of the tunnel was stable.

Careful observations of rock conditions and measurement of the width of the tension cracks made on June 23 showed no evidence of new movement. Consequently, it was decided that it would be safe to open the track to traffic under strictly controlled conditions. The first train was a northbound (downgrade) freight that idled through the tunnel and produced no movement of the rock.

F. C. Weeks and T. B. Trueblood, Alaska Railroad, Pouch 7-2111, Anchorage, Alaska 99510. A. Krause, Golder Associates, 715 L Street, Suite 7, Anchorage, Alaska 99501. D. C. Wyllie, Golder Associates, 224 West 8th Avenue, Vancouver, British Columbia V5Y 1N5, Canada.

To open the track to southbound (upgrade) traffic that operates under power, it was necessary to have a monitoring system that would detect movement of the rock and give a warning to train operators that traffic should be stopped. The warning system consisted of a tensioned cable anchored in the unstable rock above the portal and fixed to a stable reference point on the slope above the tunnel (Figure 2). A microswitch was set up on the reference point such that if more than $\frac{1}{2}$ in. of movement occurred, a signal light at track level would be set off. When this system had been established and all measurements of crack widths showed that no movement was occurring, normal traffic was restored. However, all trains operated at very low speed to minimize vibration of the rock.

The primary cause of the instability at the portal was the partial failure of the narrow rib of rock on the outside of the tunnel. The canyon wall at this point is as steep as 70 degrees, and the outer rib varied in width between about 10 and 20 ft. The rock in this pillar had been somewhat damaged by blasting in the original construction, and at the portals the rock had loosened and relaxed as a result of the pillar being unconfined on three sides. This weakening of the rock in the pillar resulted in a "toppling" of the rock above the tunnel into the canyon.

Tunnel 5 was originally about 175 ft long, but progressive small failures over the years had reduced its length to about 150 ft. Ground support consisted only of some timber sets at the south portal that were carrying a considerable load of loose rock, and progressive loosening of the ground was occurring. The rock is a moderately strong greywacke with near vertical bedding planes striking at approximately right angles to the tunnel axis. The rock is somewhat susceptible to weathering and blocks of rock tend to loosen with time.

STABILIZATION MEASURES

Although traffic was operating within 2 days of the collapse of the portal, it was clearly evident that extensive remedial work would be required to ensure long-term safety. During assessment of the options available, consideration was given to a number of factors.

First, traffic frequency was one train per day, so there was ample track time available for remedial work. However, this work could not cause a continuous track closure of more than 72 hr. Second, seepage into the tunnel often produced severe icing during the winter that required time-consuming and expensive deicing operations. Third, the track had to be made safe before winter weather stopped construction work, that is, within about 4 months.

The instability at both portals was so extensive that a major stabilization program was required to make the track safe. The only two alternatives considered were either to construct reinforced concrete portals at both ends of the tunnel or to remove the tunnel entirely to form a 120-ft-high slope. The merits of these two alternatives are discussed next.

Concrete Portals

Portals would provide a high degree of safety against instability and require little maintenance in the future. However, design of a structure to withstand eccentric loading applied by the toppling motion of the rock above the tunnel would have been a

complex and time-consuming task. Also, some blasting would have been required to provide the necessary clearance, and this might have caused further instability. Furthermore, it was unlikely that construction could have been completed before the onset of winter.

Tunnel "Daylighting"

The removal of the tunnel, which was estimated to take about 1 month to complete, would eliminate the need to stabilize the portals. However, it was decided that it would not be possible to carry out the blasting in a series of benches, because it was likely that vibration from the first blasts would cause further falls at the portals that would disrupt traffic. Therefore, the daylighting would have to be done in a single blast. This introduced a certain risk into the work because the one blast would have to remove the entire tunnel and form a stable slope under which equipment could work to clean away the broken rock within the 72-hr track closure. Access to the slope after the blast to trim areas of unstable rock would be difficult and time consuming. The major disadvantage of this alternative was that a high, steep slope would be formed that would require maintenance in the future.

A further potential danger was to a 30-ft span bridge located about 100 ft to the south of the tunnel. It would be necessary to protect this structure from both flyrock and ground vibration.

It was decided that the daylighting option would be adopted, mainly because it could be done within a month with no disruption to traffic while the blastholes were drilled. Another important factor in this decision was that examination of the rock showed that it would be possible to cut a steep slope in the rock and minimize the volume of the blast.

EXCAVATION DESIGN

The slope was designed at an angle of $\frac{1}{4}$:1 (76 degrees) with a 25-ft-wide ditch at the toe. This steep slope served two purposes. First, it minimized the height of the cut and the volume of rock to be excavated because no cutting was done back into the steeply sloping ground above the tunnel. Second, a steep slope reduces the rockfall hazard in comparison with a flatter one because, on a steep face, rocks tend to fall close to the toe and do not bounce outward onto the track. Also, the ditch was designed to be wide enough to catch most rocks that might fall from the slope.

It was decided that it would be possible to cut the slope at the steep angle of $\frac{1}{4}$:1 after a close examination of the rock conditions (Figure 3). The bedding planes have continuous lengths of as much as 100 ft, but they are nearly vertical and strike across the tunnel. Therefore it was not possible for any large blocks of rock to slide on these fractures. The joints have continuous lengths of only 2 to 3 ft, so they will have no effect on overall stability. Any small, loose blocks formed on the joint surfaces could be readily scaled from the slope.

BLAST DESIGN

To remove the tunnel in a single blast and then reopen the track within 72 hr, it was essential that the blast produce the following results:

- The slope face should be safe so that cleanup of the broken rock could begin immediately. This would also allow trains to operate as soon as the track was cleared.
- The rock should be uniformly broken so that no secondary blasting or slope trimming would be necessary.
- The detonation sequence should be arranged such that the impact of the falling rock and the ground vibrations would damage neither the track bed nor the bridge to the south of the tunnel.

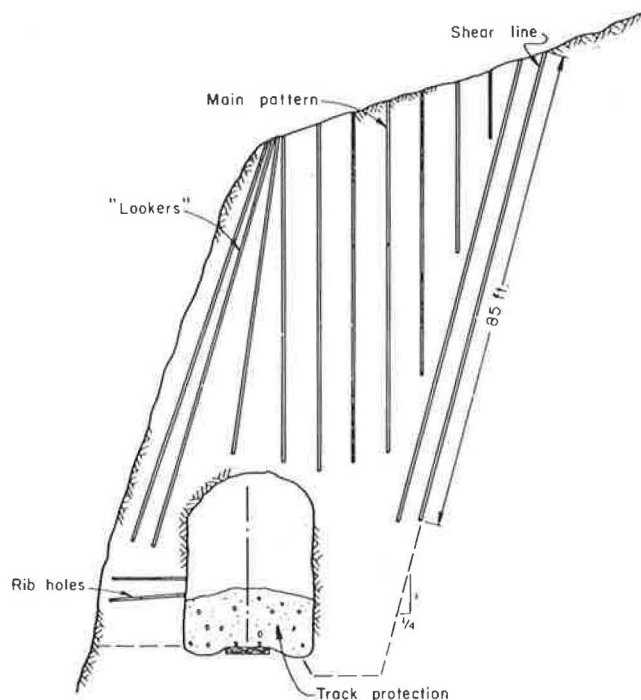


FIGURE 3 Blast hole layout.

The achievement of these results depended mainly on two factors: First, it was essential that the drillholes be evenly spaced so that there was a uniform distribution of explosive throughout the rock. This required detailed design of the more than 600 holes in the blast and then accurate location of each of these holes on the hillside with survey stakes, each marked with the inclination and depth of the hole. Also, drills would have to be carefully positioned and aligned to keep deviation to a minimum. It was decided that the maximum hole depth should be about 80 ft, because at greater depths deviation was likely to be excessive. Figure 3 shows a typical drillhole layout; note that the holes, except for the "lookers," extend only as far as the springline of the tunnel (i.e. a depth of about 80 ft). The rib pillar beside the tunnel was broken with two rows of holes drilled from the tunnel on 2-ft centers.

The total drillhole length was about 25,000 ft and was drilled during a period of 24 days by four drill rigs working 12-hr shifts.

The second factor influencing the blast results was the detonation sequence of the blastholes. Millisecond electric

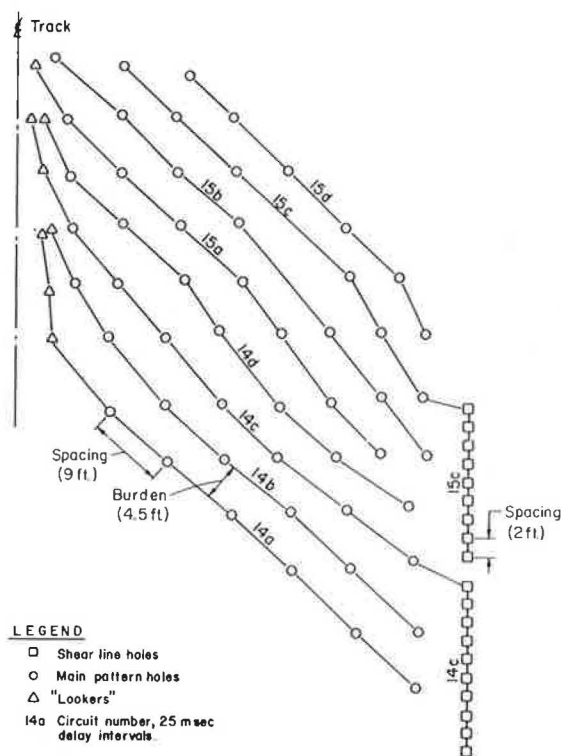


FIGURE 4 Blast hole detonation sequence.

delay caps were used to arrange the holes in a series of rows at approximately 45 degrees to the track centerline (Figure 4). Because the blast was initiated at the cut face to the north of the tunnel and the rows were detonated on 25-msec delays, every row broke to a free face. This delay sequence also moved the rock away from the bridge at the south end of the tunnel.

The shear line was detonated as a "cushion blast" with each 20-ft length of the shear line detonated with every fourth row of the main pattern. In this way, the shear line fired after the pattern holes in front of it. It was decided that a "pre-shear" would not be used because there was a high risk that concussion produced by the detonation of this back row of holes might displace the rock and cause cutoffs in holes of the main blast.

Correct sequencing of the detonation of all 600 holes was achieved by the use of an electronic sequential timer. Four rows of holes were wired into each circuit of the timer, and the interval between timer circuits was set to 100 msec. This created a uniform 25-msec delay between each row of holes.

The final holes to be detonated were the two rows in the tunnel rib that were detonated with 4,000-msec caps but were energized with the first timer circuit so that they would not be cut off by the main blast above. The rib holes were detonated last in the sequence so that the rib formed a buttress to protect the track from the impact of the blasted rock. A summary of the explosive loads follows:

- Shear line: Atlas Kleen Kut Type F, 1 3/8 in. × 36 in. powder, load factor 0.19 lb/ft.
- Production hole: Atlas Gelmax, 2 in. × 16 in. powder loaded to 8-ft collar, powder factor approximately 1.25 lb/yd³.

Total weight of powder was approximately 32,000 lb, and total volume of the blast was about 25,000 yd³. The track was



FIGURE 5 North portal showing tension crack and track protection.



FIGURE 6 Blast detonation initiated above north portal.

protected during the blast with a 6-ft-thick layer of gravel (Figure 5), and a bridge about 50 ft from the south portal was protected with heavy timbers.

All holes were double primed and had a continuous string of primer cord to avoid any breaks in detonation of the long column loads.

Loading of the explosives started on Saturday, July 21, using five two-man crews and was completed by midafternoon on July 22, after about 18 hr of working time. It was decided that no trains would operate while the loading was in progress as a precaution against accidental detonation. The blast was finally detonated at about 6:19 p.m. on Sunday, July 22 (Figure 6).



FIGURE 7 Removing broken rock from track.

RESULTS

The results of the blast were entirely satisfactory. The final face was formed exactly along the designed shear line, and there was virtually no cracking of the ground behind this line. The overall slope was stable, but there was some loose rock on the face where hole deviation had produced concentrations of explosives. The timber placed on the bridge piers proved to be quite adequate protection against the impact of flyrock, and there was no vibration damage to the concrete abutments. The only area of major instability was on the slope below the track bed, where a 30-ft-long block of rock, bounded by continuous joint planes, slid into the river. Fortunately, this failure did not undermine the track.

As soon as the dust had cleared, two bulldozers (a D6 and a D8) and a loader started to clear the broken rock, which had formed a muckpile about 30 ft high, from the tracks. These three pieces of equipment operated throughout Sunday night, and by 10 a.m. Monday morning the track was clear—after a total closure time of about 50 hr (Figure 7).

ACKNOWLEDGMENTS

The authors would like to acknowledge the valuable assistance provided by Lou Oriard and Hal Shearan, who advised on the blast design and detonation procedures, and Wilder Construction of Anchorage, who carried out all the drilling, loading, and mucking operations.

Publication of this paper sponsored by Committee on Engineering Geology.

Resolution of Some Common Problems in Highway Blasting

LEWIS L. ORIARD

In this paper is presented a description of several problems associated with highway blasting that continue to recur with undesirable results. Suggestions are offered for handling such problems so as to mitigate or eliminate their impacts on future projects. The problems discussed involve selected aspects of presplitting of slopes, oversized rock in required excavations or quarries, design and excavation of benches, blast effects, and seismic data processing. The suggested solutions require a better understanding of geology, rock mechanics, and seismology and involve all parties to the work—designers, specification writers, explosives users, and those who monitor blasting effects. The examples selected for discussion reflect actual experiences on real projects. However, neither the projects nor the individuals involved are identified by name.

Many persons involved in highway design and construction share a common desire to achieve optimum results whenever explosives must be used for rock excavation. It is also perceived that there are different incentives that affect the design and execution of the work. The most cautious and precise work with explosives is the most expensive. Designers may wish to have the best possible results, but contractors may wish to accomplish the work in the fastest and least expensive manner. To achieve a balance among time, cost, and physical result for the specific needs of a particular project, designers must understand field conditions and blasting procedures to a degree that permits realistic designs. Because of the many possible choices in the degree of caution and precision required in the work, which directly affects the time and cost of the work, specification writers must correctly convey to bidders what must be accomplished without a conflict between methods and limits. Contractors must have an understanding of the field conditions and the skills needed to accomplish the work. Those who monitor the work must have sufficient experience to make a proper evaluation and to predict the outcome and consequences of ongoing work. All parties should understand the specific needs of the project in question because these needs are not necessarily the same as those of past projects that might appear to be of similar character.

It would be easier to accomplish these goals if all field conditions were the same. This would permit the use of standardized specifications and field procedures that could be expected to produce uniformly satisfactory results. Unfortunately, that is not the case. A procedure that works well at one site may produce highly unsatisfactory results at another site. This means simply that the use of explosives is a site-specific technical art not an exact science. The following discussion is intended to help readers put into perspective some of the more

commonly faced situations that may generate unsatisfactory results, as well as to offer one or more possible solutions for each.

PRESPLITTING OF SLOPES

There are several techniques by which explosives users attempt to produce smooth, sound, final slopes along the perimeters of rock excavations. One of the most commonly used methods is known as presplitting or preshearing. This is a method of generating a crack in the rock along the desired limit of breakage in advance of the pattern blasting. Presplitting defines the limit of the excavation, and pattern blasting brings about the fragmentation of the rock to be excavated. The two are usually part of the same detonation sequence, with the perimeter holes detonating first followed by the detonation of the pattern holes. The perimeter holes are loaded with special charges that are smaller in diameter than the borehole. The annular ring of air between the charge and the borehole wall provides a decoupling of the energy. This decoupling reduces the shattering effect on the borehole wall but transmits enough energy to develop a crack between the holes by means of tensile stresses in the rock web between the holes (1,2). To predict presplit vibrations, see Figure 1 and the section on data processing.

During the 1950s and 1960s, this technique gained broad acceptance in the industry and became increasingly required by contract specifications for the final surfaces of many structural excavations and for many highway cut slopes in rock.

Unfortunately, there is one aspect of this type of blasting that is often overlooked by specification writers. That is the need for a very large "burden" of rock (the dimension between the explosive and the free face) in front of the final slope. This need becomes even more critical if the presplit holes are detonated as a separate blast. When the presplit holes are detonated, explosive gases are generated and there is a very high pressure against the section of rock in the cut area. On a through-cut in a wide hill, sufficient burden usually exists to resist this pressure, and the desired crack can be generated without shifting the hillside. However, for a side-hill cut, the results can be disastrous if there is sufficient pressure to displace the cut section.

On a side-hill cut in the state of Washington, specifications required that presplitting be done as a separate operation ahead of production blasting. The first presplit blast caused the entire cut section to be displaced outward about 18 in. This displacement was accompanied by a prominent loosening of the rock so that it could not be drilled with the track drills that the contractor had on the project. It was a technical and financial disaster for the contractor (Figure 2).

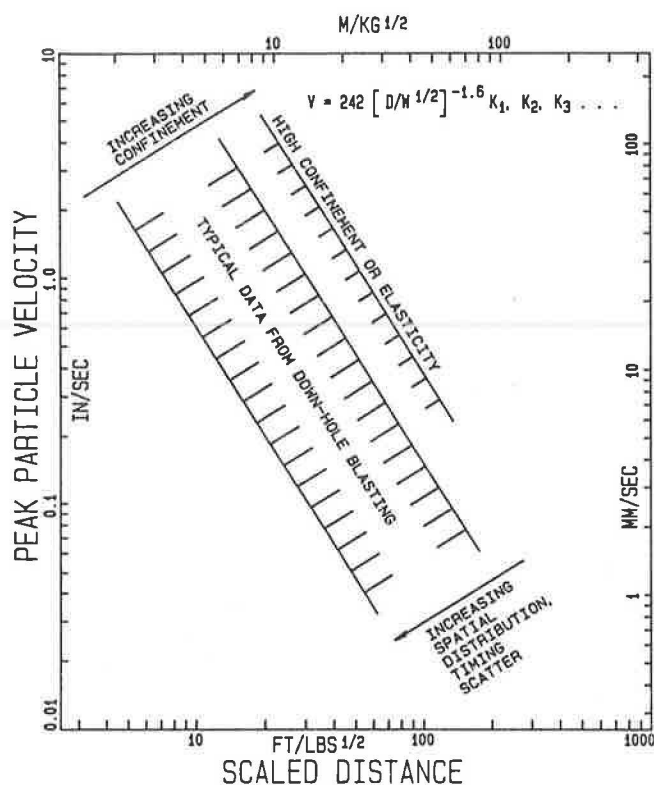


FIGURE 1 Prediction curves for ground vibrations caused by blasting.

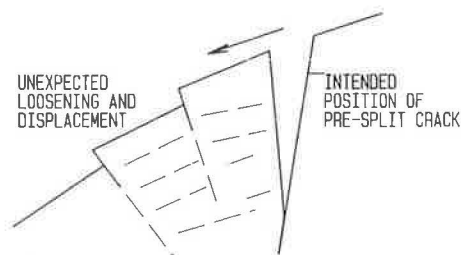


FIGURE 2 Side-hill cut displaced by presplitting.

On a major project in British Columbia, a presplit blast was detonated on the downhill side of a large through-cut. Although it was 75 ft to the outside face of the hillside, a section of rock 300 ft long by 75 ft wide by 20 ft high was shifted outward and uphill by at least 1.0 ft. Concrete was to be placed against a portion of this rock face, and the rock displacement was a serious problem for the completion of the design.

On a small side-hill cut in a southern state, an effort was made to combine presplitting with pattern blasting in a single detonation. However, the rock shifted so badly during the presplitting that some of the pattern holes were cut off, leaving undetonated explosives in the badly loosened but poorly fractured muck. An accidental detonation occurred later.

The solution to this problem is readily available. If there is any doubt about the success of this technique, because of limited dimensions of rock burden, presplitting should be replaced with an alternative technique called "smooth blasting" or "cushion blasting." In the latter technique, the perimeter holes are loaded much as they are for presplitting, but the charges are detonated last instead of first in the firing sequence.

Smooth blasting minimizes the danger of displacing the rock mass until each successive portion has been fragmented during the planned blasting sequence.

It is possible, also, to lessen the tendency of presplitting to displace rock by introducing more delays into the blast. Theoretical considerations suggest that it is necessary to detonate all presplit holes simultaneously, and it is thought by many that such a procedure must be followed in order to develop the desired crack along the rock perimeter. Field experience demonstrates that this is not necessary. It is acceptable to detonate as few as several holes per delay, thereby slowing down the action of the explosive gases against the rock section and lessening the chances of displacement.

It is possible that the first two of the three disasters mentioned could have been prevented by a judicious design of presplitting patterns using only several holes per delay, if the detonation times had been sufficiently spread out in time. However, the third could not have been prevented as long as presplitting techniques were used. Longer time intervals would only have made the problem worse, permitting more time for the rock to shift. Burden dimensions were too small.

Engineers are sometimes encouraged for aesthetic reasons not to require controlled perimeter blasting on highway projects. Such blasting produces a smooth, linear perimeter. Some persons prefer the more "natural" look achieved if there is no control of the perimeter excavation, in which case a more ragged rock profile is produced. Whichever choice is made, it should be done with the recognition that uncontrolled perimeter blasting leaves a rock slope in a loosened condition that will generate more falling or raveling rock and require a higher level of long-term maintenance. Because of this, increasing use is being made of perimeter control even on projects that do not involve public safety, such as open-pit mines. These procedures provide greater stability to mine slopes and reduce maintenance costs.

OVERSIZED ROCK IN REQUIRED EXCAVATIONS OR QUARRIES

Many highway projects have encountered serious problems with oversized rock, whether from grade excavation or from borrow areas supplying rock products for the project.

There have been many "rules of thumb" developed over the years to guide explosives users, and many of these have been developed specifically to bring about the optimum fragmentation of the rock being blasted. In general, these are not founded on theoretical considerations but are the consensus of opinion of experienced users for average or typical field conditions. They can be quite valuable for inexperienced users and may prevent disasters, especially those associated with such safety considerations as flyrock. However, most of the rules of thumb were developed for midwestern quarries in highly jointed limestone or similar sedimentary types of rock. If these rules are followed for that type of setting in relatively uniform rock, the explosives user can expect good fragmentation. Unfortunately, the results would not be as good in other settings.

Perhaps the most important contribution that can be made to the subject of rock fragmentation is to develop an understanding of the manner in which the fragmentation is controlled by the specific characteristics of the site in question. The question

is not to develop a rule for blasting but to develop an understanding of rock characteristics so that the explosives user can refine his field procedures to achieve the optimum fragmentation for the site and project in question. The word "optimum" is used to describe the best results that can reasonably be achieved within the cost and time constraints of the project. The demands of one project may require fine fragmentation regardless of cost. The demands of another may permit hauling of oversized rock to waste sites at less cost.

As has been implied, problems with oversized rock in the excavation of highway cuts, or in quarries used to supply rock products for highway construction, are strongly related to the geology of the site in question and hence regional in character. There are several commonly encountered geological settings that contribute to the production of oversized rock. One of these is a setting characterized by a hard cap rock overlying softer rock or separated from the underlying material. An example in sedimentary rock might be a hard dolomite or sandstone over soft shale. In volcanic rock, an example might be a hard basalt overlying an interflow zone of clay or ash.

In such settings, it is difficult to break the cap rock unless it is naturally composed of highly jointed rock that will break readily into smaller particles. With ordinary blasting methods, explosive energy is expended in the soft zones (the path of least resistance) and does little to damage the overlying hard cap rock. After blasting, the cap rock may be found as huge slabs or blocks of unbroken rock mixed with pulverized particles of the underlying material. Usually, the oversized rock must be sorted and stockpiled for later secondary drilling and blasting—a very expensive process.

There is a normal tendency to reduce the time and cost of blasting operations by designing blasts for larger-diameter blastholes widely spaced. Under the field conditions described, such a procedure would exacerbate the problem of oversized blocks. The situation is improved by drilling more holes of smaller diameter so as to distribute the explosives into a greater number of smaller charges. Also, the less concentrated charges can safely be placed closer to the ground surface to break the cap rock. In more severe cases, it is necessary to place separate, small charges in the upper parts of the holes (called "deck" or "decked" charges) or to add short satellite holes to provide even more charges in the cap rock, or both. Satellite holes are placed between the deeper pattern holes to provide an overall pattern of closer spacing (Figure 3).

In igneous rock, an example of oversize problems would be those sometimes found in certain weathered granites. One illustration is found in a project near the continental divide in Montana, where a contractor was forced into bankruptcy because of problems in excavating a long, deep through-cut

through weathered granite. Because of low velocities measured during seismic refraction studies, it was thought that the rock could be excavated without blasting. And, indeed, it was possible to excavate without blasting. However, the material proved to be large residual remnants of weathering ("core stones") embedded in decomposed granite of the consistency of a coarse sand. At the time of primary drilling and blasting, it was impossible to locate the positions and sizes of the individual boulders so that explosive charges could be placed in each. The contractor was forced to drill and blast each one individually after initial excavation. The cost was unbearable and forced the contractor into bankruptcy.

In granitic rock, it is common to find exfoliation jointing, a process of stress relief that causes separation of rock in layers parallel to the exposed rock surfaces, which may be strongly curved in many instances. This condition exhibits many of the characteristics of the cap rock described previously, but it is usually a more serious problem. The cap is often composed of very hard rock and joints may be 20 ft or more apart laterally. Further, it may be difficult to locate the curved exfoliation joints with sufficient accuracy to avoid placing explosives in the open joints when placing explosives in the hard blocks where they are needed.

Lateral variations are often found in the weathering profiles of granites, giving an unpleasant combination of cap rock and core stones. Thus, oversized blocks may be found at any location in the rock mass.

For massive rock with tight joints, it may suffice merely to increase the powder factor. It has been well proved that an increase in the amount of explosive energy does improve fragmentation. However, in cases in which the rock is highly heterogeneous, or characterized by open joints, merely increasing the powder factor is not enough. It will be necessary, also, to introduce a larger number of smaller separate charges into more portions of the rock in order to break up more of the individual blocks. In extreme cases, such as the Montana project cited earlier, the least expensive alternative is to use secondary blasting methods or haul the oversized rock to waste sites.

In cases in which most of the oversized rock comes from the top portion (stemming zone) and the face zone of each blast, it may be helpful to increase the depth and width of each blast so that these zones become smaller percentages of the zone being blasted.

Unfortunately, there is no simple adjustment of blasting techniques that solves this problem without incurring some additional costs. Therefore, it is essential that bidders for rock excavation work involving explosives have a reasonably accurate understanding of the rock type and its characteristics. Whether that understanding is developed through information provided by the project owner or obtained by the bidders, it is an essential part of the process. It is not sufficient merely to understand how to blast once the condition is revealed. Bidders must understand the field conditions, then plan the choice of equipment and blasting methods accordingly. More information about blasting products and blast designs is contained in various blasters' handbooks and references such as Dick et al. (3), as well as the selected publications noted in its bibliography.

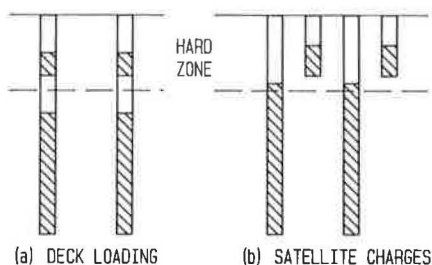


FIGURE 3 Methods of fragmenting hard cap rock.

BENCHES

A number of questions can arise concerning the excavation of benches in rock. Some of these concern the sizes and locations of the benches; some concern the methods of accomplishing the excavation.

The most common reason for excavating benches in highway cuts in rock is to improve safety. Many states have standardized rules for the width of benches and the vertical distance between benches. Unfortunately, these rules rarely include any consideration of the jointing or bedding characteristics of the rock. It is presumed that an excavated bench will be a horizontal ledge of stipulated dimension and that it will catch any loose rocks that roll down the slope, thus preventing them from striking passing vehicles or falling onto the road surface to become traffic hazards.

With appropriate blasting techniques, it is possible to achieve a reasonable approximation of this idealized picture in certain geological settings, such as those characterized by horizontally bedded sedimentary rock of good quality with well-developed horizontal joints or partings. Unfortunately, however, the addition of benches only increases the hazards in other settings. If similar rock is characterized by open, outward-dipping joints, it will be impossible to excavate horizontal benches. Wedges of rock will slide out. The benches will slope downward and outward. Not only will they be incapable of catching stones, they will deflect them farther outward toward traffic lanes than would be the case if the benches did not exist.

Small, narrow benches are rare in nature. In most rock types, bench corners tend to be unstable and will provide loose stones to roll down the slope. On the other hand, an absence of benches permits falling stones to gain great speed and momentum, thus increasing their potential for damage. It appears that a reasonable compromise must take into account the specific characteristics of the slope in question. When these characteristics are unknown, it is better to design wider benches at greater intervals than narrower benches at closer intervals. The wider the bench, the more chance there is that at least some portion of it (the inner portion) can be excavated horizontally or even slanted inward. This would improve the ability of the bench to catch falling stones (Figure 4).

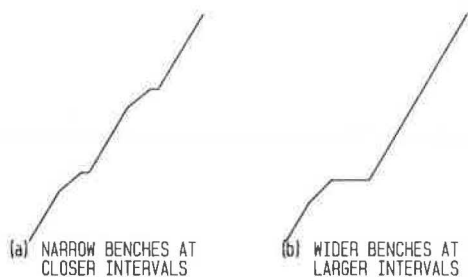


FIGURE 4 Alternative bench designs.

A case history is provided by a paved access road along a steep canyon wall leading to a dam and hydroelectric plant in one of the northwestern states. Modifications required widening of the road, and state specifications required certain horizontal and vertical limitations on benches. Because of overall

limitations on available space, conformance to these specifications would have generated a hazardous situation, providing an outward sloping bench to project stones onto the road while severely restricting the dimensions of the drainage ditch and shoulder on the inside of the road. The final solution involved eliminating the bench on the canyon wall and using that space for a wide shoulder and drainage ditch at the road level. Although the solution required a departure from standard procedures, it provided a much safer condition.

Square bench corners are rarely found in nature. Further, they are difficult to develop by blasting. The normal response of rock to blasting causes the loss of bench corners because of the natural upward block motion effects of the blast (cratering), which are caused by the combined effects of tensile slabbing and gas venting and the tearing effects of adjacent rock movement.

There are certain blasting techniques that can be used to improve the chances of preserving the corners of rock benches. However, such techniques must be designed to overcome or modify the normal site responses mentioned previously. The term "modified site response blasting" is used to describe these techniques. For example, if the rock in question is such that the explosives user finds it impossible to preserve bench corners with the normal sequence of drilling and blasting, this response may be modified on some projects by holding the rock in a confined condition while light charges are detonated along the planned lines of breakage. Holding the rock in a confined condition modifies its normal response and may permit the work to be done. If several "lifts" (consecutive benches of blasting) are required, it is sometimes possible to drill and blast a bench corner while an overlying burden remains on top of it to hold it in place. Drilling and blasting are done "in the blind." Even here, however, the precise sequence of drilling, blasting, and excavating activities is crucial to the success of the method. Because these must be custom designed for the specific characteristics of the site, it is difficult to offer generalized recommendations. Further discussion of these techniques can be found elsewhere (4). This reference work describes complex structural excavations using these techniques.

BLAST EFFECTS ON HIGHWAY FACILITIES

Along cross-country highways, there are usually relatively few structures and facilities that have any susceptibility to damage from blast effects. Of course, when these highways enter urban areas, or pass nearby, it is necessary to take into account the myriad questions of public response, residential structures, and other facilities that may not be found in outlying areas.

The main incentive for commenting on this topic in this paper is that there are still many cases in which the blasting limitations for structures of high strength are as restrictive as they might be for residences. Although this situation does not in any way represent a hazard, it sometimes represents extreme increases in cost and time for the completion of the work. A case in point is that of a large highway rock cut passing over a concrete-lined tunnel in one of the northern states. The highway department of the state in question had thought originally that the rock was sufficiently weathered that it could be excavated without blasting. Unfortunately, this turned out to be an incorrect assessment of the rock. After the work was well under

way, it was discovered that blasting would be required. Work was halted for about 2 years while the interested parties debated the restrictions for blast effects on the tunnel and obtained the required insurance. Enormous additional costs were incurred because of unnecessary concerns about the tunnel.

In particular, there were two aspects of the requirements that were unnecessarily conservative. One was the vibration limit of 2.0 in./sec for a concrete-lined rock tunnel. Such a limit is more appropriate for residences. The second requirement called for an insurance policy that would cover damage for 5 years after the completion of the work. This requirement was based on the false premise that vibration damage might not be disclosed at the time of occurrence under these field conditions.

There is ample field experience with ground vibration effects on concrete-lined and unlined underground openings in the range of 20 to 200 in./sec to indicate that the lower particle velocity limits often applied to residences are unnecessarily conservative for these tunnels. Understandably, there is no single number that fits all circumstances, but it is usually conservative to consider limits at least as high as 10 in./sec. In some instances, far higher values may be acceptable. For comparison, Tennessee Valley Authority (TVA) specifications call for vibration limits on concrete in the range of 10 to 20 in./sec, discussed later [Table 1, Figure 5, (2; 5; 6, p. 256; 7; 8)].

As a general policy, there is no need to allow higher limits than those that do not pose any additional costs or delays to the work. However, if this approach leads to extremely low particle velocities, future readers may believe mistakenly that such numbers represent the maximum allowable vibration rather

than a convenient, nonrestrictive limit. It is this type of misinterpretation that leads gradually to more and more restrictive limits, regardless of need.

It is, unfortunately, a common belief that any manner of vibration damage may reveal itself long after the event, even years later. Except for a few rare types of occurrences, that is not true. The contrary is usually true. One diagnostic characteristic of vibration damage to a lined tunnel would be its immediate appearance. This would also be true of the superstructures of bridges. Highway slabs, per se, are not susceptible to damage from elastic blasting vibrations outside the zone of block motion. However, a blanket statement cannot be made about slab foundations, such as those resting on embankments.

One approach to writing specifications that attempts to distinguish among the different mechanisms by which damage may occur is that of writing one portion of the specifications to cover simple particle velocity limits and another portion to cover the potential for block motion, that is, the shifting of ground supporting a slab or a structure. Since 1976 the TVA has used this type of specification, written by this author. It has been reported that no damage has occurred within the limits of this specification, although it appears to be far more liberal than most. The limitations are directly related to the age of the concrete and indirectly related to frequency by distance relationships. For example, for low-profile mass concrete, such as footings, slabs, and the like, with an age of 10 days or more, the allowable particle velocity is 20 in./sec for distances less than 50 ft. However, it was not found possible to damage the low-profile test concrete through elastic ground vibrations, and the writer concluded that it is generally necessary to have an additional nonelastic effect such as rupture of the supporting rock mass, some type of strong flexure of the concrete, or ground heave. For this reason, the TVA specifications include controls for such inelastic behavior of the supporting rock, and these are considered to be far more important than vibration limitations (Table 1 and Figure 5). For further discussion, see Oriard (7).

TABLE 1 TVA BLAST DAMAGE CRITERIA FOR MASS CONCRETE

Concrete Age from Batching	Allowable Particle Velocity from Blast-Induced Vibrations (ips) ^a
0 to 4 hr	$4 \times DF^b$
4 hr to 1 day	$6 \times DF$
1 to 3 days	$9 \times DF$
3 to 7 days	$12 \times DF$
7 to 10 days	$15 \times DF$
10 days or more	$20 \times DF$

^a1.0 in./sec = 2.54 cm/sec.

^bDF = Distance factor, defined as

DF	Distance from Blast to Concrete [ft (m)]
1.0	0-50 (0-15)
0.8	50-150 (15-46)
0.7	150-250 (46-76)
0.6	Greater than 250 (76)

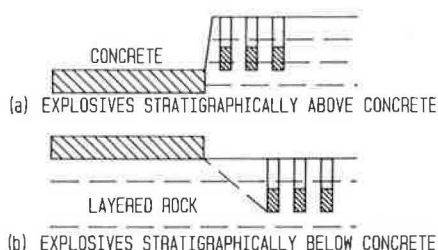


FIGURE 5 Stratigraphic position of blasting.

DATA PROCESSING

This discussion relates to the processing and analysis of ground vibration data from blasting. At first glance, it might appear that such data processing is a topic of little consequence to highway work. The reason for its presentation here is that the topic has proved to be a problem of some importance on a number of highway projects, and it is hoped that this discussion will mitigate the problem on future projects.

When ground vibrations are a matter of any interest on a highway project, it is common to monitor the blasting operations with a portable seismograph. Usually, one instrument is taken to different locations of interest as the work progresses, so many instruments are not used simultaneously. The data are usually plotted as a log-log graph of peak particle velocity versus scaled (normalized) distance, where scaled distance is the true distance scale (divided) by the square root (or cube root) of the charge weight per delay.

As the data are obtained and plotted, a trend begins to emerge, showing the manner in which the vibrations die out with distance from the blasting source. This is known as the "attenuation" of the vibration intensity with distance. A trend

line through the data is used for predicting the intensity of future vibrations at various distances for various weights of explosives. If a large number of seismographs were placed at various distances from one blast, in similar geological settings for each instrument, the data would fairly represent the manner in which vibrations would be expected to die out in that area. On the other hand, if only one instrument is used to monitor consecutive blasts, there will usually be a fair amount of scatter in the data. Eventually a data band will emerge, with parallel upper and lower bounds, but the first few data points may suggest slopes that are physically impossible, even reverse slopes. In such instances, regression lines should be avoided.

The analyst is usually pressed to give predictions from the first blast onward. If he is not sufficiently experienced, he will be tempted to place too much reliance on a few scattered data points and calculations made from them. Hand calculators and computers can quickly calculate regression lines (and they are readily approximated by eye). There is an intuitive tendency to be more comfortable with actual data and calculations than with judgment that may or may not yet appear to be supported by the data. What often happens, then, is that a regression line is drawn through a number of points that is insufficient to fairly represent the true conditions. Because the line was calculated from actual data, an inexperienced person might extrapolate it, regardless of its slope or position on the graph. A more experienced person would know what slope to expect and would be aware of representative upper and lower bounds of such data.

On some projects, the premature plotting of regression lines has brought the project to a halt because of unfounded dire predictions of calamity. This came about because the regression line was very steep and indicated catastrophic results at the closer distances that would be found later in the work. The regression line was a false line plotted prematurely, but it brought about expensive delays in the work until the question could be resolved.

On one project in the Northwest involving partial removal of an existing concrete structure, the opposite conclusions were drawn about attenuation rates. The attenuation line was nearly horizontal, bringing the analyst to the conclusion that particle velocities would be very low even at the source. A serious conflict existed between the project owner and the contractor until this question was resolved. The problem was made worse by the analyst's lack of awareness that his seismic equipment was incapable of registering the true characteristics of the vibration. He was registering only a small fraction of the energy involved, and his equipment response became progressively less effective as the vibration frequencies increased close to the source. Because of this decreasing response, he concluded that very little energy was present.

The recommended solution to these problems is to begin with a reference data base so that new data can be placed in proper perspective. For those who might not have such data, it might be convenient to use some readily available published source of such data, such as the Oriard prediction curves (Figure 1), and other works (1, 2, 8).

Figure 1 is a generalized plot of peak particle velocity versus scaled distance, where scaled distance is the true distance divided by the square root of the charge weight per delay. The data can also be represented by

$$V = 242 (D/W^{1/2})^{-1.6} k_1, k_2, k_3, \dots \quad (1)$$

where

- V = peak particle velocity;
- D = true distance;
- W = charge weight per delay; and
- k -factors = variables such as confinement, spatial distribution, timing scatter, type of explosives, and the like.

When the combination of k -factors = 1.0, the equation represents the upper bound to typical down-hole blasting data. The line shown for high confinement or elasticity is represented by increasing the factor 242 to 605.

If the new data are plotted on such curves, it is easy to see whether the new data are high, low, or average. This assists the analyst in predicting future results. Also, unless the data show otherwise, an attenuation slope of the order of -1.6 should be used. Further, it is strongly recommended that the analyst plot upper and lower bounds rather than regression lines. Usually, it is far more important to know the upper bound than to know the average, despite the usual inclination to make use of statistical procedures and plot regression lines.

Of course, it is essential that the monitoring equipment be capable of responding accurately to the frequencies and the intensities of interest. Most vibrations for close-in small-scale blasting are far beyond the range of typical off-the-shelf blast-monitoring equipment.

CONCLUSION

Blasting is a technical art that must be tailored to the specific conditions of the site in question. The results that can be achieved are controlled strongly by site conditions. The more difficult the site conditions in relation to the desired result, the more time, money, and skill must be used to achieve the results. In some cases, these expenditures may be too great for the value received. In other cases, failure may be guaranteed in advance by specifications that require inappropriate procedures. Those persons involved in design, specifications, execution, and monitoring of the work need sufficient understanding of geology, rock mechanics, and blasting processes to define optimum procedures and results. Several common problems and methods of dealing with them have been discussed.

REFERENCES

1. L. L. Oriard. *Blasting Effects and Their Control in Open Pit Mining. Proc., Second International Conference on Stability in Open Pit Mining*, Society of Mining Engineers, New York, 1972, pp. 197-222.
2. L. L. Oriard. *Blasting Effects and Their Control. In Underground Mining Methods Handbook*. Society of Mining Engineers, New York, 1982, pp. 1590-1603.
3. R. A. Dick, L. R. Fletcher, and D. V. D'Andrea. *Explosives and Blasting Procedures Manual*. Information Circular 8925. U.S. Bureau of Mines, 1983.
4. L. L. Oriard. *Modified Site Response Blasting: The Role of Rock Mechanics in Perimeter Control. Proc., Tenth Conference on Explosives and Blasting Technique*, Society of Explosives Engineers, Montville, Ohio, 1984.
5. C. O. Faris. *Dworshak Dam Underground Crushing Chamber. Symposium on Underground Rock Chambers*, ASCE National Meeting, Phenix, Ariz., 1971, pp. 147-165.

6. A. J. Hendron, Jr. Engineering of Rock Blasting on Civil Projects. In *Structural and Geotechnical Mechanics* (W. J. Hall, ed.), Prentice-Hall, Englewood Cliffs, N.J., 1977.
7. L. L. Oriard and J. H. Coulson. TVA Blast Vibration Criteria for Mass Concrete. *Specialty Session on Minimizing Detrimental Construction Vibrations*, ASCE National Meeting, Portland, Oreg., 1980, pp. 101-123.
8. R. G. Tart, L. L. Oriard, and J. H. Plump. Blast Damage Criteria for a Massive Concrete Structure. *Specialty Session on Minimizing Detrimental Construction Vibrations*, ASCE National Meeting, Portland, Oreg., 1980, pp. 125-140.

Publication of this paper sponsored by Committee on Engineering Geology.

Effects of Soil Properties on Microwave Dielectric Constants

THOMAS J. JACKSON

The electrical properties of soils can be used to estimate soil characteristics such as moisture content and density. Relationships between the dielectric properties and soil moisture are the basis for the microwave remote sensing of soil moisture and some in situ soil moisture instruments. Several soil characteristics can produce the same set of dielectric properties and only through system design can any one be isolated with complete confidence. In recent years, investigations have been conducted to isolate the effects of specific characteristics through laboratory and field experiments. A review of the results of these studies is presented, and the following soil characteristics are included: soil moisture, soil texture, bulk density, structure, salinity, organic matter content, and temperature. Of these factors, the most significant and easiest to isolate is soil moisture. Of secondary importance are texture, density, and structure, depending on local conditions. Salinity, temperature, and organic matter content are of limited significance.

The microwave region of the electromagnetic spectrum has great potential for measuring soil water conditions using both remote sensing and in situ techniques. Large contrasts in the electrical properties, primarily the dielectric constant at these wavelengths, of dry soil and water are the primary reason for exploring this region.

Early investigators had reported some limited results dealing primarily with laboratory and in situ devices. Recently, there has been a renewed interest in this area as it applies to remote sensing, particularly at wavelengths between 5 and 21 cm. These investigations have led to expanded data bases and a better understanding of the fundamental relationships. Studies have also revealed that other soil properties, in addition to soil water, affect the dielectric properties of the mixture.

In this paper the effects of soil moisture, soil texture, bulk density, organic matter content, salinity, temperature, and structure on the dielectric properties are reviewed. When possible, the effects of these properties are illustrated using recently developed dielectric simulation models. The presentation will be limited to a wavelength of 21 cm because this is the primary frequency being considered for remote sensing.

SOIL WATER EFFECTS

Soil, as measured by a dielectric device, is a mixture of air, water, and soil particles. Several studies have shown that at 21 cm the dielectric constant of a dry soil is nearly constant

regardless of variations in any of the factors that will be discussed here. The real part of the dielectric constant (k') is about 2 to 4 and the imaginary part (k'') is about 0.05 (1).

When water with a k' of 80 is introduced in relatively large proportions, significant changes in the k' of the mixture occur. One of the key developments of recent years has been the concept introduced by Schmugge (2) and refined in Wang and Schmugge (3). Laboratory studies had shown that k' was a nonlinear function of volumetric soil moisture; simple mixture formulas did not explain this phenomenon, as illustrated in Figure 1. Schmugge (2) proposed that water in the soil could be divided into two types that had different dielectric properties. Part of the water close to the surface of the soil particles was considered bound. Under such conditions the water molecules were not free and behaved more like ice. The k' of this portion of the water is small. In their model, Wang and Schmugge (3) assumed that water added to dry soil was bound until it reached a transition point beyond which it had the properties of free water.

Dobson et al. (4) developed on the basic concept of bound and free water by offering a more physically based explanation and a complete procedure for estimating the bound water capacity of a soil, which will be discussed in the next section.

On the basis of the concept just described, the dielectric constant of a soil can be determined from the proportions of air, bound water, free water, and soil particles present. A wide variety of models has been developed for soil-water-air mixtures (1, 5). Each of these models has some conceptual basis; however, the predictions can vary widely. Dobson et al. (4) used the basic approach proposed by Polder and van Santen (6) and de Loor (7), which considered the volume fraction, shape, and dielectric constant of the components. The mixing equation is

$$k_m = [3k_s + 2V_B(k_B - k_s) + 2V_F(k_F - k_s) + 2V_a(k_a - k_s)] \\ \div \left[3 + V_B\left(\frac{k_s}{k_B} - 1\right) + V_F\left(\frac{k_s}{k_F} - 1\right) + V_a\left(\frac{k_s}{k_a} - 1\right) \right] \quad (1)$$

where

- k_m = dielectric constant of the mixture,
- k_s = dielectric constant of the soil,
- k_B = dielectric constant of the bound water,
- k_F = dielectric constant of the free water,
- k_a = dielectric constant of the air,
- V_B = volume fraction of the bound water,

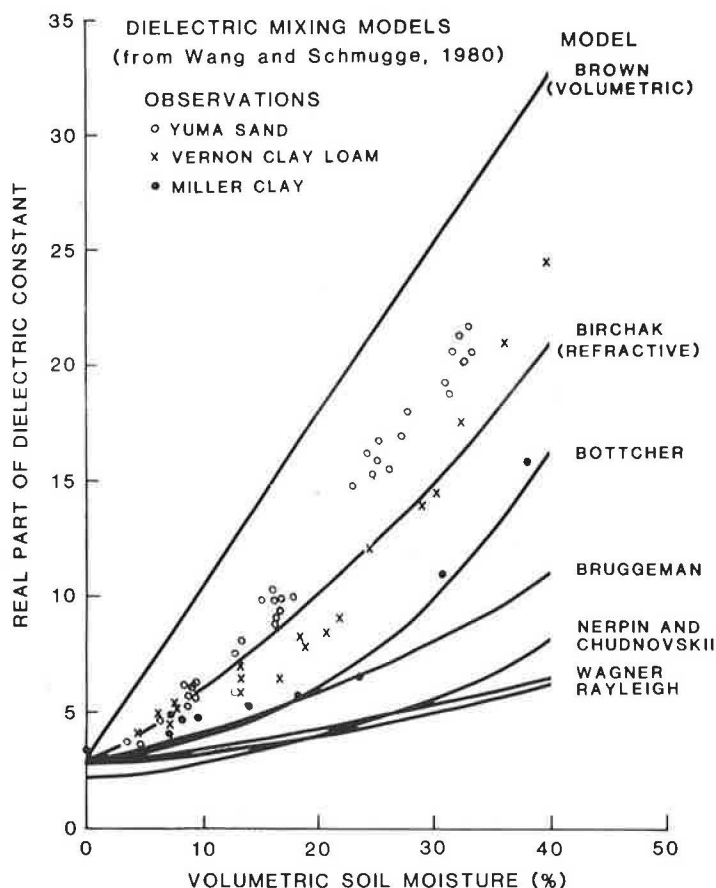


FIGURE 1 Observed and predicted relationships between volumetric soil moisture and the real component of the soil dielectric constant, adapted from Wang and Schmugge (3).

V_F = volume fraction of the free water, and
 V_a = volume fraction of the air.

Figure 2 shows the general relationship between the real and imaginary parts of the dielectric constant of a moist soil and the volumetric soil moisture. It should be noted that there are other approaches to mixture modeling that can explain the general relationship and that the model of Dobson et al. (4) was developed for a homogeneous soil-water-air mixture. This model has been tested using laboratory measurements of the dielectric constant, which can differ from actual field conditions.

SOIL TEXTURE EFFECTS

The importance of soil texture or particle size distribution, or both, on the dielectric constant of a soil-water-air mixture is easily understood using the concepts introduced by Schmugge (2), Wang and Schmugge (3), and Dobson et al. (4). The bound water fraction of the mixture is determined by the amount of water that is close to the surface of the soil particles. Two factors determine this. The first is the number of layers of water molecules that are actually bound. Dobson et al. (4) assume that three layers are involved. This point could be argued, but it appears to be an adequate approximation based on their results.

DOBSON ET AL. MODEL

BULK DENSITY = 1.3 g/cm³
 1.4 GHz H

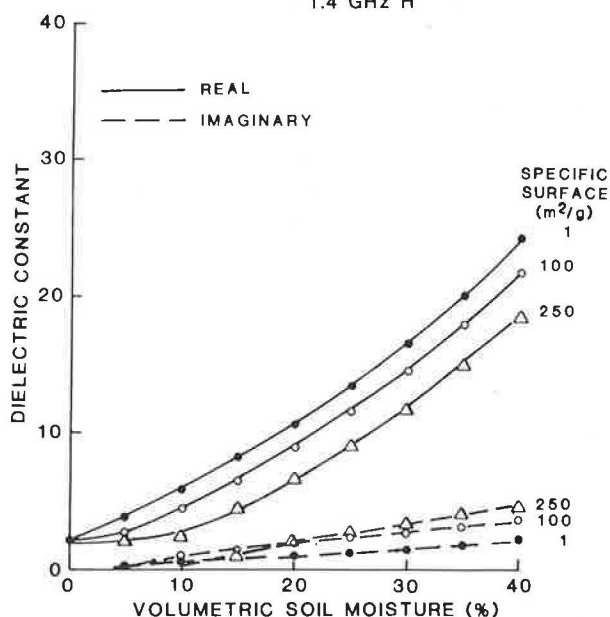


FIGURE 2 Effects of soil specific surface area on the relationship between k' and k'' and volumetric soil moisture.

The second factor that determines the bound water in the dielectric mixing models is the total surface area of the soil available to the water molecules. A sand with a specific soil surface of 1 m²/g would have a much smaller bound water fraction than a clay with a value of 300 m²/g. In the Dobson et al. (4) approach, the specific surface area of the soil is used to calculate the bound water fraction and, therefore, the bound water fraction is a function of soil texture (actually particle sizes and shapes).

The specific surface can be measured or estimated from particle size distribution data. The estimation approach presented by Dobson et al. (4) is based on a procedure developed by Ayra and Paris (8). A number of assumptions are involved in this estimation technique that make it unreliable.

Figure 2 shows the relationship between volumetric soil moisture and the dielectric constant for three soil textures, as determined by their specific surfaces. The variability in k'' is quite small; however, the effects of the specific surface on k' are large. For the same volumetric soil moisture, the k' of a sand will be larger than that of a clay because there is more free water in the sand mixture. Dobson et al. (4) tested this model using laboratory measurements of various soils and found that it worked quite well.

BULK DENSITY EFFECTS

It was noted previously that the k' - and k'' -values of dry soils did not vary much ($k' = 2$ to 4). However, a minor adjustment is made in some dielectric mixing models (4, 9) for the effects of bulk density of the soil on k' . The equation used by Dobson et al. (4) is

$$k' = (1 + 0.44 \rho_b)^2 \quad (2)$$

where ρ_b is the bulk density in grams per cubic centimeter. Because ρ_b typically varies between 1.0 and 1.7 g/cm³, the effect will be minor for most soils.

Early research on soil water-dielectric relationships, especially in remote sensing, was hindered by different opinions on exactly which soil water property should be used. Many studies used the gravimetric soil moisture and others related dielectric and emission parameters to moisture-tension characteristics. These approaches have been abandoned in favor of volumetric soil moisture. Bulk density is most important in converting gravimetric soil moisture to volumetric soil moisture.

In the Wang and Schmugge (3) model the bulk density is insignificant. The Dobson et al. (4) model uses the bulk density in its calculations of the conductance properties of the soil water that, in turn, affect the dielectric constant. Figure 3 shows the variation that might be observed. For a given soil, typical site variations on the order of ± 0.1 g/cm³ would have a minor effect. Major treatments such as tillage or compaction would have to be considered.

ORGANIC MATTER CONTENT

The effects of organic matter content have not been extensively studied. In the context of soil properties, an increase in the

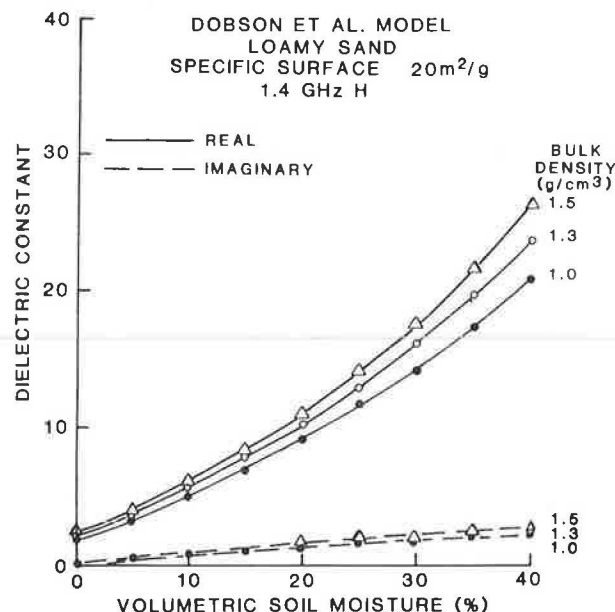


FIGURE 3 Effects of bulk density on the relationship between k' and k'' and volumetric soil moisture.

organic matter content reduces the specific surface of the soil and reduces the typical bulk density. The net effect is that the observed range of moisture is smaller at higher organic matter contents. Figure 4 is a series of emissivity observations obtained over three plots with different organic matter contents. The conditions of the plots were such that emissivity was directly related to the dielectric constant (10).

SOIL WATER TEMPERATURE

Temperature effects on the dielectric properties of water have been extensively studied (1). These effects vary with frequency

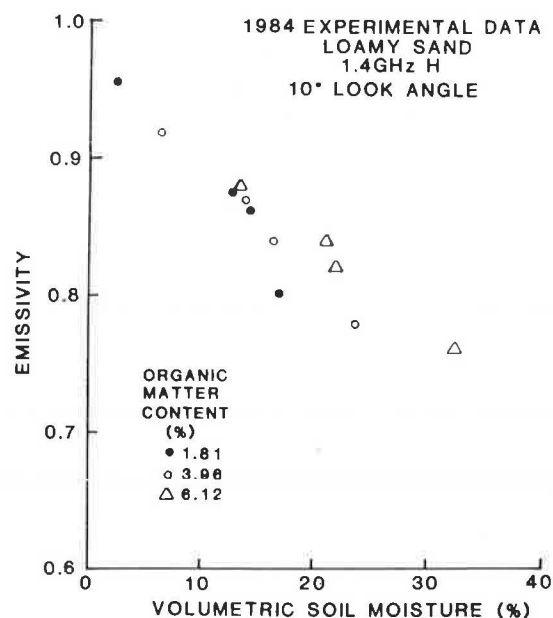


FIGURE 4 Observed values of emissivity and volumetric soil moisture on plots of varying organic matter content.

and in general are not as significant in the 5- to 21-cm wavelength range as at other wavelengths. At temperatures above freezing there is only minor variability and the same is true below freezing. However, at freezing there is a large transition in both k' and k'' as the dielectric properties of the water become those of ice. As a result, the effects can be important in the dielectric mixing models. Temperature effects can be ignored if the temperatures are above freezing.

The large difference in k' and k'' between frozen and unfrozen soils can be useful in determining such conditions using a dielectric device. If the moisture conditions are more or less uniform, the differences due to freezing would be quite apparent.

SALINITY EFFECTS

Carver (11) specifically considered the effects of salinity on the dielectric constant of a soil-water mixture. His approach was based on a straightforward adaptation of existing water-soil dielectric models using saline water values. The saline water values were based on well-known models of water at various levels of salinity. This approach is a good starting point because it considers the two variables of interest and can be adapted to any water-soil mixing model.

Some of the results found by Carver (11) on the effects of salinity include:

1. At a given microwave frequency, salinity decreases the real part of the dielectric constant and increases the imaginary part;
2. The sensitivity of the real part of the dielectric constant is relatively constant regardless of frequency (over the 1 to 10 GHz range); and
3. The sensitivity of the imaginary part of the dielectric constant to changes in salinity increases as the frequency decreases.

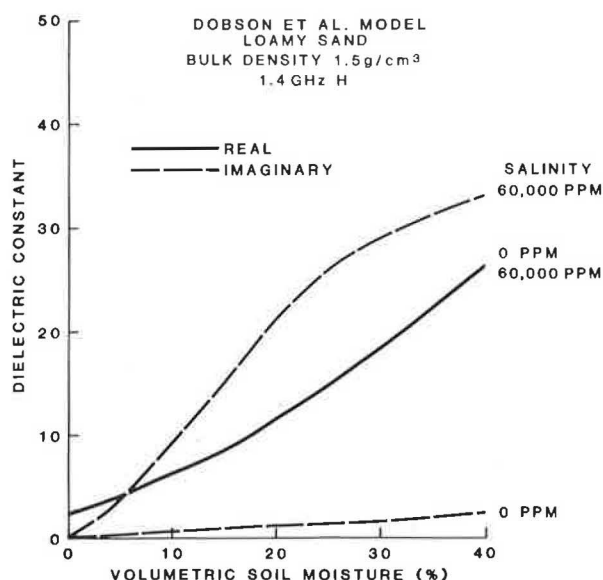


FIGURE 5 Effects of salinity of a saturated paste sample on the relationship between k' and k'' and volumetric soil moisture.

Any soil-water-mixing model can be adapted to consider salinity by including a component that adjusts the water k' - and k'' -values using a model such as that of Stogryn (12).

An alternative model for describing the effects of salinity has been proposed by Dobson et al. (4). In their approach, the dielectric constant of the mixture depends on the conductivity of the solution. Salinity, of course, changes this conductivity. The conductivity of the water is also computed using a saline water dielectric model (12). Figure 5 shows a summary of the mixture dielectric constants predicted using the Dobson et al. (4) model. At 1.4 GHz, 21-cm wavelength, salinity has no effect on k' but dramatically changes k'' . Jackson and O'Neill (13) used this model to predict emissivity in a series of controlled plot experiments and found that it reproduced observations quite well. However, it should be noted that the net effect of typical field salinity variations on emissivity is small because emissivity is not particularly sensitive to the imaginary part of the dielectric constant.

SOIL STRUCTURE EFFECTS

Jackson and O'Neill (5) found that commonly used dielectric mixing models could not explain observations of emissivity made over tilled soils with smooth surface conditions (achieved by rolling). Using data from controlled plots they were able to conclude that the reason for the inadequacy of dielectric models, such as that of Dobson et al. (4), is the structural differences between the laboratory samples these models are based on and the actual condition of tilled field soils. Laboratory soil samples are usually well mixed and consolidated or structureless. In contrast, after tillage field soil is made up of macro-aggregates and clods of varying sizes. A field soil will then retain this structure until it is broken down by wetting (irrigation or rainfall).

As mentioned previously, most theories used in developing dielectric mixing models recognize that the mixture value is the result of the component properties and their arrangement or structure. Considering the obvious physical differences between a consolidated soil and one consisting of aggregates, it appears to be logical that a mixture model that works for one condition would not work for the other.

Jackson and O'Neill (5) proposed a two-step approach to modeling the dielectric properties of a soil composed of aggregates and clods. First, the dielectric properties of the aggregates or clods are computed using a reliable model for consolidated soils such as that of Dobson et al. (4). Second, the complex dielectric constant of a soil mixture made up of aggregates and voids is determined.

This approach was evaluated using a wide range of formulations in the aggregate-void step. Figure 6 shows a summary of the emissivity results obtained for several models tested by Wang and Schmugge (3). The models are designated Type I (volumetric), Type II (refractive, dispersed spheres), and Type III (cubical array of spheres or geometric arrangement of disks). For a two-phase mixture, several of the models produce quite similar results. The category labeled Type III appears to explain the overall trend. Types I and II, which worked well in Figure 1, produced the worst results.

In addition to the formulations suggested by Wang and Schmugge (3), two methods based on a capacitance analogy of

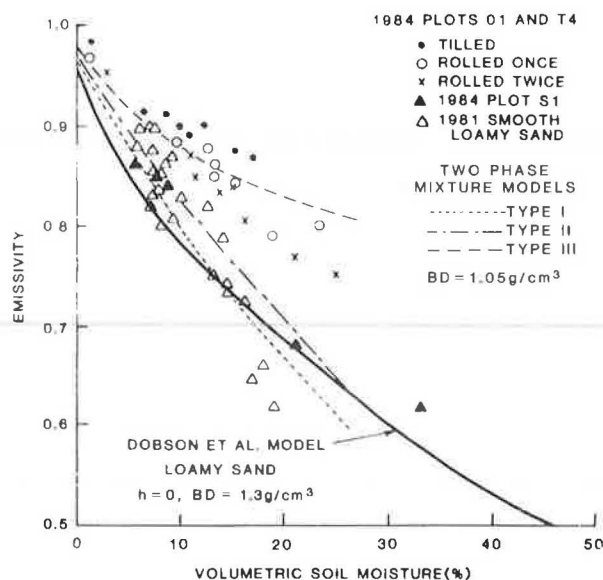


FIGURE 6 Predicted and observed relationships between volumetric soil moisture and emissivity using the Dobson et al. (4) model for the aggregate dielectric constant and the following models for the aggregate-void mixture: Type I volumetric; Type II refractive, dispersed spheres (Wagner and Bottcher); and Type III cubical array of spheres (Rayleigh) or geometric arrangement of disks (Polder and van Santen).

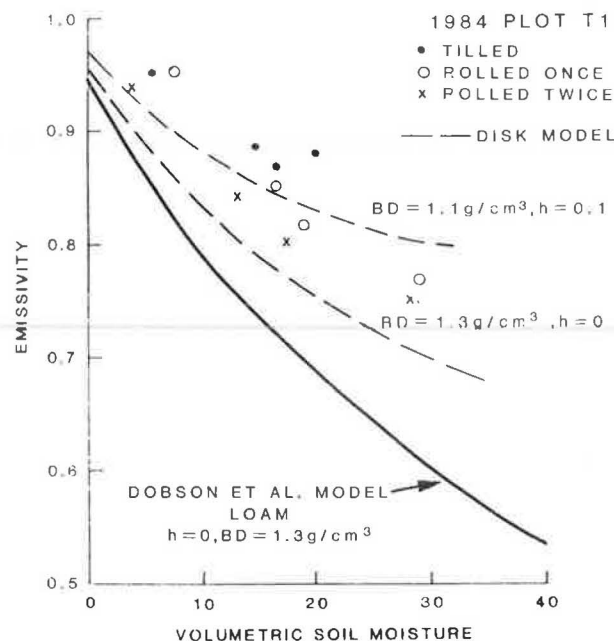


FIGURE 7 Predicted and observed relationships between volumetric soil moisture and emissivity using the disk inclusions aggregate-void dielectric mixing model for a loam.

the physical system were evaluated. In the first approach a general formulation presented by Sachs and Spiegler (14) was modified for an aggregate mixture. This model explained the data quite well; however, further analyses of the physical significance of some of the parameters is needed before this model can be widely used. The same is true of the second approach that was based on a model described by Ansoult et al. (15).

Jackson and O'Neill (5) also examined a model that was based on a theoretical representation proposed by Polder and van Santen (6) for disk-shaped inclusions in a host medium. Figure 7 shows the results obtained with this model. The authors concluded that because this model had a theoretical basis and required no parameter estimation it would be the one of choice.

SUMMARY

Microwave remote sensing has the potential for widespread use in soil moisture measurement because of the large contrast in the dielectric properties of dry soil and water. Recent research has examined the effects of a number of soil characteristics on the relationship between soil moisture and dielectric properties or emissivity. Soil texture, density, and structure have important effects that must be accounted for if soil moisture is to be estimated. Soil salinity, temperature, and organic matter content are not important at longer wavelengths.

REFERENCES

1. F. T. Ulaby, R. K. Moore, and A. K. Fung. *Microwave Remote Sensing: Active and Passive*. Addison-Wesley Publishing Co., Reading, Mass., 1986, Vol. 3.
2. T. J. Schmugge. Effects of Texture on Microwave Emission from Soils. *IEEE Transactions on Geoscience and Remote Sensing*, Vol. GE-18, 1980, pp. 353-361.
3. J. R. Wang and T. J. Schmugge. An Empirical Model for the Complex Dielectric Permittivity of Soil as a Function of Water Content. *IEEE Transactions on Geoscience and Remote Sensing*, Vol. GE-18, 1980, pp. 288-295.
4. M. C. Dobson, F. T. Ulaby, M. T. Hallikainen, and M. A. El-Rayes. Microwave Dielectric Behavior of Wet Soil, Part II: Dielectric Mixing Models. *IEEE Transactions on Geoscience and Remote Sensing*, Vol. GE-23, 1985, pp. 35-46.
5. T. J. Jackson and P. E. O'Neill. Microwave Dielectric Model for Aggregated Soils. *IEEE Transactions on Geoscience and Remote Sensing*, Vol. GE-24, 1986, pp. 920-929.
6. D. Polder and J. H. van Santen. The Effective Permeability of Mixtures of Solids. *Physica*, Vol. XII, 1946, pp. 257-271.
7. G. P. de Loor. The Dielectric Properties of Wet Materials. *IEEE Transactions on Geoscience and Remote Sensing*, Vol. GE-21, 1983, pp. 364-369.
8. L. M. Arya and J. F. Paris. A Physicoempirical Model To Predict the Soil Moisture Characteristic from Particle-Size Distribution and Bulk Density Data. *Soil Science Society of America Journal*, Vol. 45, 1981, pp. 1023-1030.
9. A. M. Shutko. Microwave Radiometry of Lands Under Natural and Artificial Moistening. *IEEE Transactions on Geoscience and Remote Sensing*, Vol. GE-20, 1982, pp. 18-26.
10. T. J. Jackson and T. J. Schmugge. Passive Microwave Remote Sensing of Soil Moisture. *Advances in Hydrosciences*, Vol. 14, 1986, pp. 123-151.
11. K. R. Carver. Microwave Remote Sensing of Saline Seeps. *Proc.*,

- Microwave Remote Sensing Symposium*, NASA Johnson Space Center, Houston, Tex., 1977, pp. 216-231.
12. A. Stogryn. Equations for Calculating the Dielectric Constant of Saline Water. *IEEE Transactions on Microwave Theory and Technique*, Vol. MMT-19, 1971, pp. 733-736.
 13. T. J. Jackson and P. E. O'Neill. Effects of Salinity on the Microwave Emission of Soils. *IEEE Transactions on Geoscience and Remote Sensing*, Vol. GE-25, 1987, pp. 214-220.
 14. S. B. Sachs and K. S. Spiegler. Radiofrequency Measurements of Porous Conductive Plugs, Ion-Exchange Resin-Solution Systems. *Journal of Physical Chemistry*, Vol. 68, 1964, pp. 1214-1222.
 15. M. Ansault, L. W. DeBacker, and M. Declercq. Statistical Relationship Between Apparent Dielectric Constant and Water Content in Porous Media. *Soil Science Society of America Journal*, Vol. 49, 1985, pp. 47-50.

Publication of this paper sponsored by Committee on Photogrammetry and Aerial Surveys.

Appalachian Folds, Lateral Ramps, and Basement Faults: A Modern Engineering Problem?

HOWARD A. POHN

Field studies and analysis of radar data have shown that cross-strike faulting in the central and southern Appalachians has affected geologic structures at the surface. These basement faults appear to have been active through much of geologic time. Indeed, more than 45 percent of modern earthquakes occur along these narrow zones here termed "lateral ramps." Because of this seismic activity, these lateral ramps are likely to be zones that are prone to slope failure. The engineer should be aware of the presence of such zones and the higher landslide potential along them.

Field studies combined with analysis of recently acquired side-looking airborne radar (SLAR) data and proprietary seismic reflection profiles for the central and southern Appalachians have shown that cross-strike basement faulting affects geologic structures at the surface. The effects are (a) abrupt changes in fold wavelength and fold plunge along strike in the Valley and Ridge Province; (b) conspicuous discontinuities in the Blue Ridge Province; and (c) the presence of long, straight river segments in the Piedmont and Coastal Plain Provinces.

The basement faults have been active throughout much of geologic time. This interpretation is substantiated by subsurface data that show active growth faulting from Precambrian through at least Ordovician times. Further evidence consists of coincident Precambrian highs and east-west border faults that cross the Mesozoic basins. Continued activity is supported by the observation that between 35 and 50 percent of historic seismicity is directly coincident with these cross-strike basement faults and their associated lateral ramps. These lateral ramps are zones in which different stratigraphic levels are connected by ramp faults that rise or fall along the strike of the Appalachian mountain chain.

More intense Alleghenian folding and faulting and continued post-Alleghenian fault movements associated with the lateral

ramps have made these localities areas of slope instabilities and therefore prone to slope failure. Mapping by Arthur P. Schultz (1) and recently by C. Scott Southworth and Schultz (2, 3) has shown that large (several square kilometers) blocks have broken away from the ridgetops and slid downslope by either catastrophic landslide or slower creep. Most of these displaced blocks and landslides occur in an area geographically close to the location of lateral ramps mapped in the field or observed on radar data (Figure 1).

As recently as the spring of 1985, a landslide buried part of Highway 250 in central Virginia along the Highland County lateral ramp, and occurrences of this type should be expected in the future.

It behooves the engineer to be aware of such zones of potential slope instability and active seismicity in the planning of major structures such as highways and dams. Efforts should be made to avoid these areas if possible or to plan structures to accommodate the possibility of slope failure or seismic activity.

REFERENCES

1. A. P. Schultz. Ancient Giant Rockslides, Sinking Creek Mountain, Southern Appalachians, Virginia. *Geology*, Vol. 14, No. 1, 1986, pp. 11-14.
2. C. S. Southworth and A. P. Schultz. *Characteristics of Giant Rockslides in the Appalachian Valley and Ridge, Virginia, West Virginia, Maryland, and Pennsylvania*. U.S. Geological Survey Open-File Report 86-94. U.S. Geological Survey, Department of the Interior, 1986, 4 pp., 3 oversized sheets.
3. C. S. Southworth and A. P. Schultz. Photogeologic Interpretation Reveals Ancient, Giant Rockslides in the Appalachian Valley and Ridge Province, Virginia and West Virginia. *Association of Engineering Geologists Newsletter*, Vol. 29, No. 2, 1986, pp. 31-33.

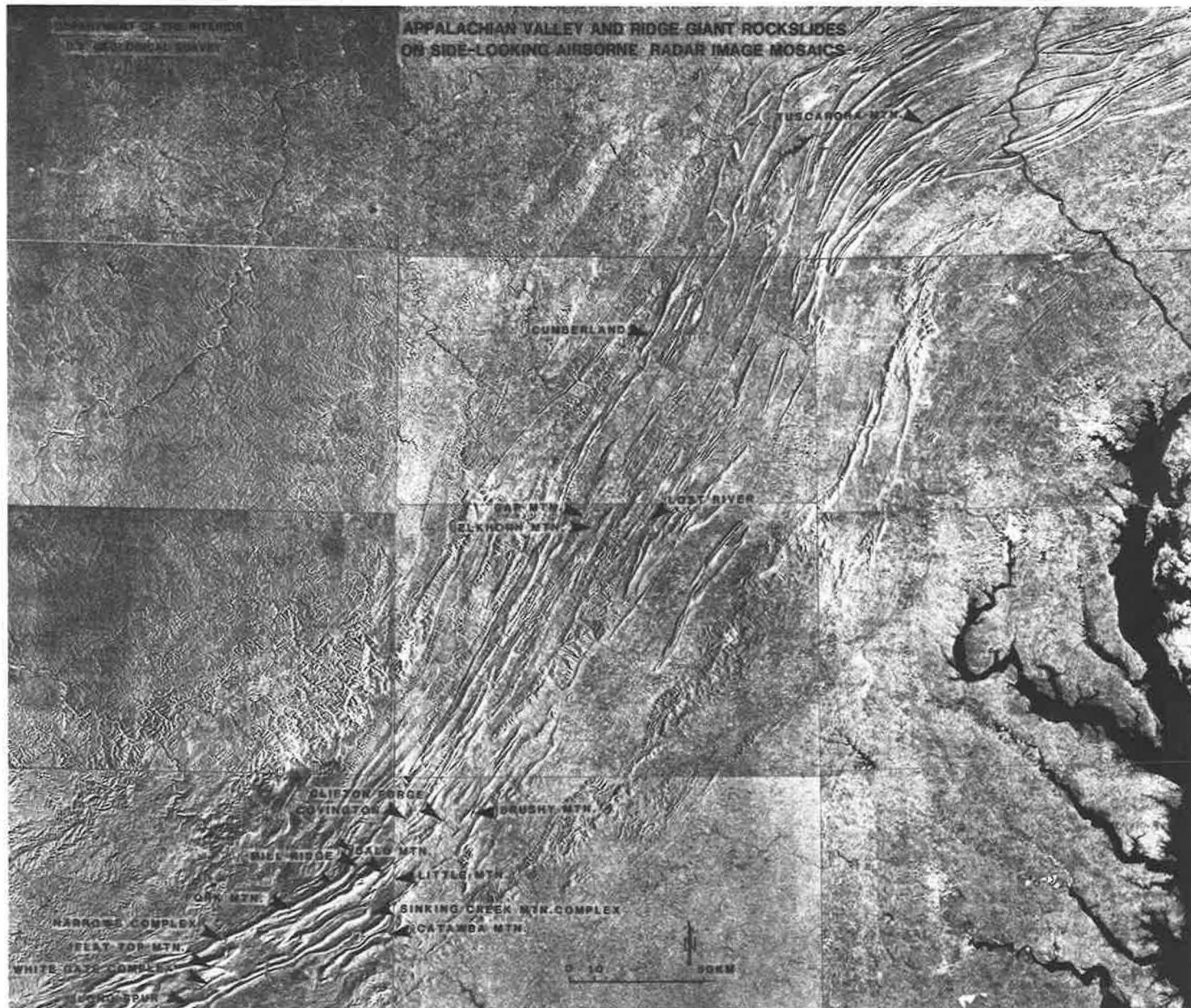


FIGURE 1 Radar image of part of the central and southern Appalachian Valley and Ridge Province showing areas of giant rockslides from Southworth and Schultz (3).

Terrain Simulation for Transportation Planning

JACK H. HANSEN AND MITCHELL J. HURST

The old adage that one picture is worth a thousand words is really a conservative estimate when applied to elevational data points. Digital elevation data presently being gathered or converted from previous mapping efforts afford valuable data for transportation planners, but these data are not readily usable. When these data are converted to an aerial photolike scene, they offer a valuable additional planning tool. Surface simulation models based on U.S. Geological Survey (USGS) digital elevation models were accomplished on a VAX 11/780 with a Vectrix VX384 display. A Hermite curve technique was used to simulate the surface configuration of the terrain. The terrain surface simulation was overlaid with USGS digital line graph data to show transportation routes. In addition to vertical views, oblique views from any direction may be shown and the direction and vertical angle of the source of lighting may be chosen.

For some years, the U.S. Geological Survey (USGS) has produced digital elevation model (DEM) and digital line graph (DLG) data for various parts of the United States. This ongoing program to make digital terrain data available for users recognizes the increasing importance of digital data for geographic data base systems. The DEM data together with a program such as Generalized Computer Aided Route Selection (GCARS) may be used to automatically locate alternate routes on the basis of terrain data (1). Other alternate routes based on such criteria as economic development or land cost may be developed and value weights may be applied to each data base to determine the best routes under various evaluation guidelines. Whether the route selection process is automated as outlined or is derived in some other manner, the various alternate routes together with existing transportation systems and other pertinent features are usually drawn on maps and possibly aerial photos for visual examination. Where topography contributes importantly to route location, topographical maps may be used to show the route's relationship to the terrain. Although such presentations are easily understood by engineers, the general public, other professionals and engineers alike, can more readily visualize topographic features when shown in three-dimensional form such as is possible with claylike models. However, the cost and time required to build such models make them impractical except for public hearings. Stereo pairs of photos may be used; this is an excellent planning tool for individuals skilled in their use, but simultaneous group use is not feasible.

Simulated terrain surfaces, however, may be viewed by groups and are adaptable to many uses. Their usefulness in

hydrology has been demonstrated (2). The scale may be selected because any portion of the DEM data base may be processed and further adjusted when reproduced as a hard copy. Much analysis may be done on the graphics-quality CRT without the need for a hard copy until the later planning stages. In this paper the terrain simulation techniques and equipment and the capabilities of the system are discussed and some of the system products are illustrated.

DIGITAL LINE AND ELEVATION MODEL DATA

The USGS produces both DEM and DLG data bases. This study uses DEM and DLG data based on the 7.5-min format that corresponds to the 7.5-min series topographic maps. The DEM data base contains the digital elevations on a 30-m grid, produced from 1:24,000-scale quadrangles or directly from aerial photography using photogrammetric digital methods. The DLG data base comprises up to five separate digital planimetric line graph data bases including transportation, hydrology, boundaries, public land survey system, and other culture information. Each DEM and DLG covers a 7.5-min quadrangle comprising approximately 157 km² (60 mi²). Two similar products of other agencies are available at smaller scales, both of which cover 1- × 1-degree blocks and are produced from 1:250,000-scale quadrangles. One data base has a ground distance of 3 arc-sec between digitized points, and the other uses a ground distance of 61 m (200 ft) between digitized points.

The Rockwood Tennessee quadrangle was selected for this study because of the availability of DEM data, the DLG transportation data, and the presence of water bodies and some fairly steep terrain in the northwestern part of the quadrangle. Portions of the digital terrain tapes were transferred to disk for processing on a Digital Equipment Corporation VAX 11/780 computer.

SIMULATION TECHNIQUES AND EQUIPMENT

Many techniques may be used to create surface models. The objective is to select a method that gives the desired accuracy within acceptable computer processing times. In the case of this study, accuracy relates to the visual realism that the terrain model affords. To obtain this realism, the technique must include shading.

Some data base primitives used in scene creation include planar surfaces, quadric surfaces, and curved surfaces. Each

primitive has an associated computation time required to calculate an arbitrary point (x, y, z) on the primitive and to accomplish continuous shading.

Planar faces offer easy storage of elevational terrain data because each planar surface can be stored as four DEM elevations. Although scene coordinates for a surface could be quickly calculated and this technique is used for many flight simulator packages because it allows real-time perspective variations, it lacks realism because the transition from one planar face to another is often quite noticeable. If enough planar faces are used, the continuous shading characteristics of a curved surface can be obtained, but then the advantages of less computational time are obviated. Quadric surfaces minimize the time necessary to solve for unknown points, but the transformation of DEM data into a set of quadrics and surfaces has yet to be done.

Both the B-spline and the Bezier surface models were considered, but the approximately 100,000 DEM points that must be processed to do only one-half a quadrangle would demand long computational times for the Bezier surface because each control point (DEM elevation) affects all points on a Bezier surface. The B-spline surface was not selected because its surface is not forced to pass through the initial control points used to create the surface. Therefore, the surface would not be correct at the DEM data points.

Curve surfaces provide the most accurate data base primitives but require considerable computational time to solve for the arbitrary points on the surface. Three-dimensional shapes can be formulated in various ways by using curved surfaces (3-7). Because obtaining surface realism is of primary importance to this study, a curved surface technique was selected, namely, the Hermite curve. Details of the mathematical definition of a Hermite curve were described in a previous publication (8). Surface patches formed by Hermite curves have first derivative continuity and local control. That the surface passes through all of the DEM elevations thus assuring data accuracy at the known control points in addition to the realism afforded by Hermite curves determined the choice of this surface technique. The essential steps of the technique used to produce the simulated terrain surfaces follow.

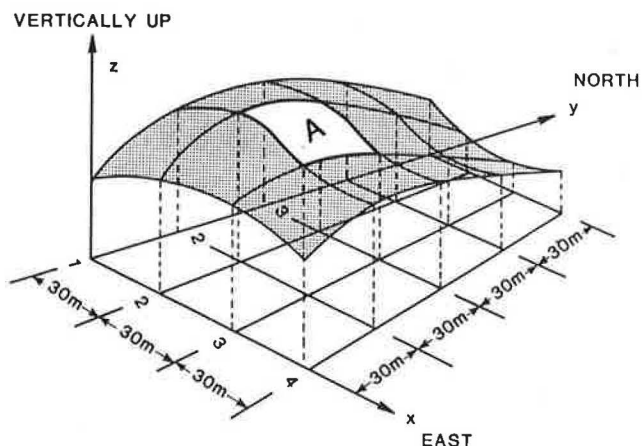


FIGURE 1 The 30-m spaced DEM data are transformed to a corresponding surface patch that initially has four known x, y, z coordinates.

- Digital elevational model data derived either directly from aerial photos by photogrammetric methods or from interpolated contour maps are the data basis.

- The digital elevation model is transformed to surface patches; each patch initially has four x, y, z control coordinates. Because the DEM data are spaced on a 30-m grid, each surface patch is made to correspond to a 30-m square. Figure 1 shows the relationship.

- Surface patches are constructed from successive interpolations of Hermite curves. The curve coordinates are calculated from the positions and tangents of the end points of the curves.

- A hidden surface and shading algorithm separately processes each surface patch.

- The surface normal at each point and the selected sun vector are used to calculate the shading intensity. The amount of light is calculated as a function (Lambert's cosine law) of the angle (θ) between the normal of Point P and the sun vector (Figure 2).

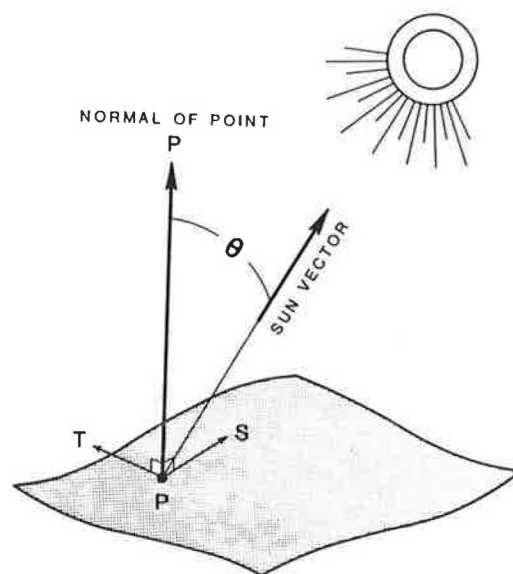


FIGURE 2 The shading intensity at each point is determined by the normal at each point and the sun vector.

- An additional intensity is assigned to match an estimate of the nondirectional scattered light component of sky light.

- Three-dimensional points are projected to the two-dimensional view plane using a transformation that gives the x, y viewing device coordinates for points on the surface patches.

- The distance that the point is away from the view plane is compared with previously calculated points and, if the distance is smaller, the new point is visible and a new intensity value and distance value take the place of the former value.

- The intensity of each point on the surface patch is calculated when it meets the criteria of being the closer scene point for a corresponding point on the screen. The result is a screen-buffer that contains the intensity values of all of the visible surface points.

- The intensity values are output to the display device.

EQUIPMENT AND DATA PROCESSING

The Digital Equipment Corporation VAX 11/780 with a VMS operating system was used for computation. Screen output was to a Vectrix VX384. All programs were written in FORTRAN 77. Processing times vary according to the portion of the DEM data quadrangle selected. It takes about 10 min to process approximately 100,000 DEM data points, which cover 78 km² (30 mi²). It is estimated that reprogramming and incorporating some new computational efficiencies could reduce processing time to 2 to 3 min for a similar scene.

The Vectrix VX384 display device has a resolution of 672 by 480 pixels. Although this device is capable of producing a multitude of colors, for this study only one selected color was used for land surface thus allowing shading and perspective to impart realism to a scene. The appearance of water bodies in some example scenes illustrates how various colors might be used to enhance visual realism or to possibly accent certain elevational zones.

All of the examples shown are produced from photographs of the Vectrix screen. Such techniques as writing to film can be employed to produce high-resolution images.

TERRAIN MODEL EXAMPLES AND COMPARISONS

The value of a terrain model may be measured by how well it depicts the topography of an area. As a comparison, a black-and-white copy of a color infrared photograph covering the land area of the most northerly 38 percent of the 7.5-min series Rockwood quadrangle is shown in Figure 3. The simulated terrain model for this same area is shown in Figure 4. This model simulates a high oblique view angle from due south and

uses lighting from the east to produce an early morning-appearing scene. Note how easily the Cumberland Escarpment is seen running northeast from the western boundary of the model. An inlet from the Tennessee River appears at the center lower edge of the simulated scene.

The three-dimensional-appearing view of the area facilitates locating possible routes over the Cumberland Escarpment. A route closely matching the existing route over the escarpment would probably be chosen by most planners given only the terrain surface model (Figure 4) together with guide instructions to advantageously use passes, saddles, and lead-in ridges to gain elevation. No vertical exaggeration was used on any of the models shown, but any desired vertical exaggeration may be employed for greater terrain emphasis. This surface model is based on approximately 75,000 DEM data points and covers about 59 km² (23 mi²).

Figure 5 is a simulated vertical view of the Rockwood area and the Cumberland Escarpment. Late afternoon sun from the west is simulated and DLG data of roads are superimposed on the DEM model. The basis of simulation is approximately 100,000 DEM data points covering about one-half of the Rockwood quadrangle (30 mi²). US-70 ascends the upper portion of the escarpment as shown on the model. The Tennessee River is shown in the lower portion of the model. Simulated terrain surfaces using brown for land areas and blue for water bodies overlaid with white roads are excellent for planning. Conversion to black-and-white images greatly degrades the terrain details and the road line sharpness as Figures 5 and 6 indicate. Examination of the model with overlaid roads reveals the general northeast direction of roads dictated by the major topography of the region. The placement of the roads in relation to relief details and water bodies appears to be accurate. However, the use of the road information derived from DLG data would be greatly improved if some method were used to



FIGURE 3 Aerial photograph of the upper portion of the Rockwood quadrangle shows the Cumberland Escarpment running northeast on the left side of the photo and the city of Rockwood, Tennessee, in the upper central portion of the photo.



FIGURE 4 A simulated oblique view terrain surface of the Rockwood area and the Cumberland Escarpment has a view angle from the south and simulated early morning lighting.

designate the relative importance of roads. The assignment of identifiers to given line segments is best done at the time of road digitization.

Figure 6 shows a smaller portion of the Rockwood quadrangle covering 25 km² (10 mi²). Detail is improved on this terrain model because the number of DEMs that make up the

scene is approximately 30,000 compared with the 100,000 DEMs included in Figure 5. This means that, because there are fewer surface patches, more points on each patch can be used and an intensity value for each point calculated. The number of points projected to the screen-buffer must be great enough to impart an intensity to each pixel on the screen so that pixel



FIGURE 5 A simulated vertical view terrain surface of the Rockwood area, the Cumberland Escarpment, and the Tennessee River has simulated late afternoon lighting and is overlaid with the road network of the area.



FIGURE 6 Smaller portions of the digital elevation model may be selected as the basis of simulating terrain; this results in greater surface detail.

number is constant for a screen device. Because the number of screen pixels is a function of the graphics output CRT, it is easy to see that elevational detail is enhanced by selecting smaller land areas (fewer DEM data points) for a terrain model so that each surface patch (30-m by 30-m ground distance) is described by more points on each surface. Note is made of the degree to which the location of roads agrees with the perceived relief.

The largest scale simulation done (not shown), which comprises approximately 11,000 DEM data points and covers an area of about 10 km² (4 mi²), may define the limits of large-scale simulation with the USGS DEM data and the equipment used in this study. Close examination of the color slide copy of the Vectrix CRT output of this terrain simulation shows a tendency toward a blocky pattern probably imparted in part by the 30-m square spacing of the DEM data, inaccuracies of the digital data bases, and the effects of a three-dimensional scene being output to a two-dimensional screen. Automated photogrammetric elevational equipment often records the elevation of the top of objects and vegetation, which contributes to some of the blockiness. This blocky effect can be seen on a slide with a scale of 1:130,000 when observed with a 10× hand lens. Projection of the slide image confirms this observation.

CONCLUSIONS

Simulated terrain models based on DEM data can be used advantageously in the planning process wherever topography is an element to be considered. The addition of DLG data, transportation information, and other boundary information as a line

overlay to the simulated terrain models increases the planning value of such displays and makes them especially useful for public hearings. The ability to select limited land areas and to realistically depict these areas as viewed from any selected vantage point with selected lighting direction is a powerful tool for transportation and land planners.

REFERENCES

1. A. K. Turner. *Computer-Assisted Procedures to Generate and Evaluate Regional Highway Alternatives*. Joint Highway Research Project, Final Report 32. Purdue University, West Lafayette, Ind., 1968, 281 pp.
2. J. H. Hansen and M. J. Hurst. *Digital Techniques for Terrain Simulation*. Proc., Fall Convention, American Society of Photogrammetry and Remote Sensing, Anchorage, Alaska, 1986.
3. B. Barsky. A Description and Evaluation of Various 3-D Models. *IEEE Computer Graphics and Applications*, Vol. 4, No. 1, Jan. 1984, pp. 38–52.
4. C. Brown and D. Ballard. *Computer Vision*. Prentice-Hall, Inc., Englewood Cliffs, N.J., 1982.
5. J. Foley and A. Van Dam. *Fundamentals of Interactive Computer Graphics*. Addison-Wesley, Reading, Mass., 1982.
6. R. Marshall, R. Wilson, and W. Carlson. Procedure Models for Generating Three-Dimensional Terrain. *Computer Graphics*, Vol. 14, No. 3, July 1980, pp. 154–162.
7. M. Pratt and I. Faux. *Computational Geometry for Design and Manufacture*. Ellis-Horwood Limited, Chichester, England, 1979.
8. M. Hurst. *Terrain Simulation of United States Geological Survey Digital Elevation Models*. M.S. thesis. The University of Tennessee, Knoxville, 1985, 59 pp.

Publication of this paper sponsored by Committee on Photogrammetry and Aerial Surveys.

Nailed-Soil Retaining Structures: Design and Practice

ILAN JURAN

Soil nailing is an *in situ* soil reinforcement technique that has been used during the last two decades, mainly in France and Germany, to retain excavations or stabilize slopes. The fundamental concept of soil nailing is the reinforcement of the ground by passive inclusions, closely spaced, to increase the overall shear strength of the *in situ* soil, to restrain its displacements, and to limit its decompression during and after excavation. The technology, construction process, design methods, and fundamental aspects of behavior and soil-nail interaction in nailed-soil retaining structures are discussed.

Soil nailing is an extension of the "new Austrian Tunneling Method" (1), which combines reinforced shotcrete and rock-bolting to provide a flexible support system for the construction of underground excavations. However, its rapid development has been considerably enhanced by the increasing use of the Reinforced Earth® technique in mountainous areas.

Soil nailing has been used in a variety of civil engineering projects including stabilization of railroad and highway slopes (2,3), construction of retaining structures for excavations as deep as 30 m (4–8), and tunneling and other civil and industrial projects (9). Typical applications are shown in Figure 1. As demonstrated by Gassler and Gudehus (10), nailed-soil retaining structures can withstand both static and dynamic vertical loads at their upper surface without excessive displacements.

In this paper are presented the technology, construction process, design methods, and fundamental aspects of behavior and soil-nail interaction in nailed-soil retaining structures. A shorter version of this paper has been published elsewhere (11).

TECHNOLOGY, STRUCTURAL ELEMENTS, AND CONSTRUCTION PROCESS

The main components of a nailed-soil retaining structure are the *in situ* ground, the resisting inclusions, and the facing. The economy of the system is predominantly dependent on the technology and construction rate. The technology of soil nailing is flexible, and both the structural elements (inclusions and facing) and installation techniques can be easily adapted, even during construction, to provide the most appropriate engineering solution for specific site conditions and soil profiles. To date, soil nailing has been used primarily in temporary retaining structures. Concerns about permanent nailed-soil systems are the durability of metallic inclusions in the ground and the

shortcomings of facing technology. Therefore, in recent years, technological developments have been mainly focused on producing low-cost, corrosion-protected nails and prefabricated concrete or steel panels that provide a more appropriate response to different aesthetic, environmental, and durability requirements.

Inclusions and Installation Techniques

The steel reinforcing elements currently used can be mainly classified as (a) driven nails, (b) grouted nails, (c) jet-grouted nails, and (d) encapsulated corrosion-protected nails.

Driven Nails

Driven nails, commonly used in France and Germany, are generally low-cost, small-diameter (15 to 46 mm) rods or bars, or metallic profiles, made of mild steel with a yield strength of 350 MPa (50 ksi). They are closely spaced (2 to 4 bars per square meter) and create a rather homogenous composite reinforced soil mass.

The nails are driven into the ground at the designed inclination using a vibropercussion pneumatic or hydraulic hammer with no preliminary drilling. Special nails with an axial channel can be used to allow for grout sealing of the nail to the surrounding soil after its complete penetration. This installation technique is rapid and economical (4 to 6 bars per hour). However, it is limited by the length of the bars (maximum length about 20 m) and by the heterogeneity of the ground (e.g., boulders).

Grouted Nails

Grouted nails are generally high-strength steel bars (15 to 46 mm in diameter) with a yield strength of 1050 MPa (150 ksi). They are placed in boreholes (10 to 15 cm in diameter) with a vertical and horizontal spacing varying typically from 1 to 3 m, depending on the type of soil. The nails are conventionally cement or resin grouted by gravity or under low pressure. Ribbed bars can be used to improve the nail-grout adherence, and special perforated tubes have been developed to allow injection of grout through the inclusion.

Jet-Grouted Nails

Jet-grouted nails are composite inclusions made of a grouted soil with a central steel rod that can be as thick as 30 to 40 cm.

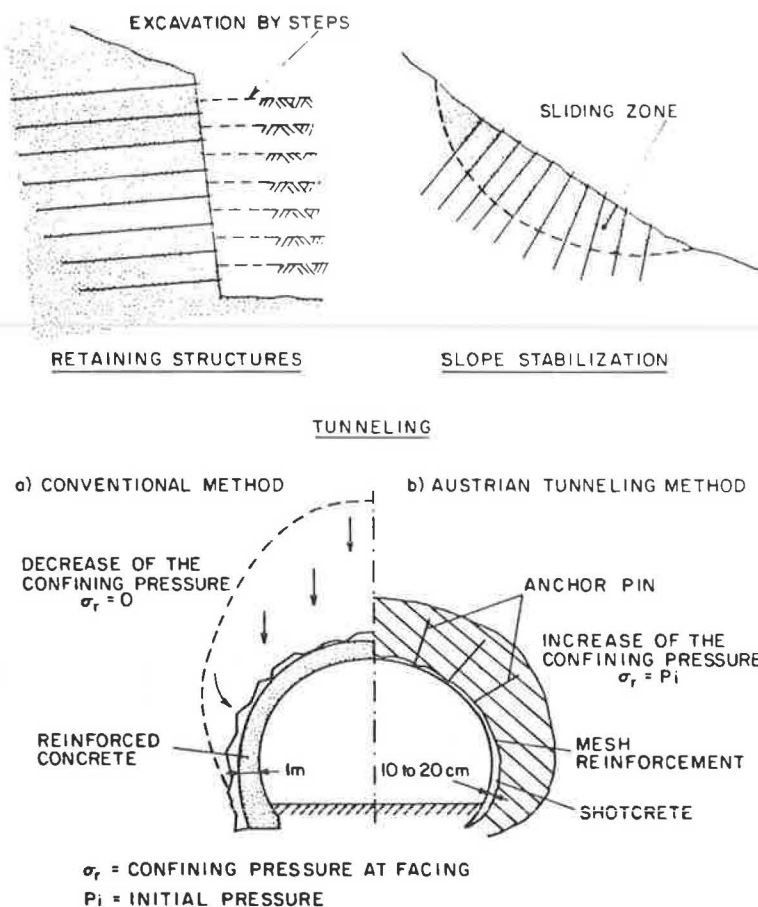


FIGURE 1 Main applications of soil nailing.

A technique that combines vibropercussion driving and high-pressure (> 20 MPa) jet grouting has recently been developed and patented by Louis (9). The nails are installed (Figure 2) using a high-frequency (up to 70 Hz) vibropercussion hammer, and cement or resin grouting can be performed either during or after installation. The grout is injected through a small-

diameter (few millimeters) longitudinal channel in the reinforcing rod under a pressure that is sufficiently high to cause hydraulic fracturing of the surrounding ground. However, for current applications, nailing with a significantly lower grouting pressure (≈ 4 MPa) has been successfully used, particularly in granular soils. The jet-grouting installation technique provides recompaction and improvement of the surrounding ground and increases significantly the shear and pullout resistances of the composite inclusion.

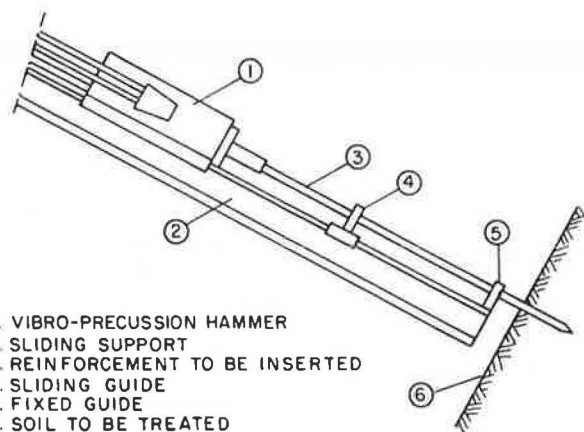


FIGURE 2 Jet nailing: Installation of reinforcing elements with or without simultaneous grouting (C. Louis, unpublished results, 1985).

Corrosion-Protected Nails

Corrosion-protected nails have been developed recently by French contractors (Intrafor-Cofor; Solrenfor) to be used in permanent structures. In this type of inclusion, the steel bars are enclosed in grout to protect against water penetration. In the Solrenfor nail (Figure 3a), the steel bar and the surrounding grout are protected by casing made of steel or plastic. In the Intrafor-Cofor nail (Figure 3b), the prestressing effect maintains the grout under compression and thus keeps it from microcracking. However, other doubly encapsulated nails similar in concept to the technology used in earth anchors could be used. In American practice, contractors have proposed and used resin-bonded epoxy nails to achieve double protection.

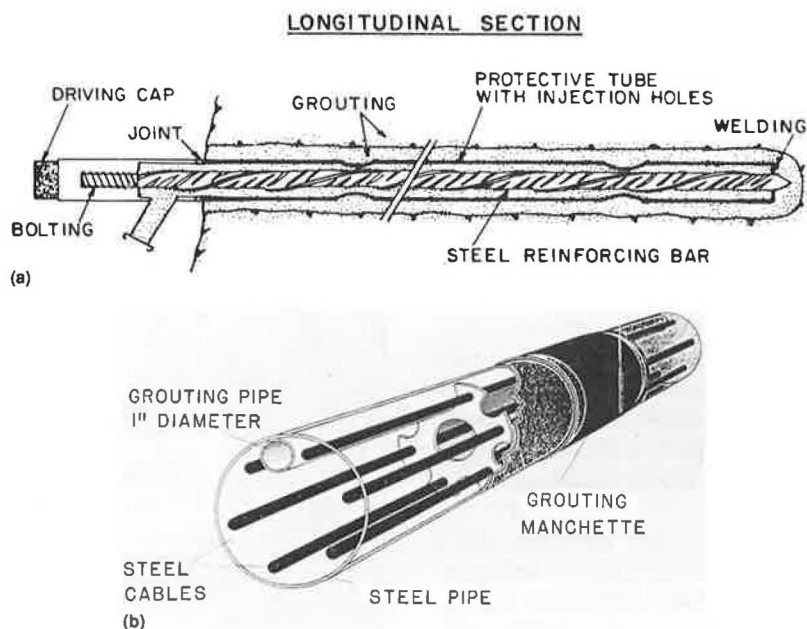


FIGURE 3 TBHA nail developed and patented by Solrenfor for permanent structures (a) and prestressed multireinforced nail, Intrapac, developed by Intrafor-Cofor (b).

Facing

The main functions of the facing are to ensure the stability of the local ground between the reinforcement layers, to limit its decompression immediately after excavation, and to protect the ground from surface erosion and weathering effects. Therefore the facing has to be continuous, fit the irregularities of the cut slope surface, and be flexible enough to withstand ground displacement during excavation. Depending on the application and soil type, four kinds of facing are presently used.

Shotcrete Facing

Shotcrete facing (10 to 25 cm thick) is currently used for most temporary retaining structures in soils. This facing technology provides a continuous, flexible surface layer that can fill voids and cracks in the surrounding ground. It is generally reinforced with a welded wire mesh and its required thickness is obtained by successive layers of shotcrete (each 9 to 12 cm thick). This technique is relatively simple and inexpensive, but it does not generally provide the technical quality and the aesthetic aspect required for permanent structures. In particular, the durability of the shotcrete facing can be affected by groundwater, seepage, and environmental factors such as climatic changes and freezing, which may induce cracking. In addition, construction of a shotcrete facing makes provision of efficient drainage at the concrete-soil interface difficult.

Welded Wire Mesh

Welded wire mesh is generally used to provide a facing in fragmented rocks or intermediate soils (chalk, marl, shales).

Concrete and Steel Facings for Permanent Structures

Cast-in-place reinforced-concrete facing is, to date, most frequently used for permanent structures. However, prefabricated concrete or steel panels are now being developed for permanent structures. These panels can be designed to meet a variety of aesthetic, environmental, and durability criteria. They provide appropriate technical solutions for integrating continuous drainage behind the facing. Figure 4 (top) shows Solrenfor metallic panels for inclined facing (C. Louis, unpublished results). The rectangular steel panels are bolted together and the soil nailing is performed through their common corners. Figure 4 (bottom) shows prefabricated concrete panels with continuous geotextile drainage. Composite panels have also been used in association with prefabricated steel panels and cast-in-place concrete.

Grout nails are generally attached to the facing (mesh or shotcrete) by bolting the bars to a square steel plate (30 to 40 cm wide), whereas driven bars are generally attached to the facing by cladding or other suitable methods.

CONSTRUCTION PROCESS AND MONITORING

Construction of a nailed-soil retaining structure involves three main repetitive stages: (a) excavation of a limited height, (b) nailing and drainage, and (c) placing the facing. The technology and the construction process are fundamentally conceived to minimize disturbance of the ground during excavation, to limit its decompression, and to prevent deterioration of the original mechanical properties of the ground. Therefore the nailing system (facing and reinforcement) has to be placed as quickly as possible after excavation.

Excavation is done with small conventional earth-working equipment in typical incremental steps 1.5 to 3 m deep. In general, the short-term cohesion of the soil is sufficient to ensure local stability of each excavation step. The cut slope must be properly excavated to prevent local instabilities that could induce movement at the upper part of the nailed-soil wall.

Where there is groundwater, an appropriate drainage system should be provided to (a) protect the facing elements by shallow drainage (plastic pipes, 10 cm in diameter, 30 to 40 cm long) and (b) prevent saturation of the nailed ground, which can significantly affect the structure's displacements and cause instabilities during or after the excavation (slotted plastic tubes that are longer than the nails are generally used). In the case of permanent structures with prefabricated panels, a continuous drain such as a geotextile composite can be placed behind the facing.

Soil-nailing technology relies on passive inclusions, and a certain soil displacement is required to effectively mobilize the resisting forces. Therefore it has been essential to monitor actual structures, to measure the facing displacements in different types of soils, and to verify that they are compatible with design criteria for admissible displacements.

BEHAVIOR AND DESIGN OF NAILED-SOIL RETAINING STRUCTURES

Soil-Reinforcement Interaction

The soil-reinforcement interaction in nailed-soil retaining structures involves two fundamental mechanisms: (a) lateral friction and (b) passive soil thrust on relatively rigid inclusions. The small-diameter inclusions, which are generally used in soil nailing, are relatively flexible. Therefore the soil displacement required to mobilize the normal passive soil thrust on the inclusion is substantially greater than that required to generate lateral friction at the soil-inclusion interface. For a given structural geometry and soil profile, the mobilized interaction mechanism depends mainly on the construction process and installation techniques, the bending stiffness of the inclusion, and its inclination with respect to the potential failure surface.

Lateral Friction

The mobilization of lateral friction along inclusions (piles, reinforcing elements, etc.) has already been extensively studied. Both laboratory studies and pullout tests on actual Reinforced Earth walls have provided experimental data for the evaluation of the effect of various parameters (surface characteristics of the reinforcement, rib effect, density and dilatancy properties of the soil, type and amount of fines, normal stress on the inclusion, etc.) on the apparent soil-to-reinforcement friction coefficient (12–15). These experimental results are presently used in design guidelines for Reinforced Earth retaining structures (16). The principles of frictional soil-reinforcement interaction in reinforced embankments and nailed-soil walls are apparently similar. Consequently, an attempt has been made by Cartier and Gigan (7) to correlate the results of full-scale pullout tests on actual nails with design recommendations for Reinforced Earth structures. The results of full-scale pullout

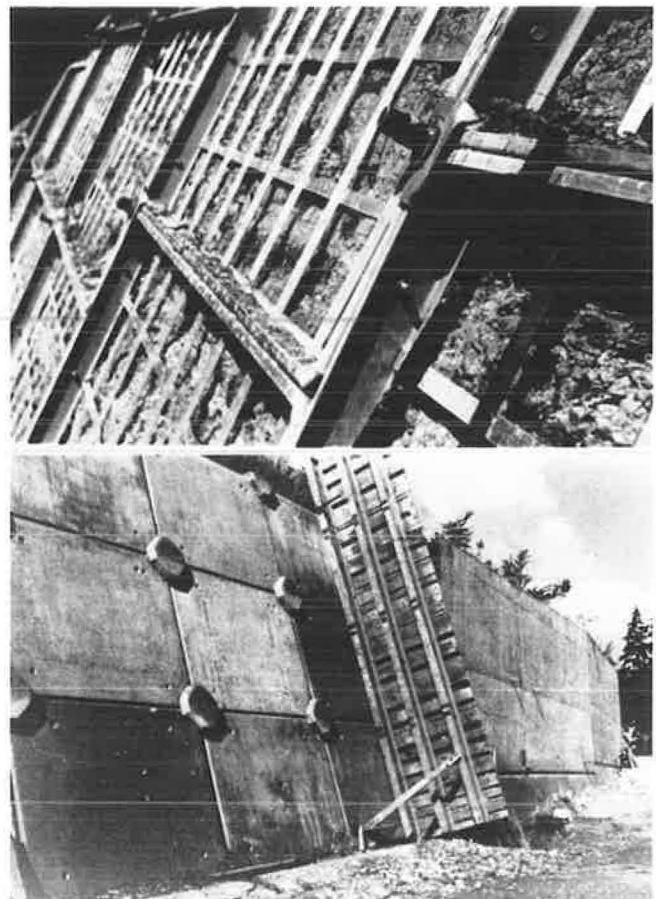


FIGURE 4 Prefabricated steel panels (top) and prefabricated concrete panels and nail connections (bottom).

tests performed by Cartier and Gigan (7) have shown (Figure 5) that the apparent friction coefficient (μ^*) between a driven nail and a granular soil corresponds to that used in the design guidelines for Reinforced Earth walls. However, as indicated by different authors (17,18), the mobilization of soil-to-reinforcement friction is highly dependent on the technique used to install the inclusions. In a Reinforced Earth wall the soil is

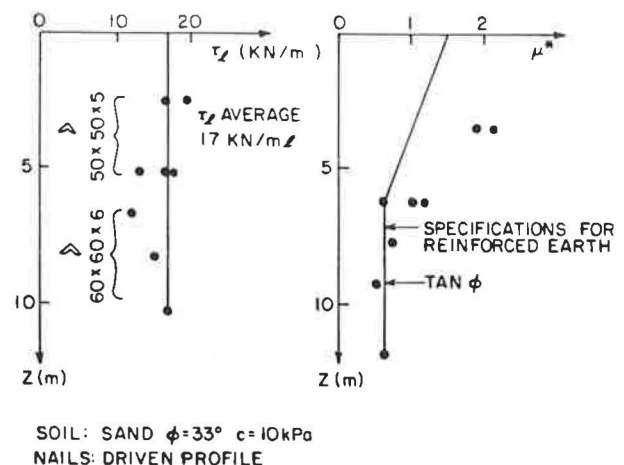


FIGURE 5 Soil reinforcement friction between a driven nail and a granular soil (7).

compacted around the inclusion and is practically at a K_0 state of stress, whereas in nailed ground the drilling of the borehole for the grouted nail produces an unloading of the disturbed surrounding soil that can significantly affect its mechanical properties. In the latter case, the soil-inclusion friction is governed by soil recompaction due to grouting and the characteristics of the soil-grout interfaces are quite different from those of metallic surfaces in Reinforced Earth walls. In addition, the granular backfill material generally used in Reinforced Earth walls is rather uniform and can be significantly different from the ground to be nailed. Therefore, design guidelines for Reinforced Earth walls should not be extrapolated to nailed-soil structures, and pullout tests are required to obtain a reliable estimate of the limit lateral interface shear stress (or the apparent friction coefficient).

In soil nailing it is practical to use design parameters derived from the results of in situ tests. Guilloux and Schlosser (18) have shown (Figure 6) that empirical design methods for fric-

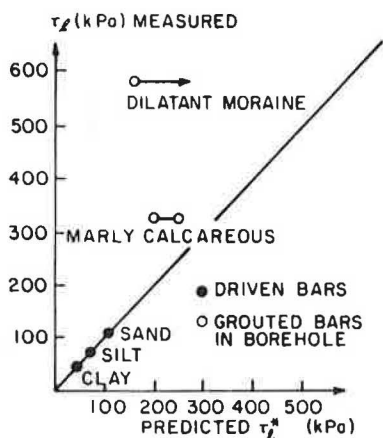


FIGURE 6 Comparison of measured soil-bar lateral friction and design guidelines for friction piles using pressuremeter test results (18).

tion piles using pressuremeter test results can provide a reasonable estimate of the lateral limit shear stress for driven nails. However, their results indicate that such empirical methods tend to significantly underestimate the limit shear stress along grouted bars in compacted dilatant soils. Figure 7 shows the variation of pullout resistance of grouted nails with adherence length in different types of soils. The large variation of pullout resistance with type of soil clearly indicates that in situ pullout tests are required to obtain site-relevant design parameters. However, correlations between limit lateral shear stress and in situ measured soil properties can be developed to provide an appropriate data base for preliminary design considerations.

Normal Passive Soil Thrust on Inclusions

In general, in nailed-soil structures, the small-diameter inclusions currently used are relatively flexible. Therefore tension is the major resisting force developed in the inclusions under

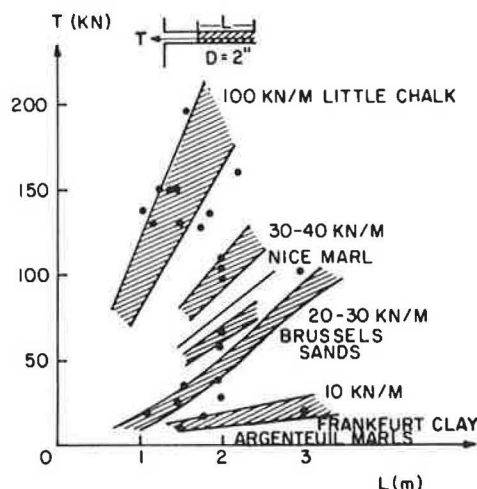


FIGURE 7 Variation of pullout resistance of reinforcing elements with depth of embedment (cement or resin grout) for different soils (C. Louis, unpublished results, 1985).

working stress conditions. However, the development and potential use of stiffer reinforcing elements, such as jet-grouted nails or large-diameter nails, can result in mobilization of a normal lateral soil pressure on the inclusion at both sides of the failure surface. Consequently, this inclusion will have to withstand tension forces, shearing, and bending moments.

The normal soil pressure on the nail can be calculated using the conventional p - y method for laterally loaded piles. Because the nails are relatively flexible, available solutions for laterally loaded infinitely long piles can be used for design purposes. The lateral passive soil pressure on the inclusion must be less than the ultimate pressure (p), which is attained as the soil reaches limit state of plastic flow between the inclusions.

Facing Displacement

Several full-scale experiments have been reported on nailed-soil retaining structures (4,5,7,10,19,20). Figure 8 shows field measurements of facing displacements and ground movement in four instrumented structures. In spite of the significant differences among the types of inclusions, installation techniques, and soil profiles, the experimental results indicate that in non-plastic soils maximum facing displacement does not exceed 0.3 percent of the structure height.

The variations of the tension forces along the inclusions are similar to those observed on Reinforced Earth walls. The locus of maximum tension forces separates, in the nailed-soil mass, the "active zone" behind the facing from the "resistance zone" where the inclusion is being retained by the friction mobilized at the interfaces. It constitutes a potential failure surface for the nailed-soil mass and is quite different, even in a granular soil, from the Coulomb's failure plane that is conventionally considered in design of rigid retaining walls with a granular backfill.

Although there is an apparent similarity between nailed-soil cut slopes and reinforced embankments, there are significant differences between these two retaining systems, particularly

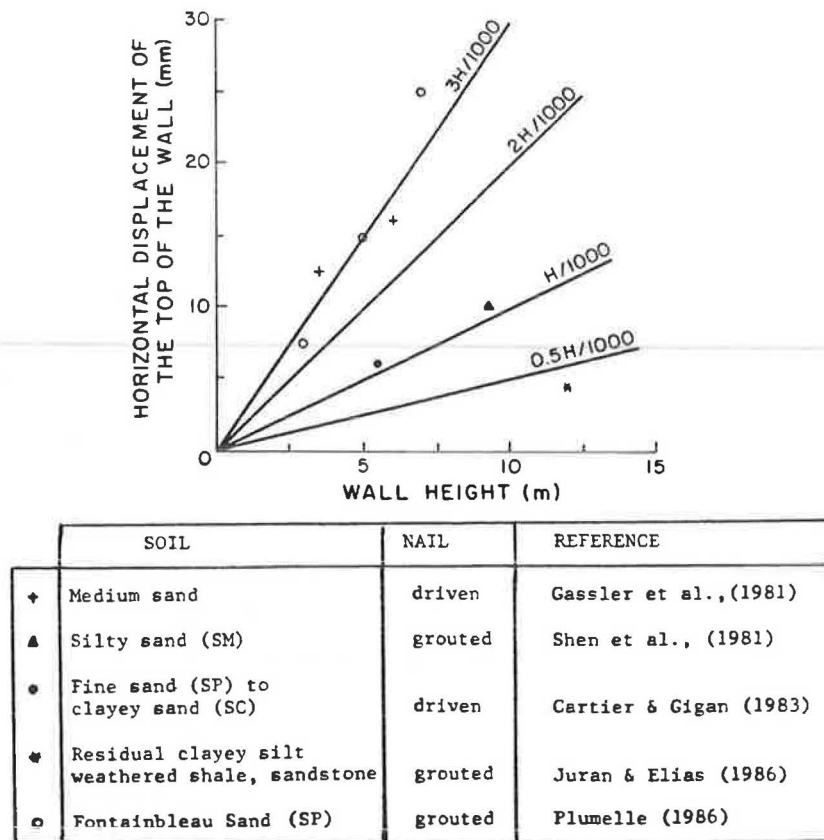


FIGURE 8 Horizontal displacement of nailed-soil walls.

(a) the construction process, (b) the installation technique used for the inclusion, (c) the inclination of the inclusion and of the facing, and (d) the bending stiffness of the inclusion.

Effect of Construction Process

The substantial differences between the construction process for nailed-soil and Reinforced Earth walls (excavation versus

embankment) result in a significantly different displacement mode of the facing and stress history of the retained soil. Figure 9 shows the maximum tension forces measured in a Reinforced Earth wall (21) and in a nailed-soil wall (7) with driven nails in granular ground. In both structures, the reinforcement tends to maintain the retained soil in a K_0 state of stress; however, the differences in construction process lead to quite different distributions of the maximum tension forces with depth. Reduced-scale laboratory model tests performed by Juran and coworkers

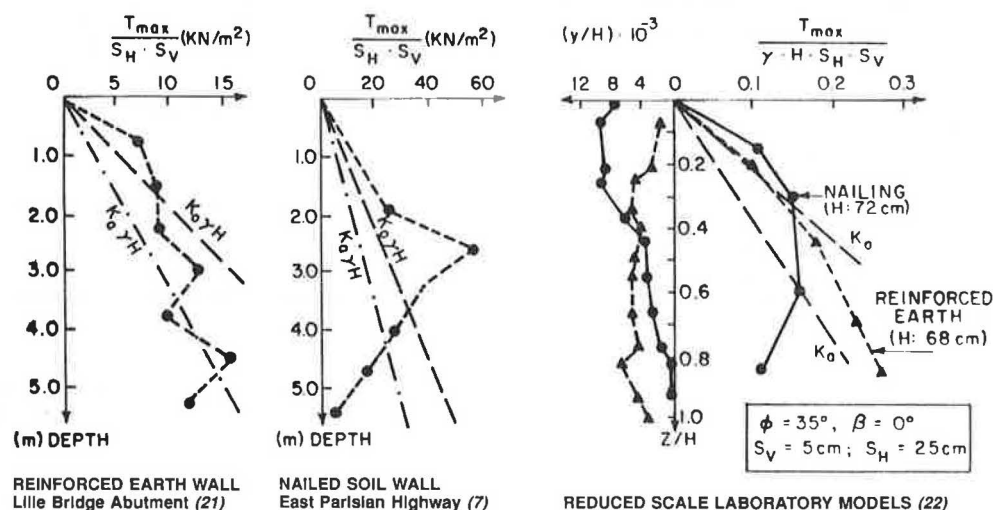


FIGURE 9 Effect of construction mode on facing displacements and maximum tension forces.

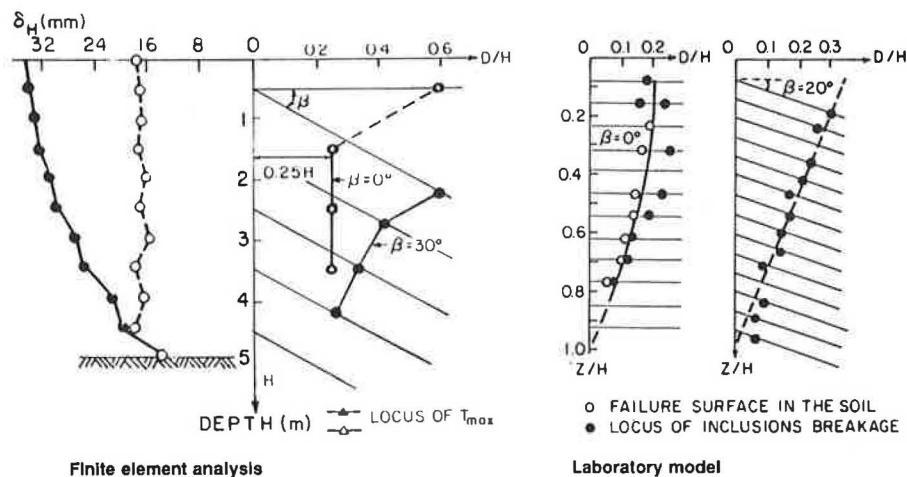


FIGURE 10 Effect of Inclination of Inclusions on facing displacement and on locus of maximum tension forces (22).

(22) indicated that these distributions are associated with two different displacement modes of the facing.

Inclination of Inclusions

Inclination of the inclusions may be an important design parameter. Laboratory model studies and finite element analyses (23) have indicated (Figure 10) that the locus of maximum tension forces in the inclusions and the failure surface in the soil are practically perpendicular to the inclusions at the upper part of the structure. Consequently, inclining the inclusion downward leads to a larger potential failure surface and re-

duces the pullout resistance of the inclusions. These studies also showed that increasing the inclination of the reinforcement results in a significant increase of the facing displacement (Figure 10). The effect of the inclination of the reinforcement on the tension forces generated in the inclusions depends primarily on the construction process. As shown in Figure 11, in a Reinforced Earth model wall the inclination of the reinforcement results in a decrease of maximum tension forces, which approach the K_a line of the active earth pressure distribution, whereas in a nailed-soil model wall the increase of the facing displacement during excavation is associated with an increase of tension forces in the nails. However, within the range of inclinations encountered in practice ($\beta = 10$ to 20 degrees) the effect of inclination on tension forces is not significant.

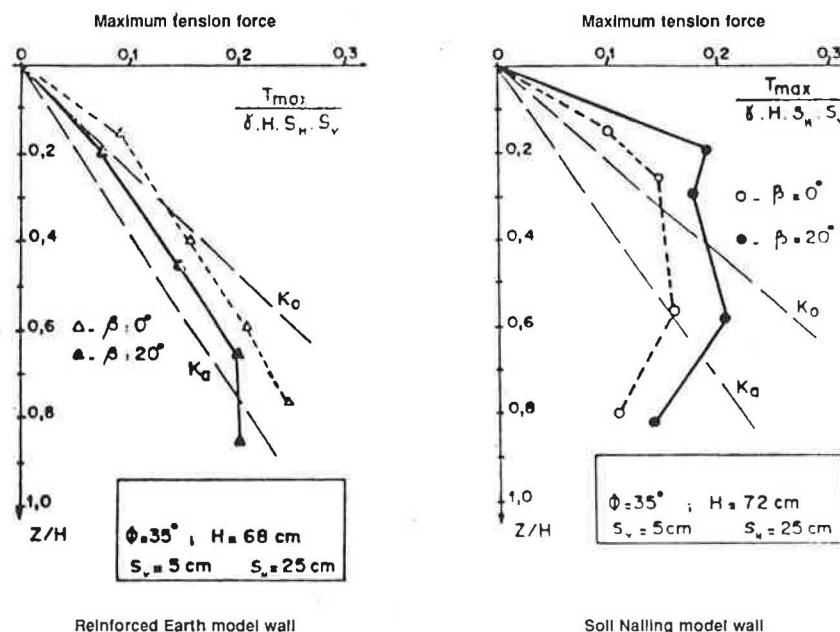


FIGURE 11 Effect of inclination of inclusions on maximum tension forces (22); commas should be read as decimals.

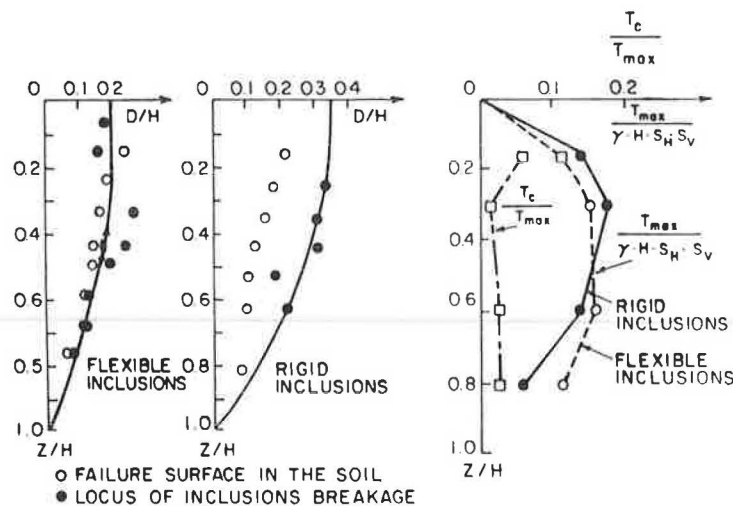


FIGURE 12 Effect of bending stiffness of inclusions on maximum tension forces and on failure of nailed-soil model walls (22).

Bending Stiffness

Bending stiffness can significantly affect the mobilized resisting forces and the failure mechanism. Its effect on nail forces is highly dependent on the inclination of the inclusion with respect to the potential failure surface. The small-diameter nails presently used are relatively flexible. However, installation techniques such as jet grouting lead to the introduction of high-strength composite grouted inclusions that can be quite stiff. As indicated previously, the soil displacement required to mobilize the shear resistance and bending stiffness is significantly larger than that required to generate tension forces. Therefore, as long as the soil displacements are relatively small, the bending stiffness of the inclusions has practically no effect on the behavior of the structure. Both laboratory model tests and finite element analyses (23) have shown (Figure 12) that, under working stress conditions, the shear forces (T_c) mobilized in the inclusions are relatively small ($T_c/T_{max} < 10$ percent) and have practically no influence on the locus and values of maximum tension forces (T_{max}).

The laboratory model tests have also demonstrated (Figure 13) that, at failure by breakage of the inclusions, increasing their bending stiffness results in a significant decrease of the

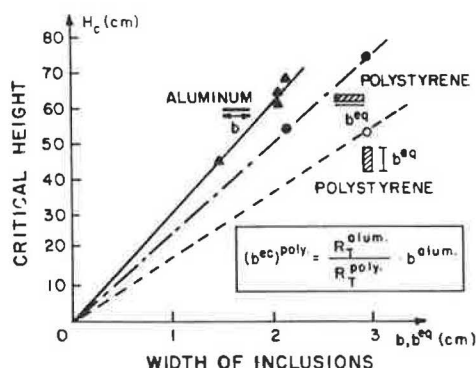


FIGURE 13 Effect of bending stiffness on failure height of a nailed-soil model wall (22).

critical failure height of the model wall. In these models, the polystyrene strips (6 mm thick) have the same tension resistance ($R_T \cdot b$: b = width of the strips) as the aluminum strips (15 μ m thick) but a significantly larger bending stiffness, which depends on their vertical or horizontal position. As is shown in Figure 12, in the case of failure by excessive bending of the inclusions, the locus of breakage points (points of maximum bending) is located behind the failure surface in the soil. The bending stiffness appears to have practically no effect on the failure surface in the soil, which corresponds to the locus of maximum tension and shear forces in the inclusions. However, further research is required to develop a better understanding of the potential effect of reinforcement bending stiffness on the behavior of nailed-soil structures.

DESIGN METHODS

The design criteria for nailed-soil structures include

- Stability with respect to the potential failure of the soil, the inclusion (excessive tension or bending), and their interaction (pullout failure or plastic flow of the soil between the inclusions);
- Admissible displacements with respect to expected performance of the structure;
- Durability requirements for permanent structures, particularly in aggressive environments;
- Environmental and architectural aspects; and
- Design of the facing generally done after conventional structural analysis.

Two fundamentally different design approaches have been developed: (a) modified slope stability analysis and (b) kinematic limit analysis.

Modified Slope Stability Analysis

The first design approach is based on rather conventional slope stability analysis procedures that have been adapted to evaluate the safety factor of the nailed-soil mass and the surrounding

ground with respect to failure along potential circular or wedge-shaped sliding surfaces. When such a method is used for the design of a nailed-soil structure, the conventional slope stability analysis procedure is modified to account for the available limit shearing, tension, and pullout resistance of the inclusions crossing the failure surfaces.

Available design methods that are derived from this approach (4,6,19) involve different assumptions about the definition of the safety factors, the shape of the failure surface, the type of soil-reinforcement interaction, and the resisting forces in the inclusions. Stocker and coworkers (4) proposed a force equilibrium method that assumes a bilinear sliding surface, whereas Shen et al. (6) proposed a similar design method with a parabolic sliding surface. Both methods consider only the tension capacity of the inclusions.

A more general solution, including the two fundamental mechanisms of soil-inclusion interaction (lateral friction and passive lateral soil reaction), has been developed by Schlosser (19). This solution involves a slices method (e.g., Bishop's modified method or Fellinius's method) with a multicriteria analysis procedure. As shown in Figure 14, this method takes into account both the tension and the shearing capacity of the inclusions as well as the effect of their bending stiffness. When the inclusion is expected to withstand both tension (T_{max}) and shear (T_c) forces, the available limit resisting forces in the inclusion depend on its inclination with respect to the failure surface. These limit forces are calculated according to the principle of maximum plastic work and considering Tresca's failure criterion. However, a parametric study on the effect of various design parameters (24) appears to indicate that, in the case of nailed-soil retaining structures, the bending stiffness of the inclusion has only a limited effect on the calculated safety factor (less than 6 percent). Therefore, for the practical purpose of a working stress design, a simplified stability analysis can be done assuming that the inclusions withstand only tension forces. In this analysis no consideration is given to the mo-

ments generated in the nails, which, as shown in Figure 13, can significantly affect the critical height at failure by excessive bending of brittle reinforcements. In the case of steel reinforcement, local plastic bending will not generate rupture of the reinforcement, which will withstand tension and shear forces.

These design methods do not provide a solution for the maximum tension and shear forces developed under the expected working loads. They can only be used to evaluate the safety factors with respect to the shear strength characteristics of the soil and the soil-inclusion lateral friction. It is implicitly assumed that the safety factors with respect to soil cohesion (F_c), friction angle (F_ϕ), and limit lateral shear stress (F_l) are equal and the required safety factor has to be greater than 1.5. These methods have been successfully used to predict or analyze failures in centrifugal models (6) as well as in a limited number of full-scale structures (24,25).

It should be noted that most failures that have been reported in the literature occurred as a result of pullout of the inclusions. Postfailure analyses have shown that the failure could be approximately predicted using an appropriate value of the limit shear stress mobilized at the soil-inclusion interfaces. These observations strongly suggest that pullout tests on actual inclusions should be carried out during excavation to verify the assumed design value of the soil-inclusion lateral friction.

Kinematic Limit Analysis

The second design approach (26) is based on a limit analysis that associates a kinematically admissible displacement with a failure mode as observed on model walls with a statically admissible limit equilibrium solution. The main design assumptions, shown in Figure 15, are that (a) failure occurs by a quasi-rigid body rotation of the active zone that is limited by a circular failure surface perpendicular to the uppermost inclusions; (b) at failure, the locus of maximum tension and shear forces coincides with the failure surface developed in the soil; (c) the quasi-rigid active and resistant zones are separated by a thin layer of soil at a limit state of rigid plastic flow; (d) the shearing resistance of the soil, as defined by Coulomb's failure

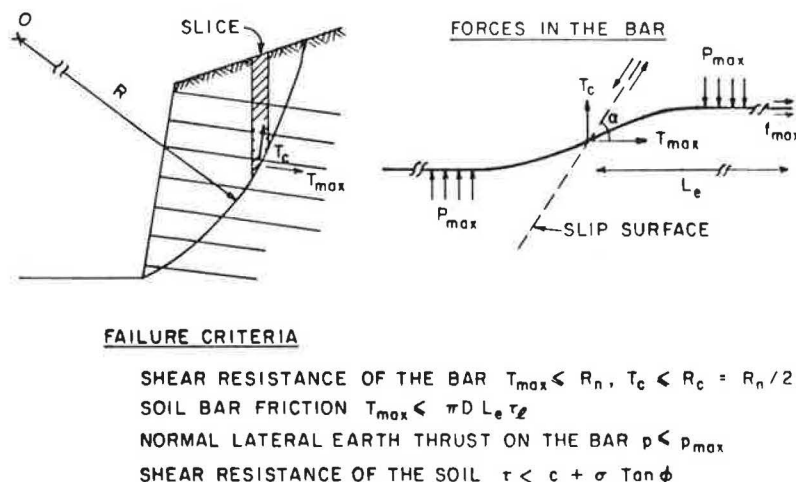


FIGURE 14 Multicriteria slope stability analysis method for design of nailed-soil retaining structures (19).

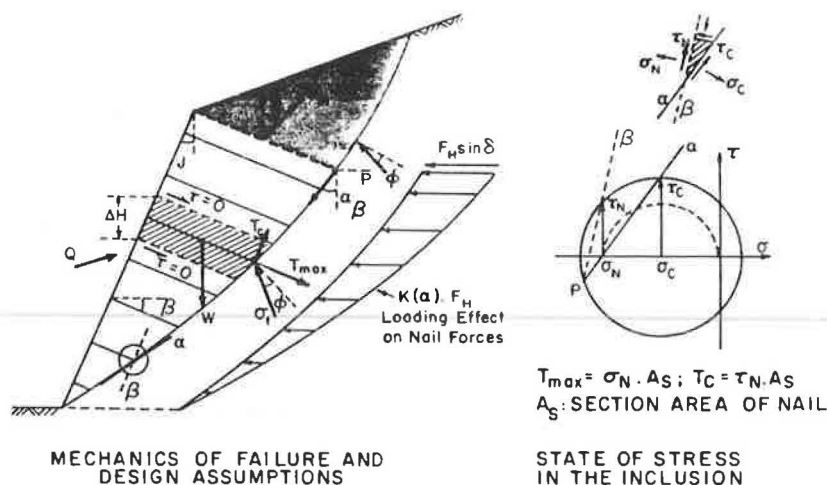


FIGURE 15 Kinematic limit analysis approach (26).

criterion, is entirely mobilized all along the failure surface; (e) the horizontal components of the interslice forces acting on the slices shown in Figure 14 are equal; and (f) the effect of a slope (or a horizontal surcharge) at the upper surface of the nailed-soil mass on the forces in the inclusions decreases linearly along the failure surface.

The effect of the bending stiffness is analyzed considering available solutions for laterally loaded infinitely long piles. It is assumed that the maximum shear stress in the inclusion (τ_c) is mobilized in the direction (α) of the sliding surface in the soil. Therefore, the ratio of T_c to T_{max} depends only on the inclination of the inclusion with respect to the failure surface ($\alpha-\beta$), where the actual inclination of the deformed reinforcement is calculated from the elastic solution for laterally loaded piles. A unique circular failure surface that verifies all of the equilibrium conditions of the active zone can be defined. The normal soil stress along this failure surface is calculated using Kotter's equation, and the tension and shear forces in each

inclusion are calculated from the equilibrium of the slice comprising this inclusion. This design approach provides an estimate of the locus and values of maximum tension and shear forces mobilized in the inclusions.

Figure 16 shows a comparison between predicted and measured values of maximum tension forces in a nailed-soil model wall (22) and in a 7-m-deep experimental wall in granular ground [field data obtained on this wall were reported by Plumelle (27)]. The values of maximum tension forces (T_{max}) are represented as a nondimensional parameter [$k = T_{max}/(\gamma \cdot H \cdot S_H \cdot S_V)$] at the relative depth (z/H), where H is the total structure height, S_V and S_H are, respectively, the vertical and horizontal spacings, and γ is the unit weight. This comparison indicates that the proposed design approach provides a reasonable estimate of tension forces mobilized in the inclusions. However, this design method can only be used to analyze cases involving relatively simple geometry and homogeneous ground with no water flow.

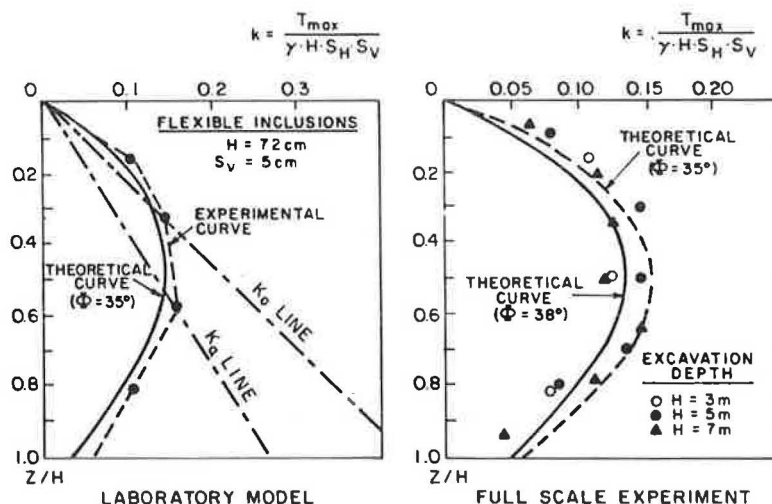


FIGURE 16 Comparison of measured tension forces in a laboratory wall model (22) and a full-scale structure and theoretical predictions using the kinematic method (27).

The main drawback of the design methods presented is that, as limit analysis procedures, they do not consider allowable displacements that are a key design criterion. This limitation is also associated with conventional slope stability analyses in which the required safety factor is generally related to the anticipated displacements by empirical correlations that depend on the site or the soil type. Further research and observations on full-scale structures are required to develop such empirical correlations for nailed-soil retaining structures as a function of soil type and nailing technology.

ADVANTAGES, LIMITATIONS, AND CONCLUSIONS

Soil nailing provides engineering solutions that can economically replace more conventional cut-slope retaining systems such as cast-in-place reinforced-concrete walls, soldier pile walls, and bracing systems. Its main advantages are its

- Relatively low cost, particularly in difficult site conditions. Typically a significant economy can be achieved by using the in situ ground as a main construction material with relatively cheap inclusions. The shotcrete or prefabricated facing has only a local role and it is therefore relatively thin and inexpensive.
- Flexibility in adapting the technology (nails, installation technique, facing) to site conditions and soil profile and the use of light construction equipment, which is of particular interest in sites with difficult access. It is also relatively easy to modify or optimize the initial design during construction.
- Structural flexibility, which provides the nailed-soil retaining system with the capacity to withstand larger total and differential settlements compared with more conventional rigid cut-slope retaining structures.

Nailed-soil retaining structures are both flexible and massive and are therefore expected to have high resistance to dynamic loads. Consequently, this technique can be of particular interest in seismic zones. However, the seismic resistance of nailed grounds has not yet been investigated.

At present the main limitations of the technology concern

- Application in clayey soils where saturation and creep can significantly affect soil-inclusion interaction and structure displacements and
- Durability of inclusions for permanent structures in aggressive environments.

The design methods presently used provide an efficient engineering tool for evaluating an assumed structure design and assessing the stability of the structure with respect to the potential failure of the soil, the inclusions, or their interaction. However, they do not provide an estimate of either the structural displacements or the resisting forces mobilized in the inclusions under the expected working loads. The proposed kinematic approach appears to provide a reasonable estimate of nail forces.

Because most failures that have been reported in the literature occurred as a result of pullout of the inclusions, tests on actual inclusions should be carried out during excavation to verify the assumed design value of the soil-inclusion lateral friction.

Finally, it should be emphasized that development of soil-nailing technology has been essentially empirical and field experience has significantly preceded theory and fundamental research. However, with the increasing application of soil nailing in permanent structures, full-scale experiments as well as laboratory experimental and theoretical studies on the system behavior and soil-inclusion interaction in different types of soils are required. These studies should lead to improvement of the available design methods, to development of appropriate guidelines for predicting structure displacements in different types of soils, and to formulation of design recommendations for nailed-soil cut slopes in soft clayey grounds.

ACKNOWLEDGMENT

A substantial part of the work summarized in this paper was done as a contribution to the NCHRP Report on Reinforcement of Earth Slopes and Embankments (Project 24-2). The contribution of F. Schlosser, l'Ecole Nationale des Ponts et Chaussées, Paris; J. K. Mitchell, University of California, Berkeley; and W. C. B. Villet, Dames and Moore, to preparation of the NCHRP report is acknowledged and highly appreciated. The author wishes also to thank C. Louis and V. Elias for numerous discussions and useful comments and A. Guermazi, Louisiana State University, for his participation in preparing this paper.

REFERENCES

1. L. V. Rabcewicz. The New Austrian Tunnelling Method, Parts I-III. *Water Power* (London), Nov., Dec. 1964 and Jan. 1965.
2. S. Rabejac and P. Toudic. Construction d'un mûr de soutènement entre Versailles-Matelos. *Revue Générale des Chemins de Fer*, 1974, pp. 232-237.
3. C. Hovart and R. Rami. Elargissement de l'emprise SNCF pour la desserte de Saint-Quentin-en-Yvelines. *Revue Travaux*, 1975.
4. M. F. Stocker, G. W. Korber, G. Gassler, and G. Gudehus. Soil Nailing. International Conference on Soil Reinforcement, Paris, France, Vol. 2, 1979, pp. 469-474.
5. C. K. Shen, S. Bang, J. M. Romstad, L. Kulchin, and J. S. Denatale. Field Measurements of an Earth Support System. *Journal of the Geotechnical Engineering Division*, ASCE, Vol. 107, No. GT12, 1981.
6. C. K. Shen, S. Bang, and L. R. Herrmann. Ground Movement Analysis of an Earth Support System. *Journal of the Geotechnical Engineering Division*, ASCE, Vol. 107, No. GT12, 1981.
7. G. Cartier and J. P. Gigan. Experiments and Observations on Soil Nailing Structures. *Proc., Seventh Conference of the ECSMFE*, Helsinki, Finland, 1983.
8. A. Guilloux, Notte, and Gonin. Experiences on a Retaining Structure by Nailing. *Proc., Seventh Conference ECSMFE*, Helsinki, Finland, 1983.
9. C. Louis. Nouvelle méthode de soutènement des sols en déblais. *Revue Travaux*, No. 553, 1981.
10. G. Gassler and G. Gudehus. Soil Nailing—Some Soil Mechanical Aspects of in situ Reinforced Earth. *Proc., 10th ICSMFE*, Stockholm, Sweden, Vol. 3, 1981, pp. 665-670.
11. *Soil Improvement—A Ten Year Update*. Special Geotechnical Publication 12. ASCE, New York, 1987.
12. F. Schlosser and V. Elias. Friction in Reinforced Earth. Presented at Symposium on Earth Reinforcement, ASCE Annual Convention, Pittsburgh, Pa., 1978.
13. F. Schlosser and A. Guilloux. Le frottement dans le renforcement des sols. *Revue Française de Géotechnique*, No. 16, 1981.
14. A. Guilloux and F. Schlosser. Etude du frottement sol-armature en laboratoire. Presented at International Conference on Soil Reinforcement, Paris, France, 1979.

15. V. Elias. Friction in Reinforced Earth Utilizing Fine-Grained Backfills. *International Conference on Soil Reinforcement*, Paris, France, 1979, pp. 435-438.
16. F. Schlosser and I. Juran. Design Parameters for Artificially Improved Soils. *Proc., Seventh ECSMFE*, Brighton, England, 1979.
17. I. Juran. General Report on Speciality Techniques. Presented at Seventh Asian Regional Conference on Soil Mechanics and Foundation Engineering, Haifa, Israel, 1983.
18. A. Guilloux and F. Schlosser. Soil Nailing—Practical Applications. Presented at Symposium on Soil and Rock Improvement Techniques, A.I.T., Bangkok, Thailand, 1984.
19. F. Schlosser. Analogies et différences dans le comportement et le calcul des ouvrages de soutènement en Terre Armée et par clouage du sol. *Annales de l'Institut Technique du Bâtiment et des Travaux Publics*, No. 418, 1983.
20. I. Juran and V. Elias. Soil Nailed Structures: Analysis of Case Histories. Submitted to the ASCE Spring Convention, Atlantic City, April 1987.
21. I. Juran, F. Schlosser, M. F. Long, and G. Legeay. Full-Scale Experiment on a Reinforced Earth Bridge Abutment in Lille. *Proc., Symposium on Earth Reinforcement*, ASCE, Pittsburgh, Pa., 1978, pp. 556-584.
22. I. Juran, J. Beech, and E. Delaure. Experimental Study of the Behavior of Nailed Soil Retaining Structures on Reduced Scale Models. Presented at International Symposium on In-situ Soil and Rock Reinforcement, Paris, France, 1984.
23. I. Juran, S. Shafiee, and F. Schlosser. Numerical Study of Nailed Retaining Structures. Presented at 11th International Conference on Soil Mechanics and Foundation Engineering, San Francisco, Calif., 1985.
24. M. R. Pelkey. An Evaluation of Design Approaches for Soil Nailing in Excavations. Master's report. Louisiana State University, Baton Rouge, 1986.
25. F. Blondeau, M. Christiansen, A. Guilloux, and F. Schlosser. TALREN, méthode de calcul des ouvrages en terre renforcée. *Proc., International Conference on In-situ Soil and Rock Reinforcement*, Paris, France, 1984, pp. 219-224.
26. I. Juran and J. Beech. Theoretical Analysis of Nailed Soil Retaining Structures. Presented at International Symposium on In-situ Soil and Rock Reinforcement, Paris, France, 1984.
27. C. Plumelle. Special Lecture for the French National Committee of Soil Mechanics, 1986.

Publication of this paper sponsored by Committee on Transportation Earthworks.